

EXPERIMENTAL INVESTIGATION OF THE TENSILE FAILURE OF ROCK IN EXTENSION

A thesis submitted to the University of London

by

Despina Kosta Al-Samahiji

Магистер Наук (Master of Science, Moscow), M.Sc., D.I.C.

In fulfilment of the requirement for the Degree of
Doctor of Philosophy

Department of Geology
Royal School of Mines
Imperial College of Science, Technology and Medicine
University of London

June 1992

LIBRARY
University of Bahrain

ABSTRACT

This research has studied the behaviour of intact rock in extension, as observed by the behaviour of specimens of sandstone and marble. The thesis consists of four parts: the first part, presents a literature review of the behaviour of rock in extension, the fracture mechanics used to describe this behaviour and observations of natural fractures formed in extension.

In the second part a new way of measuring the ultimate strength of rock in extension, the Hoop tension test, has been extensively investigated both in theory and in practice. Experimental investigations using photoelasticity, holography and SEM observations are used to corroborate the theoretical findings of the mathematical and FEM analyses relating to the tensile and compressive regions which exist in the hoop shaped specimens.

The third part of the thesis is concerned with the application of the Hoop tension test to the behaviour of sandstone and marble in extension and the influence of rate of loading, saturation, hoop size and boundary conditions between rock and platens. This part concludes with a comparison of the results obtained from conventional tensile tests and the Hoop test.

Part four is devoted to the conclusions of this research which may be summarised as follows:

- the Hoop tension test provides a trustworthy and predictable method of failing rock in extension, and studying the behaviour of rock in extension.
- rock behaviour in extension appears to be a far more sensitive indicator of the contribution that fabric and possibly mineralogy, and stored strained energy, may make to the mechanical behaviour of intact rock, than measures of cohesion, friction and stiffness gained from compressive shear.

DEDICATED

TO MY PARENTS
for making me the person I am
and

TO MY CHILDREN
for their unwavering support and encouragement during
the time that this thesis has taken to be completed.

ACKNOWLEDGEMENTS

When one writes the Acknowledgements one knows that the "end of the trail" is approaching and this is the time to reflect upon those who have in any way contributed to the completion of the project.

In my case, I wish to express my gratitude to the University of Bahrain for the scholarship and the support provided throughout the time this project has taken to be completed.

My grateful appreciation goes to my supervisor Dr Michael H. de Freitas for his guidance, advice and support at all times. I gratefully acknowledge the value of my long discussions and practical assistance generously provided by my other supervisor Dr John W. Cosgrove.

My sincere appreciation is expressed to Mr R. Marsden whose extensive experimental experience was invaluable with the servo controlled testing, the Direct and Brazilian tests and at the initial stages of setting-up the GDS loading system. Mr B. Clarke for his assistance and advice on many aspects of experimental work and the running of laboratory equipment. Dr I. Leifer and Dr W.M.C McKenzie for allowing me to use the laboratories at Napier Polytechnic to conduct the experiments on Holography and for providing the expertise and knowledge which enabled me to complete the analysis. Mr R. Giddens for his practical assistance and expert advise with the SEM work and Mr N. Royall for sample preparation. Professor M.S. King for the cheerful help with the measurement of the elastic moduli. Dr P. Hooker and Dr B. Menzies of the GDS who readily provided advice on the running of software. Mr K. O'Hara who assisted with the set-up of this equipment. Dr P. Bush, Dr H. Shaw and Dr M.S. Rosenbaum for very useful discussions. Mr J.W. Dennis, Mr M.B. Thompson and Mr A.R. Jones for the sample preparation. Mr P.J.A. Freemantle, Mr C.R. Jerrard

and Mr E.A. Rogers who manufactured the many devices used throughout this research work. Mr Adolfo Cash for the photographic work. Mr M.A. Ahmed for his help with the equipment in the Sedimentology laboratory. Mr Steve Colback for broad discussions on experimental techniques. Mrs Ella Ng Chieng Hin for her expert advice on the figures and the printing of this thesis. Miss Carol Kilby who readily provided the necessary information on administrative matters.

I wish to thank my colleagues Sixtus, Paulo, Mahmoud, Louis, Uta, Christine, Graham, Park and Paul who, in the course of time that we spent together as members of the Engineering Geology research group, have become dear friends and have enriched my life with their experience and their individual background.

I am grateful to my family at home and in this country who were always willing to offer encouragement when the going was tough. My husband who, in his own way, has initiated this experience.

Above all I am most thankful to my children Alex and Dina-Linda, who stoically withstood my many expressions of anxiety and without whose support it could not have been possible to successfully complete this work.

TABLE OF CONTENTS

ABSTRACT 1
DEDICATION 2
ACKNOWLEDGEMENTS 3
TABLE OF CONTENTS 5
LIST OF FIGURES 10
LIST OF TABLES 19
ABREVIATIONS 21

PART ONE 22
CHAPTER ONE 23
INTRODUCTION 23

1.0 INTRODUCTION 23
1.1 TENSILE STRENGTH AND TENSILE TESTING 23
1.2 THE TENSILE STRESS-STRAIN CURVE 24
1.3 TENSILE TESTING 26
1.4 OBJECTIVES OF THIS THESIS 26
1.5 STRUCTURE OF THESIS 27

CHAPTER TWO 29
BRITTLE FAILURE AND THE EXPRESSION OF TENSILE FAILURE IN ROCKS 29

2.0 INTRODUCTION 29
2.1 A BRIEF INTRODUCTION TO RELEVANT PRINCIPLES 29
2.1.1 Stress 29
2.1.2 Effective stress 33
2.1.3 The relationship between principal stresses and brittle failure 35
2.1.4 Failure when the least principal effective stress is tensile 41

2.1 5 The hydraulic fracture mechanism of brittle failure 42
2.1.6 Hybrid extension shear failure 45
2.2 DYNAMICS OF FAILURE 47
2.2.1 Basic aspects of dynamic crack growth 47
2.2.2 Crack branching 50
2.2.3 Basic principles of crack arrest 52
2.3 DESCRIPTION OF NATURAL VEINS 55
2.3.1 Implications of the two types of veins to the process of fracturing 62
2.4 CONCLUSIONS 69

CHAPTER THREE 70
PRINCIPLES OF FRACTURE MECHANICS FOR ROCK 70

3.0 INTRODUCTION 70
3.1 NATURE OF FLAWS 72
3.1.1 Description of flaws 72
3.1.2 Performance of flaws 76
3.2 LINEAR ELASTIC FRACTURE MECHANICS 82
3.2.1 Griffith's theory of rupture 82
3.2.2 Irwin's modification to the Griffith's theory 86
3.2.3 Crack tip plasticity 89
3.3 ELASTIC PLASTIC FRACTURE MECHANICS 94
3.3.1 The J integral 95
3.3.2 The Crack Opening Displacement (COD) approach 98
3.3.3 The relation between J and COD 101
3.4 APPLICATIONS TO ROCK 102
3.4.1 Crack initiation 103
3.4.2 Case studies 110
3.5 CONCLUSIONS 116

PART TWO 119
THE HOOP TEST 120
CHAPTER FOUR 120
THEORY AND PREDICTION 120

4.0 INTRODUCTION 120
4.1 MATHEMATICAL AND FINITE ELEMENT ANALYSES 121
4.1.1 Mathematical analysis 121
4.1.2 The Finite Element model 124
4.2 PHOTOELASTIC ANALYSIS 127
4.2.1 Principles of observation and their interpretation 127
4.2.2 Experimental work 129
4.2.3 Results 131
4.3 CONCLUSIONS 135

CHAPTER FIVE 137
REAL PERFORMANCE 137

5.1 PERFORMANCE OF THE HOOP 137
5.1.1 Tests using the closed loop servo-controlled machine 137
5.1.2 Testing using Pressure Controller (GDS) 142
5.2 HOLOGRAPHIC INVESTIGATIONS 144
5.2.1 Introduction to Holography 145
5.2.2 Two-exposure Holographic Interferometry 146
5.2.3 Experimental procedure 153
5.2.4 Principles of observation and actual visual observations from interferograms and their photographs 155
5.3 CONCLUSIONS 161
5.3 SCANNING ELECTRON MICROSCOPY (SEM) 165
5.3.1 The SEM and the technique 165
5.3.2 Experimental procedure 167

5.3.3 Principles of observations and actual observations 169
5.3.4 Conclusions 177
5.4 CONCLUSIONS FROM THE THEORETICAL AND PREDICTIVE STAGE TO THE REAL PERFORMANCE OF THE HOOP TENSION TEST 180

PART THREE 182
ROCK PERFORMANCE IN EXTENSION 182
CHAPTER SIX 183
DESCRIPTION OF MATERIALS 183

6.0 INTRODUCTION 183
6.1 DESCRIPTION OF SANDSTONE 183
6.2 DESCRIPTION OF MARBLE 185
6.3 SAMPLE STRATEGY 190
6.4 CORING STRATEGY 190
6.5 CONVENTIONAL TENSILE TESTS 196

CHAPTER SEVEN 205
INVESTIGATIONS USING HOOP TENSION TESTS 205

7.0 INTRODUCTION 205
7.1 RESULTS OBTAINED FROM THE GDS PRESSURE CONTROLLER 206
7.1.1 Suggestions for the qualitative interpretation of the obtained curves 208
7.2 INFLUENCE OF THE RATE OF LOADING 210
7.3 INFLUENCE OF VARIOUS OTHER PARAMETERS ON THE BEHAVIOUR OF MARBLE AND SANDSTONE 210
7.3.1 The behaviour of marble 220
7.3.2 The behaviour of sandstone 226

7.4 THE TERRA-TEK TESTING 235
7.4.1 Quantitative interpretation of results 236
7.5 CONCLUSIONS 239
7.5.1 Ultimate strength 239
7.5.2 Load vs deformation in extension 248

PART FOUR 260
CHAPTER EIGHT 261
CONCLUSIONS 261

8.0 Introduction 261
8.1 SOUNDNESS OF THE HOOP TENSION TEST FOR INVESTIGATING THE BEHAVIOUR OF ROCK IN EXTENSION 261
8.2 OBSERVED BEHAVIOUR OF THE ROCK IN EXTENSION 263
8.3 DIFFERENCES BETWEEN CRYSTALLINE AND POROUS ROCKS 266
8.4 FUTURE WORK 267

REFERENCES 269

APPENDIX TO CHAPTER FIVE 277

APPENDIX TO CHAPTER SIX 287

APPENDIX TO CHAPTER SEVEN 304

GENERAL APPENDIX 350

LIST OF FIGURES

Fig. 1.1 Force vs Displacement curve represents the gradual failure of a specimen tested with (a) a stiff system, and (b) with a conventional system. 25

Fig. 2.1 An inclined surface within a prism subjected to normal and shear stresses resulting from a uniaxial compression of the prism. 32

Fig. 2.2 Normal and shear stresses acting on an inclined surface within a prism which is subjected to biaxial compression. 32

Fig. 2.3 The Mohr's circle: a graphical representation of a biaxial stress field. 32

Fig. 2.4 A porous medium with the representation of fluid pressure developed when the medium is subjected to compressive stress. 36

Fig. 2.5 A graphical representation by Mohr's stress circles of the total stress and the influence that fluid pressure has on it. 36

Fig. 2.6 A graphical representation of the Navier-Coulomb failure envelope (CAN') which is assumed to be valid in both the tensile and the compressive regions. 36

Fig. 2.7 Griffith's failure envelope. 40

Fig. 2.8 Combined Griffith/Navier-Coulomb failure envelope. 40

Fig. 2.9 Hybrid and tensile failure conditions as prescribed by the geometry of the parabolic failure envelope of Griffith's failure criterion. 40

Fig. 2.10 Hydraulic fracture mechanism used to experimentally determine the tensile strength of rock based on $(S_3-p)>T$; in this case T=p because no confining principal stress exists. 44

Fig. 2.11 Secor's conceptual model used to demonstrate the effect of fluid pressure on fracturing. 44

Fig. 2.12 Two flaws under different magnitudes of external fluid pressure (a) without tendency to propagate and (b) with tendency to propagate. 44

Fig. 2.13 The end segment of Griffith's failure envelope showing the stress condition for hybrid extension/shear failure fractures and the predicted angle

(2Θ) between them. 46

Fig. 2.14 A composite diagram of the Griffith/Navier-Coulomb failure envelope showing the Mohr's stress circles associated with tensile and shear failure. 46

Fig. 2.15 Schematic representation of shear and tensile failure. 46

Fig. 2.16 The classical trimodal pattern, which shows the material behaviour between the subcritical crack-growth and catastrophic failure as a dependence of crack velocity vs stress intensity factor (K) or strain energy release rate, G. 48

Fig. 2.17 A diagram showing the excess in energy some time after initiation of unstable crack extension under plane strain conditions. 51

Fig. 2.18 Crack branching in glass plates with an initial notch in mode I loading; bluntness decreases from a to f. 52

Fig. 2.19 Crack arrest in terms of an energy balance for plane strain conditions with R (a) insensitive and (b) sensitive to crack velocity. 53

Fig. 2.20 Crack arrest in terms of a balance of total energies for plane strain conditions with R insensitive (a) and R sensitive (b) to crack velocity. 54

Fig. 2.21 Effect of initial crack length on G_{arrest} for a strain rate insensitive material under plane strain conditions. 64

Fig. 2.22a Examples of "wide" veins where (a_i) the termination is not controlled by a lithological boundary, and (a_{ii}) the termination coicides with a lithological boundary. 57

Fig.2.22b and c A "wide" vein with a short thin projection at the tip (b), and a "wide" vein with gradual thinning towards termination resulting into a thin tip (c). 58

Fig. 2.22d_i A wide" vein with sharp tip termination; at the left of the photograph the tip of another fracture is seen. 59

Fig. 2.22d_{ii} Two "wide" fractures whose tips extend a great distance into the matrix. 60

Fig. 2.23 "Thin" veins with the characteristic diffused zone around and at their tips (a) and with equigranular crystal infill (b). 61

Fig. 2.24 A schematic drawing illustrating the syntaxial and antitaxial growth in natural veins. 63
Fig. 2.25 Examples of the process zone expressed as a dilation zone around, and, at the tips of the "thin" veins. 65
Fig. 2.26 Examples of multiple branching. 67
Fig. 2.27 The influence of lithology on the width of a continuous fracture. 68
Fig. 3.1 The three modes of failure of materials. 70
Fig. 3.2 Uniaxial tensile stress vs strain curves for a range of material responses. 71
Fig. 3.3 Crack-crack and crack-pore interactions. 75
Fig. 3.4 Crack extension from an open flaw subjected to compression. 77
Fig. 3.5 Normal stress applied at surface of elliptical open and closed flaws 78
Fig. 3.6 Stresses around a partially closed flaw 79
Fig. 3.7 Flea-on-flea flaw extension 81
Fig. 3.8 Persimmon seed chip formation 81
Fig. 3.9 Griffith's through-cracked plate. 83
Fig. 3.10 Energy balance of a crack in an infinite plate when no work is done by external forces 86
Fig. 3.11 Variation in fracture toughness with specimen thickness 90
Fig. 2.12 An infinite plate containing a crack, loaded biaxially. 90
Fig. 3.13 The Irwin plastic zone 92
Fig. 3.14 Schematic of Irwin's analysis 92
Fig. 3.15 Schematic of Dugdale's analysis 93
Fig.3.16 Dimensionless plane stress and plane strain plastic zones from the Von Mises yield criterion 93
Fig. 3.17 Non-linear elastic behaviour of a loaded uncracked plate. 95
Fig. 3.18 Ranges of applicability of LEFM and EPFM for describing fracture behaviour 99
Fig. 3.19 The influence of structure scale on the concept of continuum in rock mechanics 104

Fig. 3.20 An opening loaded in a biaxial compressive stress field. Ratio of P/Q=0.15 104
Fig. 3.21 Stress-strain relationship for uniaxial tensile loading under strain control 105
Fig. 3.22 Results from a FEM analysis showing the predicted crack growth history in a plate containing a circular opening loaded in compression 106
Fig. 3.23 Model of the process zone in a strain softening geomaterial 109
Fig. 3.24 A representation of the process zone in rock 109
Fig. 3.25 Normal stress distribution along line OA in example case I 112
Fig. 3.26 COD profiles for example problem in case I 113
Fig. 3.27 Normal stress distribution along line OA in example problem in case II 114
Fig. 3.28 COD profiles for example problem in case II 115
Fig. 4.1 A vertical cross section showing the experimental set-up of the Hoop tension test. 120
Fig. 4.2 Diagram showing the loading configuration in a Hoop test. Arrows show the direction of loading. P-platens, S-sample. 122
ig. 4.3 Superimposition principle of pure bending and direct tension applied to the analysis of hoop stresses. 122
Fig. 4.4 Curved beam in pure bending and normal traction. 122
Fig. 4.5 The curvilinear hoop stress distribution. Point C is the location where the tensile stresses become compressive. 124
Fig. 4.6 Distribution of stresses obtained from the finite element analysis 125
Fig. 4.7 The distribution of stresses (MPa), in the hoop obtained from finite element analysis. 126
Fig. 4.8 The pattern of principal stress trajectories in the stressed hoop obtained from the finite element analysis. 126
Fig. 4.9 A series of photographs used for the analysis of isoclinics: the position of polarizer and analyzer is at (a) 0°, (b) 15°, (c) 30°, (d) 45°, (e) 60°, (f) 75°, from the initial position. 132
Fig. 4.10 The pattern of stress trajectories, in the hoop. Solid lines represent

the direction of the minimum principal stress σ_3, and dashed lines the direction of maximum tensile stress σ_1. 133

Fig. 4.11 A series of photographs showing the development of isochromatics in the hoop at various loads: (a) 689.5 (b) 4137 (c) 5516 (d) 10342.5 (e) 13790 (f) 48255 MPa. 134

Fig. 5.1 A load - deformation curve of a sample tested with a stiff system; the post peak sample deformation is possible because the strain energy released by the testing system is less than that required to fail the sample. 138

Fig. 5.2 A drawing and photograph showing the experimental set-up for the closed loop servo-controlled testing 140

Fig. 5.3 Results obtained from testing with the servo-controlled system. The curves have been obtained from information transmitted from the LVDTs on the platens (a,b) and sample (c,d) shown in fig. 5.2 141

Fig. 5.4 Typical curves obtained from testing with the GDS from sandstone (a) and marble (b). 143

Fig. 5.5a The interference of two plane waves, one from the object and the other from the reference beam,travelling toward the same side to create a transmission hologram. 147

Fig. 5.5b The creation of a reflection hologram by two plane waves travelling from opposite sides toward the photographic plate. 147

Fig. 5.6 A schematic diagram showing fringe formation. The irradiance in a plane where fringes are visible consists of a rapidly varying speckle pattern which constitute the fringes of holographic interferometry. 148

Fig. 5.7 Diagram showing the illumination and viewing directions in Single Beam Reflection Holographic Interferometry. 151

Fig. 5.8 Individual diagrams showing each viewing direction and their corresponding planes: the hoop surface lies in the (X - Y) plane. 152

Fig. 5.9 Plan of the optical system for recording and reconstruction in Single Beam Reflection Holography. 154

Fig. 5.10 Experimental set-up. 154

Fig. 5.11 Interferograms from viewing direction V_2: (a) a very even and almost horizontal pattern of fringes is exhibited at 3.0 to 3.2 MPa load, (b) the fringes acquire a different pattern and they are less dense in view of the microcracking which is seen opposite the platen opening at 3.8 to 4.0 MPa load, (c) a high concentration of fringes is built-up at the higher load of 4.4 to 4.8 MPa. The shape of fringes opposite the platen opening clearly shows the tensile and compressive regions in the hoop as well as the isotropic point (see fig. 4.10). 158

Fig. 5.12 Clockwise, the viewing directions are V_1, V_2 and V_3 of the interferogram at loading interval 3.8 to 4.0 MPa, exhibiting the density and direction of fringes as well as the kinks of the fringes. 159

Fig. 5.13 Interferogram from V_3 at loading interval 3.4 to 3.6 MPa, showing the radial pattern of fringes opposite the platen opening. 160

Fig. 5.14d Pre-failure stage: this final stage, before the catastrophic failure of the sample records the highest strains, expressed in the number and thinness of fringes. 164

Fig. 5.15 A schematic representation of the SEM. 166

Fig. 5.16 A plan of the SEM stage with a specimen held by an o-ring 170

Fig. 5.17 A schematic representation of the part of Hoop specimen and platens used in the experiment. 170

Fig.5.18 Micrographs showing the unchanged position of platen-sample boundary opposite the platen opening at 480 kPa (a) and 13200 kPa (b). The sample failed at 15900 kPa. 172

Fig. 5.19 The increasing brightness due to the break-up of the thin sample coating because of the dilation of grain boundaries. 173

Fig. 5.20 The general increase in brightness close to the platen opening at point 6. (a) 5000 kPa and (b) 10900 kPa. 174

Fig. 5.21 The visible dilation of grain boundaries opposite the platen opening: load at (a) 11000 kPa and at (b) 13000 kPa. 175

Fig. 5.22 The fracture as occurred in marble at 15900 kPa, followed from point 6 to point 0 immediately after failure occurred. 176

Fig. 5.23 The widening gap between the platens with increasing load before the sample failed catastrophically.(a) at 1000 kPa, (b) at 5100 kPa and (c) at 6100 kPa load. 178

Fig. 5.24 The development of a zone in sandstone opposite the platen opening before the catastrophic failure of the sample. (a) at 6050 kPa, (b) at 6100 kPa and (c) at 6150 kPa load. 179

Fig.6.1 The Penrith sandstone as seen through the microscope. 184

Fig.6.2 Two photos , plane and crossed Polars of marble 186

Fig. 6.3 Schematic diagram showing the relation between the direction of bedding and place of induced failure in Direct Tension (a_1), Brazilian (b_1) and Hoop Tension (c_1) tests, and a view of the failure surface which in each case (a_2, b_2, c_2) cuts orthogonally to the plane of bedding. 192

Fig. 6.4 Schematic drawing showing the sample orientation for Hoop (HTT), Direct (DTT) and Brazilian (BT) tension tests in respect to Green (GRN) and Black (BLK) directions in sandstone blocks. 193

Fig. 6.5 A schematic drawing showing the sample orientation for Hoop (HTT), Direct (DTT) and Brazilian (BT) tension tests in respect to Green and Black directions in marble slabs. 195

Fig. 6.6 Two photographs showing the rig manufactured for positioning the core at the centre of the platens. 197

Fig.7.1 A schematic representation of a typical Force vs Displacement curve obtained when testing using a GDS system. 207

Fig. 7.2 A schematic representation of the value of Force (a), the value of Displacement (b) and the Work (c) used for calculations. 209

Fig. 7.3 Diagram showing the block of sandstone and the location of samples for the investigation of the rate of loading. 211

Fig. 7.4 Semi-logarithmic plots of $work_{(i)}$ (a), $work_{(ii)}$ (b) and $work_{(iii)}$ (c)for the three rates of loading (common time axis). 214

Fig. 7.5 Linear plots of $work_{(i)}$ (a), $work_{(ii)}$ (b) and $work_{(iii)}$ with logarithmic regression, showing the influence of the rate of loading (common time axis). 215

Fig. 7.6a Diagram showing (stipled), the total failure area in a Hoop tension test. 219

Fig.7.6b Diagram showing the location of the third fracture in a hoop. The shaded area illustrates the range within which the fracture took place. This location could have been on either side of the platens. 220

Fig. 7.7 Plots showing (a) the work per unit area, and (b) the "ultimate strength in extension" experienced by hoops of various diameters in marble at failure. 224

Fig. 7.8 Plots showing the work consumed per unit area (a), and the "ultimate strength in extension"(b), experienced by hoops of various diameter ratios in sandstone at failure. 232

Fig. 7.9 A schematic representation of the suggested three variations of work, considered in the Terra-Tek testing. 237

Fig. 7.10 Schematic representation of apparent brittleness and stiffness of marble and sandstone tested with the GDS system. 250

Fig. 7.11 Diagram showing the pre-failure behaviour of sandstone: (a) shows the short yield before failure and (b) the more gradual yield before failure. 257

Fig. 7.12 Diagrams showing the pre-failure behaviour of marble: (a) illustrates the "pop-in", (b) the concave upwards shape of the displacement and (c) the peculiar form that the curve obtained sometimes. 258

Fig. 8.1 Diagrammatic representation of the tensile and compressive regions in the hoop. 262

Fig. 8.2 Plots of ultimate strength of material in extension vs ratio of diameters of saturated and dry sandstone (a) and marble (b) to illustrate the range of difference between the saturated and dry results, as well as the range of difference within results obtained from the same testing conditions. The plots also show the strength of the rocks in relation to hoop dimensions. 265

LIST OF TABLES

Table 3.1 Description of flaws at micro-scale. 72

Table 6.1 Physical and mechanical characterization of sandstone. 187

Table 6.2 Physical and mechanical characterization of marble. 189

Table 6.3 Table showing the sizes of various hoop classes. 190

Table 6.4(a) Direct Tension tests on oven dry sandstone. 199

Table 6.4 (b) Direct Tension tests on saturated sandstones. 200

Table 6.5 Direct Tension tests on oven dry marble. 201

Table 6.6 (a) Brazilian test results on oven dry sandstones. 202

Table 6.6 (b) Brazilian tests on saturated sandstones. 202

Table 6.7 (a). Brazilian tests on oven dry marble. 203

Table 6.7 (b). Brazilian tests on saturated marble. 203

Table 6.8. Fracture Toughness results on oven dry sandstone. 204

Table 7.1 Results obtained from experiments on the influence of the rate of loading. 213

Table 7.2 Results show the COV between the average values of the three variations of work at the three rates of loading. 217

Table 7.3 Results showing the $Work_{(ii)}$ required to fail the marble hoop samples. 222

Table 7.4 Results showing the "ultimate strength in extension" of the marble hoop samples. 223

Table 7.5 Results showing the $Work_{(ii)}$ required to fail the sandstone hoop samples (Nm/m^2). 228

Table 7.6 Results showing the ultimate strength in extension of the sandstone hoop samples. 230

Table 7.7 Results on the influence of saturation of sandstone. 234

Table 7.8 Results obtained from the closed loop servo-controlled, Terra-Tek testing system. 238

Table 7.9 A simplified table of results obtained from testing with the Terra-Tek. 239

Table 7.10(a) Composite table of ultimate strength results on tension tests in marble. 241

Table 7.10(b) Simplified composite table of ultimate strength results on tension tests in marble. 242

Table 7.10(c) The ratios among the various tension tests in marble. 242

Table 7.11(a) Composite table of ultimate strength results on tension tests on sandstone. 243

Table 7.11(b) Simplified composite table of ultimate strength results on sandstone. 245

Table 7.11c The ratios among the various tension tests on sandstone. 246

Table 7.10(d). Illustration of the position of the ratios relative to each other and the difference of values of ultimate strength in crystalline and porous materials. 246

Table 7.12(a) Results of apparent brittleness, stiffness and ratio of work on marble. 251

Table 7.13(a) Results of apparent brittleness, stiffness and ratio of work on sandstone. 252

Table 7.12(b) A summary of results of table 7. 12(a) for marble with mean values, Std. Dev. and COV. 253

Table 7.13(b) A summary of results of table 7.13(a) for sandstone with mean values, Std. Dev. and COV. 254

Table 7.13(c) Range of values and their differences for apparent brittleness, stiffness and ratio of work $W_{(i)}/W_{(ii)}$. 255

ABBREVIATIONS

BLK = Black direction

GRN = Green direction

BSS = Black Smooth Saturated

BSD = Black Smooth Dry

BRS = Black Rough Saturated

BRD = Black Rough Dry

GSS = Green Smooth Saturated

GSD = Green Smooth Dry

GRS = Green Rough Saturated

GRD = Green Rough Saturated

T-T = Terra-Tek

GDS = Geotechnical Design Systems

SS = Smooth Saturated

SD = Smooth Dry

RS = Rough Saturated

RD = Rough dry

CL = Class, refers to hoop size:

Class I = 1:5, 30/150 mm inner and outer diameter respectively

Class II = 1:3, 50/150 mm " " " " "

Class III = 1:333, 30/100 mm inner and outer diameter respectively

Class IV = 1:2, 50/100 mm " " " " "

SAMP = Sample

OR = Orientation i.e BLK or GRN

LY = Layer, denotes location of hoop in relation to its position on the block.

M.D = Mean Deviation

Std. Dev = Standard Deviation

COV = Coefficient of variation

AVE = Average

BT = Brazilian Test

DTT = Direct Tension Test

HTT = Hoop Tension Test

ISRM = International Society of Rock Mechanics

FR T = Fracture toughness

APP BRIT = Apparent brittleness

STIF = Stiffness

PART ONE

Part one contains three chapters which introduce the basic elements of the subjects used in this research.

Chapter one outlines the basic reasons for doing this work and the general approach that has been adopted during this research to study the behaviour of rock in extension; here it should be emphasized that intact rock is being studied and not rock masses.

Chapter two outlines the basic principles that are used in the thesis particularly those relating to the mechanics of rock and illustrates natural fractures that have been produced in rock by extension; these are the natural equivalent of the laboratory generated tensile fractures reported in this research.

Chapter three reviews the approach to deformation and failure in extension that has been developed by material scientists; it largely concerns fracture mechanics.

CHAPTER ONE

INTRODUCTION

1.0 INTRODUCTION

The starting place of this thesis is the fact that rock fails in extension regardless of the external arrangement of forces which ultimately cause failure to occur. Such externally applied forces can be configured to promote failure in either compression or in shear, but internally and at the scale of micro-crack initiation and propagation, the cracks are forming and propagating in zones where the applied system of forces has been locally rearranged to be in extension. The strength of rock in extension is therefore of considerable significance to understanding the response of rock to stress relief which accompanies unloading, to the use of rock strength in engineering design and to overcoming the strength of rock during drilling, blasting, cutting and comminution: in short it is of interest to geologists, engineers and technologists from many disciplines. It may thus be imagined that a considerable volume of data now exists on the behaviour of rock in extension but this is not so. The compressive strength of rock has been extensively investigated and a vast bank of data now exists regarding this property, yet little data exists for the behaviour of rock in extension.

1.1 TENSILE STRENGTH AND TENSILE TESTING

In a simple manner and in analogy to the compressive strength, the tensile strength of rock may be defined as the maximum stress that a specimen may withstand before failure. However, the question immediately arises as to what this tensile strength implies in relation to the strength of rock in situ. Hudson (1970), has extensively researched the concept of tensile strength and tensile testing and investigated the reasons for the variations in the values of tensile strength obtained

when this property is measured either with the same test or with different tests. Hudson attributes these variations to several factors:

(a) The probabilistic nature of strength. If it is assumed, based on Griffith's theory of rupture, that failure of a specimen is associated with severe flaws present within a specimen, then failure will depend on the most severe flaw present in each specimen, which will vary in intensity from one specimen to another.

(b) Size effects. Larger specimens have greater probability of containing more severe flaws and hence indicate a lower tensile strength. The scatter of values decreases as the specimen size increases because larger specimens are more likely to contain the severe flaws which cause the failure.

(c) Type of tensile testing. The variations in the results obtained from different tensile tests exist because in each test a different critically stressed volume is involved. This variation is based on the fact that rock is inhomogeneous and contains flaws or zones of weakness distributed throughout the rock mass.

1.2 THE TENSILE STRESS-STRAIN CURVE

The general Force vs Displacement curve obtained if a servo-controlled stiff testing machine is used is shown in fig. 1.1a; it represents a gradual micro-structural damage from the onset of failure at point **A** to the complete collapse of the specimen at point **C**. At all times from point **B** to just before point **C** the specimen is sustaining loads, however lesser than the maximum bearing i.e the specimen does not yet fail. If a conventional testing system is used the same Force vs Displacement curve acquires a shape as shown in fig. 1.1b, where **A** is the onset of failure and **B** represents the complete failure of the sample which is usually catastrophic because of the fast fracture. Compressive and tensile tests conducted on a closed-loop servo-controlled machine illustrate behaviour similar to that shown in fig. 1.1. These test results demonstrate that although in both compressive and tensile tests the relevant strengths are calculated from the maximum load bearing capability of the specimen, the evidence shows that failure

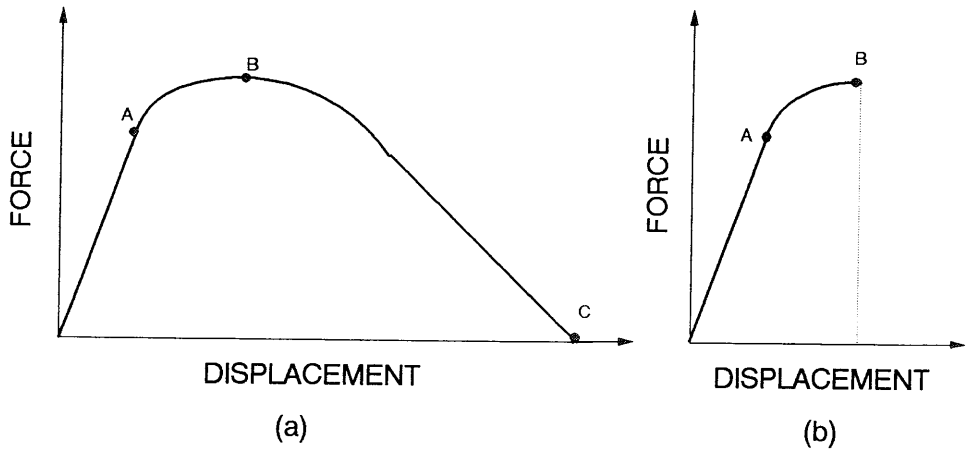


Fig. 1.1 Force vs Displacement curve represents the gradual failure of a specimen tested with (a) a stiff system, and (b) with a conventional system.

initiation and specimen collapse are not synonymous.

A structure-breakdown model developed by Hudson (1970), suggested that the peak of the stress-strain curve, both in tension and compression, is a function of the inhomogeneity of the applied disturbance. (The applied disturbance is the applied strain from a closed-loop servo-controlled machine). This indicates that the peak of the curve should not be regarded as a material property since it is a function of experimental conditions. The only mechanical strength properties are the individual strengths of grains and grain boundaries. All the other apparent material properties or experimental values should be calculated from the elemental mechanical properties and the progression of failure in each test.

The calculation of maximum tensile stress by the theory of linear elasticity also does not inspire confidence in the rightness of the results. For the linear elasticity theory to be valid, the rock must have a linear stress-strain relationship and to be a continuum. However, experimental investigations show that, in general, rock does not behave linearly and in addition cracks which develop during testing prior to peak load render the rock not continuous with respect to the original test geometry.

1.3 TENSILE TESTING

The most widely used tensile tests, such as the Brazilian and the Direct tension tests, have been criticised because of the difficulties they present in their performance. On one hand the Brazilian test can only be valid if the failure initiates in the region of tensile stress (Jaeger and Hoskins, 1966b, and Colback 1966) a fact that is not always achieved even with load distributors at the position where the loading platens come in contact with the specimen disk. On the other hand, the Direct tension test although it appears simple is plagued with difficulties which originate from the fact that the deformation in the specimen is corrupted by the behaviour of the adhesive bonding the ends of the specimen to the loading platens of the test machine.

1.4 OBJECTIVES OF THIS THESIS

In view of the above discussion and despite the suggestion that the tensile strength is not regarded as a material property a need exists to study either the behaviour of rock in extension and to measure the work involved to fail a specimen in extension, because this will provide the geotechnologist at large with a value, which is of paramount importance to understanding rock behaviour under load. Therefore this thesis attempts to

(a) make a contribution towards improving a tensile tension test, which allows such studies to be made, and

(b) to systematically investigate the behaviour of rock in extension.

The first objective, regarding a tensile tension test, has been attempted by the further investigation and development of the Hoop tension test, introduced by Xu et al at Imperial College (1988). In doing so, the effort was concentrated on determining the stress distribution within the deforming hoop. Once a satisfactory understanding of the behaviour of the Hoop test was reached, although by no means complete, this test was used to systematically study the behaviour of a porous and a crystalline rock in extension.

1.5 STRUCTURE OF THESIS

This thesis consists of eight chapters grouped in four parts. Part I consists of the Introduction, which is the present chapter, followed by chapter 2 and chapter 3. These two chapters are largely a review of the existing literature on the subject of fracturing in general and more specifically the failure in rock. Chapter 2 is concerned with brittle failure and the expression of tensile failure in rocks. At the beginning a brief introduction to fundamental principles such as stress, effective stress, the hydraulic fracture mechanism and the basic failure criteria are introduced. The description of some natural veins at micro-scale, such as to corroborate processes described, concludes chapter 2. In chapter 3 the nature of flaws is described, followed by the principles of Linear Elastic and Elastic Plastic Fracture Mechanics.

Part II is totally devoted to the Hoop tension test. It consists of two chapters. In chapter 4 the theory surrounding the hoop as predicted by mathematical and finite element methods and by the experimental technique of photoelasticity is discussed. In this chapter the greater input is placed in the analysis of stress distribution within the hoop. In chapter 5, experimental investigations are presented, which confirm the theoretical predictions of chapter 4. These investigations consist of Hoop tests conducted on the servo-controlled machine and with the pressure controller, a system of loading, the application of Holographic Interferometry to

investigate the hoop behaviour during testing and the use of the Scanning Electron Microscope to examine and record a Hoop tension test in action.

Part III is concerned with the investigation of the behaviour of porous sandstone and crystalline marble in extension. This part, like part II, consists of two chapters. Chapter 6 is totally devoted to the physical and mechanical characterization of the two rocks and to the conventional tensile tests conducted. Chapter 7 is concerned with the results of the Hoop tension tests obtained from tests conducted on sandstone and marble. Here, various parameters have been examined such as the rate of loading, the effect of saturation, the influence of the friction and frictionless boundary conditions at the platen-hoop contact, and the effect of hoop size as expressed by different diameter ratios.

Part IV consists solely of chapter 8, and discusses the findings of this research and suggests some aspects for future investigation.

CHAPTER TWO

BRITTLE FAILURE AND THE EXPRESSION OF TENSILE FAILURE IN ROCKS

2.0 INTRODUCTION

Processes occurring at fracture tips are crucial in the failure behaviour of materials; local conditions at these regions are very different from those obtained in the bulk of the material. Considerable effort has gone into the study of the relationship between the bulk and local conditions within a material, starting with the seminal work of Griffith (1924) and the concept of local stress magnification at fracture tips. It thus seems likely that the special conditions, i.e stress states etc., at fracture tips will result in the occurrence of local deformation processes which do not characterize the behaviour of the rock as a whole.

This chapter is divided into two parts: in the first part an introduction to relevant fundamental principles of stress and brittle failure mechanisms is given; in the second part natural examples of extensional failure (veins) are described and an attempt is made to gather any evidence of the special conditions occurring at fracture tips, expressed mainly as the process zone in front of and around these tips.

2.1 A BRIEF INTRODUCTION TO RELEVANT PRINCIPLES

2.1.1 Stress

Stress is defined as the force per unit area. When a force is applied perpendicular to a surface it results into a corresponding stress which is called principal stress. (By definition any normal stress acting on a surface along which there is no shear stress, is a principal stress). If only one principal stress acts on a body, it is said

to be subjected to uniaxial loading; when two or three principal stresses act on a body the conditions are called biaxial or triaxial loading. If a plane within a body is inclined to the direction of the applied force, that force may be resolved into two components acting on the plane: one acting normal to the plane (F_n) and the other acting parallel to it (F_t). In the same way, if a principal stress is considered to act on the same inclined plane within the body, the corresponding normal compound is called the normal stress (σ_n) and the corresponding parallel compound is called the shear stress (τ).

If one considers a prism subjected to uniaxial compression (fig. 2.1) with an internal inclined surface at θ to the principal stress, the magnitude of the normal stress, (S_n), and shear stress, (τ), on that plane are given by

$$S_n = S_1 \sin^2\theta \tag{2.1}$$

$$\tau = S_1 \sin\theta\cos\theta \tag{2.2}$$

These relationships give the normal and shear stress on any plane inclined at an angle Θ to the principal stress. If a condition of biaxial compression is considered (fig. 2.2) the corresponding normal component is given by

$$S_n = \frac{(S_1+S_3)}{2} - \frac{(S_1-S_3)}{2}\cos 2\Theta \tag{2.3}$$

and the corresponding shear component is given by

$$\tau = \frac{(S_1 - S_3)}{2} sin2\theta \qquad (2.4)$$

If the magnitude of the principal stresses are known, the values of the normal and the shear stresses on any plane with inclination θ varying from 0° to 180°, can be determined, using the above equations. Equations (2.3) and (2.4) have been expressed graphically by Mohr, who plotted the shear against the normal stress for all the values of θ. The resulting plot is known as the Mohr's stress circle. (see fig. 2.3).

Stresses S_1 and S_3 (S_z and S_x), plot on the axis S_n because they are principal stresses and therefore act on surfaces which have no shear stress acting along them. It can be seen from the geometry of fig. 2.3 that S_3 is **OA**, S_1 is **OB**, the distance **OC**, is given by $(S_1+S_3)/2$ and the radius of the circle **AB/2** is given by $(S_1-S_3)/2$. From the geometry of the Mohr circle it can also be seen that the magnitude of the shear stress τ on a plane inclined at θ to S_1 is represented by **XP** and that

$$XP = \frac{S_1 - S_2}{2} sin2\theta \qquad (2.5)$$

Similarly, the magnitude of S_n is **CO** minus **CP**. As can be seen from the fig. 2.3 it follows that

$$S_n = \left(\frac{S_1 + S_3}{2}\right) - \left(\frac{S_1 - S_2}{2}\right) \cos 2\theta \qquad (2.6)$$

As can be seen this is identical to equation 2.3. From the above it is clear, that

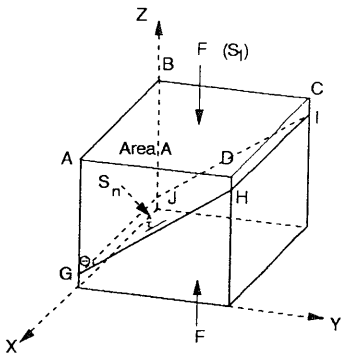


Fig. 2.1 An inclined surface within a prism subjected to normal and shear stresses resulting from a uniaxial compression of the prism. (From Price & Cosgrove, 1990)

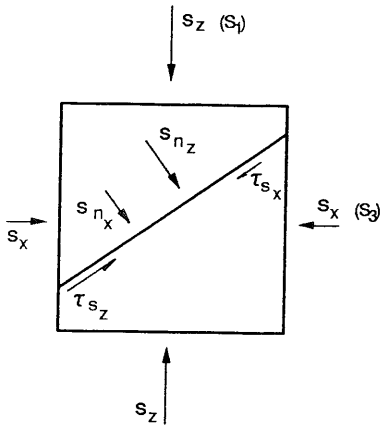


Fig. 2.2 Normal and shear stresses acting on an inclined surface within a prism which is subjected to biaxial compression.(From Price & Cosgrove, 1990)

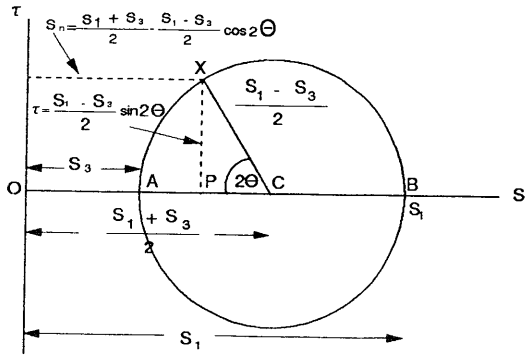


Fig. 2.3 The Mohr's circle: a graphical representation of a biaxial stress field, (From Price & Cosgrove, 1990)

if the two principal stresses, which are represented by points **A** and **B** on the diagram, are known, the Mohr's circle can be constructed, and consequently the normal and shear stresses acting on any plane making an angle Θ with the maximum principal stress can be determined.

The situation where the principal stresses are equal is usually termed a hydrostatic stress, because this is the stress experienced by a fluid at rest. A non-hydrostatic stress system can be described by the mean stress ($\bar{S}$) which is defined by

$$\bar{S}=\frac{S_1+S_2+S_3}{3} \tag{2.7}$$

and is considered to be the hydrostatic part of the stress system because it is only responsible for the **volumetric** changes. The deviatoric stress (S') which is defined by

$$S'=S_n-\bar{S} \tag{2.8}$$

is a measure of how much the normal stress deviates from the mean or hydrostatic in any direction. Deviatoric stress is responsible for **distortional deformation.** Another useful parameter is the differential stress (S_1-S_3) which is a further measure of the ability of a stress field to cause deformation.

2.1.2 Effective stress

It is known that fluids in rocks, whether water, brine or hydrocarbons, have a certain influence on rock strength. This influence is both chemical and mechanical.

It has been noted that the chemical effect of water is related to the fact that adsorbed water reduces the surface energy of the walls of a pore, flaw or microfracture and in this manner enhances the ease of propagation of that surface, provided suitable stress conditions exist. The adsorbed water also affects the rock chemically by promoting pressure solution at high temperatures and by facilitating the migration of inorganic species. However, after wetting has occurred on a surface the chemical effect is small compared with the mechanical influence of liquid pressures. This mechanical effect reduces the ability of rock to withstand the effects of differential stress and influences the mode of deformation i.e when a rock is subjected to modest confining pressures and low fluid pressures it may deform as a brittle material, but if the fluid pressures approach the magnitude of the confining pressure the rock tends to behave in a ductile manner.

The influence of pore fluid pressure present in a porous medium on the total stress acting on this medium has been known since 1923 when Terzarghi investigated the behaviour of soils. Consider a porous medium as shown in fig. 2.4 which is subjected to a bulk compression (S); stresses (σ) occur in the grains and fluid pressure (p) develops in the fluid occupying the pores. The relationship between these stresses is represented by

$$\sigma' = S - p \qquad (2.9)$$

where σ' is the effective stress, responsible for the deformation of the granular mass.

If equations (2.3), for normal stress and (2.4) for the shear stress are rewritten to take in consideration the fluid pressure, they become

$$\sigma_n = S_n - p \tag{2.10}$$

$$\tau = T_r \tag{2.11}$$

where S_n and T_r are the total normal and shear stresses respectively, acting on an internal surface, which makes an angle Θ with the axis of maximum compression.

Hence, the influence of the pore fluid is such that it reduces the effective normal stress acting on any arbitrary plane, but has no effect on the shear stress. If the total and effective stresses are represented graphically on the Mohr circle, it is clear that the effective stress circle is transposed to the left by the amount of fluid pressure while the shear stress acting on any plane at an angle Θ to the axis of maximum principal stress, remains unchanged. This is shown in fig. 2.5.

2.1.3 The relationship between principal stresses and brittle failure

The relationship between S_1 and S_3 at failure for some rocks is linear and their relationship can be expressed by the following equation:

$$\sigma_1 = \sigma_0 + k\sigma_3 \tag{2.12}$$

where σ_0 is the uniaxial compressive strength of the rock and k a constant.

Often rock specimens fail in shear when subjected to biaxial compression. Usually the specimens fail along one shear plane but occasionally they exhibit two conjugate shear planes of failure. The acute angle (2Θ) between them, is bisected

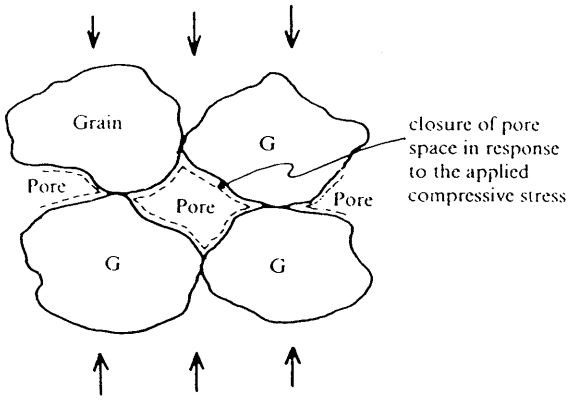


Fig. 2.4 A porous medium with the representation of fluid pressure developed when the medium is subjected to compressive stress. (From Price & Cosgrove,1990)

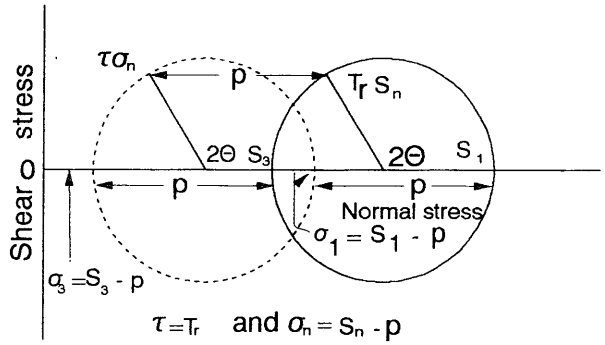


Fig. 2.5 A graphical representation by Mohr's stress circles of the total stress and the influence that fluid pressure has on it. (From Price & Cosgrove, 1990)

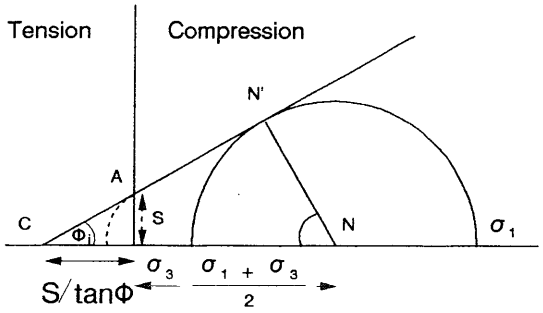


Fig. 2.6 A graphical representation of the Navier-Coulomb failure envelope (CAN') which is assumed to be valid in both the tensile and the compressive regions. (From Price & Cosgrove 1990)

by the axis of the maximum principal stress (σ_1). If the rock specimen fails obeying the linear equation (2.12), the angle 2Θ is kept constant regardless of the change in values of the confining pressure. However, if the rock exhibits a curved relationship between principal stresses at failure, 2Θ is not constant but increases with the confining pressure (σ_3). To explain this phenomenon, two failure criteria have been proposed, namely the Navier-Coulomb and the Griffith criteria.

Navier-Coulomb criterion of shear failure.

This is based on Amonton's Law of frictional sliding which is given by

$$\tau = \sigma_n \tan\phi_i \tag{2.13}$$

where Φ_i is the angle of sliding friction on the potential fracture plane, τ and σ_n the shear and normal stresses acting on that plane.

The relationship between the angle of sliding friction and the coefficient of the friction (μ) is given by

$$\mu = \tan\phi_i \tag{2.13a}$$

and prior to fracturing the cohesion of the rock (C_0) must be overcome, the complete shear failure criterion may be written as follows:

$$\tau = C_0 + \sigma_n \mu \tag{2.14}$$

This relationship has been determined empirically from rock deformation

experiments in which the load (σ_1) needed to fail a sample was determined for a variety of confining stresses (σ_3). The stress states (σ_1 and σ_3) at failure can be represented by Mohr circles. As mentioned earlier, some rocks exhibit a linear relationship between principal stresses at failure (equation 2.12). For such rocks the tangent to the Mohr circle on fig. 2.6 will be a straight line AN'. This failure envelope represents graphically the Navier-Coulomb failure criteria (equation 2.14). An important feature of this failure criterion is that the angle Θ, which the shear failure plane will make with the axis of maximum principal stress, can be predicted. In order to determine the orientation θ of the plane along which the failure criteria is first met, the biaxial stress equations (2.3 and 2.4) are substituted into the Navier-Coulomb criteria (eq. 2.14). Differentiation of the resulting expression with respect to θ enables the value of θ along which failure will first occur to be determined.

$$\pm\Theta = (45° - \frac{\phi_i}{2}) \qquad (2.14a)$$

or

$$2\Theta = 90° - \phi_i \qquad (2.14b)$$

The angle 2Θ can be determined graphically from the Mohr circle. It is the angle between the line joining the centre of the circle to the point where the circle touches the failure envelope and the normal stress axis, fig. 2.6.

A notable disadvantage of the Navier-Coulomb failure criterion is that the signs of the stresses are not taken into consideration and consequently the tensile strength (T_p) predicted by this criterion is

$$T_p = C_0 \cot \phi_i \qquad (2.15)$$

In cases of the angle Φ_i being less than 45° (i.e for all rocks), it follows that the predicted tensile strength (T_p) is larger than the cohesive strength; this is contrary to the experimental data which suggests that the tensile strength is always smaller than and frequently approximately half, the cohesive strength. Clearly a different failure criterion is required to explain tensile failure.

The Griffith criterion of brittle failure.

Although Griffith's theory (1924) will be considered in Chapter 3, it is thought useful to mention it here in conjunction with the Navier-Coulomb failure envelope.

Griffith's failure envelope is shown in fig. 2.7. The non-linear relationship between principal stresses at failure is expressed as a Mohr's envelope with the equation

$$\tau^2 + 4T\sigma_n - 4T^2 = 0 \qquad (2.16)$$

It may be noted that according to equation 2.16 the "cohesive strength" C_0, is twice the tensile strength, a fact that is in good agreement with experimental data.

McClintock and Walsh (1962) demonstrated that both failure criteria, the Navier-Coulomb's and Griffith's, were the end members of a continuum of failure conditions and combined the two as shown in fig. 2.8. The equation derived from Griffith's theory represents a linear relationship between principal stresses at

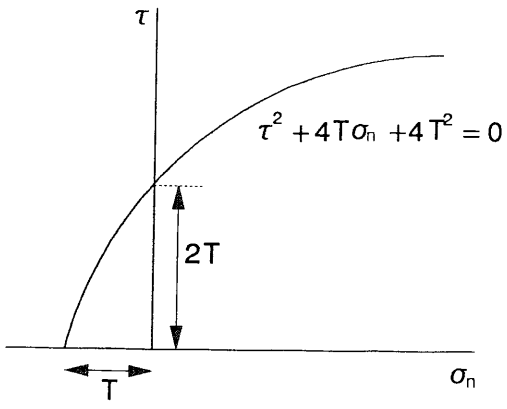


Fig. 2.7 Griffith's failure envelope. (From Price & Cosgrove, 1990).

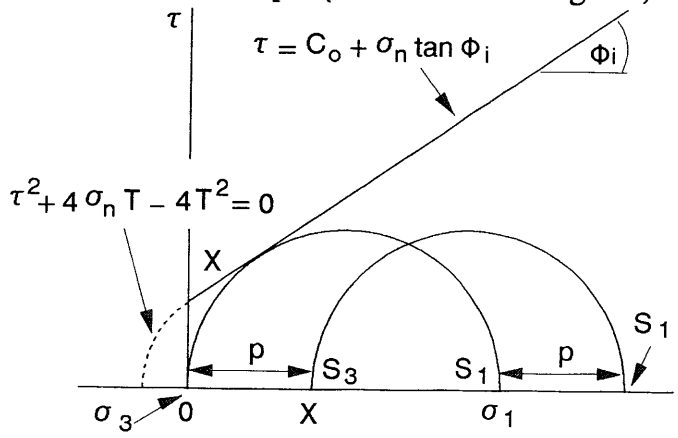


Fig. 2.8 Combined Griffith/Navier-Coulomb failure envelope. (From Price & Cosgrove, 1990).

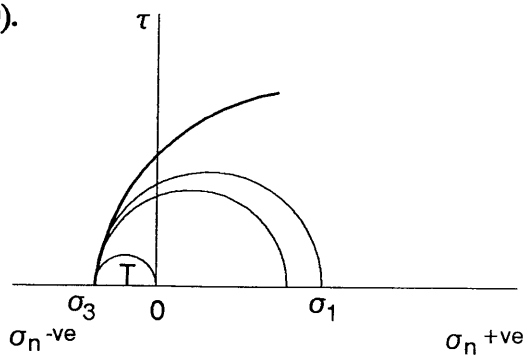


Fig. 2.9 Hybrid and tensile failure conditions as prescribed by the geometry of the parabolic failure envelope of Griffith's failure criterion. (From Price & Cosgrove, 1990).

failure, which has the following form

$$\tau = 2T + \sigma_n \mu \qquad (2.17)$$

The difference between this relationship and the Navier-Coulomb failure criterion (eq. 2.14) is only the cohesive strength which is replaced by 2T.

2.1.4 Failure when the least principal effective stress is tensile

Principal stresses do not always act in compression. In crustal conditions, the fluid pressures may be high and greater in magnitude than the total least principal stress (S_3), resulting in the least effective stress (σ_3) being tensile. Depending upon the magnitude of the value of the least principal stress and the value of the differential stress (S_1-S_3), expressed in terms of the tensile strength of rocks (T), failure may occur in the following ways:

(a) If $(S_3-p)>T$ and also $(S_1-S_3)<4T$ failure will be tensile and one or more fracture planes will develop perpendicular to the axis of least principal stress (S_3) as the result of hydraulic fracture, and

(b) If $0.8T<(S_3-p)<T$ and also

$4T<(S_1-S_3)<5.5T$

hybrid extension and shear forms of failure may occur.

The stress criteria as cited in (a), indicates that the least effective principal stress must attain a value sufficiently great to overcome the inherent resistance of the rock to fail in tension. The second failure criteria is better understood if fig. 2.9 is considered, because it is based on the geometry of the parabolic failure envelope predicted by the Griffith failure criterion. It is clear from fig. 2.9 that the stress circles which touch the failure envelope at the coordinates (0, -T) cannot have a diameter greater than 4T. Those circles with a diameter greater than 4T

will touch the failure envelope at some other coordinate and consequently will give rise to failure in shear rather than in tension.

2.1 5 The hydraulic fracture mechanism of brittle failure

The features characteristic of hydraulic fracturing are manifested at all levels of geological activity: (a) at the microscopic level, microfracturing and rock disaggregation and possibly cataclastic flaw are prominent, (b) at the macro- and mesoscopic levels the mechanism is responsible for the generation of veins, joints and fracture cleavage and (c) on a large scale this mechanism is the key to the formation of dykes, sills and possibly the initiation of some diapirs.

Because the hydraulic fracturing mechanism is so important in the formation of the various features mentioned above, it is useful to discuss this process more thoroughly.

When the fluid is initially **external** to a system, as in the case of the intrusion of dykes and sills, and is introduced to a system at high pressures, then the appropriate failure criteria for hydraulic fracturing is

$$(S_3 - p) > T \tag{2.18}$$

This process can be used to determine the tensile strength of the rock experimentally as shown in fig. 2.10 and is the basis of much in-situ testing (Ljunggren,C. et al, 1988 and Stewart,I. and Monaghan,B.G. 1988)

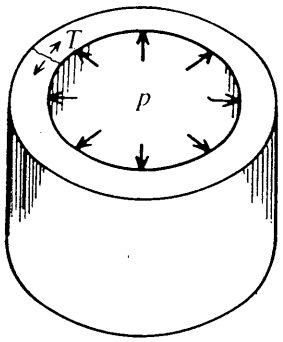
This situation is different when the fluid pressure is generated **internally**. Secor's (1968) conceptual model shown in fig. 2.11 in which a homogeneous and isotropic body containing randomly oriented and relatively widely spaced elliptical flaws

joined by capillaries, is used to explain this situation of internally generated fluid pressure and its effect on fracturing. In this model an elliptical flaw, in which there exists a fluid pressure that subjects the flaw to an effective tensile stress, will generate tip stresses identical to those suggested by Griffith. These tip stresses will enable the flaw to propagate, but once this is done the fluid pressure inside the flaw drops because its volume increases. However, Secor argues, that because the pressure within the rock mass (around the flaws) continues to be greater than the fluid pressure inside the flaw, this fluid will flow into a "preferred oriented" flaw i.e aligned with its long axis perpendicular to the least principal stress S_3, and so further extension becomes possible. Secor uses the equation $\sigma'=S-p$, the equation of effective stress, for his model. The concept is valid provided that the fluid pressure is completely communicated throughout the model, otherwise any tendency for a flaw to propagate will be resisted by "external" to the flaw fluid pressure. A more general relationship exists between fluid pressure and stresses (fig. 2.12b), where **a** is a material constant which has a value of 3 to 5% for many rocks. Equation 2.10 becomes

$$\sigma=S-p(1-a) \tag{2.19}$$

Where $a=K_b/K_m$, K_b and K_m are the bulk moduli of the whole rock and the minerals respectively.

The relationship used by Secor (eq 2.19) is clearly a special case of equation 2.10. The (1-a) part of the equation means that although fluid pressure inside the flaw is 100% effective, the same is not true about the fluid pressure within the rock mass where it is not 100% effective. It is inferred, therefore, that Secor's model works provided that the effective stresses satisfy the general conditions of equation 2.10. Experimental data confirming the above are quoted by Fyfe, Price and Thompson (1978).



Hollow cylindrical specimen sealed top and bottom, subjected to a hydraulic pressure 'p'
T = Tensile strength
($T = p$ for this walled cylinder)

Fig. 2.10 Hydraulic fracture mechanism used to experimentally determine the tensile strength of rock based on $(S_3\text{-}p)>T$; in this case T=p because no confining principal stress exists. (From Price &Cosgrove, 1990).

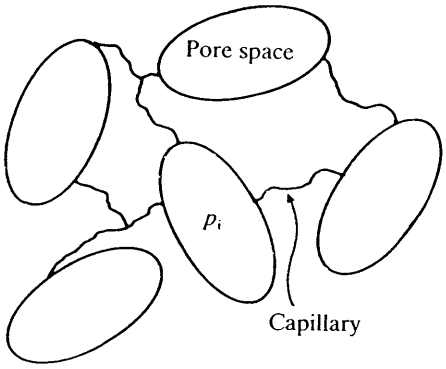


Fig. 2.11 Secor's conceptual model used to demonstrate the effect of fluid pressure on fracturing. (From Price & Cosgrove, 1990).

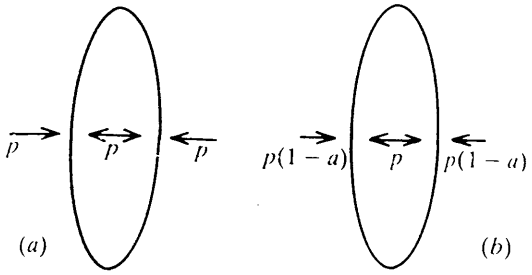


Fig. 2.12 Two flaws under different magnitudes of external fluid pressure (a) without tendency to propagate and (b) with tendency to propagate. (From Price & Cosgrove).

2.1.6 Hybrid extension shear failure

Earlier (2.2.4) it was noted that if

$0.8T<(S_3-p)<T$ and

$4T<(S_1-S_3)<5.5T$

hybrid extension/shear failure occurs. A more detailed examination of the junction zone between the Griffith's failure envelope and the Navier-Coulomb envelope will now be considered (fig 2.13) to examine these modes of failure. Mohr pointed out that if a tangent is drawn to the failure envelope at the point where the stress circle touches it, then the angle that a line, drawn perpendicular to this tangent, makes with the normal stress axis, defines the angle (2Θ) between conjugate shear surfaces. For the stress and failure conditions shown in fig. 2.13, it can be inferred that the normal stress acting on the fracture plane will be tensile and that a shear stress acts along the failure plane which results in shear displacement. Therefore, the failure plane is a hybrid extension/shear fracture. The geometry of the failure envelope, (fig. 2.13), also suggests that should conjugate hybrid failure planes develop, the acute angle between them will be less than 45°. A summary diagram is given in fig. 2.14.

It is interesting to note that although there seems to be a fundamental difference between shear and tensile failure, they are often achieved by the formation of a common fracture oriented in the direction of maximum principal stress, opening in the direction of least principal stress and thus propagating in the direction of orientation i.e in the direction of maximum principal stress (fig. 2.15a and b). Clearly this basic tensile fracture forms a key element in all the failure mechanisms in fracturing.

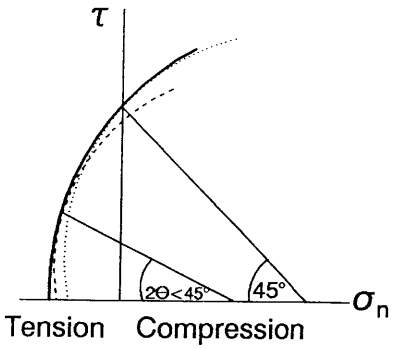


Fig. 2.13 The end segment of Griffith's failure envelope showing the stress condition for hybrid extension/shear failure fractures and the predicted angle (2Θ) between them. (From Price & Cosgrove, 1990).

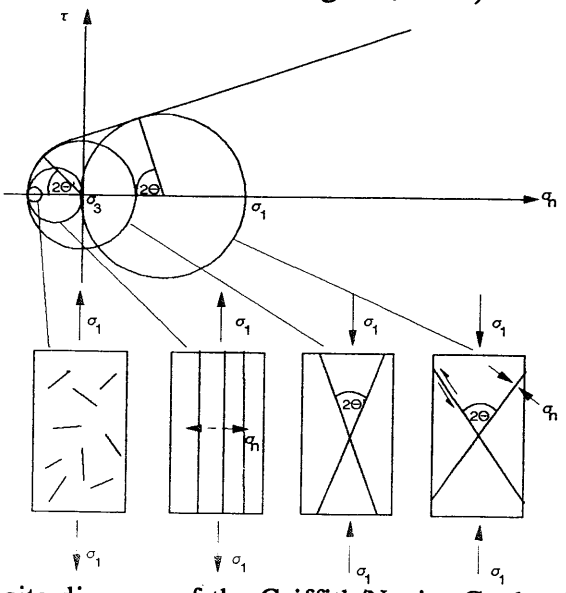


Fig. 2.14 A composite diagram of the Griffith/Navier-Coulomb failure envelope showing the Mohr's stress circles associated with tensile and shear failure.

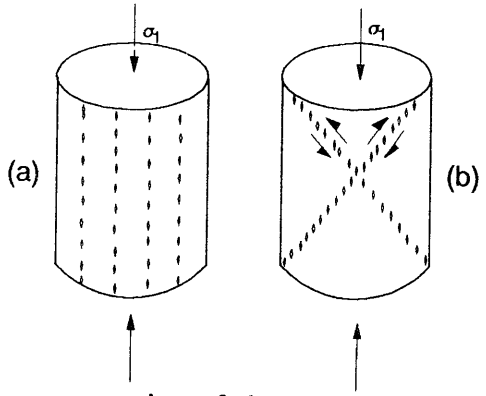


Fig. 2.15 Schematic representation of shear and tensile failure.

2.2 DYNAMICS OF FAILURE

In chapter 3 the principles of Fracture Mechanics will be highlighted in terms of the energy required for the initiation and propagation of a crack. In the present chapter the relationship between principal stresses and brittle failure as expressed through the Navier-Coulomb/Griffith failure criteria and Mohr diagrams have been discussed. To complete the background discussion about the processes of fracturing the following section on the dynamics of failure is included.

2.2.1 Basic aspects of dynamic crack growth

The onset of instability in crack growth usually means failure of the sample as a whole. However, in some instances a partial failure may occur without leading to a catastrophic failure of the whole sample. The concept of unstable (dynamic) crack growth and its arrest is of great importance to rock failure. Two aspects of dynamic crack growth will be considered.

(a) The finite velocities of crack propagation and

(b) Crack branching. This is in regards to macro- rather than micro-branching occurring commonly during all kinds of crack growth.

It is worth mentioning here the classical trimodal pattern shown in fig. 2.16 (exhibited by glass in aqueous environments) which demonstrates the behaviour of many materials at subcritical crack growth. In region 1 of the figure the crack extension velocity is controlled by the rate of stress corrosion reactions at crack tips (as known to be affected by chemical reactions which weaken the lattice of the solid). In region 2, crack velocity growth is controlled by the rate of transport of reactive environmental species to crack tips. In region 3, the curve becomes asymptotic to the critical value, denoted by "c" on the figure. Here the crack growth is mainly controlled by mechanical and thermally activated bond rupture and is relatively insensitive to the chemical environment. A lower limit is thought to exist, below which no crack growth will occur. The existence of such a

subcritical crack growth limit has been demonstrated for various glass/water systems but has not yet been confirmed for rocks and polycrystalline ceramics.

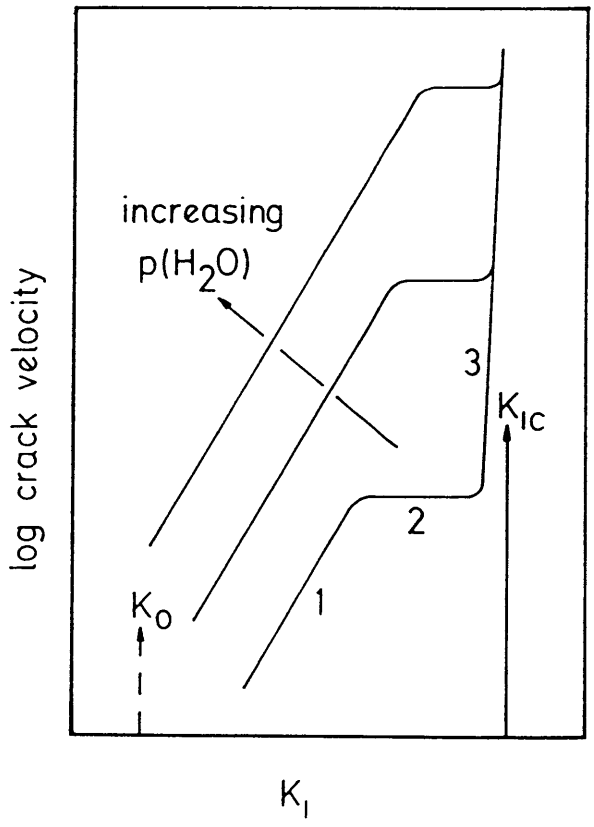


Fig. 2.16 The classical trimodal pattern, which shows the material behaviour between the subcritical crack-growth and catastrophic failure as a dependence of crack velocity vs stress intensity factor (K) or strain energy release rate,G. (From Atkinson, B.K. and Meredith B.G., 1989). K and G are further explained in Chapter 3 but may here be taken to represent a measure of the energy required to propagate a fracture: they are considered to be a constant for a material in a given environment but will change with a change in environment.

Finite velocities of crack propagation. The dynamic crack growth may be considered in terms of energy balance. Fig. 2.17 shows a simplified crack resistance diagram. After the initiation of unstable crack extension there is excess energy in the surrounding bulk which increases during crack growth. By the time the crack reaches a (given) length a_i, the total excess energy amounts approximately, to the shaded area as shown in fig. 2.17. Note, that in reality, the energy release rate of the bulk (G) may not increase linearly with increasing crack length and the crack resistance of the bulk (R) may not remain constant during dynamic growth. However, the approximation in the diagram is convenient and adequate for further analysis to indicate that the crack velocities are finite. The change in the elastic strain energy caused by the increase of a crack length a_o to one of length a_i may be expressed as

$$U_a = \frac{\pi \sigma^2}{E'} (a_i - a_0)^2 \qquad (2.20)$$

where $E'=E/(1-\nu)^2$ which expresses a condition of plane strain as long as $R=G_{IC}$ is assumed to be constant, E is the modulus of elasticity, σ is a remotely applied stress which has caused the crack to propagate and G_{IC} is the critical energy release rate for opening mode I (tension).

It is conventionally argued that for a propagating crack the excess energy is stored as kinetic energy within the bulk, a postulate that was later confirmed experimentally. A simple expression for the kinetic energy may be obtained from the opening displacement (v), of the crack flanks.

$$\frac{a}{V_g} = \sqrt{\frac{\pi}{k} \left(1 - \frac{a_o}{a_i}\right)} \qquad (2.21)$$

where V_g is given by $\sqrt{(E'/\rho)}$, the velocity of a longitudinal wave in a material, $E'=E/(1-\nu^2)$, ρ is the density of the material and k is a function of crack length.

For long propagating cracks where a_i is much greater than a_o equation 2.21 has a limit value of $\sqrt{(\pi/k)}$. This limit value has been calculated to be much less than unity and this has been confirmed experimentally. It can be stated therefore, that the maximum velocity of a propagating crack will always be a fraction of the longitudinal wave speed. Meredith (1990), shows that fracture propagation velocities can approach the velocity of sound in the medium. The more ideally brittle the material, the closer the dynamic fracture velocity approximates to the sonic velocity. Because of inertia effects, the terminal velocity is generally determined to be less or equal to the Rayleigh wave velocity, although diffracted body waves propagating ahead of the crack tip can, in special circumstances, lead to rupture velocities close to the compressional wave velocity.

2.2.2 Crack branching

Dynamic crack growth may be accompanied by multiple branching of the crack. Attempts have been made to explain this phenomenon in terms of kinetic energy, however, high speed cameras used in experiments have shown no changes in crack velocity during branching. If kinetic energy was used for crack branching the velocity would decrease. Experiments have shown (Ewalds and Wanhill after Field,J.E., 1986), that crack branching in the tensile mode occurs only when a specific stress intensity factor described either by G or R (as will be further explained in 3.3.2.) is exceeded. An experiment was set up where six glass plates, containing notches of increasing sharpness as crack starters, were loaded under "mode I loading" i.e tension (see fig. 2.18). The denser branching occurred in the plate with the blunter notch and almost no branching was apparent in the plate with the sharpest notch. These results showed that the blunter the notch, the higher the stress required to initiate fracture. The dependence of crack branching on the stress intensity factor is explained in the following manner. When a specific stress intensity factor is exceeded new cracks initiate ahead of the main crack. Initially these cracks are so close to the main crack they are overtaken by it. Eventually, the initiation of new cracks is sufficiently far ahead of the main

crack that they accelerate to a velocity where they are no longer overtaken. Evidence of this explanation is provided by the roughening of the surfaces of the main crack just before branching in brittle materials.

Crack branching can be promoted by the finite geometry of the specimens. This effect has its origin in the maximum crack velocity being less than the velocities of waves in the material. Shock waves caused by impact loading and/or dynamic crack growth travel faster than the crack. The shock waves reflect from the back surface of the specimen and on arriving back at the crack tip they suddenly increase the stress intensity factor which often causes multiple branching. Under such conditions, crack branching and bifurcation can cause the material to fail by fragmentation. This is a very important process, especially for engineering in rocks.

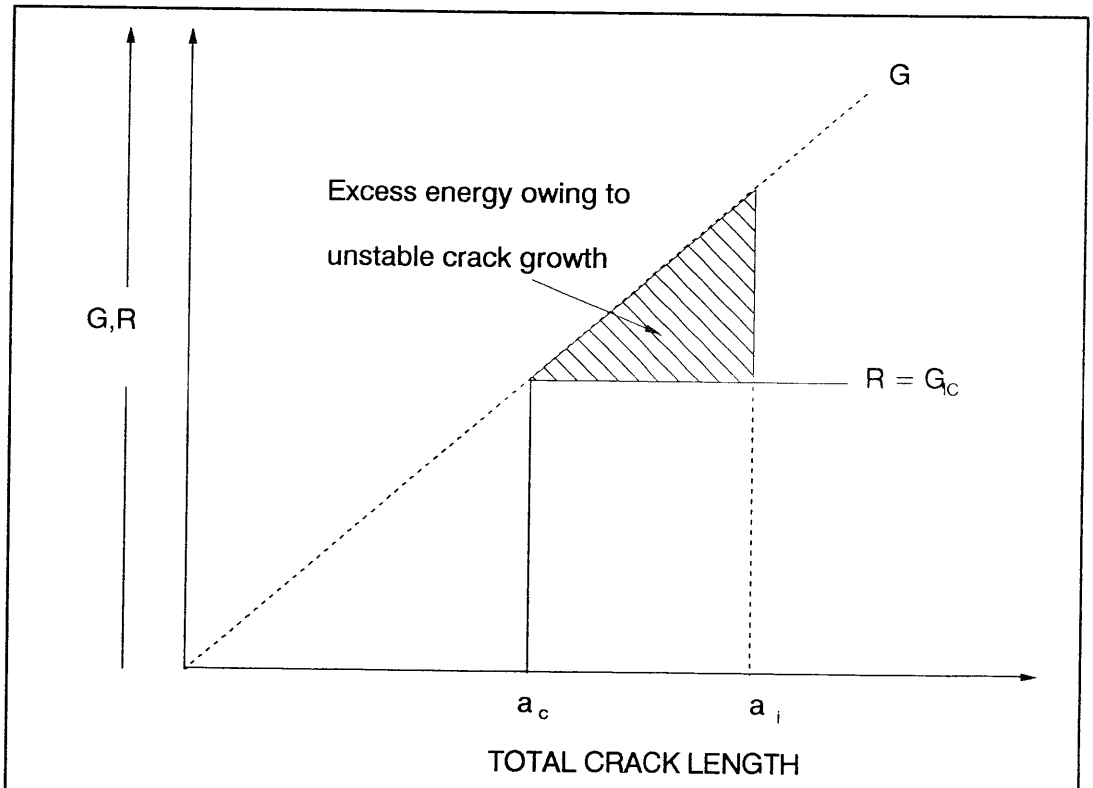


Fig. 2.17 A diagram showing the excess in energy some time after initiation of unstable crack extension under plane strain conditions (From Ewalds and Wanhill, 1986).

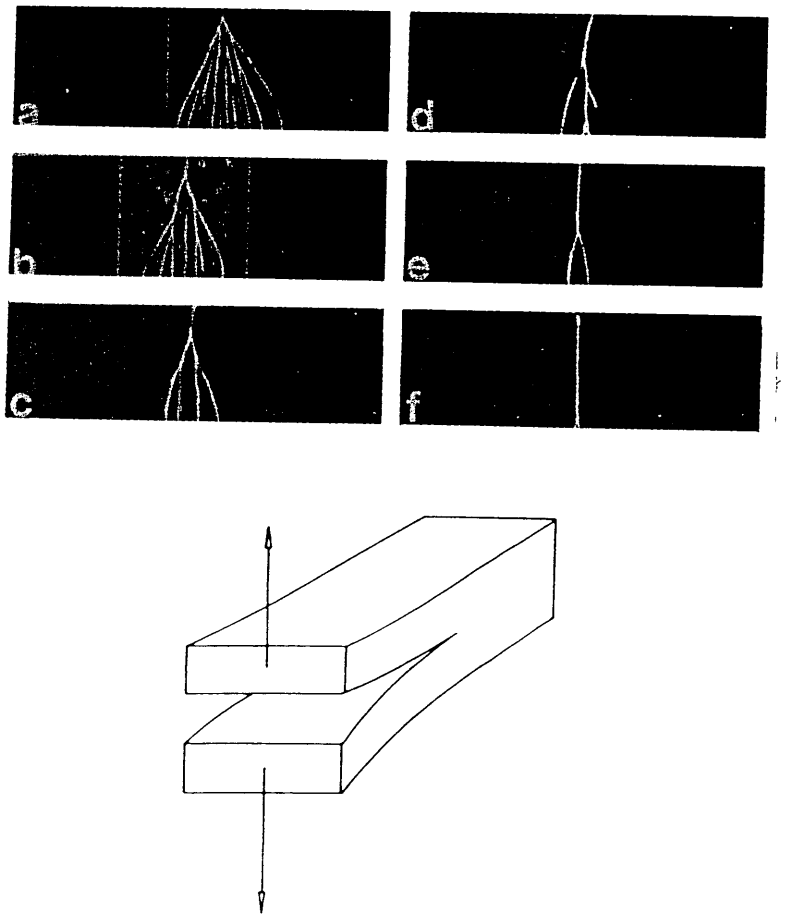


Fig. 2.18 Crack branching in glass plates with an initial notch in mode I loading; bluntness decreases from a to f. (Courtesy J.E.Field, Cambridge University, Ewalds and Wanhill, 1986).

2.2.3 Basic principles of crack arrest

Crack arrest may also be considered in terms of energy balance. It is suggested that the crack stops when the energy release rate (G) decreases below the crack resistance (R). For conditions of plane strain when R is constant the situation is

shown schematically in fig. 2.19(a).

However, crack resistance does not remain constant in all materials. This happens because the material in front of a fast running crack will be loaded at very high strain rates, and, for materials sensitive to the strain rate, the yield strength increases with increasing strain rate. In turn, a higher yield strength decreases the amount of crack tip plasticity and hence the crack resistance (R) which is mainly plastic energy. This situation is shown in fig. 2.19(b).

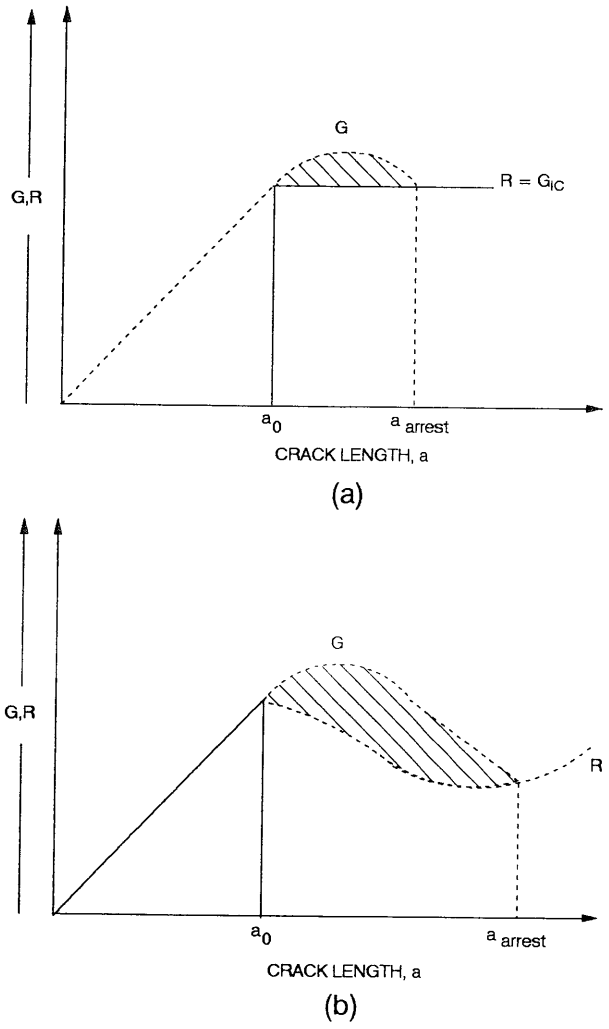


Fig. 2.19 Crack arrest in terms of an energy balance for plane strain conditions with R (a) insensitive and (b) sensitive to crack velocity; shaded area denotes the excess energy due to unstable crack growth. (From Ewalds and Wanhill, 1986).

In fact the energy balance approach based on the rates at which energy is provided and used, is an over-simplification. The excess energy after instability is converted to kinetic energy, which can be used for crack propagation, a fact that renders invalid the instances illustrated in fig. 2.19(a) and (b). The problem can be resolved by equating the **total** amounts of energy and not just **energy rates.** This is shown schematically in fig. 2.20 for plane strain conditions. For strain rate sensitive materials, as shown in the figure, crack resistance (R) increases as the arrest point is approached because the decrease in kinetic energy is accompanied by a decrease in crack velocity and therefore lower strain rates, which result in lower yield strength ahead of the crack. Although it is very difficult to imagine that all the kinetic energy of a fast running crack becomes available for crack propagation, the situations shown in fig. 2.20 are generally accepted as representative of actual crack arrest behaviour in many materials, since they are qualitatively consistent with experimental results.

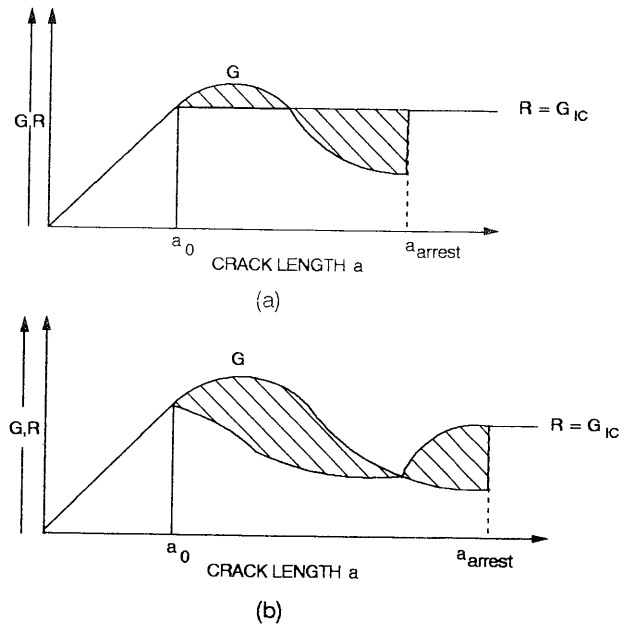


Fig. 2.20 Crack arrest in terms of a balance of total energies for plane strain conditions with R insensitive (a) and R sensitive (b) to crack velocity. (From Ewalds and Wanhill, 1986).

An important consequence of crack arrest depending on a balance of total energies is that the value of energy release rate (G) at arrest is not a material constant, as is shown in fig. 2.21. It depends on the variation of both energy release rate and crack resistance with crack length and velocity.

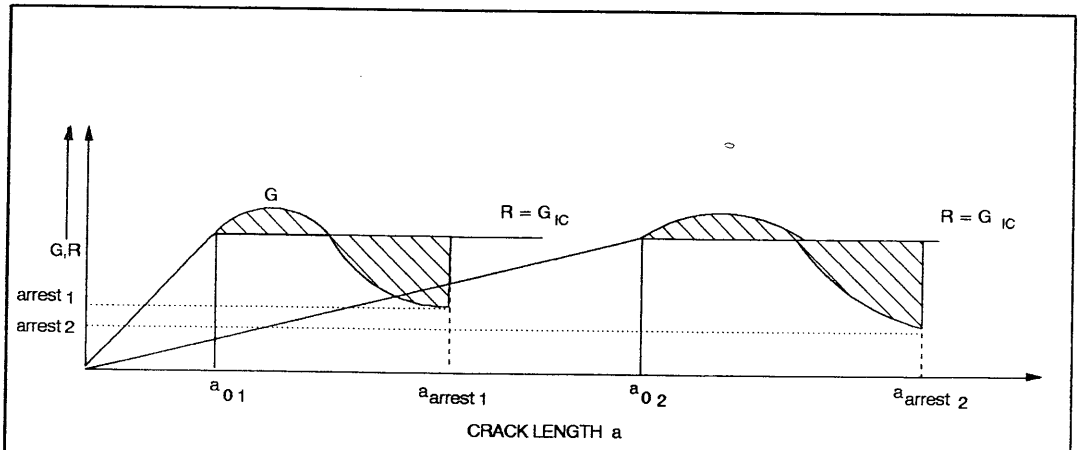


Fig. 2.21 Effect of initial crack length on G_{arrest} for a strain rate insensitive material under plane strain conditions. (From Ewalds and Wanhill, 1986).

2.3 DESCRIPTION OF NATURAL VEINS

In Fracture Mechanics the concept of a "plastic zone" ahead of a crack tip will be introduced to accommodate the difference between real material behaviour and that predicted for it using Fracture Mechanics theories based on Linear Elasticity: the concept was analyzed by Irwin and Dugdale (1958). This zone is a region at the crack tip which deforms plastically above the yield stress. Ingraffea (1987), presents a conceptual model of this zone as applied to rocks which he calls process zone.

Pollard and Aydin (1988) point out that the form of joint termination in a rock mass and the associated deformations are not well known. Experimental data obtained from rocks and engineering materials indicate the existence of a "plastic"

zone which is represented by a zone of micro-cracking at fracture terminations. Such inelastic deformation reduces the stress concentration at joint tips and, as the joint tip propagates from its origin to final termination, a relic zone may be left behind which should influence crack surface morphology.

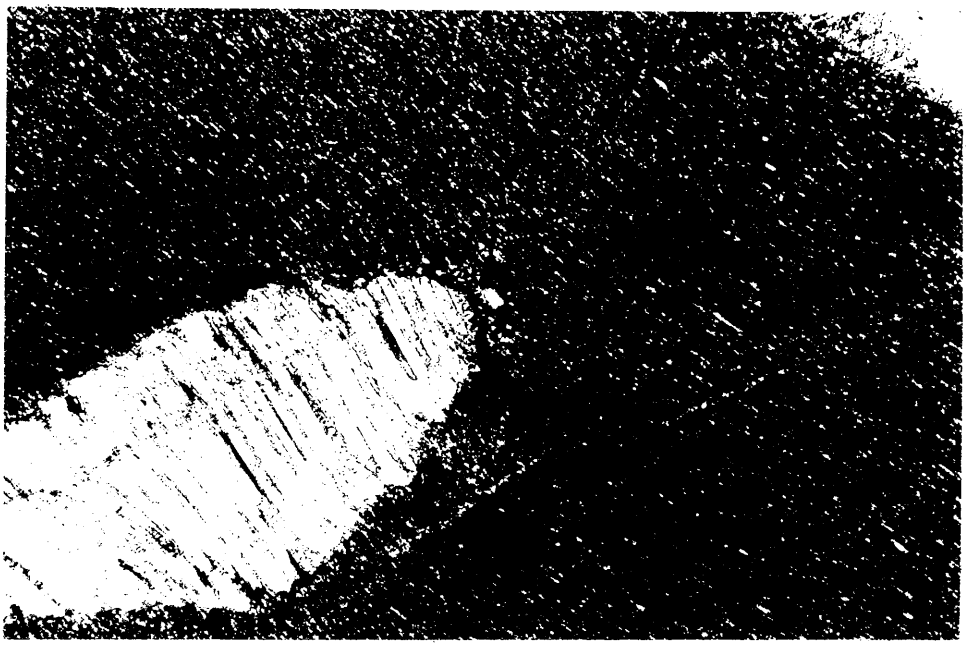
It is useful to examine tensile fractures preserved as vein systems in rocks to see if there is any evidence for the existence of a process zone and to investigate the phenomenon of crack branching. A series of veins were selected to show up clearly against the matrix eg. a calcite vein in a black argillaceous shale, and, examined under an optical microscope . The marked colour, textural and morphological differences between the vein infill and the country rock not only allowed the morphology of the veins to be clearly seen but also enabled the extent of local deformation around the vein to be established.

The veins examined fall conveniently into two morphological groups:

1 **Wide veins** infilled with fibrous crystals, and

2 **Thin veins** filled mainly with equigranular crystals. These veins have a distinct diffused zone around and at their tips.

The wide veins of group 1 have been seen in argillaceous shales. They have a relatively low aspect ratio (length/width), typically 8 (although many thin sections contain only parts of veins and it is not possible to specify the aspect ratio). Group 1 veins have two types of crystal infill. The marginal grains which are equigranular and the central grains which are fibrous. The veins of group 1 can be subdivided on the basis of the geometry of their tips which vary from very blunt rounded tips to very thin sharp ends. It is clear that there is a gradation between these two extremes as shown in fig. 2.22 (a-d) and it can be seen from fig. 2.22a that the termination of these veins is not controlled by major lithologic changes (fig. 2.22a_i), although some of the vein tips do coincide with a lithologic boundary (fig.2.22a_{ii}). Fig. 2.22b illustrates a wide vein with a short thin vein projection at the tip. It is clear from this figure that the fabric in the matrix is

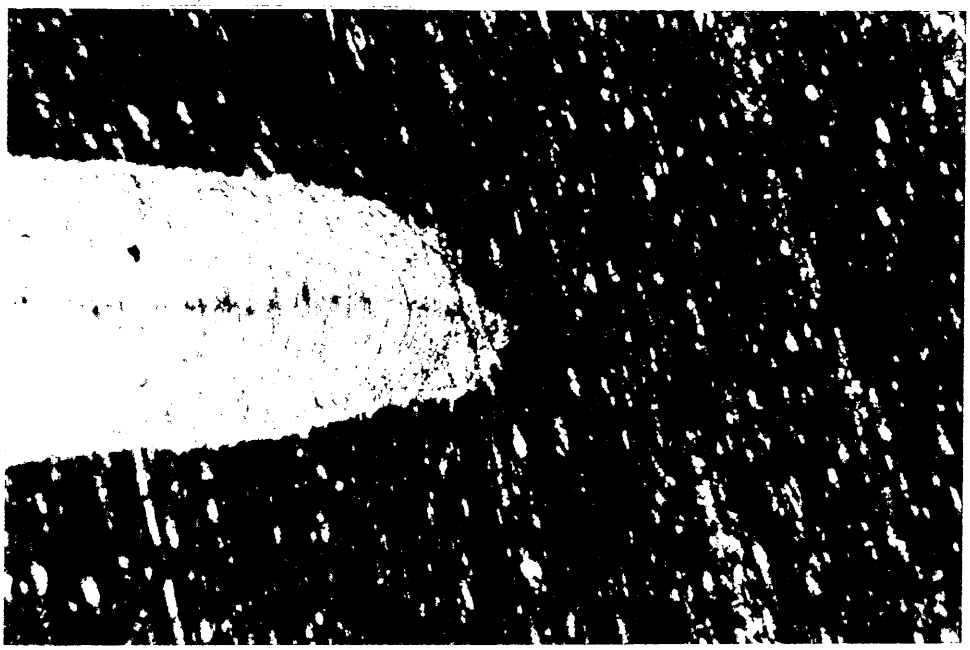


(a_i)

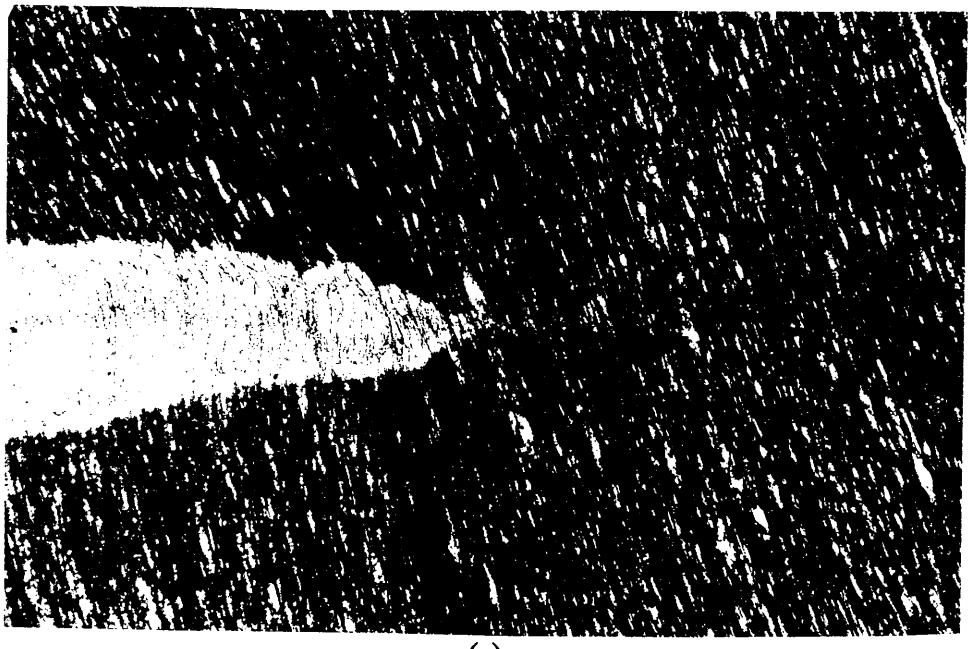


(a_{ii})

Fig.2.22a Examples of "wide" veins where (a_i) the termination is not controlled by a lithological boundary, and (a_{ii}) where the termination coincides with a lithological boundary. 1 m m



(b)



(c)

Fig.2.22b and c A "wide" vein with a short thin projection at the tip (b), and a "wide" vein with gradual thinning towards termination resulting into a thin tip (c).

1 m m



Fig. 2.22d$_i$ A "wide" vein with sharp tip termination; at the left of the photograph the tip of another fracture is seen.

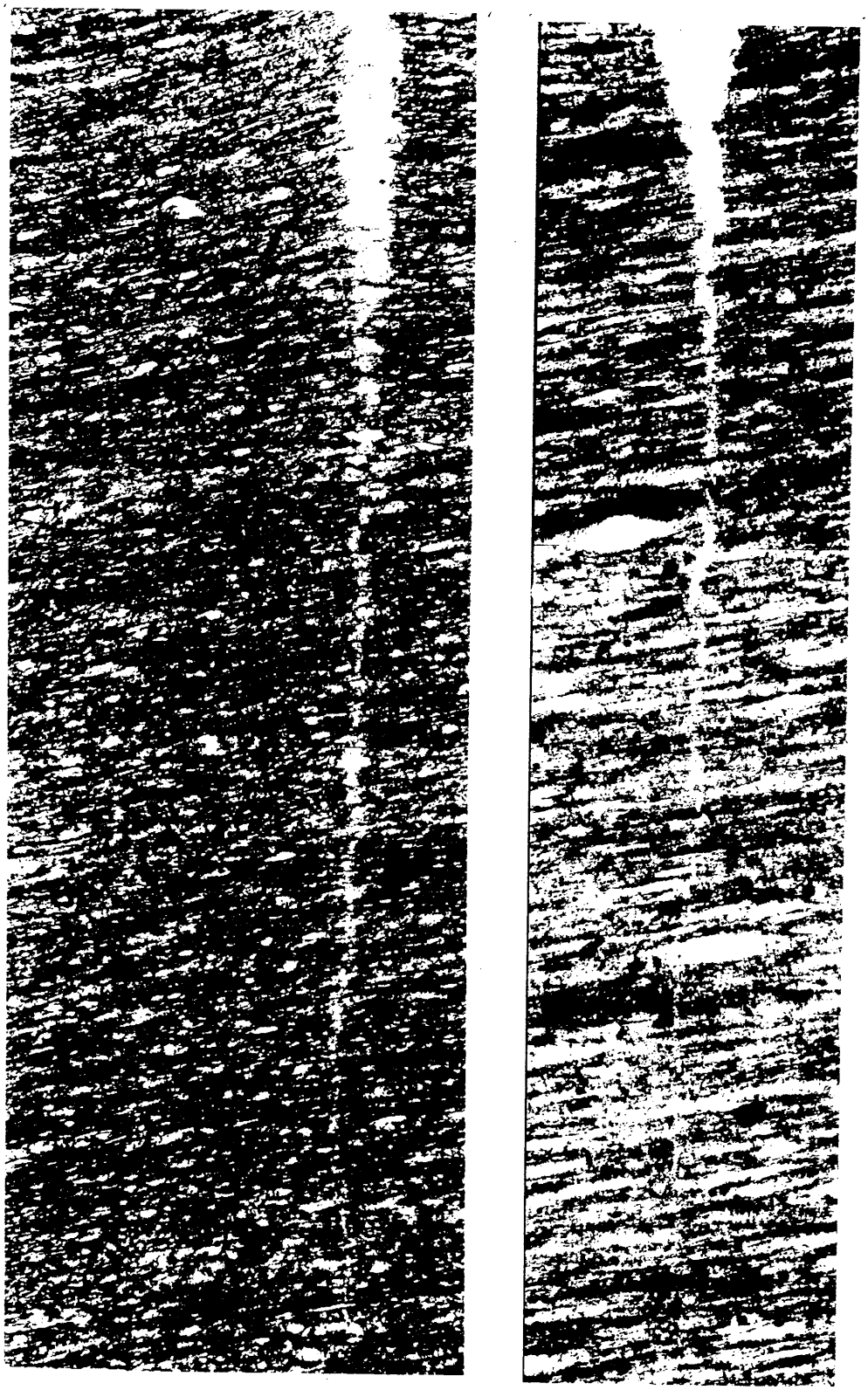
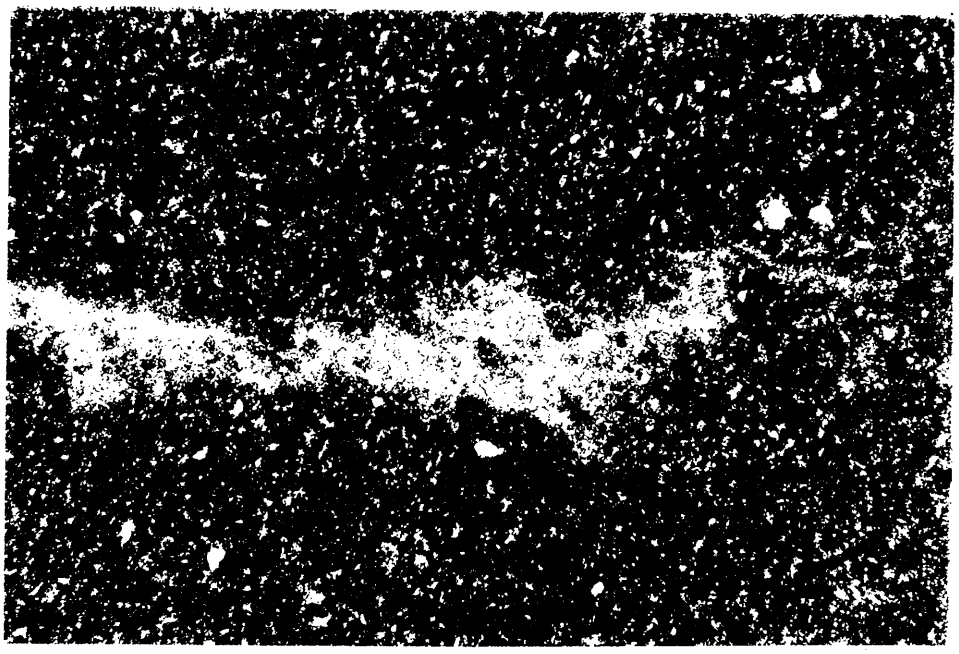
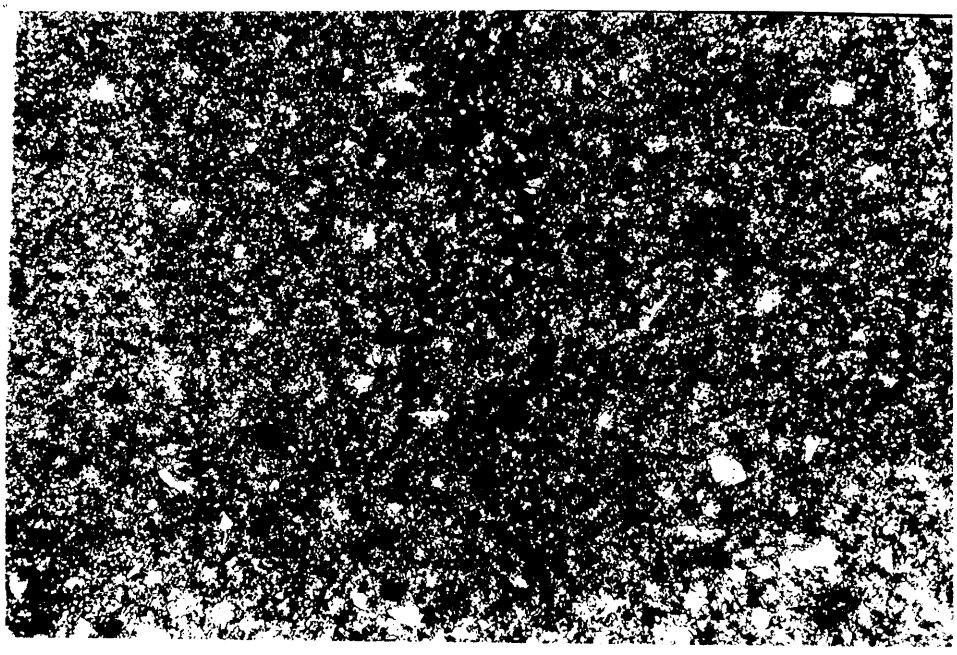


Fig. 2.22d$_{ii}$ Two "wide" fractures whose tips extend a great distance into the matrix.



(a)



(b)

Fig. 2.23 "Thin" veins with the characteristic diffused zone around and at their tips (a) and with equigranular crystal infill (b). 1 m m

deflected at the tip region. Fig. 2.22c shows a vein with a sharper thin tip. As with example of the vein in fig. 2.22b the vein tip in fig. 2.22c is not controlled by a lithologic boundary. Fig. 2.22d shows sharp fracture terminations. Sometimes these terminations do not extend far into the matrix (fig. $2.22d_{(i)}$), in other examples the fracture tip extends a great distance into the matrix (fig. $2.22d_{(ii)}$).

The second morphological division of veins i.e thin veins, is represented mainly by thin quartz veins in mudstones. The main characteristics of this type of vein are (a) the diffused zones which are present around and at the tips of the veins and (b) the equigranular crystal vein infill. Examples of this kind of veins are shown in fig. 2.23a and b.

2.3.1 Implications of the two types of veins to the process of fracturing

In a search for evidence of the process zone it is important not to confuse syntaxial and antitaxial features within the crack with those produced in the process zone ahead of the crack.

Syntaxial growth is characterised by an equigranular crystal growth at the walls of the veins and a fibrous crystal morphology at the centre of the veins (fig. 2.24a). The two types of crystals are compositionally identical or very close. If the wall rock has several components then the syntaxial vein acquires fibres of different compositions growing together in a subparallel fashion. In thin sections the optical orientation of fibres is seen to be parallel to the parent grain in the wall. The fibres occur in two distinct groups attached to either wall of the vein and each group is crystallographically related to the corresponding wall crystals; the contact between the two groups of vein fibres is a centrally located suture. Generally these crystals are free from inclusions, (except at their contact with rock wall crystals), and they form clean vein crystals. The direction of crystal growth is from the vein walls to the centre. These bands suggest a continuous history of

crack opening.

Veins formed by antitaxial growth (fig. 2.24b), exhibit several features which are different to those associated with syntaxial growth: The material which fills the veins is different from that of the vein walls and hence, they have no crystallographic continuity. The fibres, therefore do not form two wall-related groups but run with crystallographic continuity from one wall of the vein to the other. A line of wall rock fragments which have been incorporated as solid inclusions, usually runs along a central line of the vein forming the median line (m.l.). The fragments are either the debris derived from the walls of the fissure or are material brought in during hydraulic fracturing. Inclusion bands of wall material may be seen, arranged in neat lines parallel to the vein walls. These appear to mark successive openings along the vein-wall contact, rendering a cloudy appearance to the antitaxial vein crystals. These bands suggest a periodic opening and crack filling, a process called **crack-seal** mechanism. The crystal growth in an antitaxial vein is from the inside to the outside.

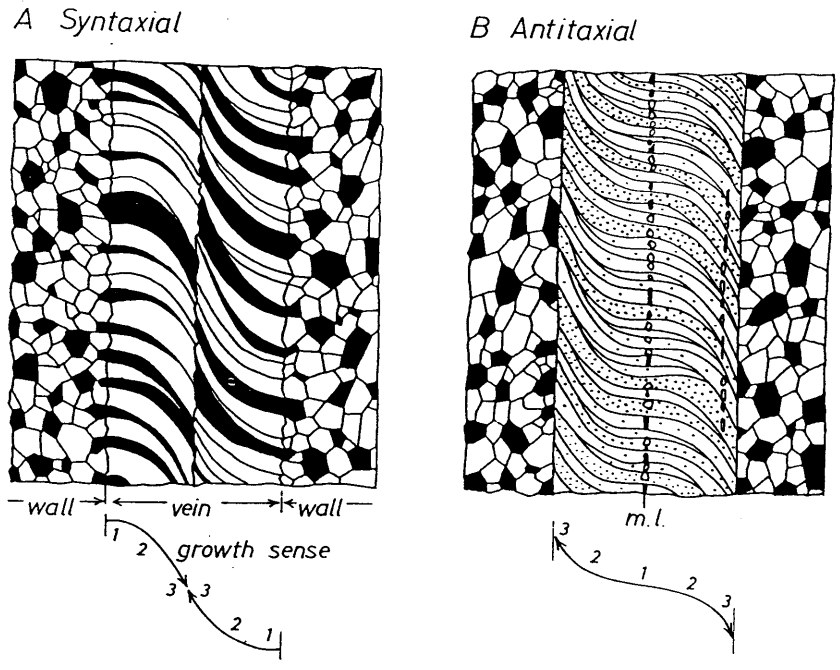


Fig. 2.24 A schematic drawing illustrating the syntaxial and antitaxial growth in natural veins (From Ramsay, 1983).

A careful examination of the "wide" veins (group 1), i.e those exhibiting the fibrous crystal morphology, reveals that these possess the characteristics of syntaxial veins and indicate that the halo of quartz crystals around these veins is not a remnant of a process zone. However, some of these syntaxial veins, as for example the veins shown in fig. 2.22d_{ii}, have a long thin fracture zone ahead of the main vein termination. This may indeed represent a process zone.

The veins of group 2 of the morphological classification, show clearly remnants of the process zone. This is expressed in a general dilation zone which is not only present at the tip of the veins but also runs along both sides of the vein. Examples of the process zone as expressed in the thin sections studied as part of this project are shown in fig. 2.25. The width of the dilation zone is not constant either along the sides of the veins or at their tips. Where adjacent veins are close to each other, the dilation zones overlap resulting in a wide dilation zone connecting one vein to the other. An examination of the dilation zone at high magnifications shows it to be made up of apparently randomly oriented micro-fractures.

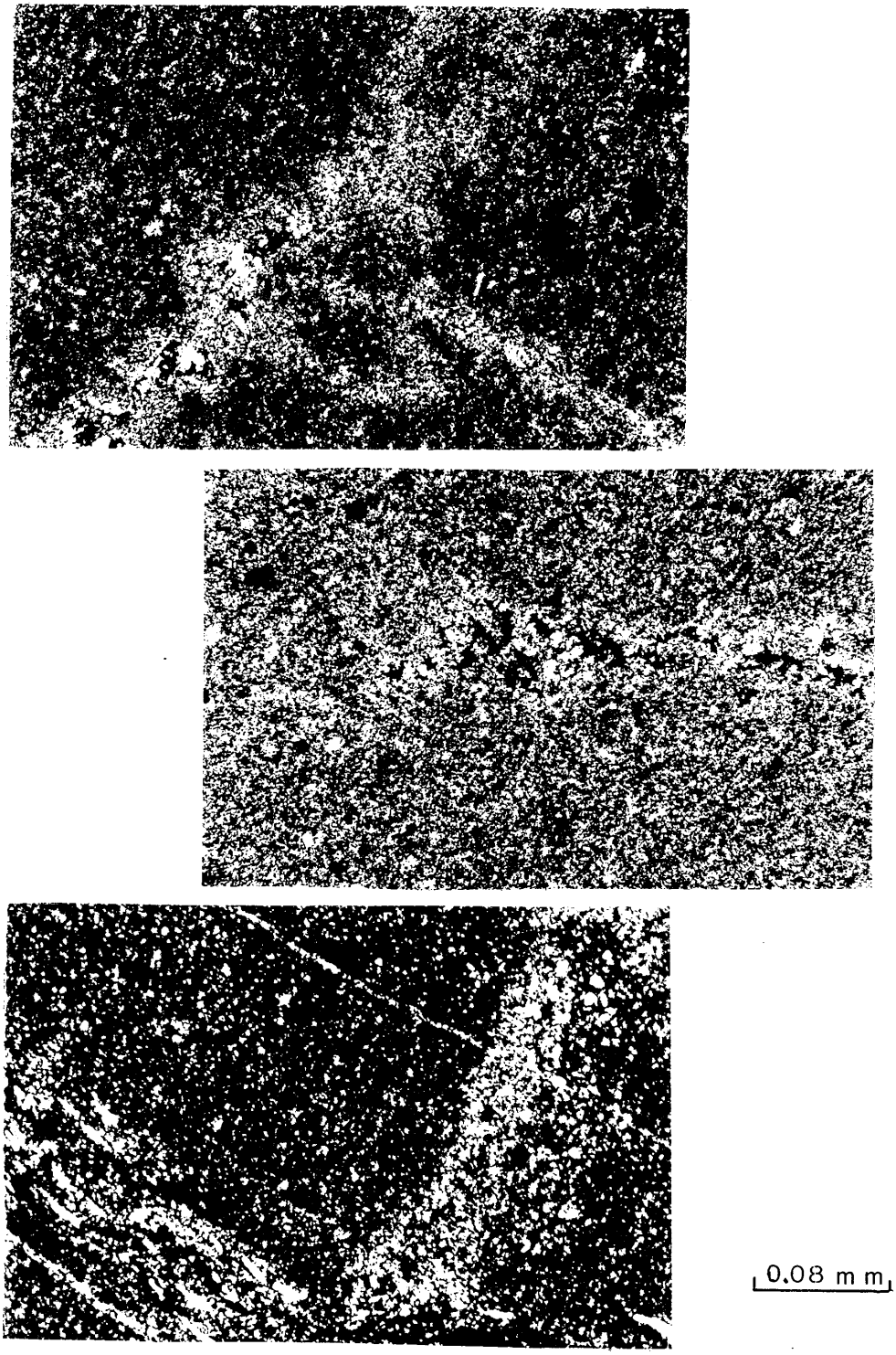


Fig. 2.25 Examples of the process zone expressed as a dilation zone around, and, at the tips of the "thin" veins.

Branching of veins. In the collection of thin sections examined, the "wide" veins exhibit branching, an observation which is in good agreement with the experimental work reported earlier (see fig. 2.18). Examples of multiple branching are shown in fig. 2.26 (a-d).

Influence of lithology on fractures. Inspection of veins which transect the junction between two lithologies, indicate that the veins are more likely to form in the fine grained units (argillaceous bands) than in the relatively coarse units (silts and sands). It is suggested that this is because the fractures are induced by hydraulic fracturing and that high fluid pressures are more likely to build up in the less permeable lithology.

Examples of the influence of lithology on vein development are shown in fig. 2.27 (a-c). In fig. 2.27 it can be seen that variation in the width of the vein gives a sensitive indication of the variation in either permeability or its derivatives viz. stiffness or strength. This is dramatically illustrated in fig. 2.27c where a vein experiences a large reduction in width where it meets a more permeable horizon but locally expands in width where it crosses two thin, low permeable lenses.

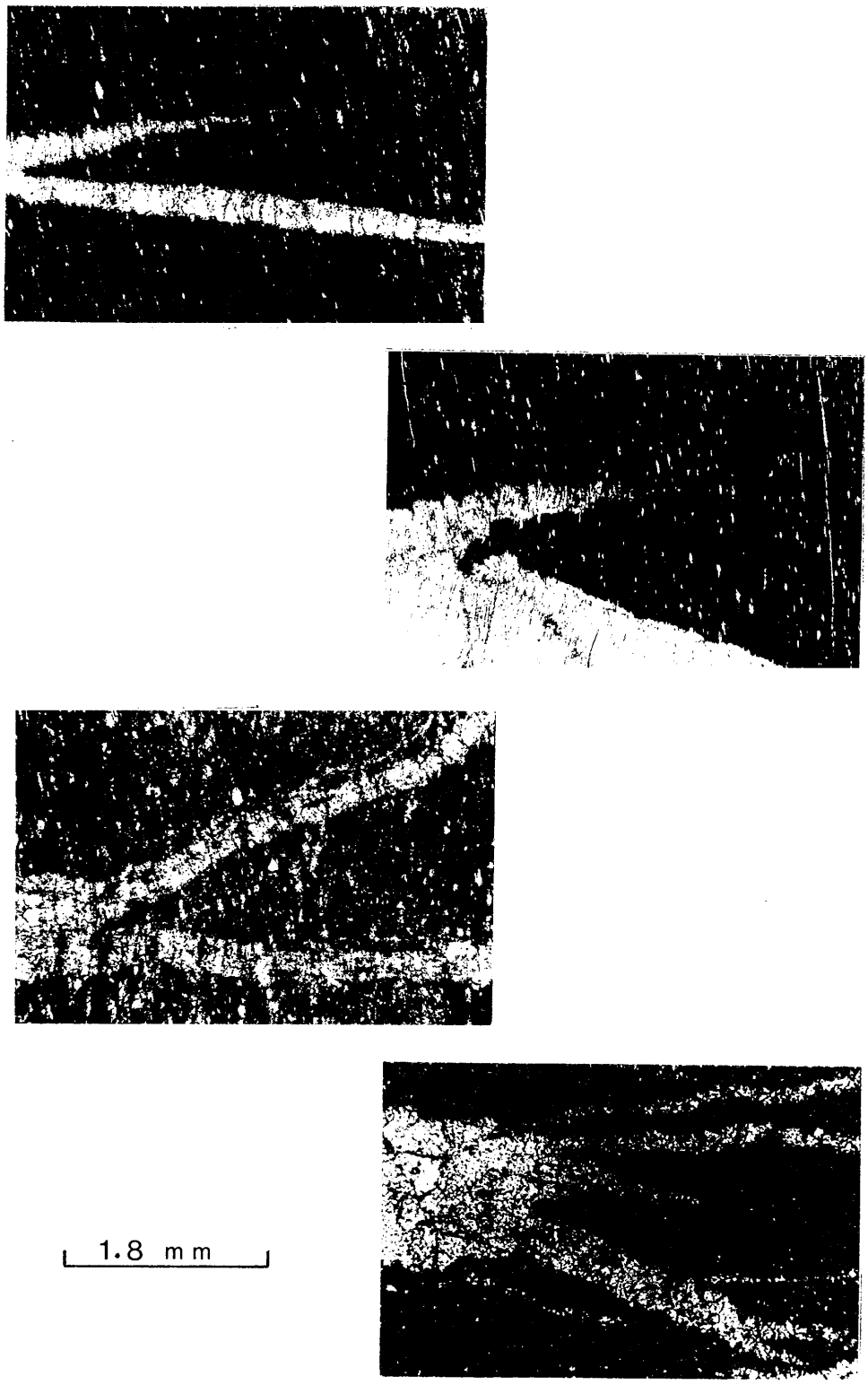


Fig. 2.26 Examples of multiple branching.

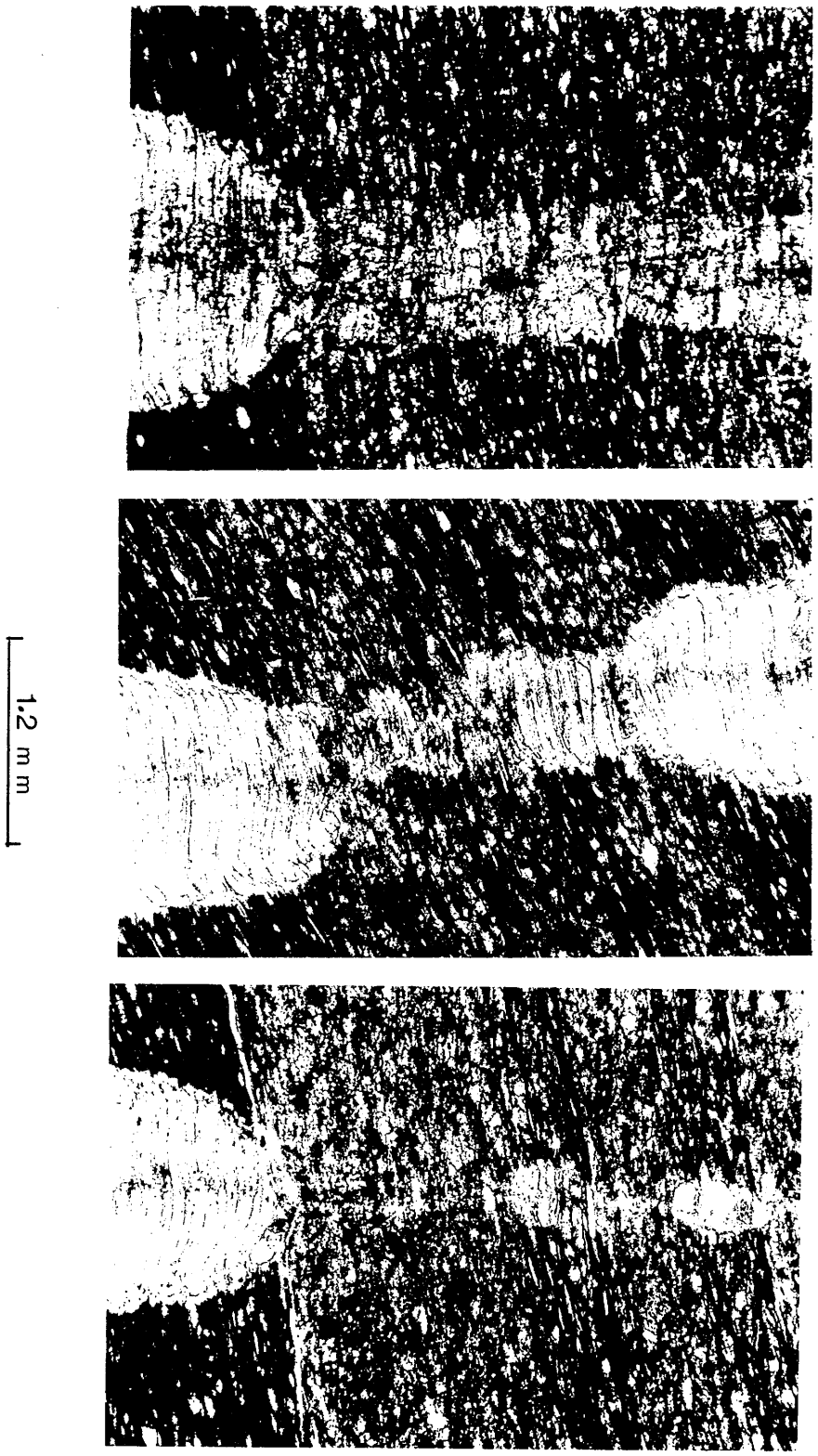


Fig. 2.27 The influence of lithology on the width of a continuous fracture.

2.4 CONCLUSIONS

In this chapter the basic principles of stress and brittle failure in rocks have been outlined as these are essential for understanding fracturing.

A study of naturally occurring tensile fractures shows that they are exceedingly sensitive to surrounding conditions, widening and thinning in response to lithological variations; and that their crack tips can be similar to, as well as different from, those diagrammatic representations used in Fracture Mechanics. These points are pertinent to any assessment of the extent to which the apparent details of Fracture Mechanics theory are applicable to rock. There is no doubt that the basic concepts of Fracture Mechanics are applicable to rock, however the study of veins shows that great care must be exercised when the details for fracture, as defined from Fracture Mechanics theory, are applied to rock in an attempt to understand the failure of rock. The concept of flaws and stress concentrations at the flaw tips is manifestly helpful, but once questions relating to the shape and size of these flaws arise, then theory jumps ahead of our practical knowledge.

A review of Fracture Mechanics now follows.

CHAPTER THREE

PRINCIPLES OF FRACTURE MECHANICS FOR ROCK

3.0 INTRODUCTION

The interest in the mechanical properties of rock materials has increased in recent years as Fracture Mechanics has entered the field as an aid to understanding rock behaviour. Also numerical analysis such as Finite Element Methods have been developed which require comprehensive material methods. This combination of Fracture Mechanics and numerical analysis has been the driving force in the increasing investigation of Rock Mechanical properties, both experimentally and theoretically.

Three modes of failure of materials are distinguished in material Science which apply to geomaterials as well (fig. 3.1). Although it is difficult to separate one mode of failure from another in natural processes the subject of the present investigation will be mode I.

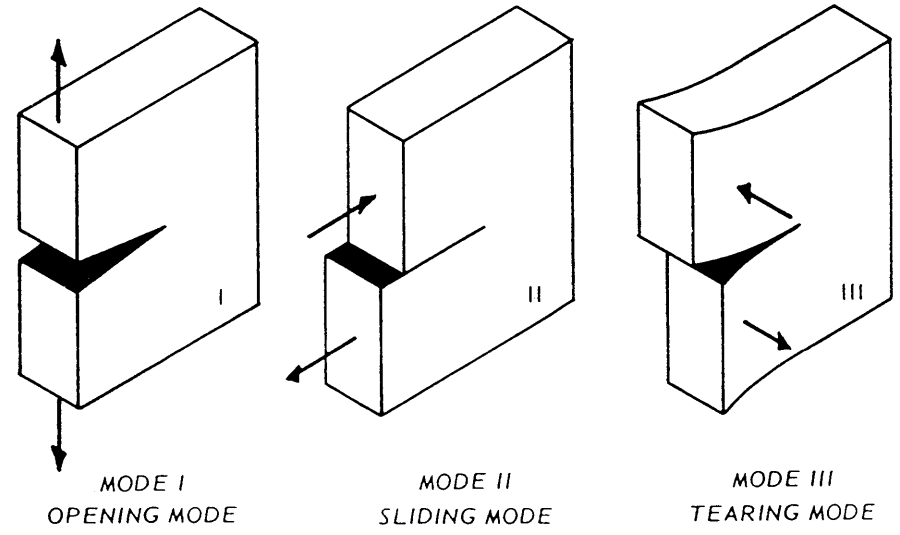


Fig. 3.1 The three modes of failure of materials.

The nature to which material in a crack initiation region at a rock engineering scale conforms is shown in fig. 3.2(a-d). Fig. 3.2a shows the linear-elastic behaviour where no softening, no damage, no cracking, no shear localisation is acceptable. Fig. 3.2b shows the elastic perfectly plastic relation behaviour, typical of a structural steel. Fig. 3.2c shows strain softening after a peak stress carrying capacity has been reached, a behaviour recently observed in rock. As in the case of elastic plastic behaviour a material behaving in this manner shows gradual damage zone development and an off-loading of stress to undamaged material. Fig. 3.2d represents the elastic-brittle behaviour usually assigned to rock at normal engineering scales. The behaviour represented in fig. 3.2d forms the basis of the "strength of materials" approach. It shows that at the material's tensile strength, σ_T, there is an instantaneous drop in load carrying capacity. This model does not allow for a damage zone associated with a nucleation site or a crack tip. The effects of the elastic-brittle (3.2d) and strain-softening (3.2c) responses are the core of the interaction between structure scale and material non-linearity.

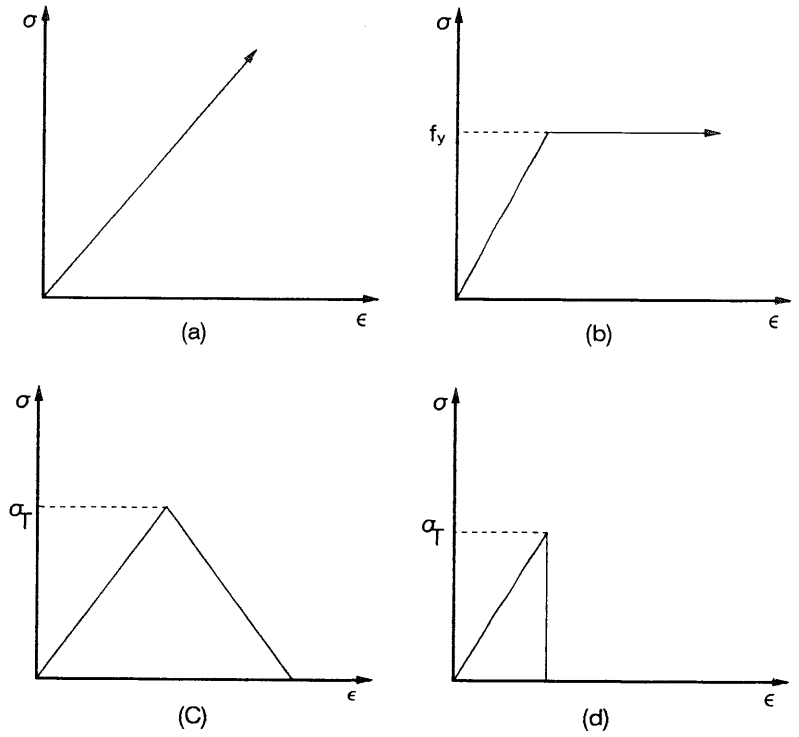


Fig. 3.2 Uniaxial tensile stress vs strain curves for a range of material responses. See text for explanation.

All real materials contain flaws, and this is especially so for rocks. Flaws are the centres from which failure initiates because they concentrate applied stresses to their boundaries. A brief review of flaws is then necessary.

3.1 NATURE OF FLAWS

Nearly all rocks contain microcavities. Sandstones typically have 5-30% porosity where crystalline rocks may contain less than 1% porosity. Natural cavities in rocks exist in two scales (Howarth, 1987) the micro-scale where the rock is considered intact and the macro-scale where the rock mass is considered.

3.1.1 Description of flaws

Naturally occurring cracks and pores and their shape, together with their approximate sizes are presented in table 3.1.

Table 3.1 Description of flaws at micro-scale

Microcavity	Shape	Approximate size (μm)
Vesicule	Equant	100-1000*
Pore	Equant	10-2000
Cracks/Cavities	**Shape**	**Approximate size**
LARC-grain boundaries	Long and thin	~ 0 - 1
HARC-within grains	Equant	~ 0.4 - 7

Naturally occurring microfracturing in rocks, where LARC is a Low Aspect Ratio Cavity and HARC is a High Aspect Ratio Cavity. Aspect ratio is the ratio of minimum to maximum opening dimensions.

In crystalline rocks cracks are designated LARC or HARC. LAR-cavities are characteristics of grain boundaries on both stressed and unstressed rocks, although some may be found inside grains (transgranular), eg. along cleavage directions. HAR-cavities occur as scattered, nearly equant cavities generally manifesting

themselves within grains, and others seem to align along certain crystallographic directions.

In non-crystalline rocks flaws are dependent on grain size and shape, grain distribution and orientation, degree of compaction, cement/matrix characteristics and weathering. Such flaws are mainly associated with porosity.

Porosity can be defined in two ways, **total** and **apparent.** Apparent porosity is a measure of the volume of interconnected pores and cracks linked to the external surface of the rock, and total porosity includes the total volume of pores and cracks, those interconnected to the external surface and those having no connection to the external surface of the rock.

Porous rocks such as sandstones fail in uniaxial compression by a continuous increase in the number of short micro-fractures (Sangha et al, 1974). These microcracks invariably resulted due to the failure of the cement rather than the quartz grains. The direction of the fractures which led to failure was predominantly parallel to the direction of loading. An observation by the authors suggests that in high quartz sandstones (≈85%) the fracture mode was predominantly intra-granular, whereas in low quartz content sandstones (<60%) the predominant failure mode was inter-granular. The predominant fracture failure may be inter-granular or intra-granular depending upon the grain quality and its percentage as compared to that of the cementitious matter.

In stressed crystalline rocks sharp ended brittle cracks form, LAR-cavities widen and the transgranular ones become abundant. The preferred orientation of these micro-cavities is near to the direction of the maximum compression.

Naturally occurring micro-cavities can influence the location and propagation of cracks. In crystalline rocks the LAR-cavities join together to form longer cracks, a process associated with the propagation and coalescence of fracture. Literature

reports (Tapponier and Brace, 1976) that at about 75% of the peak stress, new transgranular cracks appear. Pores and cracks in the interior of grains also strongly influence crack propagation.

In examining the rock fracture mechanisms several workers suggested various stages in their development: Bieniawski, 1967, suggested the following stages of brittle fracture of rock in multiaxial compression:

1 **Closing of pre-existing cracks.**

2 **Fracture initiation.**

3 **Stable fracture propagation.**

4 **Unstable fracture propagation.**

5 **Forking (branching and forming of new cracks) and coalescing.**

Olsson and Peng, 1976, suggested four sequential events associated with rock fracture failure:

1 **Crack nucleation.** Formation of centres in a previously continuous material from which definable cracks can initiate.

2 **Crack initiation.** Is the onset of the extension of cracks from the above described centres or from pre-existing cracks.

3 **Crack propagation.** This is the progressive extension of crack.

4 **Coalescence.** It is the formation of a continuous fracture surface by the coalescing of the network of extended cracks.

In addition to the sequence of events described above it is also realised that during these stages certain interactions can occur between the failure surfaces. Observations of crack interactions in granite by Kranz, 1979 suggest the following stylised crack interactions: **en echelon, en passant** and **crack-pore**, as shown in fig. 3.3. Fig. 3.3a and b show linkage between two micro-cracks; in fig. 3.3a shear linkage is observed when cracks are at some angle to the applied stress, while in fig. 3.3b the linkage is vertical or near vertical as branch cracks grow towards the maximum stress. The en passant interaction is also exhibited in two

ways: the first form shows two cracks approaching each other on different planes; initially they are only influenced by the applied stress but as they approach each other's zone of influence they deflect towards each other as it is seen in fig. 3.3c. The second form shows interaction when there is no overlap as in fig. 3.3d. The cracks respond towards the applied stress direction; the linkage is usually seen perpendicular to the cracks and is attributed to the release of locally stored strain upon unloading of the sample. The third type of crack interaction is the crack-pore; in fig. 3.3e it is seen how cracks can be deflected from their preferred path by the zone of influence of a nearby pore or void boundaries. Although this is not strictly a crack-pore interaction they infer the influence of local stresses.

A conclusion may be reached from the above observations, that the external stress on the rock sample is not necessarily the same stress experienced by cracks within individual grains. More observations confirm that fractures form by the intersection or coalescence of micro-cracks most of which are extensional in nature; they thus open in the direction of least compression and propagate towards the direction of maximum compression.

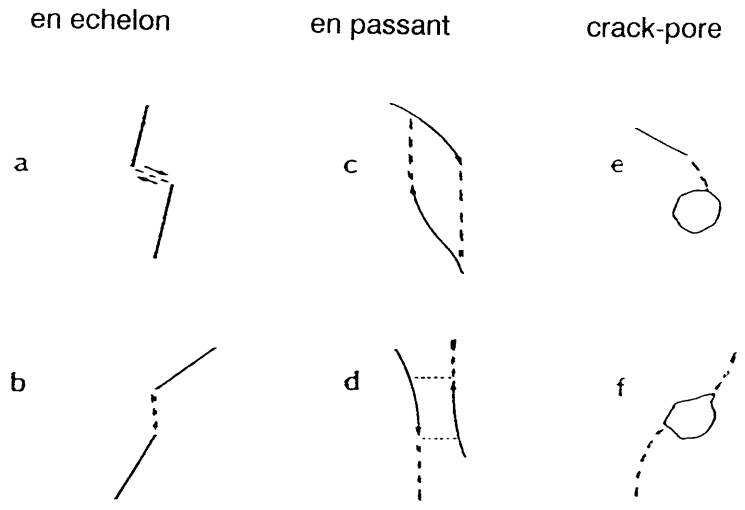


Fig. 3.3 Crack-crack and crack-pore interactions. A uniaxial stress applied vertically is assumed. Dashed lines indicate extensional links or branch paths. Dotted lines indicate strain-relief links due to off-loading. (From Kranz, 1979).

3.1.2 Performance of flaws

Adams and Sines 1978, have categorised flaws and their performance in materials into three types:

Type I. Flaws which are opened.

Type II. Flaws which are closed and where the sliding of the contacting faces is resisted by the friction between them.

Type III. Flaws which are closed and their faces locked by mechanical interference of weak bonding.

These types of flaws are discussed below.

Type I. Open flaw. In a two-dimensional model such as shown in fig. 3.4 an opening is subjected to compression. The nature of crack extensions from the tips of the flaws is a function of the applied stress and their direction tends to be parallel to that of the compressive stress.

Type II. Closed flaws with sliding faces. If an open flaw closes, there is no concentration of stress at the tips as the stress is spent towards the closure of the flaw and what remains is transmitted across the flaw faces, fig.3.5a. Within fig. 3.5b the tensile stress around the tip of the flaw ($\sigma_{\beta\beta}$) arises from the intensification of the shear stress in the plane of the flaw, minus the frictional resistance (τ-τ_f) in the plane and from intensification of the normal stress up to the value of the closure (σ_c). Flaws that close and slide under applied stresses exhibit various patterns of behaviour according to McClintock and Walsh (1962):

(i) When the flaw is open the compressive stress (σ_{xx}), normal to the plane of the flaw, is concentrated at the tips and this concentrated stress, when added to the concentrated tensile stress caused by the applied shear τ_{xz}, results in a lower maximum tensile value of $\sigma_{\beta\beta}$, in the vicinity of the tips, fig. 3.6 If the flaw closes under a very small applied compressive stress and if also the coefficient of friction between the two faces is very low, then the crack initiation will depend only on the resolved shear stress on the crack plane. This type of closed flaw will

initiate cracks at lower applied stresses than its open counterpart, as the compressive stress σ_{xx}, is no longer concentrated at the tips of the flaw after it reaches the value σ_c needed to close it, thus the local tensile stress $\sigma_{\beta\beta}$, is higher than when the flaw is open.

(ii) If the compressive stress needed for the closure of the flaw σ_c, is minimal but the friction is high ($\mu \geq 1$), crack initiation will occur at applied stresses higher than its open counterpart, because the resolved shear is reduced by the opposing frictional shear traction on the flaw faces.

(iii) A flaw will close from the centre out if it has flat faces and rounded tips and from the tips inward if the flaw has sharp tips. If the flaws close partially, the open portions behave like open flaws. The normal stress on the plane will be concentrated only at the ends of the part of the flaw 2c' as shown in fig. 3.6. The shear stress τ, creates a tensile stress at the tips of the open portion (position A in fig. 3.6), when it is smaller than the frictional shear resistance ($\tau<\tau_f$); in the opposite case, when the shear resistance is greater than the frictional shear resistance ($\tau>\tau_f$), the closed portions of the flaw slide and the stress diminished by the frictional shear, is concentrated at the tips of the full flaw length before its partial closure (position B in fig. 3.6).

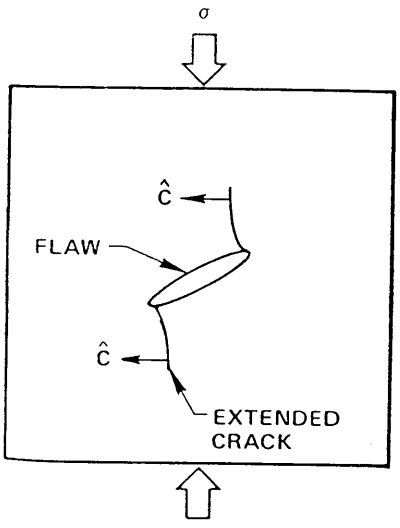


Fig. 3.4 Crack extension from an open flaw subjected to compression. From Adams and Sines, 1978).

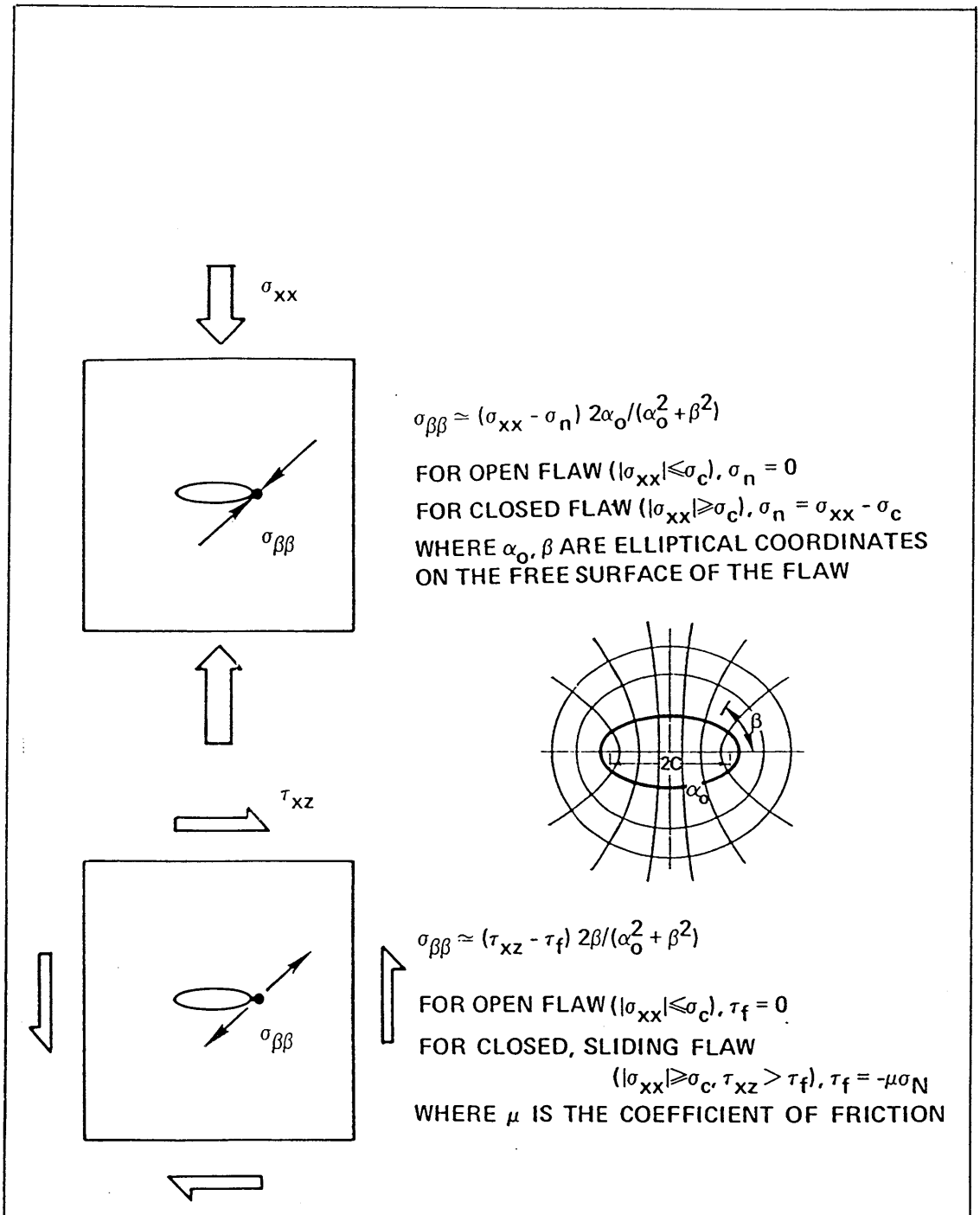


Fig. 3.5 Normal stress applied at surface of elliptical open and closed flaws (From McClintock and Walsh, 1962).

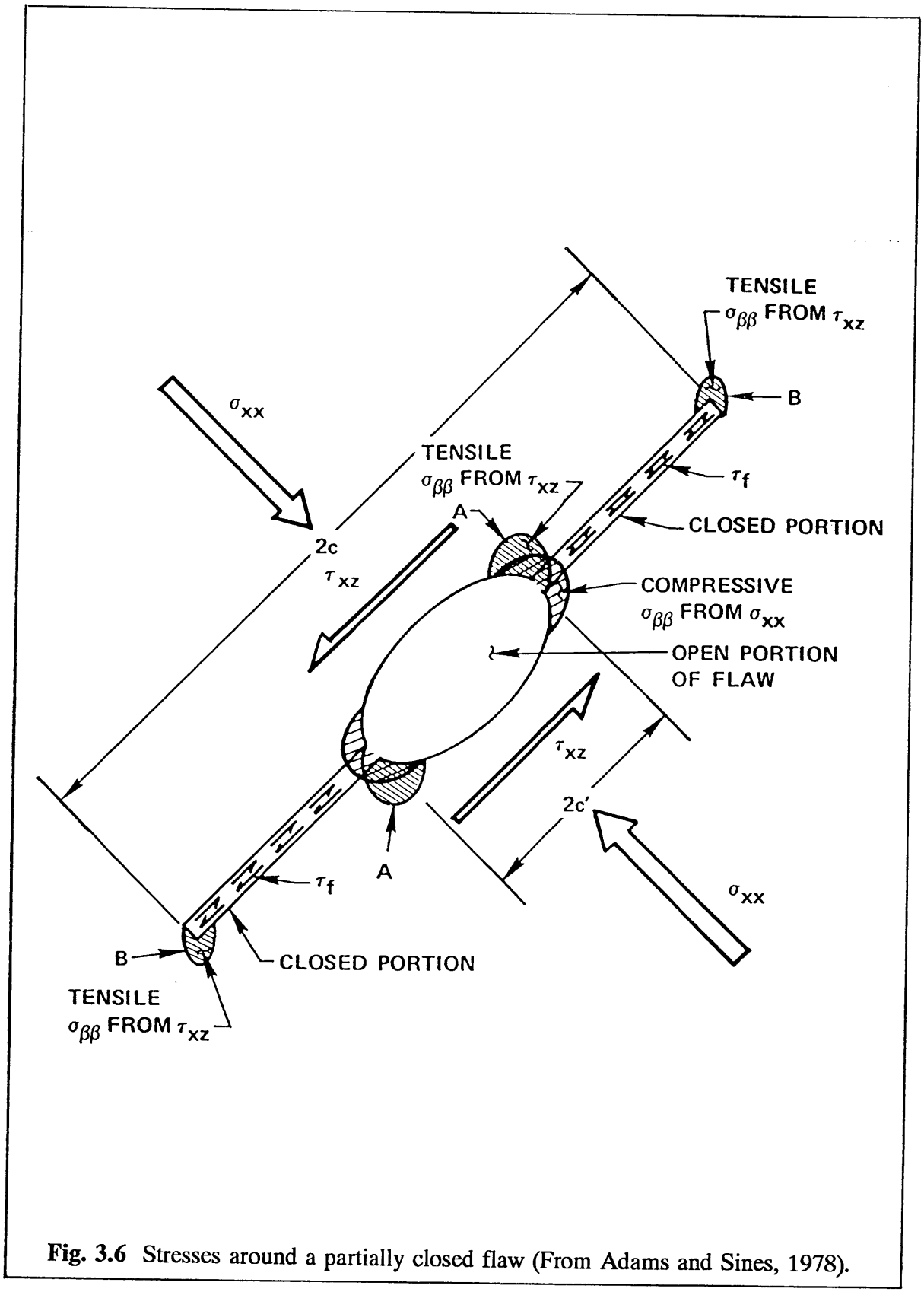


Fig. 3.6 Stresses around a partially closed flaw (From Adams and Sines, 1978).

Type III. Closed flaws which are locked. These types of flaws are similar to the ones of type II except that the sliding displacements are prevented either by weak bonding or by mechanical interlocking between the faces. The stress concentrations around a mechanically locked flaw are quite complex until its faces break free. When the faces slide the stress intensification is the same as that for type II flaw with the exception of the occurrence of a dynamic effect which causes a momentary higher level of concentrated stresses. Type III flaws exhibit different kinds of behaviour depending on the relationship between the shear stress necessary to overcome the lock (τ_u) and the shear stress necessary to initiate a crack at an equivalent type II flaw (τ_{crit}). If the shear stress necessary to overcome the lock is smaller than the shear stress necessary to initiate a crack ($\tau_u<\tau_{crit}$), the applied stress level for crack initiation will be controlled by τ_u and crack initiation will occur at stress levels lower than those required for type II flaws. Thus, an earlier crack initiation and greater crack extension may lead to a structural collapse of a material with type III flaws than for material with type II flaws.

Studies of the performance of flaws therefore make quite clear that considerable advantages are to be gained in any study of rock in extension by imposing upon a specimen as uniform a condition of extension as can be achieved, avoiding therefore flaw closure and sliding, and by using a system to do this which accurately dictates where maximum stress in extension is to occur so that observations of failure may be directed there.

Two other items of information are relevant at this stage, the presence of flaws-on-flaws and the effects of interactions at the boundaries of a specimen or at often free faces, such as flaws.

Flaw tips. Very small flaws in the vicinity of a large flaw (called Flea-on-Flea by Adams and Sines, 1978) may extend cracks at applied stresses lower than those required at an isolated large flaw (see fig. 3.7). The stress effective on the small flaw can be almost of the same magnitude as that of the intensified stress at the

tip of the large flaw ($\sigma_{\beta\beta}$). The intensified stress decreases as the inverse square root of the distance of the small flaw from the large flaw.

Persimmon model. If two open flaws intersect the free surface of a body and are oriented in such a way so that the stress fields produced at their tips overlap, cracks extending from each flaw tend to link up and this can be considered as "squeezing out" the particle between them (see fig. 3.8).

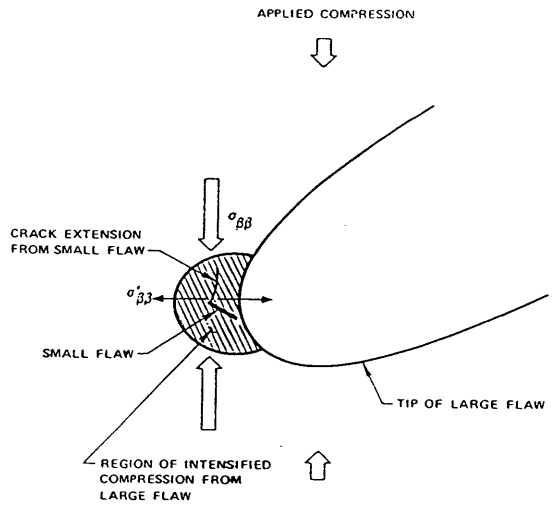


Fig. 3.7 Flea-on-flea flaw extension (From Adams and Sines, 1978)

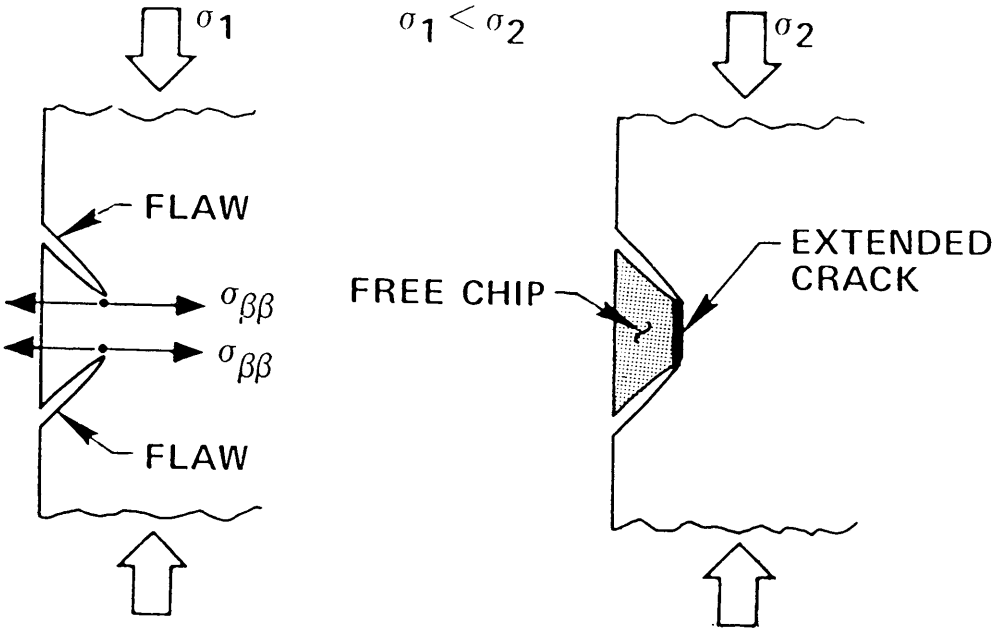


Fig. 3.8 Persimmon seed chip formation (From Adams and Sines, 1978).

3.2 LINEAR ELASTIC FRACTURE MECHANICS

From the mathematical theory of elasticity and in an effort to estimate the strength of solid bodies, attempts have been made to construct the theory of rupture of solids. As described above, rocks contain flaws and so Griffith's theory has an important place in theories for understanding rock behaviour because it assumes that continuum materials contain flaws which act as concentrators of stress, thus enabling the level of stress at the extremities of these flaws to exceed by far the overall level of stress applied to the material.

3.2.1 Griffith's theory of rupture

The concept of this theory is outlined: In a solid, as in a liquid, the bonding surfaces posses a surface tension which implies the existence of a corresponding amount of potential energy. If a crack is developed or a pre-existing crack is extended a quantity of energy proportional to the area of the new surface must be added but under the condition that no increase in the total potential energy of the system should take place. This means that the increase of the potential energy due to the surface tension of the crack must be balanced by the decrease in the potential of the strain energy and the applied forces.

Griffith considers a plate of unit thickness, containing a through-thickness crack of length 2a. The plate is subjected to uniform tensile stress,σ_T, applied at infinity, (fig. 3.9). The total energy U, of the cracked plate may be written as:

$$U = U_0 + U_a + U_\gamma - F \tag{3.1}$$

where U_o is the elastic energy of the loaded uncracked plate (a constant), U_a is the change in the elastic energy caused by the introduction of the crack to the plate, U_γ is the change in the elastic surface energy caused by the formation of the

cracked surfaces, F is the work done by the external forces (F=load x displacement). This must be subtracted from the internal (potential) energy of the plate since it is not part of it.

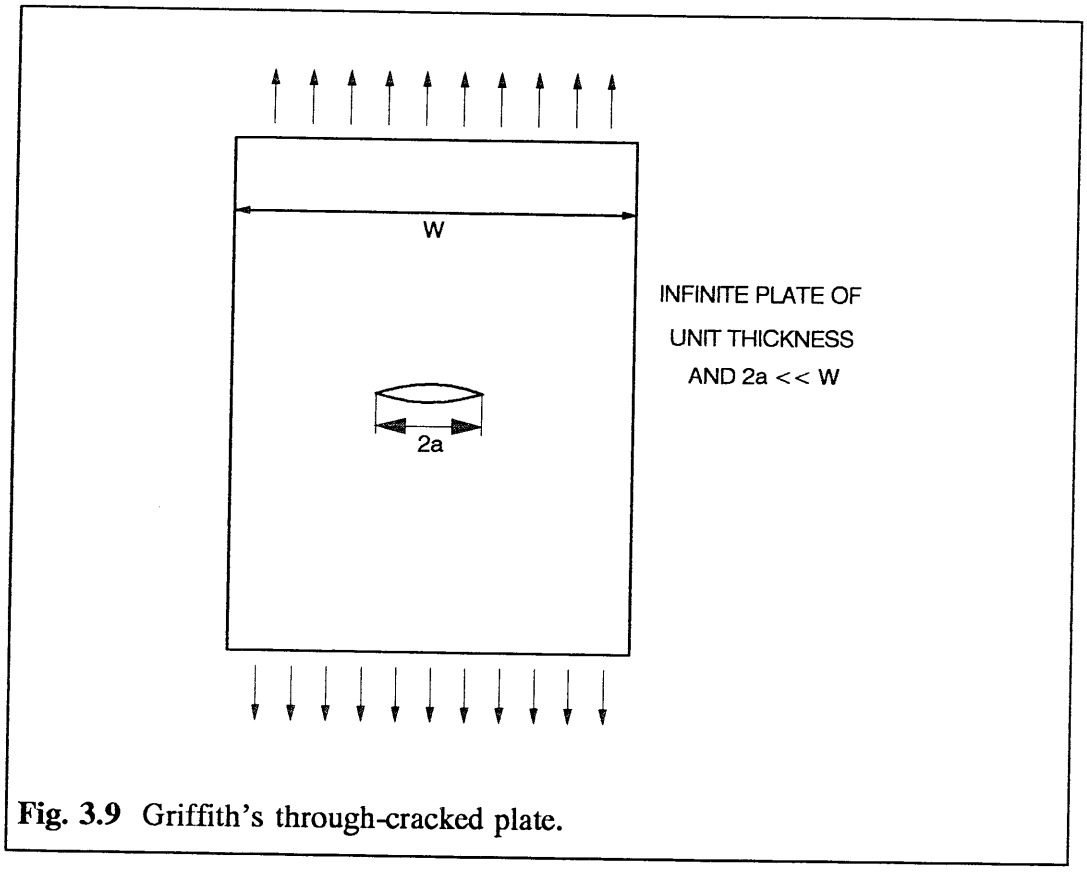


Fig. 3.9 Griffith's through-cracked plate.

So one can say that the Total Energy equals the Internal stored energy plus any additions to internal energy created by adjustments for the presence and growth of any crack minus the losses in energy of opposing external forces. Since the theoretical energy balance values did not agree with experimental data it was concluded that at the moment of rupture the energy of the test piece was not uniformly distributed and that there were severe concentrations of energy at the points where cracks occur. These concentrations may be present at locations of inherent material flaws or initial microcracks. In rocks, fractures initiate either in grain boundaries or at inherent cracks and discontinuities, thus fulfilling the assumption of the theory that, fractures initiate at such locations and propagate when a tensile stress is induced at the tip under load (as described in Section 3.2.2).

Griffith (1924), used a stress analysis developed by Inglis to show that for unit thickness the absolute value of U_a is given by

$$U_a = \frac{\pi \sigma^2 a^2}{E} \qquad Joules \quad (i.e. \quad Nm) \tag{3.2}$$

The change in elastic surface energy, U_γ, caused by the formation of cracks is equal to the product of the elastic surface energy of the material, γ_e, and the new surface area of the crack

$$U_\gamma = 2\,(2a\gamma_e) \tag{3.3}$$

For the case where no work is done by external forces (F=0, called the grip condition when testing materials), the change in elastic energy U_a caused by introducing a crack is negative, and expression (3.1) becomes

$$U = U_0 - U_a + U_\gamma \tag{3.4}$$

because there is a decrease in the elastic strain energy of the plate as it loses stiffness; the load applied by the fixed grips drops.
Substituting U_a (3.2) and U_γ (3.3) in (3.4) gives

$$U = U_0 - \frac{\pi \sigma^2 a^2}{E} + 4a\gamma_e \tag{3.5}$$

Since U_0 is constant, dU_0/da is zero, and so the equilibrium condition is obtained by setting dU/da=0.

$$\frac{d}{da}\left(-\frac{\pi\sigma^2 a^2}{E}+4a\gamma_e\right)=0 \qquad (3.6)$$

The above equation is shown schematically in fig. 3.10a where the surface energy $4a\gamma_e$ and the decrease in elastic strain $(\pi\sigma^2a^2)/E$ and their sum are shown as functions of the introduced crack length 2a. Fig. 3.10b represents the derivative dU/da. When the elastic energy release, which may be introduced to the system due to a potential increment of crack growth, da, is greater than the demand for surface energy for the same crack growth, then the introduction of a crack will lead to its unstable propagation. From the equilibrium condition one obtains

$$\frac{2\pi\sigma^2 a}{E}=4\gamma_e \qquad (3.7)$$

which can be arranged to

$$\sigma\sqrt{a}=\left(\frac{2E\gamma_e}{\pi}\right)^{\frac{1}{2}} \qquad (3.8)$$

Equation (3.8) indicates that crack extension in ideally brittle materials is governed by the product of the remotely applied stress, the square root of the crack length and by material properties. The right hand of the equation is equal to a constant value characteristic of a given ideally brittle material (as E and γ_e are material characteristics). Consequently, equation 3.8 indicates that crack extension in such materials occurs when the product $\sigma\sqrt{a}$ attains a constant critical value.

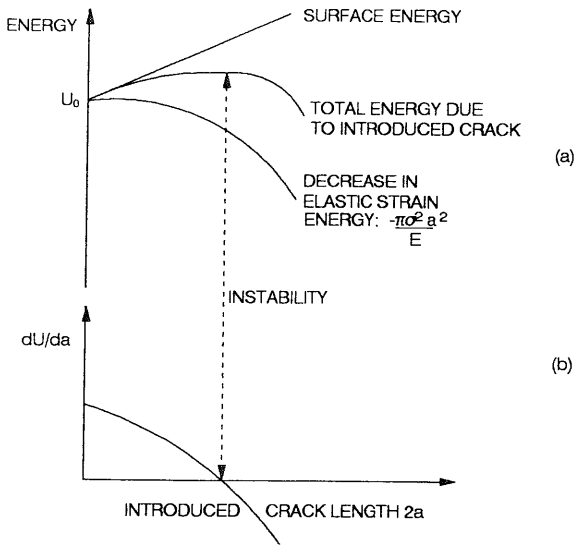


Fig. 3.10 Energy balance of a crack in an infinite plate when no work is done by external forces (From Ewalds and Wanhill, 1986)

3.2.2 Irwin's modification to the Griffith's theory

Equation 3.7 may be rearranged in the form of

$$\frac{\pi\sigma^2 a}{E} = 2\gamma_e \tag{3.9}$$

The left hand part of the equation is the **energy release rate, G,** representing the elastic energy per unit crack surface area that is available for infinitesimal crack extension. The right hand part of the same equation represents the increase in surface energy occurring due to infinitesimal crack extension and is designated the **crack resistance, R.** The energy release rate, G, must be at least equal to crack resistance, R, before unstable crack growth occurs. If the crack resistance, R, is constant a fracture will occur if the energy release rate, G, exceeds a critical value G_c. Fracture then occurs when

$$\frac{\pi\sigma^2 a}{E} \geq \frac{\pi\sigma^2 A}{E} = G_c = R \qquad (3.10)$$

The critical value G_c, is determined when σ_c, required to fracture a plate with a crack of length 2a is measured. A suggestion by Irwin (1948) and a proposal by Orowan resulted in the modification of Griffith's theory for ideally brittle materials to apply to both brittle materials and those which exhibit plastic deformation.

$$\frac{\pi\sigma^2 a}{E} = 2\,(\gamma_e + \gamma_p) \qquad (3.11)$$

The modified formula shows that a material's resistance to crack extension is equal to the sum of its elastic energy, γ_e, and the plastic strain work, γ_p, accompanying crack extension. As the energy balance approach is limited to defining the conditions required for instability of an ideally sharp crack it is obvious that this approach does not present the solutions to such problems as slow crack growth as expressed during fatigue or stress corrosion cracking. Therefore, a value **K**, was introduced by Irwin (1950), as the stress intensity factor which gives the magnitude of the elastic stress field. K, is linearly related to stress and is directly related to the square root of a characteristic length, the crack length. The general form of stress intensity factor is given

$$K = \sigma\sqrt{\pi a} \qquad Nm^{-2}/\sqrt{m} \qquad (3.12)$$

Irwin demonstrated that if a crack is extended by an amount **da**, the work done by the stress field ahead of the crack when moving through the displacements

corresponding to crack length **(a+da)** is equivalent to **the change in strain energy, Gda.** Thus the critical stress intensity factor, K_c, is equivalent to the Griffith-Irwin energy balance approach, which requires the achievement of stored elastic strain energy equal to G_c. For tensile loading the relationships between K_c, and G_c are:

$$G_c = \frac{K_c^2}{E} \qquad \textit{plane stress} \tag{3.13}$$

$$G_c = \frac{K_c^2}{E} - (1-\nu^2) \qquad \textit{plane strain} \tag{3.14}$$

where ν is the Poisson's ratio.

The Griffith-Irwin solution for a through-cracked plate may be written as

$$\sigma = \sqrt{\pi a} = (2E(\gamma_e + \gamma_p))^{\frac{1}{2}} = (EG)^{\frac{1}{2}} = K \tag{3.15}$$

and the failure criterion becomes

$$\sigma\sqrt{\pi a} \geq \sigma_c\sqrt{\pi a} = K_c \tag{3.16}$$

i.e crack extension occurs when the product $\sigma\sqrt{a}$ attains a constant critical value. The value of this constant can be experimentally determined by measuring the fracture stress for a large plate containing a through-thickness crack of known initial length. This value can also be measured by using other specimen geometries, or can be used to predict critical combinations of stress and crack

length in geomaterials.

As the geometry of finite size specimens has an effect on the crack tip stress field, the expressions for stress intensity factors are modified by the addition of correction factors so as to enable their use in practical problems. A general form for such a modified expression is

$$K_I = C\sigma\sqrt{\pi a}\ f\left(\frac{a}{W}\right) \tag{3.17}$$

where C and f(a/W) are correction factors related to the geometries of specimens and have to be determined by stress analysis.

There are very few closed form solutions to the above equation. Most expressions are obtained by numerical approximation methods.

The critical stress intensity, $\mathbf{K_c}$ **(plane stress)**, or $\mathbf{K_{IC}}$ **(plane strain)** is called the **fracture toughness.** Fracture toughness is a powerful concept for quantifying tensile fracture. It depends on specimen thickness and constraint and is considered to be a material property (see fig. 3.11).

3.2.3 Crack tip plasticity

Structural materials deform plastically above yield stress and so in reality a plastic zone surrounds the crack tip. To describe the plastic zone in terms of size and shape is difficult, so models widely known from literature adopt one of two approaches: either they give a better approximation of the size but use a select shape, like Irwin and Dugdale (1960), or they give an impression of the shape but retain the first size approximation. The elastic stress distribution in the vicinity of crack tip shows that the stresses become infinite as **r**, tends to zero, i.e there is a stress singularity at the crack tip (see fig. 3.12).

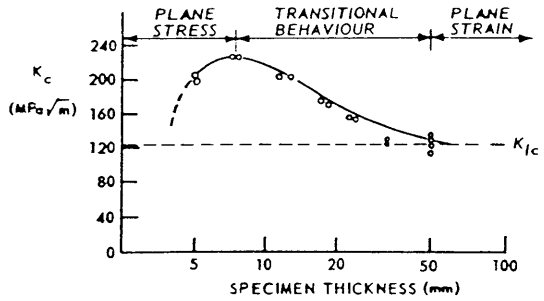


Fig. 3.11 Variation in fracture toughness with specimen thickness (from Ewalds and Wanhill. 1986)

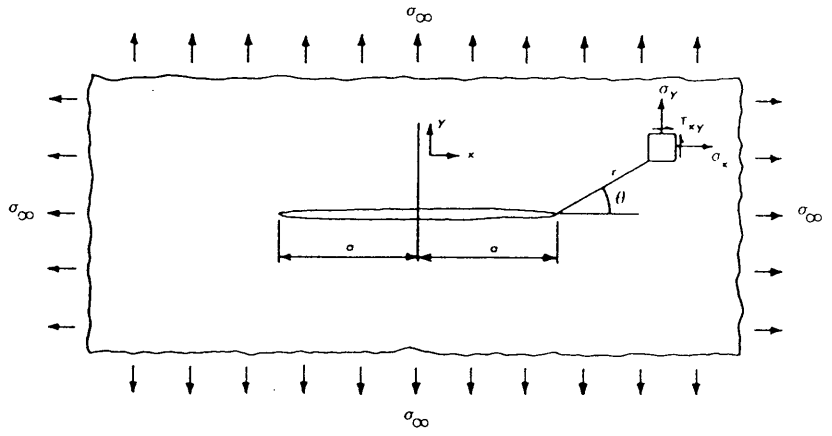


Fig. 3.12 An infinite plate containing a crack, loaded biaxially.

Irwin considered a circular plastic zone to exist at the crack tip under tensile loading as shown in fig. 3.13. He argued that plasticity makes the crack behave as if it were longer than its physical size and he showed that the crack may be viewed as having a hypothetical tip a distance r ahead of the real tip and a yielded region r_y beyond this. Since the same stress intensity factor K, gives the same plastic zone size for materials with the same yield stress, the effect of crack tip

plasticity corresponds to an apparent increase of the elastic crack length by r_y. The concept of Linear Elastic Fracture Mechanics may cope only when the plastic zone is small compared to the crack size and the cracked body still behaves in an elastic manner. Irwin in his analysis of plastic zone reached the conclusion that the plastic zone diameter is twice that reached as a first approximation. This also means that the natural crack length extends to the centre of the circular plastic zone.

$$a_n + r_y = 2r_y \tag{3.18}$$

where a_n is the notional crack increment which accounts for redistribution of stresses, that were above yield stress σ_{ys}, in the elastic case (see fig. 3.14).

Dugdale assumed that the plastic deformation zone concentrates in a strip in front of the crack as shown in fig. 3.15. The equation

$$a_n = 0.393 \left(\frac{K_I^2}{\sigma_{ys}}\right) \tag{3.19}$$

shows that the size of the plastic zone is somewhat larger than the diameter of the plastic zone according to Irwin's analysis.

The reason that a first order approximation to the plastic zone size is used in well known models for determining its shape, is that the calculations employ classical yield criteria, like those of Von Mises or Tresca, to give only the boundaries where the material begins to yield. The procedure is similar to the one that Irwin and Dugdale use but instead of calculating r_y, only for $\theta=0$, (fig. 3.12) the value of r_y over the range $(-\pi \leq \theta \leq +\pi)$ is determined. Fig. 3.16 illustrates the shapes of the plane stress and plane strain plastic zone in dimensionless form from the Von Mises yield criterion for tensile loading.

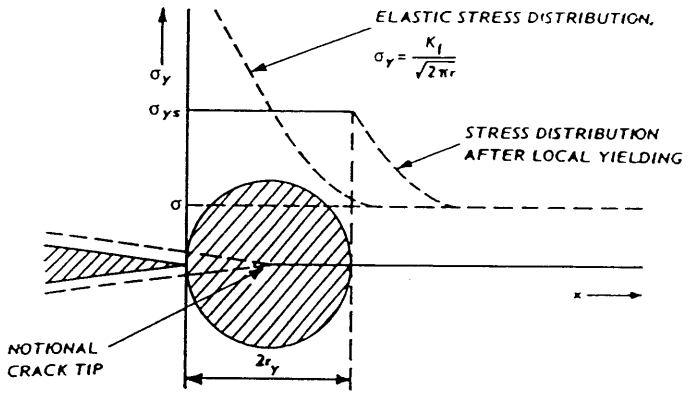


Fig. 3.13 The Irwin plastic zone (From Ewalds and Wanhill, 1986)

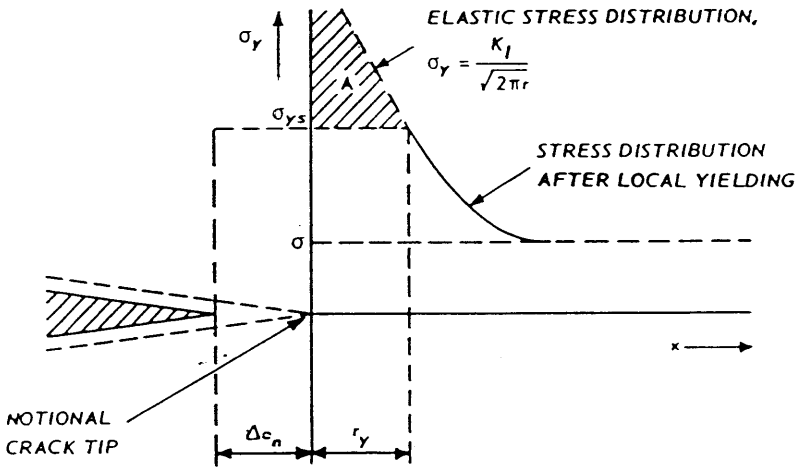


Fig. 3.14 Schematic of Irwin's analysis (From Ewalds and Wanhill, 1986).

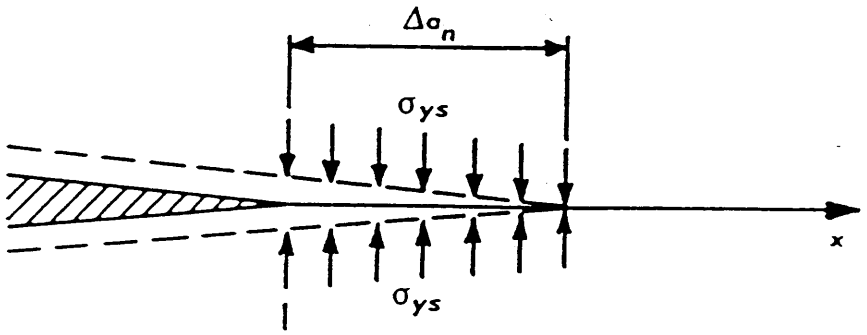


Fig. 3.15 Schematic of Dugdale's analysis (From Ewalds and Wanhill, 1986)

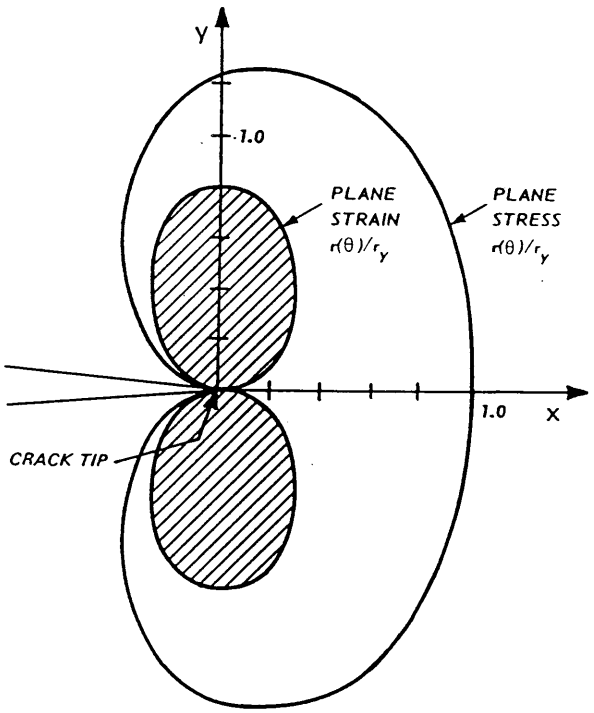


Fig.3.16 Dimensionless plane stress and plane strain plastic zones from the Von Mises yield criterion (From Ewalds and Wanhill, 1986)

There are more advanced approaches now for the proper description of plastic zone size and shape: the experimental and finite element analysis. Experimental techniques include the use of silicon iron which enables plastically deformed regions to be selectively etched and made visible. Electron microscopy and optical interferometry are also used to experimentally study the development of plastic zones.

3.3 ELASTIC PLASTIC FRACTURE MECHANICS

Concepts of EPFM were developed to deal with materials which are too ductile to permit analysis of their behaviour by LEFM. Methods in the category of EPFM extend the description of fracture behaviour beyond the elastic regime but they also cannot cope with the occurrence of general yield leading to plastic collapse. Within the context of EPFM two general objectives to solve fracture problems are identified.

(1) A search for characterising parameters such as fracture toughness, K, and energy release rate G.

(2) Attempts to describe the elastic-plastic deformation field in detail in order to find a criterion for local failure.

It is generally accepted that a proper description of elastic-plastic fracture behaviour, which usually involves stable crack growth, is not possible by means of a straight forward, single parameter concept. Also, detailed studies of stress fields around elastic-plastic crack tips are most unlikely to give results suitable for practical use. So far the only notable success of EPFM for practical applications is the ability to predict one or two parameters. The two most widely accepted concepts for this purpose are the **J integral,** and the **Crack Opening Displacement, COD.** Of less widespread recognition are the **Extended Dugdale Approach** and the **Equivalent Energy Method.**

3.3.1 The J integral

This concept is based on an energy balance approach and was first introduced by Rice, 1978. Consider the energy balance approach as given in equation (1.1).

$$U=U_0+U_a+U_\gamma-F$$

Although the set up about energy balance previously was linearly elastic, this equation remains valid as long as the theoretical treatment of the behaviour remains elastic but not necessarily linear. Thus, even for a material as given in fig. 3.17 the equation is valid provided the material is elastic. An important

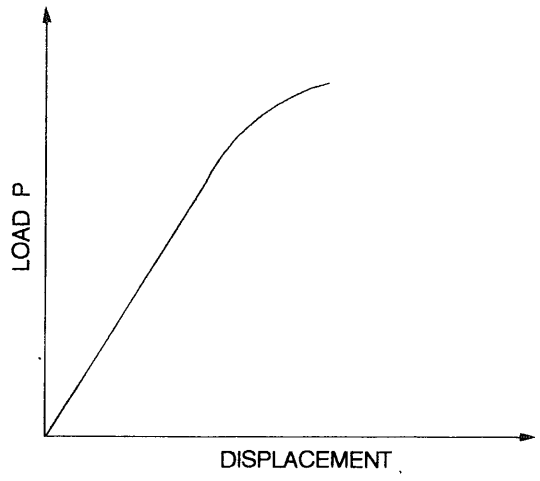


Fig. 3.17 Non-linear elastic behaviour of a loaded uncracked plate.

consequence of this extended validity of the equation is that under certain restrictions this non linear behaviour can be used to model plastic behaviour of a material. This is known as the deformation theory of plasticity.

The main restriction is that no unloading may occur in any part of a body since for actual plastic behaviour the plastic part of the deformation is irreversible. As

long as equation (3.1) remains valid a non-linear elastic equivalent to energy release rate G, representing the elastic energy available for infinitesimal crack extension may be derived, leading to

$$J=\frac{d}{da}(F-U_a) \tag{3.20}$$

By definition **J=G** for elastic behaviour. Returning to equation (3.1) the potential energy U_p, may be defined as

$$U_p=U_0+U_a-F \tag{3.21}$$

i.e

$$U=U_p+U_\gamma \tag{3.22}$$

Potential energy contains all the energy terms that contribute to nonlinear elastic behaviour, while the change in elastic surface energy owing to crack extension U_γ, is generally irreversible. Since the change in elastic energy U_0, is a constant, differentiation of potential energy U_p, gives

$$\frac{dU_p}{da}=\frac{d}{da}(U_a-F)=-\frac{d}{da}(F-U_a) \tag{3.23}$$

Substituting in equation (3.20) the J integral becomes

$$J=-\frac{dU_p}{da} \tag{3.24}$$

Since dF/da represents a decrease in potential energy provided by the external force F, per increment of crack extension and dU_a/da represents the increase in elastic energy owing to the external work dF/da, then dU_p/da represents the change in stored energy. Consequently equation (3.24) represents a decrease in potential energy (negative sign), which means a release of crack driving energy J, in order to provide the required energy dU_γ/da, for an increase in crack surface by da.

Some remarks about the J Integral concept. It is helpful at this point to address some remarks concerning the whole concept.

(1) It was stated initially, that J integral would be derived from the assumption that the deformation behaviour is non-linear elastic and therefore reversible. However, plastic deformation is not reversible and the energy dissipated cannot be transformed into other kinds of energy. Thus, with true plastic deformation the transformation of energy terms in some vital steps of the derivation are not legitimate.

(2) It was also stated that the assumption of non-linear elasticity is compatible with actual deformation behaviour only if no unloading occurs in any part of the material. But the material is unloaded at the crack tip when the crack grows. It follows that J integral is in principle applicable only until the onset of crack extension and not for crack growth.

(3) In the derivation of J the strains and the displacements on a body are the controlling parameters. Limitations of the derivation to a biaxial case in order to simplify the analysis means that no effect of strain in the thickness direction has been taken into account. Thus, J may be valid only for situations of plane strain; for practical purposes this restriction is not serious since J is primarily useful for predicting the onset of crack extension in thick sections, which are generally in plane strain.

(4) By definition J=G for the linear elastic case. By analogy the units of J are energy/length per unit thickness of a material i.e Joules/m^2 or N/m. A further analogy with LEFM enables J to be written as

$$J=G=\frac{K^2}{E} \qquad \textit{for plane stress} \tag{3.25}$$

$$J=G=\frac{K^2}{E}(1-\nu) \qquad \textit{for plane strain} \tag{3.26}$$

(5) Again, in agreement with LEFM, it is to be expected that there is a critical material parameter J_c, which predicts the onset of crack extension.

Obtaining solutions for J integral in actual specimens has proved to be difficult (Ewalds and Wanhill. 1986). Although some simple expressions have been developed for standard specimens, it is generally necessary to use finite element techniques.

3.3.2 The Crack Opening Displacement (COD) approach

The COD approach was introduced by Wells in 1961. Referring to fig. 3.18 it is shown that in cases A,B,C, and partly D the stresses and strains in the vicinity of a crack or defect are responsible for failure. At crack tips, plastic deformation occurs once the stresses exceed the yield strength σ_{ys}; therefore, failure is brought about by stresses and hence strains exceeding certain respective elastic limits. Wells' argument continues to point out that the stress at a crack tip always reaches the critical value and consequently it is the plastic strain in the plastic tip region that controls the fracture. A measure of the amount of crack tip plastic energy strain is the displacement of the crack flanks, especially at or very close to the tip. Therefore, at the onset of fracture this value of **Crack Opening Displacement** or δ_t, has a critical value for a particular material and consequently could be used as a fracture criterion.

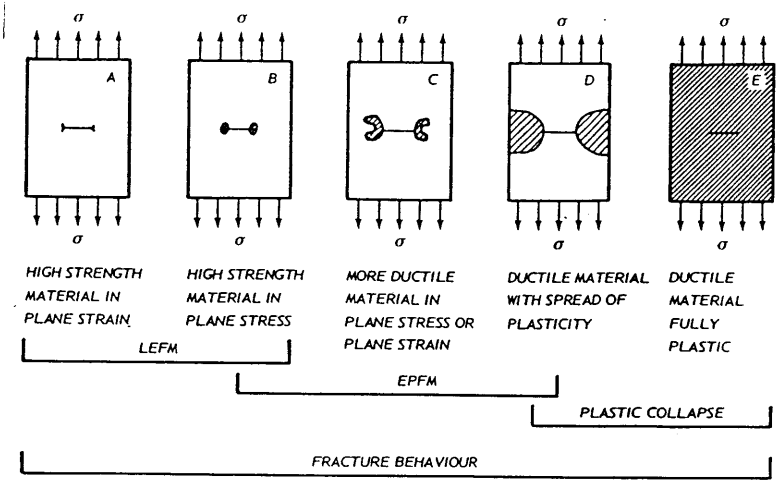


Fig. 3.18 Ranges of applicability of LEFM and EPFM for describing fracture behaviour (from Ewalds and Wanhill,1986).

Burdekin and Stone (1966), provided an improved basis for the COD concept by using Dugdale's strip yield model. The result is shown in the equation below:

$$\delta_t = \frac{8\sigma_{ys} a}{\pi E} \ln \sec\left(\frac{\pi\sigma}{2\sigma_{ys}}\right) \tag{3.27}$$

It was said earlier that under LEFM conditions there are direct relations between δ_t and K_I. Thus, for the Dugdale analysis COD becomes

$$\delta_t = \frac{K_I^2}{E\sigma_{ys}} \tag{3.28}$$

and for the Irwin circular plastic zone analysis COD equals

$$\delta_t = \frac{4}{\pi}\frac{K_I^2}{E\sigma_{ys}} \tag{3.29}$$

Although these relations are important because they show the compatibility of the COD approach to LEFM, it is also obvious that the approach is not restricted to LEFM as the occurrence of crack tip plasticity is inherent to it. The major disadvantage of the COD approach is that equation (3.27) is valid only for an infinite plate and it is not possible to derive similar formulae for practical geometries unlike the situation with the stress intensity factor K_I and J integral concepts. Therefore, a characteristic value of COD at the onset of fracture can be used to compare the fracture resistance of materials but not to calculate a critical length in a structure. In an attempt to overcome this problem COD design curves have been constructed but again the discrepancy between the theoretical and the empirical COD design curves is considerable (Ewalds and Wanhill, 1986).

Dawes (1980), suggested that the maximum permissible size a_{max}, is obtainable from equations (3.30) and (3.31), for different ranges of the ratio σ_1/σ_{ys}, shown below:

$$a_{max} = \frac{\delta_{tcrit} E\sigma_{ys}}{2\pi\sigma_1^2} \quad for \quad \frac{\sigma_1}{\sigma_{ys}} < 0.5 \tag{3.30}$$

$$a_{max} = \frac{\delta_{tcrit} E}{2\pi(\sigma_1 - 0.25\sigma_{ys})} \quad for \quad 0.5 < \frac{\sigma_1}{\sigma_{ys}} < 2 \tag{3.31}$$

where σ_1 is the sum of all stress components, general and local. Note that σ_1 may reach values twice as high as σ_{ys}.

3.3.3 The relation between J and COD

In the late 1970s a number of expressions relating J integral with COD were published. They all take the form of

$$J=M\delta_t\sigma_{ys} \tag{3.32}$$

where M varies between 1.15 and 2.95 and is a function of σ_{ys}/E and the strain hardening exponent n.

Hutchinson (1979) using Dugdale's strip yield model derived the following expression relating the J integral and COD:

$$J=\sigma_{ys}\delta_t \tag{3.33}$$

Some remarks concerning the J integral and COD.

(1) Hutchinson has used only the definition of the strip yield model and consequently his analysis is valid under both LEFM and EPFM conditions. The analysis, though not a definite proof since it uses a model, clearly demonstrates the existence of a relation between J and COD.

(2) More complex calculations, using finite element methods, also arrive to the same result of equation (3.32).

(3) Experimental values of M are approximately 2 in contrast with equation (3.33) where M=1. Most probably, the higher values of M are due to the real plastic zone behaving differently from that assumed by the Dugdale approach.

3.4 APPLICATIONS TO ROCK

The following discussion is taken from Ingraffea (1987) and is included here to illustrate the problems that arise with the application of either the strength of materials or the LEFM to the solution of problems with real rock.

Classic theories on fracture mechanics assume either material with cracks in it and high concentrations of stresses at the tips of these cracks from where a crack propagates, or material which, although seemingly a continuum, it contains flaws (crystals, pores etc.), that act as locations for high stress concentrations from where a crack initiates and propagates.

The purpose of the following examination is to provide some appreciation for the prediction of crack initiation in structures in rock. Two approaches are used as basic tools to crack initiation:

a) The strength of materials, and

b) Linear Elastic Fracture Mechanics.

The examination will elucidate two fundamentally important concepts in rock fracture, the effects of scale, and material non-linearity.

Effects of scale: Both approaches, strength of materials and LEFM assume continuum behaviour, a concept which is only relative in rock mechanics. Fig. 3.19 illustrates this point: fig. 3.19a represents a microscopic view of grains and fig. 3.19c depicts a jointed rock mass. Neither one of these two conditions represent a situation applicable to the initiation of fracture from such initial flaws because the cracks shown in these figures are close to length l_c, which is the characteristic dimension of the structure at this particular viewing scale. In other words the concept of continuum is being used to predict the initiation of a crack that is of similar size to discontinuities which are already present and have to be included in any model for predicting failure. However fig. 3.19b illustrates a structure in which the assumption of continuum behaviour is acceptable. From a practical engineering perspective, the cracks of concern fall within the scale

range of fig. 3.19b and fig. 3.19c.

3.4.1 Crack initiation

The problem of crack initiation in rock structure such as tunnels and boreholes has been approached in practice with elementary concepts of strength of materials and/or LEFM.

A strength of materials approach involves the following points:
(1) The basis for prediction of crack initiation is to compare a computed tensile stress to a given tensile strength of rock.
(2) It is assumed that the material behaviour is elastic-brittle as shown in fig. 3.2d and therefore the initiation is instantaneous.
(3) No information regarding the length of the initiated crack is available.
To illustrate the oversimplification of points (2) and (3) let us consider a tunnel or a borehole, loaded in a biaxial compressive stress field where, Q and P are the horizontal and vertical stresses respectively as shown in fig. 3.20. A strength of materials analysis predicts crack initiation at the crown and at the invert of the tunnel at applied stress P_{cr} not of equal magnitude to σ_τ but

$$P_{cr}=\sigma_\tau+3Q \tag{3.34}$$

where σ_τ is the tensile strength of the rock.

Peng (1975) and later Peterson (1981) and Labuz and al. (1985) have observed the qualitative behaviour of geomaterials in strain control tensile tests, as shown in fig. 3.21. From the figure it is obvious that geomaterial does not fail as a purely brittle material and that considerable energy absorption takes place after the tensile strength has been reached. Hence, the strength of materials approach is unlikely to adequately define P_{cr}.

The second approach to crack initiation, more popular in research than practice, is based on LEFM. As highlighted at length previously and presented here summarised, the basic tenets of this approach are the following:

(1) A crack tip in a loaded structure is associated with a stress-intensity factor, K_I, which can be computed.

(2) A critical stress intensity factor, K_{IC} is a material property.

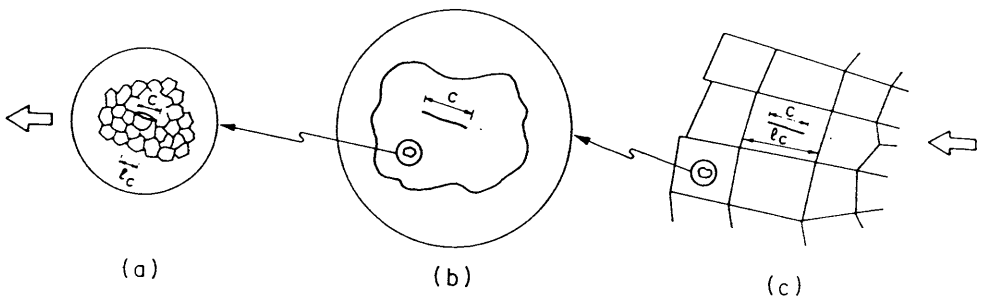


Fig. 3.19 The influence of structure scale on the concept of continuum in rock mechanics (from Ingraffea, 1987)

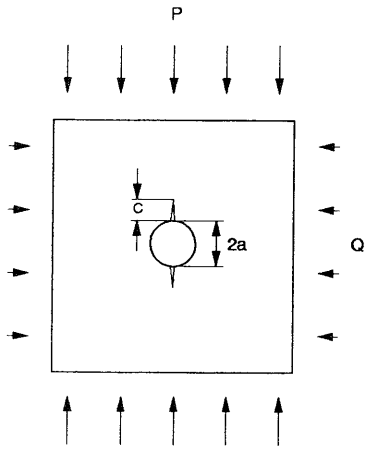


Fig. 3.20 An opening loaded in a biaxial compressive stress field. Ratio of P/Q=0.15 (from Ingraffea, 1987)

(3) Material behaviour in the near crack-front region can be inelastic and non-linear. However, as long as this process zone is small compared with other dimensions of the structure, the crack advances if

$$K_I = K_{IC} \tag{3.35}$$

A crack will stop propagating when

$$K_I < K_{IC} \tag{3.36}$$

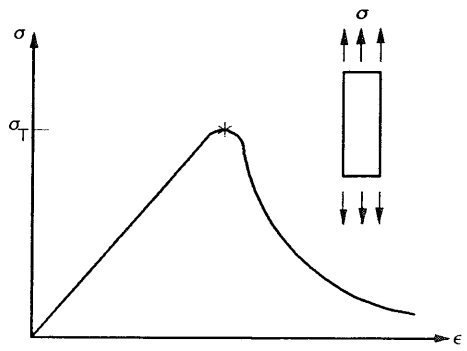


Fig. 3.21 Stress-strain relationship for uniaxial tensile loading under strain control (from Ingraffea, 1987)

Ingraffea (1979) considered the same biaxially loaded tunnel or borehole described above to investigate the crack growth history using LEFM and some results are shown in fig. 3.22. This figure shows that for an assumed fracture toughness of 1.65 MPa $m^{1/2}$, a load level P=62.9 MPa will allow stable extension to a length C_1 and a load P=227.7 MPa will do the same to a length C_2 i.e a higher load produces a longer stable crack. The first criticism of LEFM approach to this problem is that it cannot predict crack initiation. LEFM is inapplicable to

problems without cracks. As shown in fig. 3.22 crack growth can only be predicted if there is an initial flaw at the crown and the invert equal to C_i. The length of C_i is smaller for a higher load.

The second point of criticism of the LEFM approach is the fact that it does not account for the possibility that concepts of stress intensity and fracture toughness might be meaningless for the assumed, initial flaw size. The K_{IC} curve in fig. 3.22 is only valid above an absolute crack length longer than C_i. For shorter crack lengths, fracture mechanics may still be applicable but not the LEFM variety. From the above discussion it is clear that neither the strength of materials approach or the LEFM is totally satisfactory for crack initiation and propagation in rock.

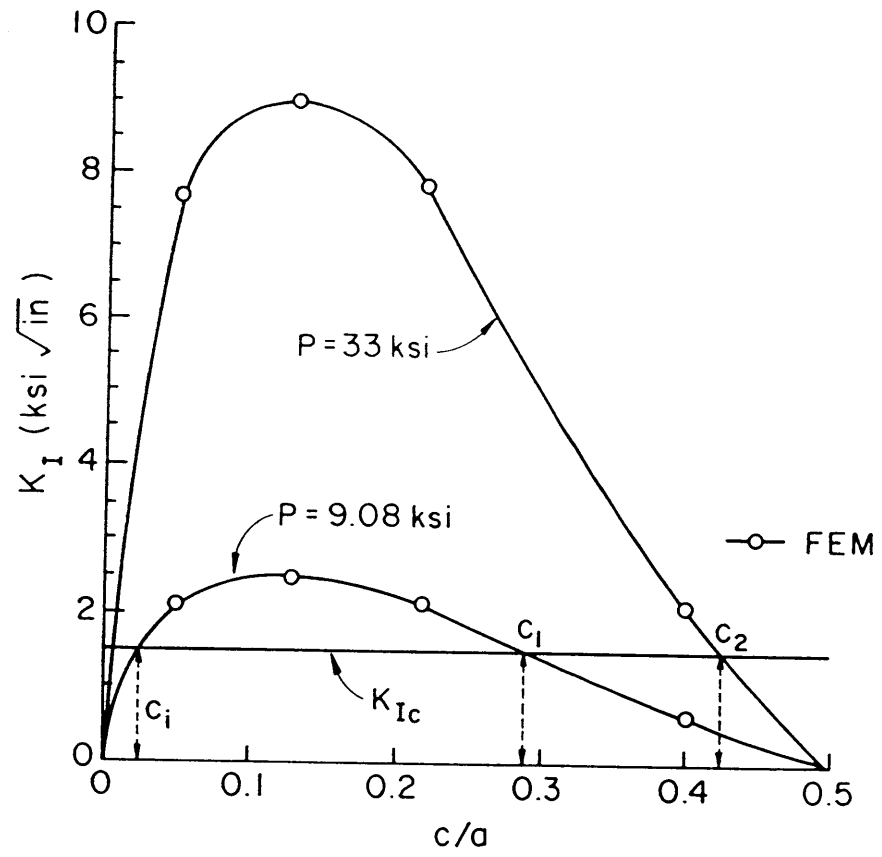


Fig. 3.22 Results from a FEM analysis showing the predicted crack growth history in a plate containing a circular opening loaded in compression (from Ingraffea, 1987)

To combine both approaches to create a comprehensive model is not possible as neither approach incorporates the material behaviour shown in fig. 3.21 and the implied scale dependence.

The same example of a tunnel is used again to illustrate that the condition $\sigma=\sigma_T$ at crown and invert shows only the beginning of the initiation process because as fig. 3.21 illustrates, this process is not instantaneous i.e there is no guarantee that load level σ_T provides a crack length of C_i, the critical length required for a smooth transition to LEFM (fig. 3.22).

Scale effects must be considered for LEFM to be applied to cracking in rocks. As long as the process zone region is small in comparison with the smallest critical dimension of the structure, the crack will advance if the stress intensity factor K_I, is equal to the critical stress intensity factor K_{IC}. If these scale conditions are not met, a non-linear approach will be applicable. The above discussion indicates the need of a comprehensive model, which will acknowledge both the material behaviour and scale effects in order to be able to predict the crack initiation process and the consequent transition to LEFM.

Ingraffea et al (1984a), and Ingraffea and Gerstle (1984) used such a model which incorporates actual material behaviour and scale effects from the point of view of discrete representation of a crack in a finite element model. The basis for any process zone size estimate, whether it is for a plastic deformation zone in metals or for a region of inelastic response in rock, is a constitutive model for the material in this zone. To describe the inelastic behaviour in the process zone of a crack initiating or propagating in rock the following assumptions were made by the authors:

(1) The only constitutive modelling required for process zone description in pure mode I is the stress vs COD relation which can be obtained from a displacement controlled, direct tension test shown in fig. 3.23.

(2) Assumption (1) implies that normal stress will continue to be transferred

across a displacement discontinuity which may or may not be visible to the naked eye. It is assumed that this stress transfer is due to grain bridging and the undulating, 3-dimensional nature of the opposing crack surfaces.

(3) It is assumed that the process zone localises due to the rapid softening behaviour shown in fig. 3.23 into a narrow band ahead of the true crack tip, or in the region of tensile stress concentration, as in the case of the crown and the invert of the biaxially loaded tunnel or borehole. Ingraffea's finite element analysis (1987) suggests that, all softening is confined to one dimensional interface elements lying in the crack plane ahead of the true crack tip, or normal to the concentrated tensile stresses.

The above assumptions are schematically shown in fig. 3.24. The model shows that the inelastic stress distribution is defined by the direct tensile strength which is influenced by the stress normal to the crack front and the shape of the postpeak stress-COD relationship and is also influenced by the crack opening displacement δ_c, which occurs at the crack tip. These parameters are related to the LEFM parameters G_{IC} and K_{IC} in the manner shown below:

$$G_{IC}=\int_0^{\delta_c}\delta(\Delta)\,d\Delta \tag{3.37}$$

$$G_{IC}=\frac{K_{IC}^2}{E} \quad plane\ stress \tag{3.38}$$

Equation (3.37) is useful only if LEFM conditions prevail but equation (3.38) is more general. It indicates that true crack front has ridden completely down the curve in fig. 3.23 absorbing all the energy G_{IC} in the process. Given these observations and assumptions, the following practical questions become important.

(i) How large must the critical dimension be for the application of LEFM to be

valid? Or considering assumption (3) how long is the process zone?

(ii) How sensitive is the process zone length r_p, to the constitutive model which drives it and to the structural geometry?

Ingraffea has given an answer to these questions by using numerical analysis based

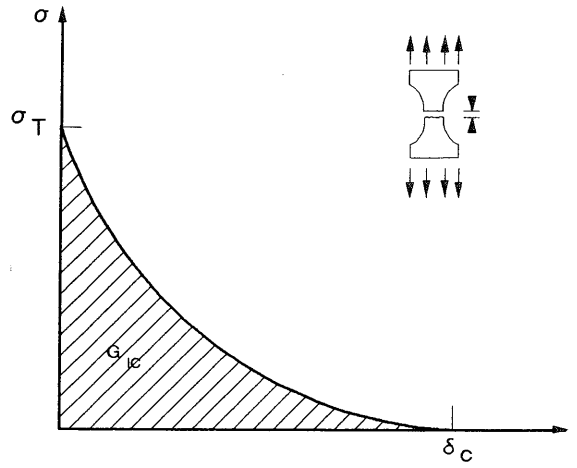


Fig. 3.23 Model of the process zone in a strain softening geomaterial (from Ingraffea, 1987)

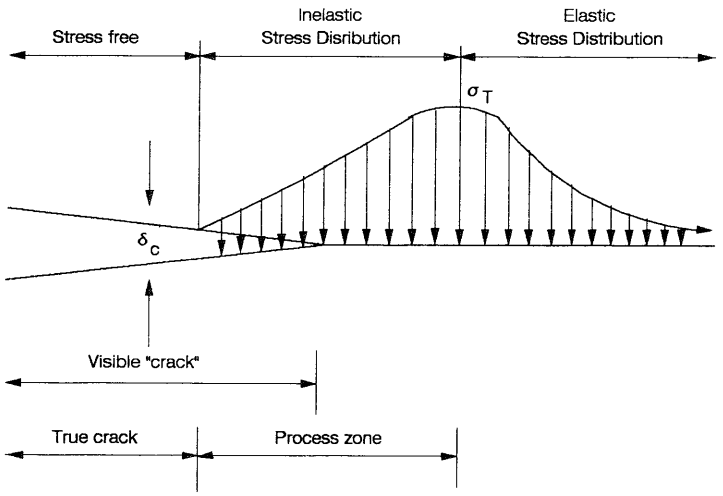


Fig. 3.24 A representation of the process zone in rock (from Ingraffea, 1987)

on Finite Element Methods (FEM) and his case studies are now briefly considered.

3.4.2 Case studies

Solutions suggested by Ingraffea regarding the critical dimensions of the flaws and the magnitude of the applied loads is shown in the following examples solved by FEM.

The example problem is the one shown in fig. 3.20. The objectives are to show how the above described constitutive model uses non-linear fracture mechanics to describe the crack initiation process and how it accommodates the effects of structure scale in the process.

The problem is solved twice: in case (I) the size of the hole, which represents a borehole or a tunnel, 2a equals 0.01905 m while in case II all structure dimensions are increased by a factor of one hundred. All material properties are the same in both cases and have been estimated (i.e E = 138 GPa, ν = 0.2, σ_T = 34.5 MPa, σ_c =573 MPa and K_{IC} =6.6 MPa $m^{1/2}$), except for the unconfined compressive strength σ_c, which was experimentally measured. Based on equation (3.34), the critical load P_{cr}, required for crack initiation is 62.8 MPa. Ingraffea's model examines the correctness of this "strength of materials" approach. By applying incremental loads in the model fig. 3.25a,b,c,d is obtained. This figure shows the computed stress distribution normal to the line OA, which is the expected cracking direction.

In case 3.25a the load is 62.8 MPa, which is the load predicted by the strength of materials approach required for crack initiation. Note, that the peak tensile stress at point 0, the crown, is close to the tensile strength (34.5 MPa, an estimated material property), and the tension reaches zero over a length of about 1/3 the hole radius.

The load was increased to 103.5 MPa and the curve 3.25b was obtained. The

observations worth noting here are the following:

(i) The stress at the crown has decreased in response to the beginning of the crack initiation process. (ii) The location of the peak tensile stress has moved into the rock. (iii) Stress redistribution has occurred and the tensile stress region now extends to a distance of about 1/2 the hole radius. (iv) No true cracking occurred.

Fig. 3.25c shows the computed stress distribution at P=227.7 MPa. All of the observations made for fig. 3.25b are also valid here with the exception of the tensile zone which has moved to a depth of about 2/3 of the hole radius; but still no true cracking has taken place. The final load was 345 MPa and the result is shown in fig. 3.25d. At this load the tensile stress level at the crown has just reached zero and true cracking is initiated at this point.

The process of crack initiation prediction can also be viewed in fig. 3.26. Here the computed COD profiles, for each load level which caused the evolution of the process zone, are shown. The critical COD δ_c, as assumed for this material, is 1.83×10^{-2} mm. It is seen from the figure that true cracking at the highest load level, extends to a distance of less than one tenth of the opening radius and the process zone which is the length over which COD $< \delta_c$ is approximately six times greater than the true crack length.

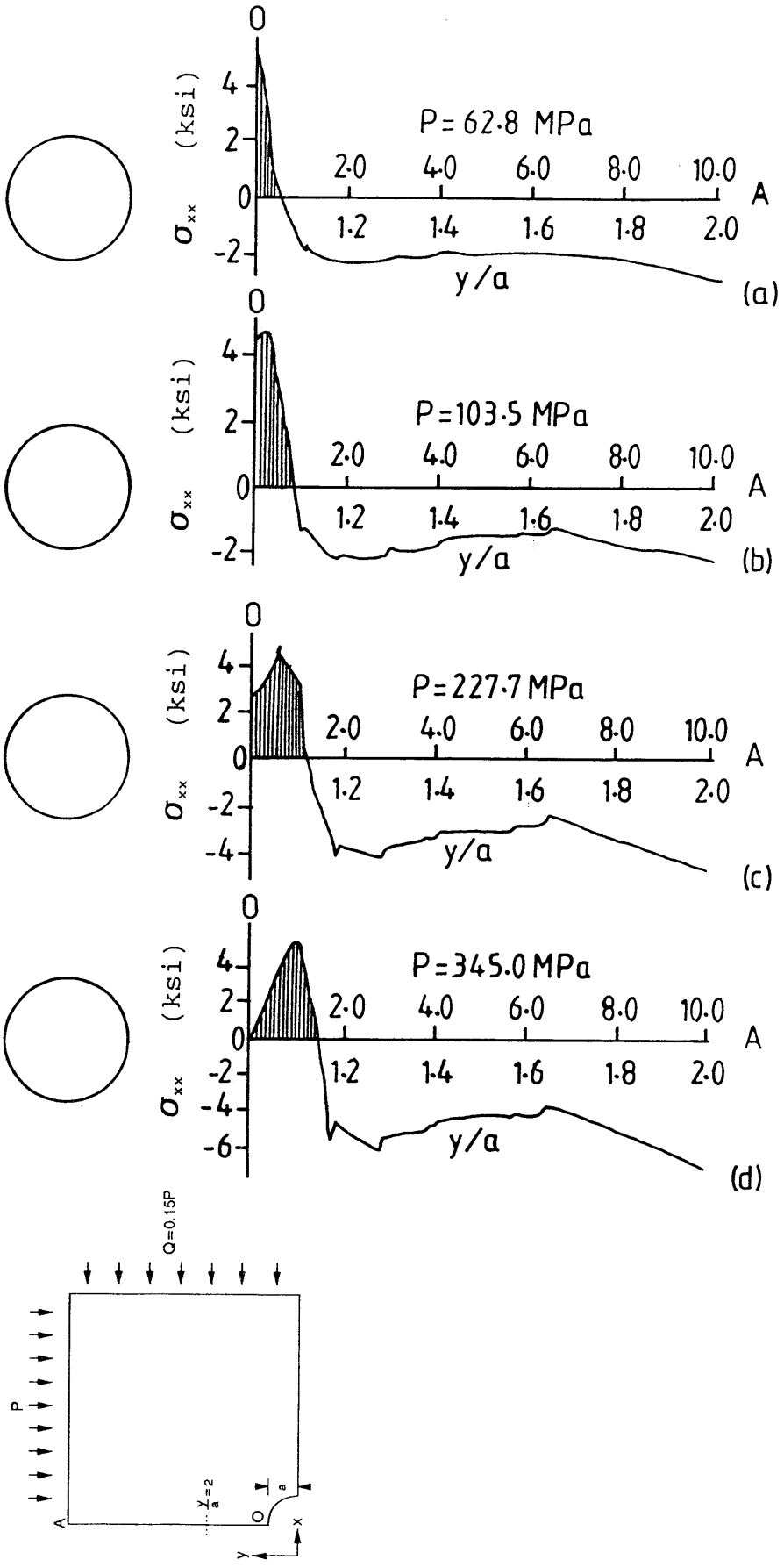


Fig. 3.25 Normal stress distribution along line OA in example case I.

y/a renumbered according to text. Shaded area represents tensile stresses. 1 ksi = 6.895 MPa.

(After Ingraffea, 1987 p82-84. Modified for this thesis).

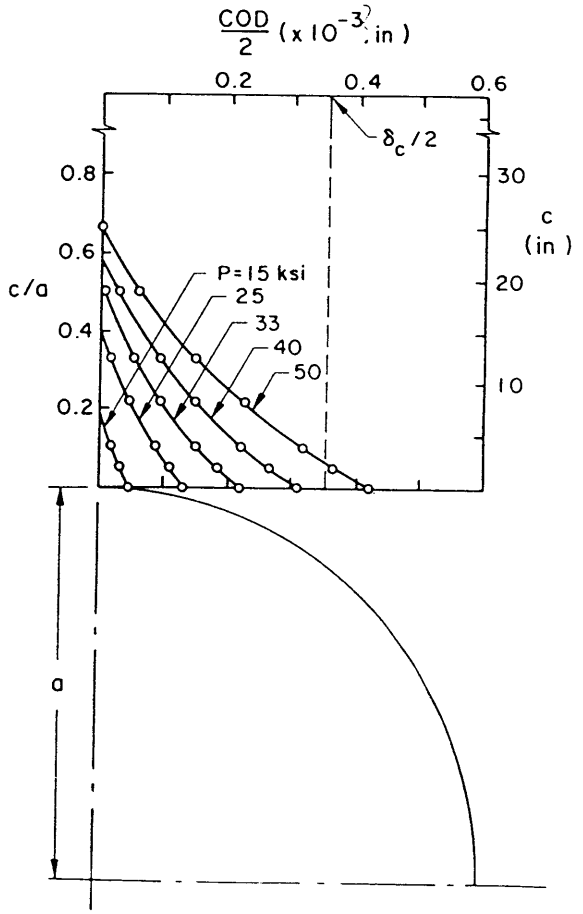


Fig. 3.26 COD profiles for example problem in case I (From Ingraffea, 1987)

Two important conclusions may be drawn from the analysis of case I:

(1) A crack initiation prediction based on the strength of materials approach (eq. 3.34) is extremely conservative since no true cracking was computed until a load of over five times that predicted was applied.

(2) LEFM is not applicable to this structure-material combination. Even after a true crack was initiated the process zone length was about 6 times the true crack length. This is contrary to the understanding that the process zone length is very small in comparison with true crack length.

In case II of the problem the radius of the opening becomes 1.91 m. At load levels up to 62.1 MPa the computed results were the same as for case I as the elastic tensile stress concentration factor at point 0 is independent of the scale of this problem but the similarity ends here. When the load was increased to 62.7 MPa, the breakdown process at the crown and invert began. But in this case it continued until the stress distribution obtained the shape shown in fig. 3.27a. If one compares this figure to the one corresponding to the same load in case I (fig. 3.25a), then one can see that whereas in case I process zone development had just began, in case II it had been completed over a length of more than 1/3 the hole radius. Fig. 3.28 shows that the process zone, which is the length over which COD is smaller than δ_c, is a small percentage of the true crack length. Fig. 3.27b and fig. 3.28 show the stress and COD distributions at P=227.7 MPa respectively. They show that true cracking has extended to nearly 3/4 of the hole radius and that the process zone has become almost negligible.

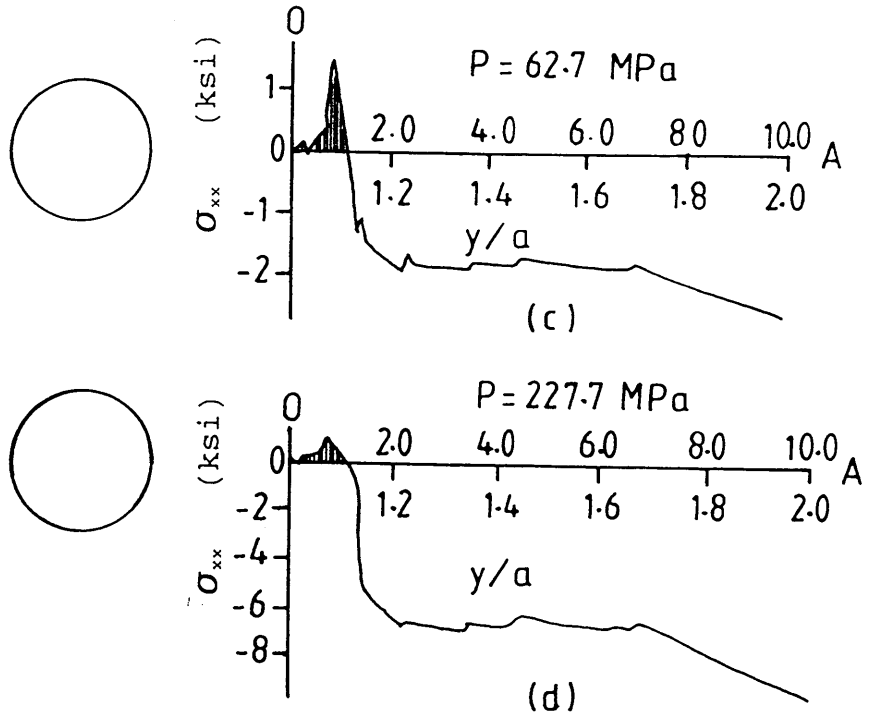


Fig. 3.27 Normal stress distribution along line OA in example problem in case II; y/a renumbered according to text. 1 ksi = 6.895 MPa.
(After Ingraffea, 1987 p86. Modified for this thesis).

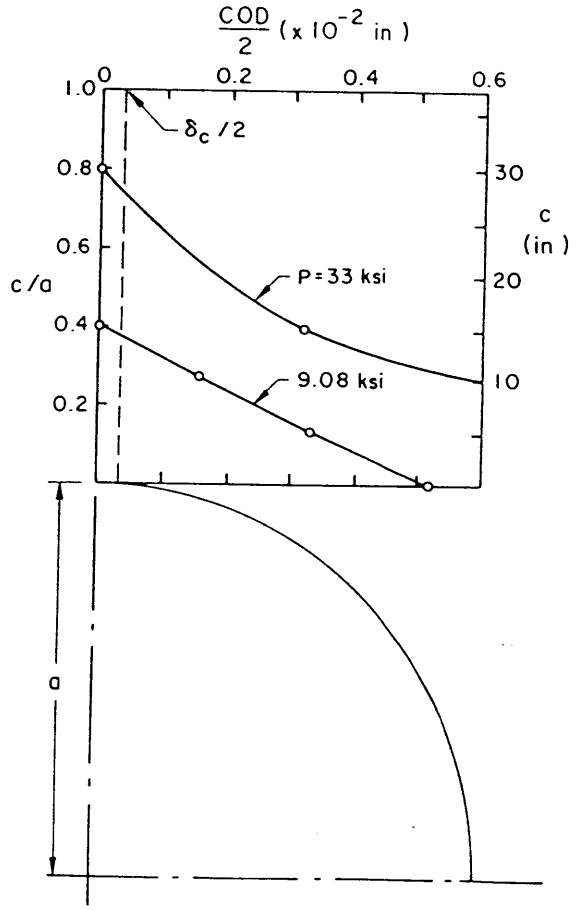


Fig. 3.28 COD profiles for example problem in case II (From Ingraffea, 1987).

The conclusions to be drawn from case II are the following:

(1) The crack initiation prediction based on the strength of materials approach (eq. 3.34) is quite accurate. This was achieved by increasing the scale of the structure while the material constants remained the same. The question now is whether it is possible to quantify the relationship between structure scale, tensile strength, (as an indicator of ideally brittle behaviour) and G_{IC}, (as an indicator of ductility) so that the analyst would be able to predict which approach to employ for a given problem. Theoretically it is possible.

To accommodate this, a concept of a structure-material brittleness number (s) has

been proposed by Carpinteri, 1982, which relates the structure-material brittleness and the characteristic length of the structure

$$s = \frac{(G_{IC}E)^{\frac{1}{2}}}{\sigma_T a^{\frac{1}{2}}} \tag{3.39}$$

where G_{IC} is proportional to σ_T and δ_c and therefore the above equation is proportional to the ratio of the material and structure scale parameters.

(2) The second conclusion is that a transition to LEFM behaviour can be made at the crack initiation load. Fig. 3.27 and fig. 3.28 show that sufficient cracking has occurred at this load level for the ratio of process zone length to true crack length to become small; this implies that a stress intensity factor approach to crack propagation from the nucleated crack is valid.

3.5 CONCLUSIONS

No study of the strength of rock as a material can commence without some comment being made upon the mechanics of the processes involved. There is no doubt concerning the role of flaws in the stages leading to failure nor in the value of an appreciation of the energetics involved gained from a Griffith's based approach to crack propagation. However, the problems arise when these concepts are transferred to a naturally occurring material where no quality control has been exerted upon its manufacture and all of microscopic structures may be present at a variety of scales and preferred orientations.

The above example with its two cases has demonstrated that the prediction of crack initiation is not a simple problem in practice and at scales relevant to most engineering in rock; more over it has shown that both the strength of materials and the LEFM approaches have limitations: The former is unrelated to scale

while the latter requires guess work just to make it applicable. The most important conclusion is that rock mechanics problems relevant to crack initiation deserve a reevaluation based on the behaviour of rock materials shown in fig. 3.21.

Application to real rock mechanics problems of the concepts and theories discussed in this chapter are increasingly adapted to Finite Methods. The power of FM lies in the relationship it has established between stress and crack length. This has been shown to work well as long as the stress condition is adequately modelled through some combination of the various modes of failure. The immediate problem in rocks is associated with the definition of the "starting crack". Most authors consider the average grain size as the "suitable" critical crack length. However, attempts to find the critical length from independently measured tensile strength and fracture toughness data often lead to strange results. Experiments conducted on granite and limestone (Lajtai et al, 1989) where the tensile strength and fracture toughness were both measured predicted a computed critical crack length greater than even the largest crystal in granite.

Since there appears to be no acceptable way to measure the size, the shape and orientation of the "critical" starting flaw, the selection of relevant parameters becomes arbitrary. Concentrating on the selection of the elements of the "critical" starting crack distracts the attention from the real cause of fracture which is the stress concentration. Although it is possible to build a theory for rocks around a flaw that cannot adequately be identified, there is little argument about the concept that fractures are nucleated from stress concentrations.

But can the concept of stress concentration help in materials such as rock? At the moment it seems unable to do so. Thus it is reasonable to return to the behaviour of rock in extension and the basic parameters which can be measured with known accuracy viz. load and displacement. These parameters provide a means of measuring the work required to cause failure in extension and provided this is

should supply a basis for describing rock that is at least as sound as that given by a measure of rock performance in compression. For this reason there is value in studying the role of the Hoop test in this work: this is the subject of Part II.

PART II

THE HOOP TEST

This part is exclusively dedicated to the Hoop tension test. It consists of two chapters: chapter 4 and chapter 5.

Chapter four is concerned with the theory of the test and the investigation of a hoop model using the photoelastic method. Confidence is thereby gained for the theory predicting tension in the Hoop test.

Chapter five is concerned with the verification of the findings of chapter four when applied to real rock. The two materials, porous sandstone and crystalline marble, which are studied further in the third part of this thesis, were used for this purpose. Initially the performance of rock hoops was investigated using two different testing systems, a closed loop servo-controlled machine (Terra-Tek) and a loading system using a pressure controller manufactured by the Geotechnical Design Systems (GDS). The performance of the tests was satisfactory with both systems. With the performance of real rock hoops established, the corroboration of the mathematical and photoelastic analyses was pursued using Holographic Interferometry and the Scanning Electron Microscopy, both of which methods resulted in good agreement with the findings of the theory discussed in Chapter four.

CHAPTER FOUR

THEORY AND PREDICTION

4.0 INTRODUCTION

The Hoop tension test, introduced by Xu, de Freitas and Clarke (1988), is a new way to study the behaviour of rock in extension and the tensile strength of rock. The specimen is ring shaped and a pair of half cylindrical shaped platens is inserted into the centre of the rock annulus. An hydraulic "jack" is contained within the platens and pressure is applied through it to force the platens apart until failure of the hoop occurs. The position of failure is predicted where the maximum stress in extension is applied, i.e opposite the gap separating the platens. The Hoop specimen is positioned symmetrically about the platens; this is made possible by the use of a rigid plate and three adjustable screws, as shown in fig. 4.1.

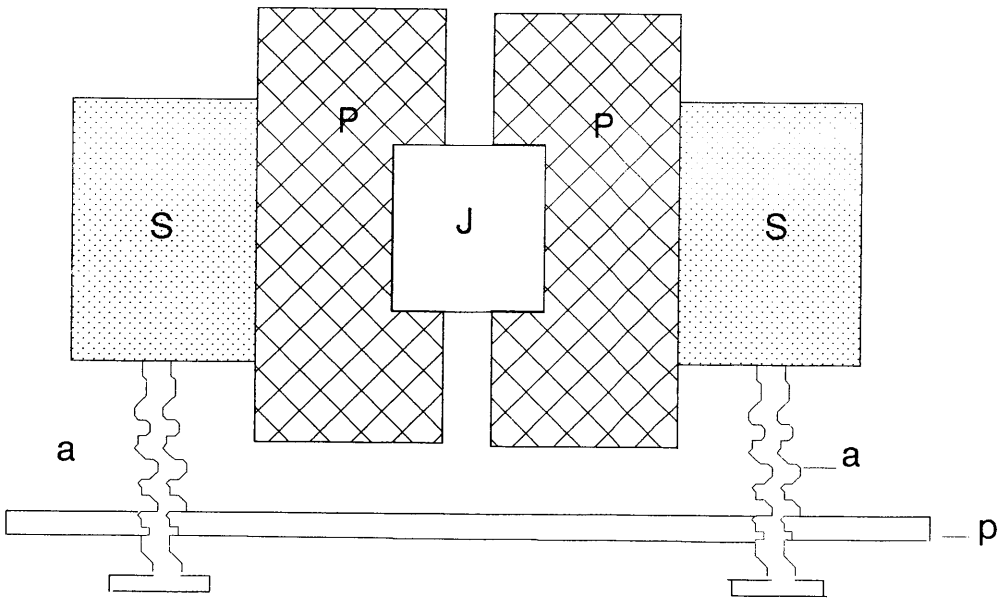


Fig. 4.1 A vertical cross section showing the experimental set-up of the Hoop tension test. P-platens, J-hydraulic jack, S-sample, a-adjustable screws, p-platform. (after Xu et al, 1988)

This section is concerned with the study of the behaviour of the Hoop, in quite different conditions from those described by Xu et al; those authors used a very soft testing system with a hand pump for the application of load, and without a response of applied load to specimen deformation.

4.1 MATHEMATICAL AND FINITE ELEMENT ANALYSES

A mathematical analysis and a finite element model of the stress distribution in the hoop has been presented by the author and others (7th International Congress of Rock Mechanics Aachen, 1991 Vol I pp 513-518). The analysis is summarised below.

4.1.1 Mathematical analysis

The loading configuration of the Hoop Tension test is shown in fig. 4.2. The two semi-cylindrical platens are hydraulically pushed apart. The stress state which forms in the hoop is considered to be the result of superimposition of the bending and the direct tension stresses as shown in fig. 4.3. The various types of equations necessary to describe the hoop stresses are introduced with the aid of a curved beam, represented in fig. 4.4. For a beam in pure bending and in a linear elastic continuum, equilibrium conditions in the z direction are satisfied when,

$$\sum F_z \int \sigma_{\theta\theta} dA - N = 0 \qquad (4.1)$$

and for moments about the centroidal X-axis

$$\sum M_x = \int \sigma_{\theta\theta} (R - r)\, dA - M_x = 0 \qquad (4.2)$$

where, F=force in the z direction, normal to the cross sectional area of the

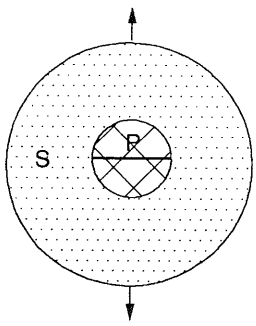


Fig. 4.2 Diagram showing the loading configuration in a Hoop test. Arrows show the direction of loading. P-platens, S-sample.

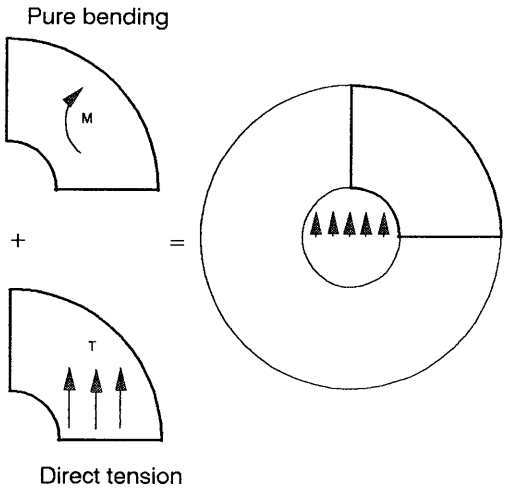


Fig. 4.3 Superimposition principle of pure bending and direct tension applied to the analysis of hoop stresses.

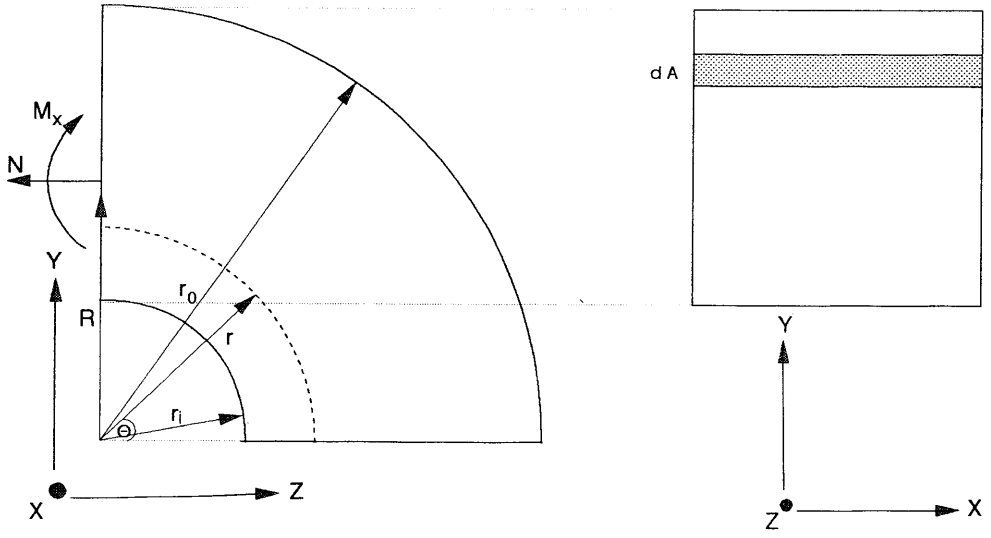


Fig. 4.4 Curved beam in pure bending and normal traction.

curved beam; N=normal traction in the z direction at the centroid of the curved beam; ΣM_x=sum of the moments about the x direction; A=cross section area of the curved beam; R=distance from centre of curvature to centroid of the curved beam; $\sigma_{\theta\theta}$=hoop stresses.

If $\int dA/r$ is represented by the notation A_m, the hoop stress distribution is (from the analysis by Boresi et al, 1978)

$$\sigma_{\theta\theta}=\frac{N}{A}+\frac{M_x(A-rA_m)}{A_r(RA_m-A)} \tag{4.3}$$

Hartog (1952), using Airy's stress function (ϕ), has shown that if

$$\sigma_{\theta\theta}=\frac{\delta^2\phi}{\delta r^2} \tag{4.4}$$

and ϕ given the form

$$\phi=f(r)\sin\theta \tag{4.5}$$

where

$$f(r)=C_1r^3+C_2r+C_3\ln r+\frac{C_4}{r} \tag{4.6}$$

where C coefficients are integral constants, then,

substituting equations (4.5) and (4.6) in (4.4), the hoop stresses become

$$\sigma_{\theta\theta}=\left(6C_1r+\frac{C_3}{r}+\frac{2C_4}{r^3}\right)\sin\theta \tag{4.7}$$

Both equations (4.3) and (4.7) express the hoop stresses distribution shown in fig. 4.5.

The result of superimposing a tensile component upon the pure bending component is the movement of point C towards the outer diameter in fig. 4.5. The stress distribution is non-linear because of the curvilinear nature of the hoop geometry. The maximum stress shown in fig. 4.5 will lead to the onset of tensile failure in the Hoop tension test at the inner boundary and hence to an eventual value for "tensile strength" of the rock hoop.

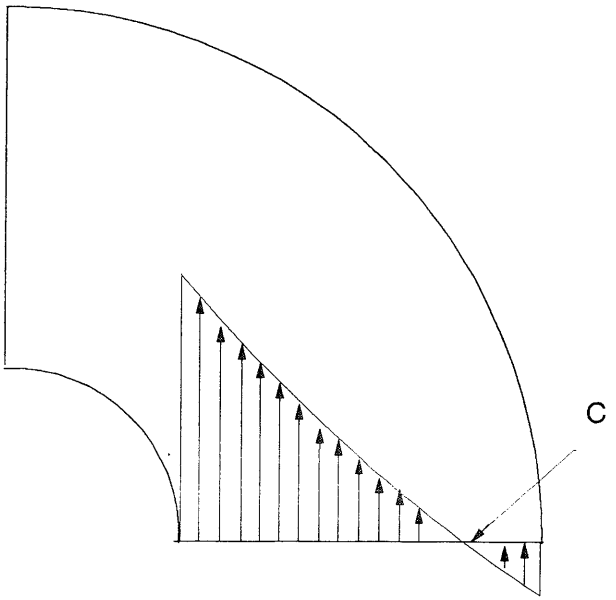


Fig. 4.5 The curvilinear hoop stress distribution. Point C is the location where the tensile stresses become compressive.

4.1.2 The Finite Element model

Work on the FEM of the hoop was started by John, and is being continued at present by H.D. Park, (PhD thesis in preparation for 1993) as part of the parallel numerical studies carried out with the experimental investigations undertaken by the author. The findings from the FEM are mentioned here because of their

relevance to the comparisons with findings from the photoelastic analysis.

The finite element model was created with the PC-based COSMOS package. Due to the symmetry of the hoop only one quadrant of the specimen is modelled. A 2-dimensional, linear elastic, isotropic plane stress model was adopted because the analyses was also of a 2-dimensional, linear elastic type. The simulation of the platen movement during the hoop tension test was performed by applying a uniform pressure to the inner bore of the model; this load was considered to be a uniform, unidirectional pressure to the entire inner surface area of the hoop, although in reality, only part of this surface area will act as the load-bearing surface.

The results obtained from the finite element analysis regarding the hoop stress distribution through the annulus of the hoop specimen are shown in fig. 4.6. Note, these runs were designed to study the direction and distribution of stress rather than its absolute magnitude. Three different loads were simulated, 6, 20 and 41 MPa. The abscissa on fig. 4.6 is the radius of the hoop specimen normalised with the thickness dimension (r_0 - r_i), see fig. 4.4. The distribution of stress is seen to cross from tensile at the inner diameter to just about compressive at the outer boundary, as predicted by equation (4.3 and 4.7) and illustrated in fig. 4.5.

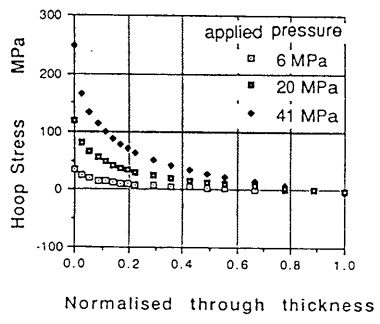


Fig. 4.6 Distribution of stresses obtained from the finite element analysis opposite the platen opening.

Fig. 4.7 shows the stress distribution in the Y-direction in the quadrant of a hoop. Note that the concentration of the highest stresses is predicted to occur at the location corresponding to that exactly opposite the separation of the platens. The principal stress trajectories in the stressed hoop obtained from the FE analysis is presented in fig. 4.8

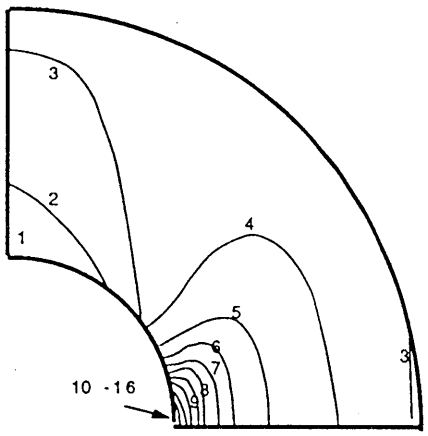


Fig. 4.7 The distribution of stresses (MPa), in the hoop obtained from finite element analysis. 1=40.6, 2=21.5. 3=23.0, 4=16.8, 5=35.9, 6=55.1, 7=74.6, 8=93.4, 9=112.5, 10=131.7, 11=150.8, 12=170.0, 13=189.1, 14=208.3, 15=227.4, 16=246.6

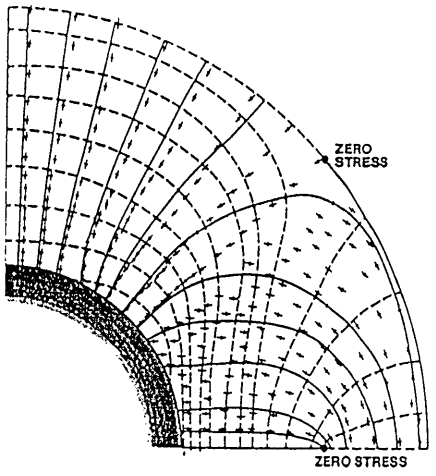


Fig. 4.8 The pattern of principal stress trajectories in the stressed hoop obtained from the finite element analysis.

4.2 PHOTOELASTIC ANALYSIS

Photoelasticity, in comparison with other methods of investigation, is cheap and rapid and yields valuable information about the direction and magnitude of stresses in a real material with real boundary conditions associated with loading. Thus, although computer facilities are available, with many problems of stress analysis being solved using finite element methods, the contribution made by the photoelastic method of stress analysis remains very valuable.

The method consists of the examination of a model by polarised light, the model made of transparent material and having special optical properties. The model, when examined under similar conditions to the ones which will be applied in reality, exhibits a pattern of fringes, from which the investigator can calculate the direction and magnitude of stresses using the theory of elasticity.

The objectives to be achieved using this method were:
(i) To define the direction of principal stresses and
(ii) To obtain a visual pattern of the magnitude of principal stresses, within the hoop.

4.2.1 Principles of observation and their interpretation

In order to enable the understanding of the interpretation of the obtained results from this investigation, a brief review and definition of the basic principles is required.

Photoelasticity relies on the interpretation of two interference patterns, one produces "**isoclinics**" the other "**isochromatics**" **Isoclinic lines** are created by the loci of points where the direction of principal stresses in the sample are parallel to the axes of crossed Polaroids. They appear as black bands. If the Polaroids, in their crossed position, are rotated, the isoclinic lines will move with them to

other points within the field. By combining in one diagram isoclinic lines obtained by rotation of the axes of the Polaroids at convenient intervals of 5°, 10° or 15° etc., a system of isoclinics covering the entire specimen is drawn. This is accomplished by tracing the lines of different fringes onto tracing paper or from photographs.

The isoclinic pattern is independent of the magnitude of the load employed and the fringe value of the material used for the model, therefore the loads applied should be sufficiently high so that isoclinics are not influenced by any initial or residual stresses present in the material.

It is observed, that sometimes all the isoclinics pass through a particular point. At such a point the principal stresses are equal in magnitude and sign so that $(\sigma_1-\sigma_3) = 0$; the material is in pure hydrostatic state of stress and behaves as if it were optically isotropic in the plane of the polaroid plate. Such points are known as **isotropic points.** If the stress in every direction is zero, the isotropic point is called a **singular point.**

A **stress trajectory, line of principal stress** or **isostatic** is a line whose direction at any point coincides with that of one of the principal stresses at that point. Since the two principal stresses at any point of a two-dimensional stress system are mutually perpendicular, it follows that a system of stress trajectories will consist of two sets of curves perpendicular to each other. One of these sets indicates the directions of σ_1 (algebraically greater) principal stresses and the other, those of σ_3 stresses.

Isochromatic fringes or simply **isochromatics** are the loci of points of equal relative retardation of propagating polarized light; fringes of equal colour thus follow the loci of points of equal principal stress difference i.e $(\sigma_1-\sigma 3)$=constant, along the same fringe. If monochromatic light is used they appear as dark bands. However, there is nothing in these fringes to indicate the order of any fringe or

the sign of relative retardation. To determine the fringe order, the development of the stress-pattern is observed as the load on the plate is gradually increasing, starting from zero; in this way the movement of the zero fringe is established and the successive fringes are counted as they appear and move across the plate with increasing $(\sigma_1-\sigma_3)$.

A better way to obtain the stress-pattern is to use white light. With this light source it is possible to determine the direction in which the fringes are increasing in order, since the colour change across any fringe is from red to blue (or pink to green in the case of higher order fringes), in the direction in which the stress difference is increasing.

The sign of the relative retardation at any point may be determined by the use of a compensator, but usually this is unnecessary as it is possible to find some points in the plate at which, the signs of the stresses can be deduced from a knowledge of the loading conditions.

4.2.2 Experimental work

Procedure. The material used was perspex, a transparent plastic with very low optical sensitivity, a property that makes it valuable for photoelastic work. A Hoop was cut from a sheet of plastic, 8 mm in thickness and having 45 mm, and 100 mm inner and outer diameter respectively. After it was cut and primarily polished on a grinding wheel, the Hoop was further polished with a metal polish "Brasso", on a glass surface and finally with a soft flannel cloth.

It is known that most plastics, as supplied by the manufacturers, have a certain amount of residual stresses in them due to the manufacturing process. To free the model from these stresses it was placed in a thermostatically controlled oven, where it was left at 115° C for 24 hours and it was cooled at the slow rate of 10° per hour to room temperature. The "destressing" process was satisfactory as the

photoelastic examination showed. The experiments were conducted on the "Jessop-Leech Bench".

To duplicate the testing conditions of the Hoop tension test, a pair of semi-cylindrical platens was inserted into the centre of the perspex hoop and load was applied through a rigid connection by a hand pump. The Hoop was held on a stand, supported by the semi-cylindrical smooth surfaced platens and the rigid connection. Two platen-Hoop boundary conditions were used to simulate a frictionless and a frictional inner boundary condition with the loading platens. The frictionless surface was simulated by lubricating the platens with petroleum jelly "vaseline", and the frictional surface was simulated by using the platens as they were.

The experiment was repeated three times for each case of lubricated and non-lubricated inner surface. The isoclinics obtained revealed no significant difference between these two cases, therefore the photographs of the non-lubricated inner surface were chosen for the analysis as such surfaces would be used in the experiments in real rocks.

The load was applied slowly and at stages of 3447 MPa until 48265 MPa. At selected intervals the load was held constant while the Polaroids were rotated from their initial position to 90°, at intervals of 15°. Photographs were taken at each interval which were later used for the analysis.

Repeatability of method. Photographs of isoclinics within one hoop when stressed under different loads are almost identical to each other (689.5, 20685, 34478 and 48265 MPa). In addition, series of photographs taken from hoops of different thickness exhibited a constant pattern of isoclinic and isochromatic fringes. Therefore, the repeatability of the method for the present experiment is unquestionable.

4.2.3 Results

In agreement with the analytical observational principles outlined in 4.2.1 a series of photographs taken with 48265 MPa load and at intervals of 15°, from 0°-90° was selected for the analysis of isoclinics; the series of photographs is shown in fig. 4.9. The isoclinics from each photograph were traced on a single sheet of paper and the corresponding positions of polariser and analyzer were marked on each one of them. Using these directions as guidelines, parallel lines to them were drawn representing the directions of maximum and minimum principal stresses, σ_1 and σ_3 respectively.

The result of this is shown in fig. 4.10. Solid lines represent the direction of minimum principal tensile stress σ_3, and dashed lines that of maximum tensile stress σ_1. The inset of fig. 4.10 shows the lines of symmetry and the isotropic points. The section of symmetry which coincides with an isoclinic is shown by lines A'B' and AC. The part of the outer perimeter of the Hoop which is represented by a dashed line, is a stress trajectory of the maximum principal stress and is on a load free boundary, while the solid line part of the perimeter represents the minimum principal stress trajectory. The same maximum and minimum trajectories are represented by the dashed and solid parts of lines A'B' and AC. Point O' on the outer perimeter and point O on line AC respectively are isotropic, singular points i.e points of zero stress difference; point O is a positive isotropic, singular point as the lines of principal stress interlock around it. At the isotropic points O and O' an apparent transformation of the sign $(\sigma_1-\sigma_3)$ takes place.

The analysis of the stress magnitudes was not performed as the primary interest for the present exercise was the stress distribution; nevertheless, the acquired pattern of stress magnitudes proves to be useful for the comparison with figures obtained from the FE model and is shown . Fig. 4.11 is a series of photographs obtained from the photoelastic experiment, where the gradual development of the

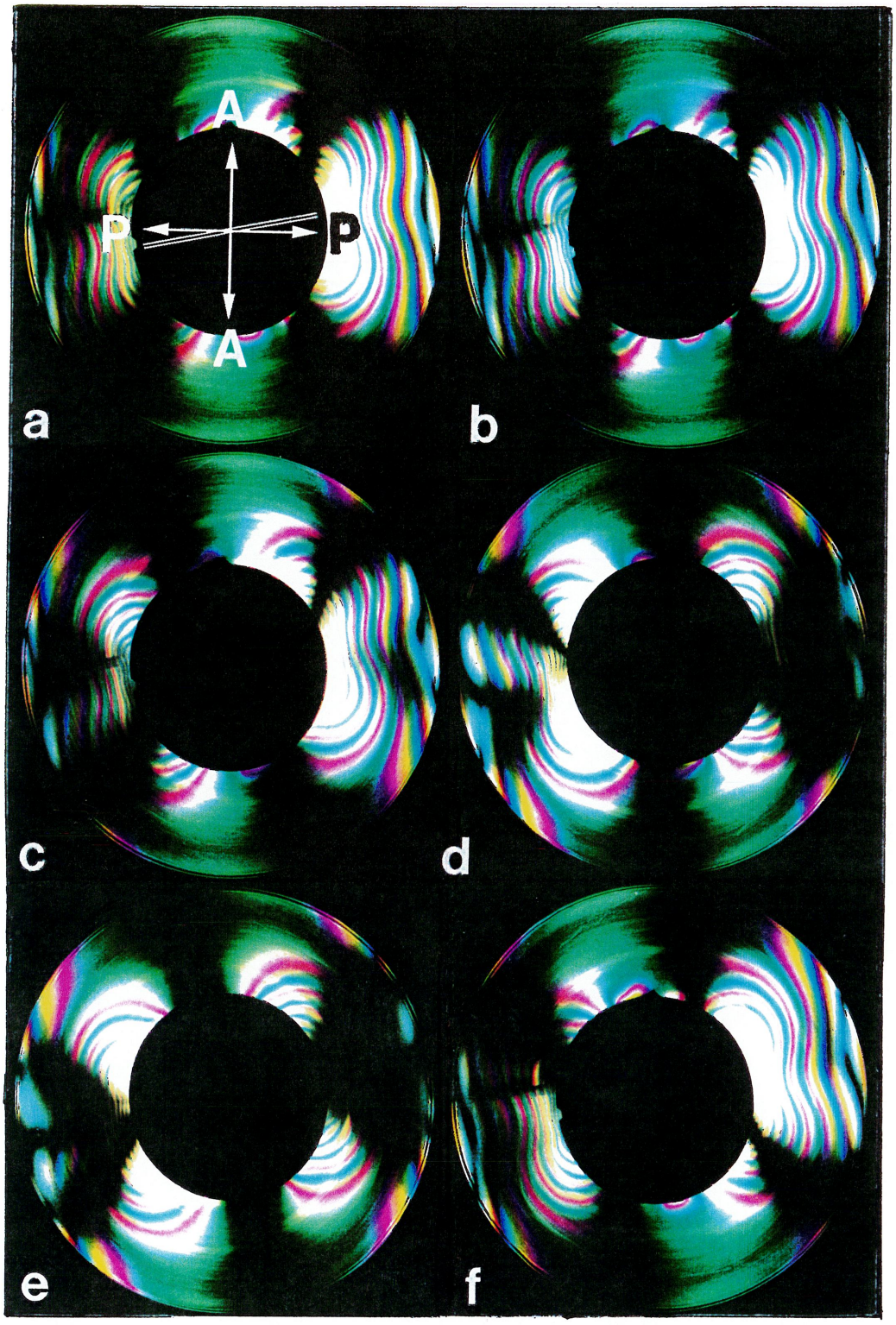
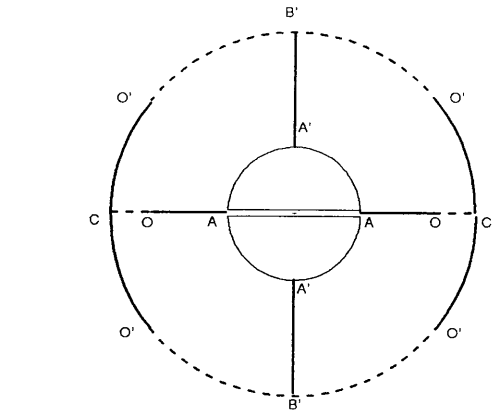


Fig. 4.9 A series of photographs used for the analysis of isoclinics: the position of polarizer and analyzer is at (a) 0°, (b) 15°, (c) 30°, (d) 45°, (e) 60°, (f) 75°, from the initial position; at 90° the photograph obtained is identical to that obtained at 0°. The direction of the arrow denotes the initial position of the analyzer and polarizer.



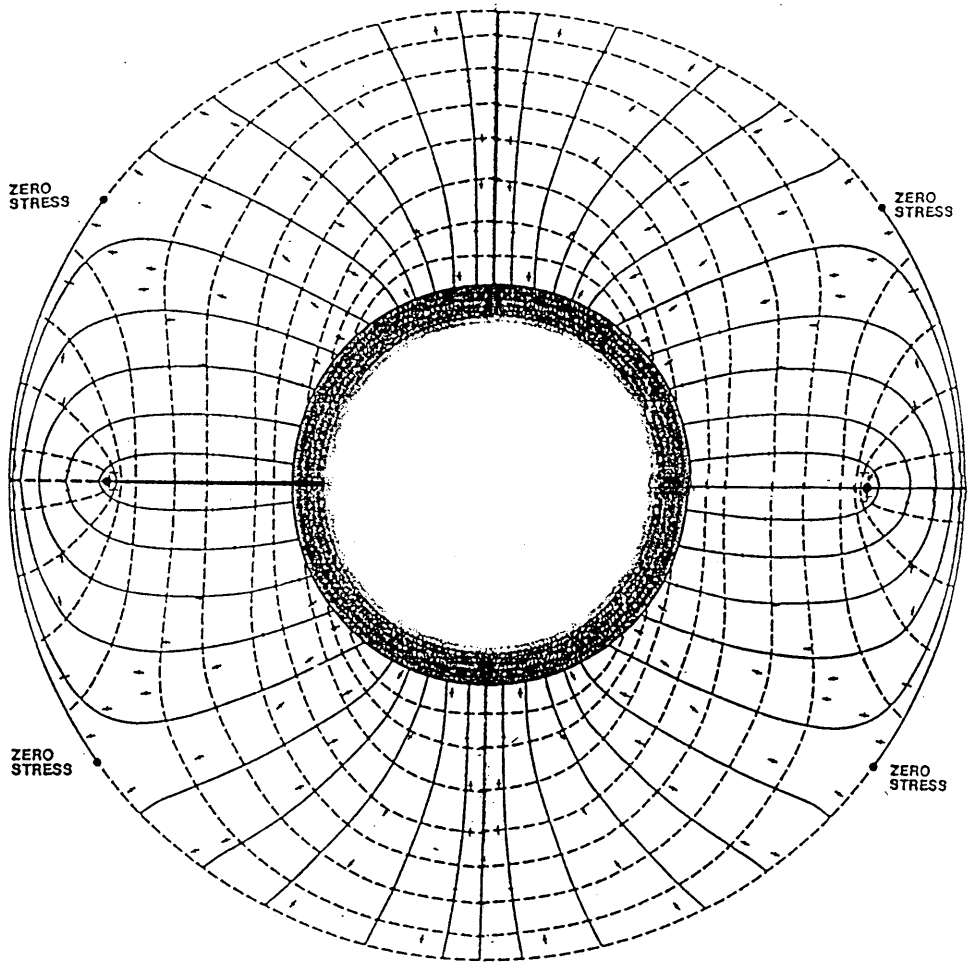


Fig. 4.10 The pattern of stress trajectories, in the hoop. Solid lines represent the direction of the minimum principal stress σ_3, and dashed lines the direction of maximum tensile stress σ_1. ⁄ = position of cross polars used for defining isoclinics.

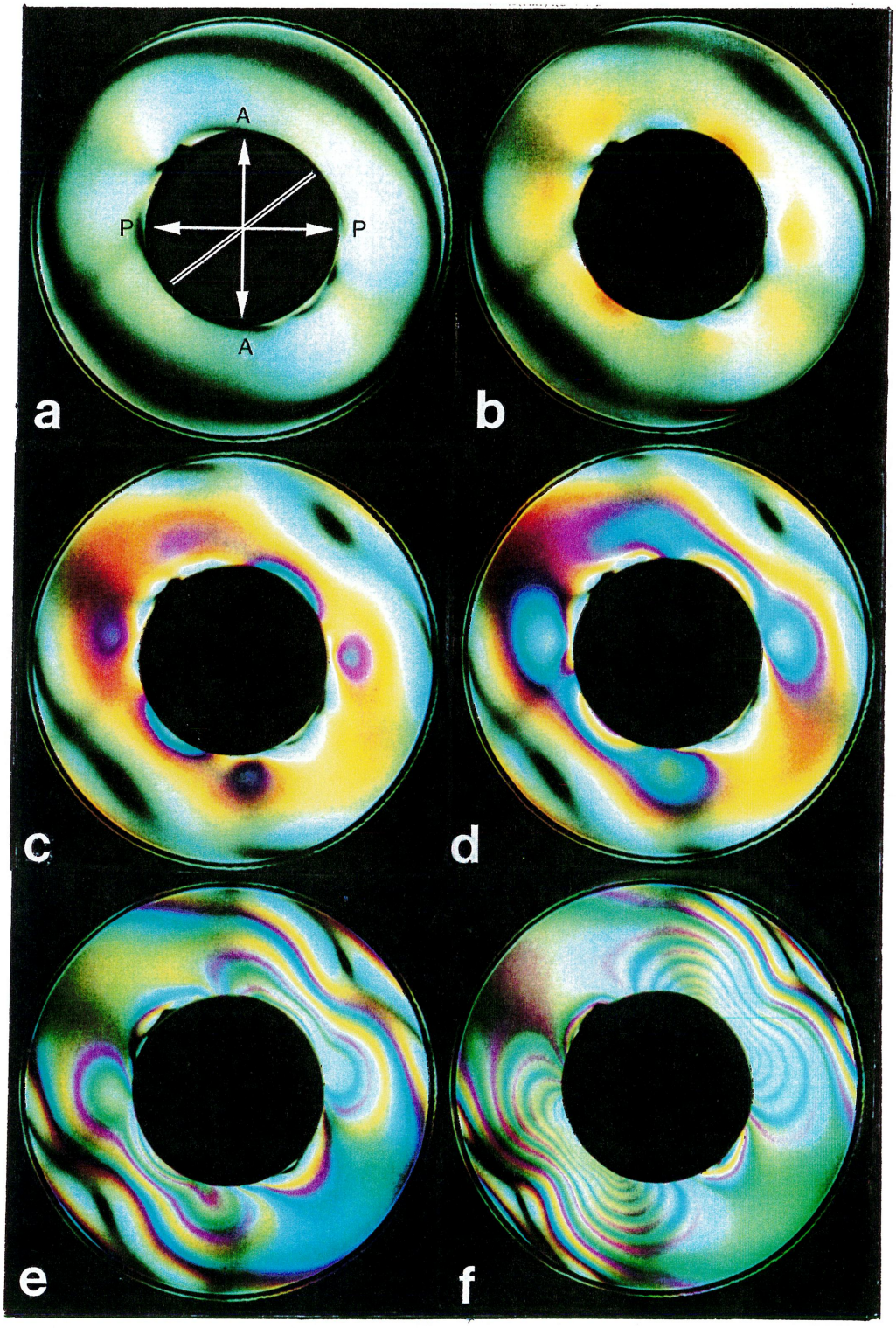


Fig. 4.11 A series of photographs showing the development of isochromatics in the hoop at various loads: (a) 689.5 (b) 4137 (c) 5516 (d) 10342.5 (e) 13790 (f) 48255 MPa.

isochromatic fringes is shown to be in accord with the predicted pattern of stress difference defined by FEM work.

4.3 CONCLUSIONS

1 From the photoelastic analysis it is possible to determine the pattern of stress trajectories σ_1 and σ_3 (fig. 4.10) and the contours of uniform differential stress $\sigma_1 - \sigma_3$ (fig. 4.11).

(i) The equipment was not calibrated in such a way as to enable the analysis of stress magnitudes to be performed i.e for the absolute values of σ_1 and σ_3 to be determined across the hoop and therefore it is not possible to determine the location of the maximum value of tensile stress σ_{1max}, i.e the site of eventual tensile failure. However, from the experimental work on samples it is known that tensile failure occurs at the location of maximum tensile stress and it can safely be concluded that in the Hoop tension test the location of the maximum tensile stress coincides with that of the maximum differential stress ($\sigma_{1max} - \sigma_3$).

(ii) The orientation of tensile stress at this location can be determined from the pattern of stress trajectories (fig. 4.10)

2 The boundary between the platens and the perspex hoop was smooth. Photoelastic experiments were carried out using both lubricated and non-lubricated boundaries. The results obtained showed no distinguishable difference in the stress field and it can therefore be concluded that after the platens have bedded in, their behaviour with respect to the boundary is the same, regardless of their initial condition of friction.

3 A comparison of fig. 4.8 and fig. 4.9 shows an excellent agreement between the behaviour of stress trajectories obtained by the methods of Finite Element and photoelastic analyses. In addition an examination of these two figures in the light

of the mathematical predictions summarised in fig. 4.5 shows the presence of the isotropic point (C) along the line cutting across the hoop opposite the platen opening; furthermore, fig. 4.5 shows the presence and location of tensile stresses and the transition of these into compressive stresses through the isotropic point C, as is also seen in the photoelastic studies.

A comparison of fig. 4.7 obtained from the FE analysis with fig. 4.11 clearly demonstrates the agreement of the outcome from both methods about the location and shape of distribution of maximum tensile stress opposite the platen opening. Tensile failure may be confidently expected to originate here.

Thus, the Hoop test provides a unique method for creating tensile failure at a known location without having to introduce to the sample any slots, cuts, notches or other artificial stress concentrators. It also provides a method of studying tensile failure in a specimen which enables the observations required to be precisely located at the point of crack initiation and propagation thus enabling load and deformation at the area of failure to be accurately compared.

CHAPTER FIVE

REAL PERFORMANCE

5.1 PERFORMANCE OF THE HOOP

The degree of certainty gained from the investigations described in Chapter four concerning the location and direction of the tensile stresses in the hoop, leads to the examination of the verification of the location and mode of fracture initiation, and propagation, using real rock.

In the experimental research of this thesis, two systems were employed to study the behaviour of the Hoop:
(i) A stiff system using an updated closed loop servo-controlled Terra-Tek machine and
(ii) A less stiff system using a pressure controller system manufactured by the Geotechnical Design Systems (GDS).

The object of these studies was to investigate the location of fracture initiation and mode of its propagation, and to obtain a Load vs Displacement graph up to, and beyond the initial failure. This was achieved by using the first system with a porous sandstone. The same objective was achieved to a lesser extent using the GDS pressure controller and specimens of the same porous sandstone and marble.

5.1.1 Tests using the closed loop servo-controlled machine

The closed loop servo-controlled system of the laboratories of Mineral Resources Engineering at Imperial College was used. The stiffness of the machine is provided by its hydraulic arrangement and the very short response time (less than 30 seconds). In a load vs displacement graph as seen in fig. 5.1, curve OAB represents the sample behaviour, where point A denotes the maximum load that

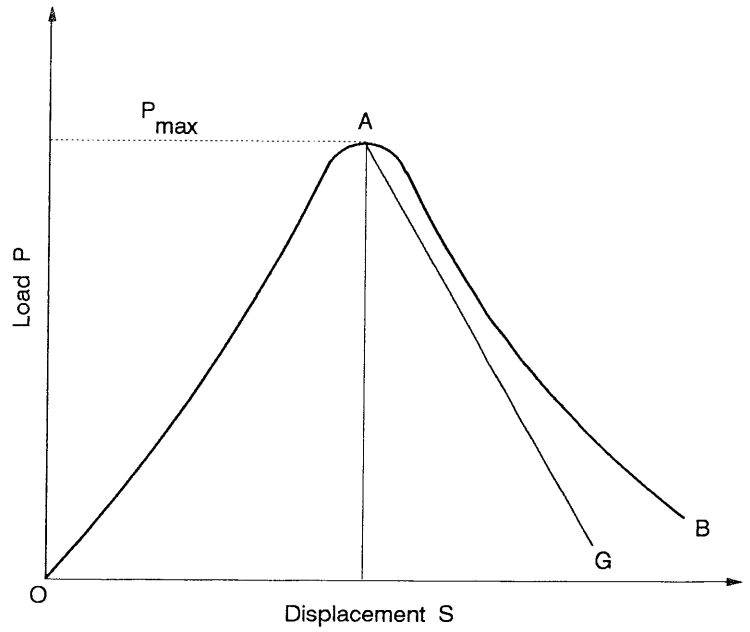


Fig. 5.1 A load - deformation curve of a sample tested with a stiff system; the post peak sample deformation is possible because the strain energy released by the testing system is less than that required to fail the sample.

the sample is capable of sustaining. At this point the sample, although partially fractured, has the capacity of withstanding loads less than Pmax, if it is deformed along the post-peak curve AB that is above line AG. Line AG represents the stiffness of the testing system; elastic strain energy released locally by the loading system at post peak deformation is less than that required to deform the sample, and the situation is thus stable.

Experimental set-up. The test arrangement is shown in fig. 5.2a and b. The Linear Variable Differential Transducers (LVDT) were used to measure the displacement parallel to the load line; these LVDTs were attached to the outermost part of the platens, across their opening, one on each side. In view of the fact that up to the time when these experiments were carried out it was not clear how the

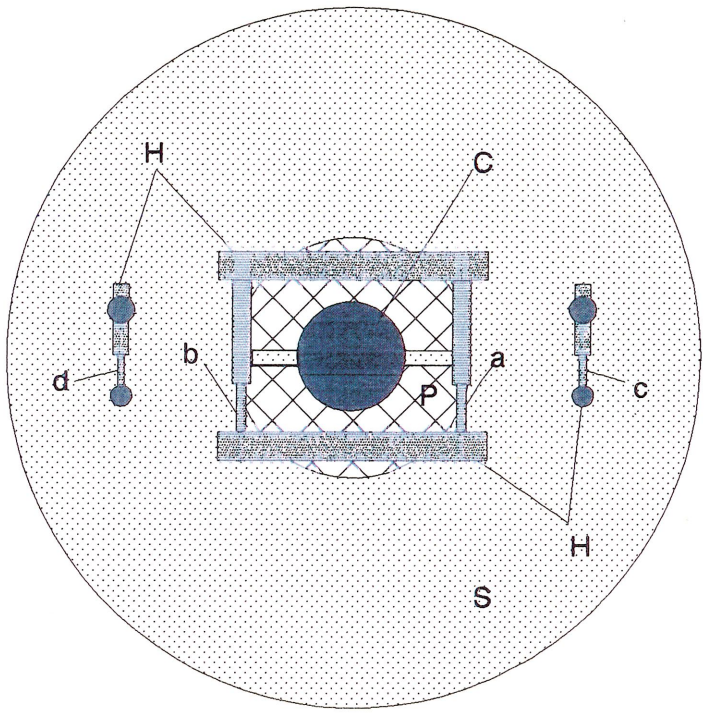
maximum deformation on the sample actually occurred, two more LVDTs were positioned on the sample at the middle of the hoop, opposite the platen opening, one on each side. One of these two transducers had the feed back to the machine, dictating the load application based on the deformation that was taking place on the sample. A light rubber band was placed around the sample, to control the possible explosion of the sample. To investigate the boundary conditions, two sets of platens have been used: one with smooth external surface, representing frictionless boundaries and one with knurled surface representing a boundary with friction sufficient to prevent all sliding on it.

Results. An example of results with a smooth surface platen is shown in fig. 5.3. Failure occurred in a smooth and progressive manner. The mean stress mentioned in the figures has been calculated by taking the total (failure) area of the sample, as shown in the equation

$$\sigma_{mean} = \frac{F}{(OD-ID)\,H} \tag{5.1}$$

where F= Pressure applied x Area of the piston, OD=Outer diameter, ID=Inner diameter, H=Height of the sample.

Points were chosen on the load vs displacement curve, to stop the test, covering the initial, yield, maximum and post-peak regions of the sample's loading situation, so that the sample could be X-rayed. The purpose of this was to detect any micro-fracturing in the sample before and after maximum load; unfortunately the exercise was not successful, as the micro-fracturing, although visible at some instances with a magnifying glass, was not developing along a surface which was cutting the sample perpendicularly to its upper and lower surfaces so giving a blurred X-ray picture: thinner samples could have resolved this problem.



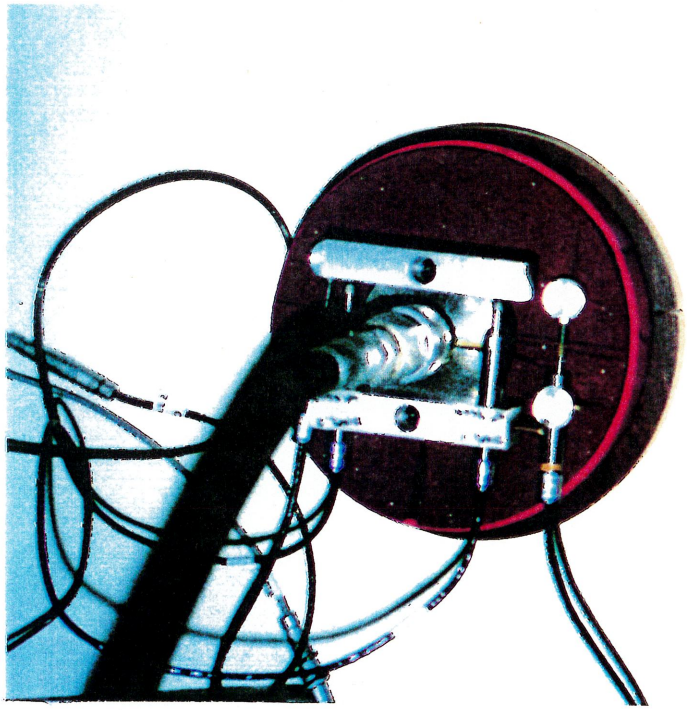


Fig. 5.2 A drawing and photograph showing the experimental set-up for the closed loop servo-controlled testing: S = specimen, P = platens, C = hydraulic connection, H = holders, a,b = LVDTs measuring displacement at the edge of the platens, c = LVDTs measuring displacement on the sample.

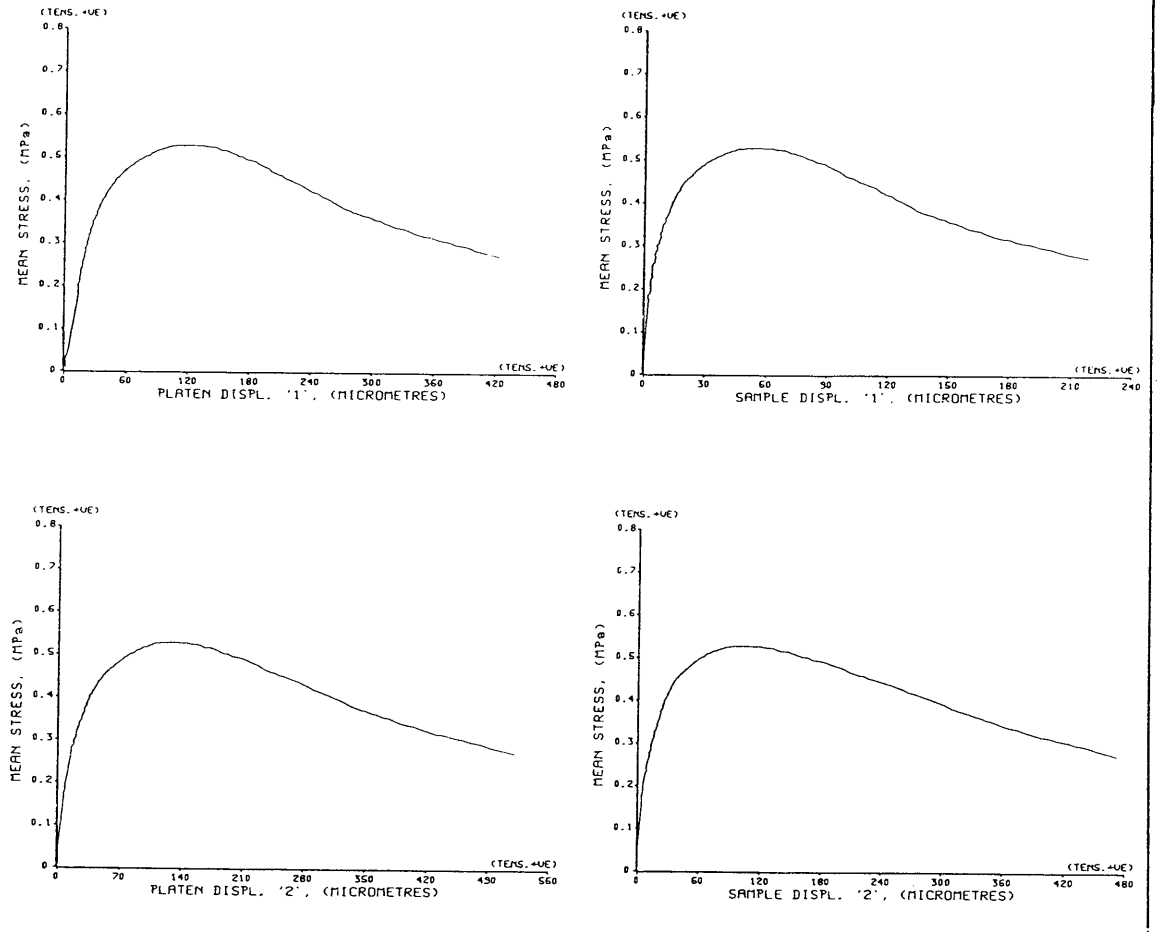


Fig. 5.3 Results obtained from testing with the servo-controlled system. The curves have been obtained from information transmitted from the LVDTs on the platens (a,b) and sample (c,d) shown in fig. 5.2

The performance of experiments conducted with the rough surface platens was similar with the occasional exception of catastrophic failure which was attributed to the extremely tight fit of the platens into the hoop specimen.

The fracture of the sample took place opposite the platen opening as predicted by the theoretical analyses presented in chapter four.

5.1.2 Testing using Pressure Controller (GDS)

In view of the fact that a closed loop servo-controlled system is very expensive and not available widely in many laboratories, an alternative testing system was used for the Hoop tension test, viz. the pressure controller (GDS). This equipment is more akin to what is used in most laboratories and is able to give accurate readings of loads up to failure. The stiffness of the system is less than that of the closed loop servo-controlled machine, as the response time is greater; to improve as much as possible the performance of the system the steel tube line from the pressure controller to the sample was kept as short as possible and the hydraulic oil used was de-aired prior to testing.

Experimental set-up. The GDS provides a choice of working either in pressure or volume control modes; both have been tried and the volume control mode was chosen as the best alternative for controlling the test. The system comprises of the pressure controller, a computer and a computer interface; the pressure controller may function either independently or through a computer control. If it functions independently, only the maximum pressure or maximum volume change rate may be used; if it functions through the computer the three parameters, time, pressure and volume may be selected and their values continuously recorded, and stored: they also can be processed.

Results. The results obtained from this system were plotted as load vs volume change curves; the volume change was converted into displacement resulting into

a load vs displacement curve. The hydraulic oil was considered incompressible for the test. Depending on the elasticity of the specimens, tests performed may yield results beyond the maximum load as shown in fig. 5.4a, where porous sandstone was tested. Brittle material, crystalline marble, gives results, a typical example of which is shown in fig. 5.4b. Failure occurred opposite the platen opening, at the location of the concentration of maximum tensile stresses.

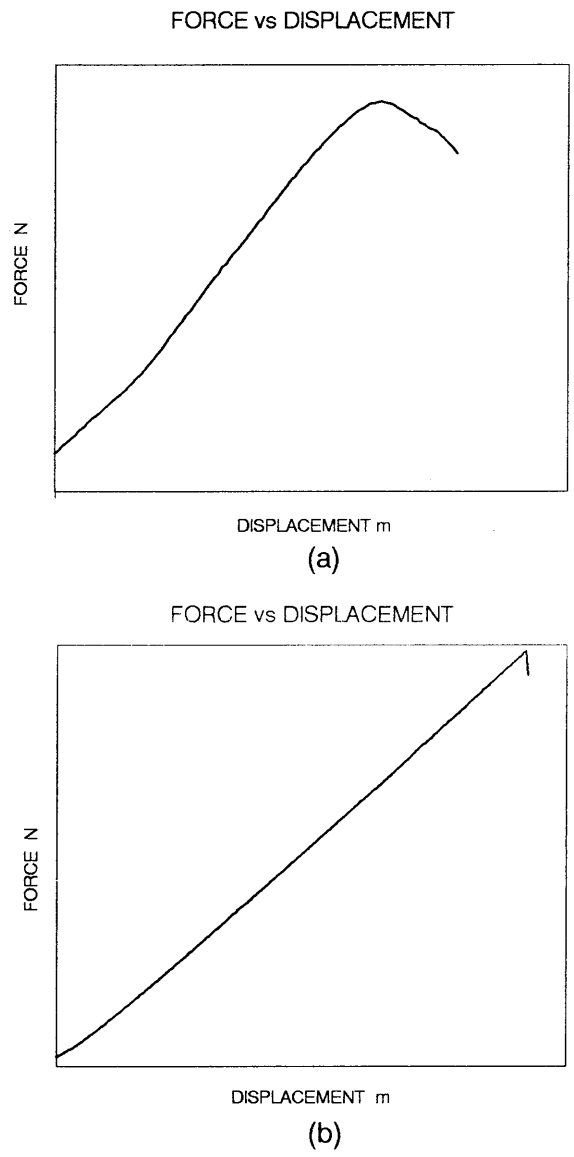


Fig. 5.4 Typical curves obtained from testing with the GDS from sandstone (a) and marble (b).

Conclusions: Having conducted tests on real rock using the servo-controlled machine and the pressure controller on two different materials, porous sandstone and crystalline marble, it is apparent that the Hoop tension test provides a controlled method of testing which enables the initiation of tensile failure to be concentrated at a predictable location where it can be studied, and the propagation of tensile cracking to occur under reasonably controlled conditions.

5.2 HOLOGRAPHIC INVESTIGATIONS

The studies made so far have utilized a knowledge of the distribution of stress within a hoop but not the distribution of strain, for displacements can only be measured on a hoop at a limited number of points by devices such as strain gauges and LVDT's. However, holography provides a method of studying displacements on the whole surface of a hoop which reveals displacements at nanometre scale, thus permitting the microstructure of any small non-uniformities in the object surface to be detected.

Holography is a procedure that enables wave fields of objects to be stored on photographic emulsions and to be reconstructed at a later time, giving a three-dimensional effect. This is made possible because, both the amplitude and the phase of the light wave emanating from an object at the time of recording can be reconstructed at a later time. When an actual object wave is made to overlap a planar, coherent, reference wave, the fringes become modulated with the information describing the object, thus resulting in the three-dimensional diffraction grating, called the reflection hologram. Through the use of holographic interferometry it is possible to produce three-dimensional images of diffusely reflecting objects which appear to be overlaid by interference fringes; these interference fringes indicate deformation by either displacement or rotation of the subject.

With the possibilities offered by the Holographic Interferometry in mind, it was

decided to use this technique to :

(i) identify the location and mode of fracture initiation and

(ii) to measure the in-plane strain, in the Hoop.

5.2.1 Introduction to Holography

Because Holography is a technique that only relatively recently started to be used on rock materials (Takemoto, 1986 and Maji and Wang,1992) it is thought useful to present an introduction to the definitions and concepts used in the experimental work that was done and the interpretation of the results obtained.

Transmission holograms are created when both the reference and the object waves are traversing the film from the same side, fig. 5.5a shows the interference of two plane waves travelling toward the same side of the photographic emulsion, which has finite thickness, to create a transmission hologram. Note that the fringes, which lie parallel to the face of the film plate, (grey straight parallel lines), bisect the angle between the reference and object waves.

A **reflection hologram** is formed when the reference and object waves traverse the emulsion from opposite sides. The fringes are straight bands which bisect the angle between reference and object waves (fig. 5.5b).

Holographic interferometry enables the production of three dimensional images overlaid by fringes, and which can be used to reveal the deformations of subjects. This type of interferometry is possible because a light wave scattered by an object can be holographically recorded and reconstructed with such precision that it can be compared interferometrically with light scattered by the same object at another time. Alternatively, it can be compared interferometrically with a second holographic construction of light scattered by the object. Therefore, holographic interferometry can be defined as the interferometric comparison of two or more waves, at least one of which is holographically reconstructed. The composite of

these two or more waves is a holographic interferogram.

5.2.2 Two-exposure Holographic Interferometry

This is a technique through which an interferogram is obtained recording the fringes indicative of deformations on the surface of the object. Initially a holographic exposure of the subject in its initial, unstressed, state is recorded by exposing the photographic plate to the object and reference wave simultaneously. The object then is subjected to stress by applying the desired load and a second holographic exposure is made on the same photographic plate. When the plate is developed and is illuminated with a reconstructing wave identical to the wave used to record it, an observer looking through the hologram will see a three-dimensional image of the object overlaid with a pattern of interference fringes; these fringes appear to be localised in space and not on the surface of the object, for they appear to shift their position and change their form if the observer views them from different directions.

The underlying principle of holographic interferometry is thus as follows: it is a linear process in the sense that two or more optical waves can be recorded sequentially in time and later can be reconstructed simultaneously. Amplitude is divided temporally in contrast to classical interferometers where the division of wavefront or amplitude is done as spatial division of light into two different paths. In this technique the waves which interfere essentially traverse the same path in space at two different times.

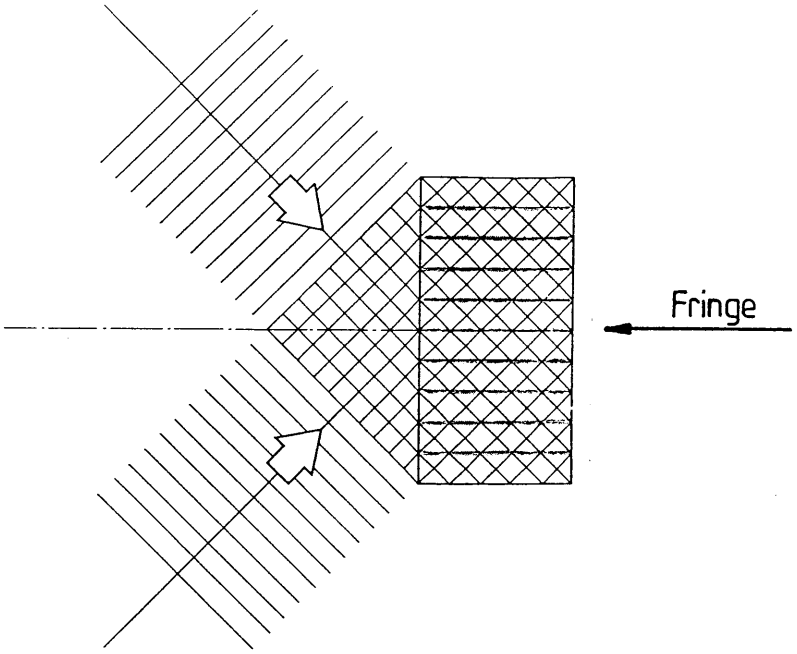


Fig. 5.5a The interference of two plane waves, one from the object and the other from the reference beam, travelling toward the same side to create a transmission hologram (from E.Hecht, 1987)

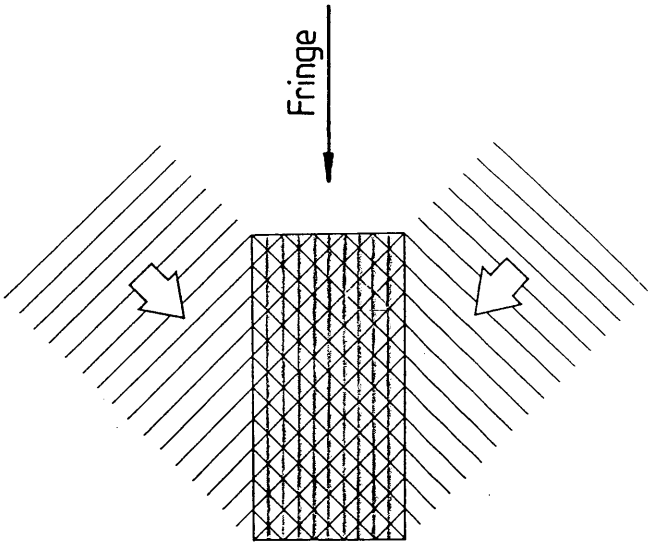


Fig. 5.5b The creation of a reflection hologram by two plane waves travelling from opposite sides toward the photographic plate (from E.Hecht, 1987)

The manner in which fringes are formed when a diffusely reflecting surface is translated or deformed is considered below: fig. 5.6 shows such a surface before and after deformation.

P and **P'**are the same point on the surface before and after deformation. Light scattered by the surface in the area surrounding **P** gives rise to a complex amplitude $\mathbf{U}_{0(x,y;z)}$ in a plane which lies a distance **Z** from the object. The corresponding irradiance, $\mathbf{I}_{0(x,y;z)}$ after imaging through a finite aperture,

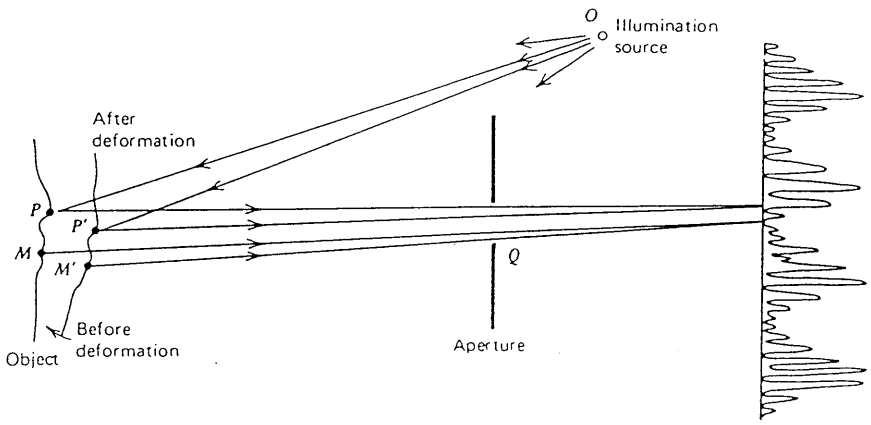


Fig. 5.6 A schematic diagram showing fringe formation. The irradiance in a plane where fringes are visible consists of a rapidly varying speckle pattern which constitute the fringes of holographic interferometry (from C.M.Vest, 1979).

results in a speckle pattern created by the random variations in the microscopic surface contour of the object.

In two-exposure holographic interferometry, a second optical wave, scattered by the object surface in the area of **P'**, is formed. This wave is nearly identical to the first, but is displaced and travels in a slightly different direction. At a given distance **Z** from the object this wave will have a complex amplitude $\mathbf{U'}_{0(x,y;z)}$, but nevertheless, at this distance **Z** from the object, $\mathbf{U}_0$ and $\mathbf{U'}_0$ will be nearly identical

except for a very small relative displacement, and a variation in phase whose spatial scale is large in comparison with the variation which gives rise to the speckle. The irradiance pattern formed when the field at this distance from the object is recorded has a fine speckle structure resulting into fringes of holographic interferometry. The fringes are said to be localised for the given viewing direction at this plane, at distance **Z** from the object. If the imaging system is focused on other planes in space $\mathbf{U_0}$ and $\mathbf{U'_0}$ will differ in detail and will not include a systematic, large-scale relative phase variation.

The phase difference Δ, the variation of which gives rise to the fringes of holographic interferometry, can be calculated by finding the change, due to the object displacement in optical path length from the source of illumination to the object point **P** and to the centre of the observing aperture **Q**

$$\Delta = \frac{2\pi}{\lambda} [(OP+PQ) - (OP'+P'Q)] \qquad (5.2)$$

It is necessary to determine the position in space at which the fringes seem to localise for a given viewing direction. This position depends upon the nature and direction of object displacement or deformation, as well as on the directions of illumination and observation.

Single Beam Holographic Interferometry is a simplified method of Single Beam Reflection Holographic Interferometry and was introduced by I. Leifer, W.C.McKenzie and J.D.Leask (1990). This method was adopted for the experimental work. The principle of the method is shown in fig. 5.7, which demonstrates the illumination and viewing directions and in fig. 5.8, which illustrates the three viewing directions V_1, V_2, V_3 and their relationship to the surface of the object.

The lines of the visible fringe pattern relate to the displacement component which lies in the direction of a sensitivity vector; this sensitivity vector is the line which bisects the illumination and viewing directions. From fig. 5.8 it can be seen that the bisector B_1 of illumination direction ID and viewing direction V_1, lies in the out of plane Z-direction; the bisector B_2 of ID and V_2, lies in the X-Z plane; and the bisector B_3 of ID and V_3, lies in the Y-Z plane. Therefore, the fringes viewed from direction V_1 can be used to determine the component of displacement in the Z direction (out of plane), and the fringes viewed from V_2 and V_3 can be used to determine the components of displacement in planes X-Z and Y-Z respectively. Once the displacement component in plane Z plane can be determined it can then be eliminated from the displacement components in X-Z and Y-Z planes resulting in the X and Y components of displacement. The analyses associated with this is reported in the Appendix to chapter 5.

Sensitivity of method. The sensitivity of method is controlled by how accurately the distance between two neighbouring fringes can be measured. The distance between two neighbouring fringes equals the wave length of the light divided by two i.e for these tests $632.8 \div 2 = 316.4$ nm, (a red light Ne laser was used). It is known that a quarter of the distance between two neighbouring fringes can accurately be measured and hence, this distance will equal $632.8 \div 8 = 79.2$ nm. Therefore the sensitivity of the method is approximately 8×10^{-5} mm.

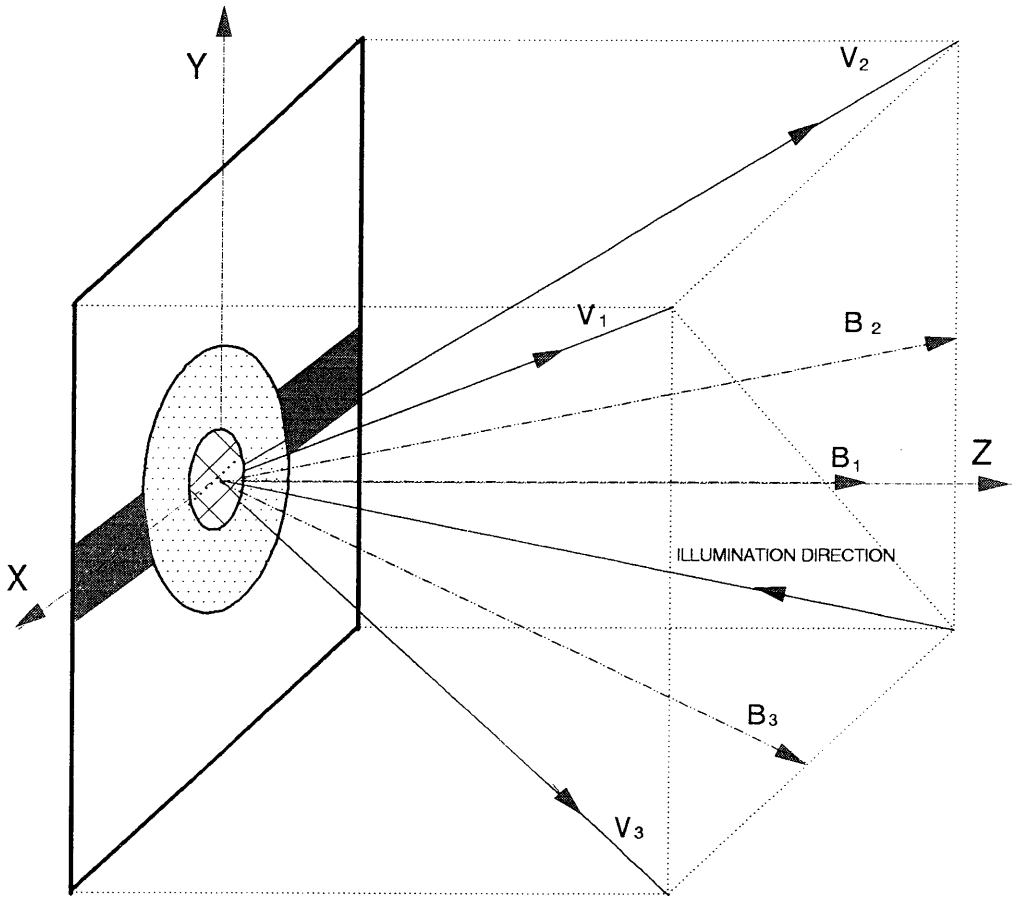
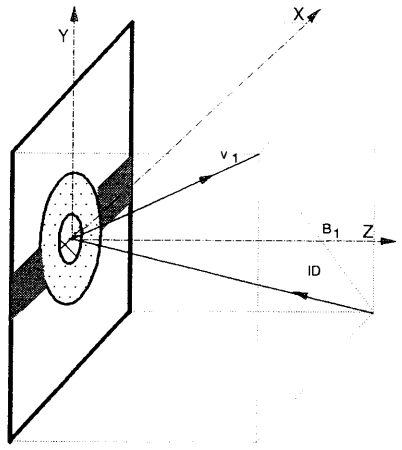
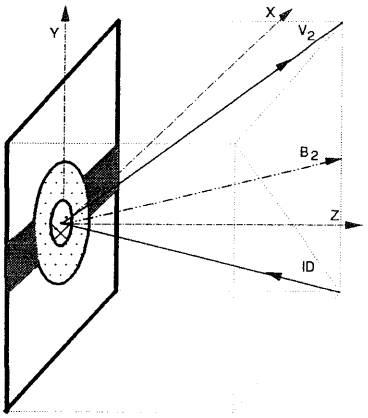


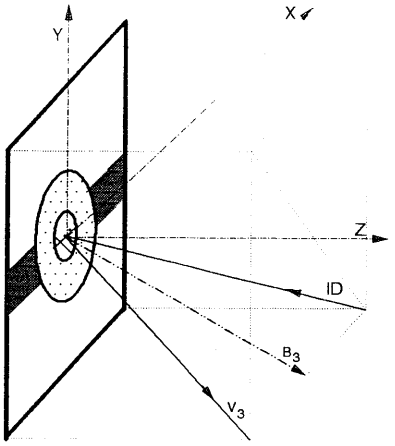
Fig. 5.7 Diagram showing the illumination and viewing directions in Single Beam Reflection Holographic Interferometry.



VIEWING DIRECTION V_1
IN THE Z-PLANE



VIEWING DIRECTION V_2
IN THE X-Z PLANE



VIEWING DIRECTION V_3
IN THE Y-Z PLANE

Fig. 5.8 Individual diagrams showing each viewing direction and their corresponding planes: the hoop surface lies in the (X - Y) plane.

5.2.3 Experimental procedure

A He-Ne laser (see appendix to chapter 5) was used to provide a red light of 632.8 nm wave length, the set-up of which is shown in fig. 5.9 and fig. 5.10. Sandstone hoops were used.

The photographic plate was held on the sandstone hoop with double sided adhesive magnets; the technique of having the photographic plate attached to the sample eliminates rigid body movements i.e tilt of the hoop relative to the photographic plate, and only the deformation occurring on the sample is recorded. A load was applied to the hoop and the photographic plate was exposed to the laser light as shown in fig. 5.10. The load was increased and the photographic plate was exposed again; thus a double exposure reflection interferogram is obtained with a fringe pattern that is indicative of events that took place in the hoop during the application of the selected load interval. The process was repeated at small load increments until the failure of the sample occurred. Examples of the interferograms obtained are shown in fig. 5.11 and 5.12.

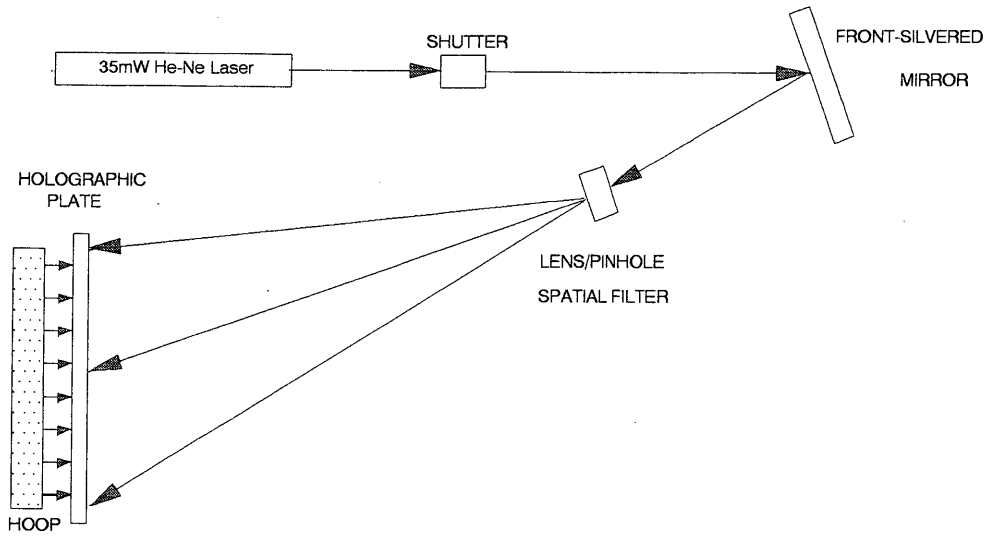


Fig. 5.9 Plan of the optical system for recording and reconstruction in Single Beam Reflection Holography (After I.Leifer et al, 1990)

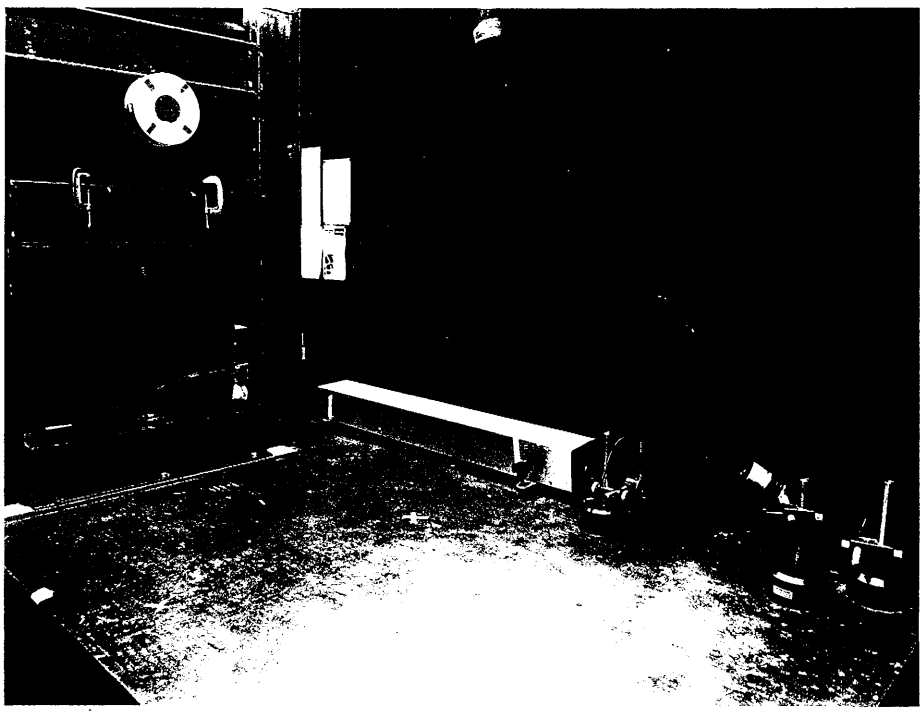


Fig. 5.10 Experimental set-up.

Repeatability of method. During the experimental session several interferograms were repeated, namely the ones with the following loading intervals: 3.4 to 3.6 MPa a,b; 3.6 to 3.8 MPa a,b; 3.8 to 4.0 MPa a,b; the interferogram with loading 3.4 to 3.6 MPa, b was repeated after the sample was left to relax overnight. A careful examination of the a and b interferograms of the same loading intervals revealed an almost identical expression of the fringe pattern, which is a strong evidence of the repeatability of the method and of course of the fact that the sample is still within its elastic range.

5.2.4 Principles of observation and actual visual observations from interferograms and their photographs

The following principles are to be followed for the explanation of the acquired fringe patterns:

(i) Slip between platens and sample is evident from the discontinuity of the fringes across the boundary.

(ii) The reversal of the curvature of the fringes on the sample is indicative of some, but not complete, stress release; it may also be an indication of torsion.

(iii) An anomalous region, perhaps a weak zone, is shown by kinks (wiggles) in the otherwise smooth fringes.

(iv) Fringe concentration is evidence of high strain concentration,thus stress concentration.

(v) Even, parallel fringes denote a region of evenly distributed stress in the same direction.

(vi) Discontinuities in fringes is evidence of fracturing.

For the purpose of presentation, the observations have been divided into three stages, viz. initial loading, intermediate and prefailure. It is easiest to examine the interferograms sequentially from one viewing direction, so as to be able to judge the behaviour of the sample at that particular plane. Therefore the observations which have been grouped into one figure (fig. 5.13) will be presented in order of

viewing directions V_1, V_2, V_3 as described in fig. 5.7, 5.8 and 5.9

Note: The holographic interferograms were recorded at regular intervals of 0.2 MPa load. After examining and deducing information from the whole series, only several were chosen from the sequence for the diagrammatic representation of the observations and hence some disagreement may seem to be present between the text and Fig.5.13a-d

Observations from viewing direction V_1, (displacements in the Z-plane. See fig. 5.14a-d) A very slow increase in the number of fringes was observed during the initial and intermediate stages of loading up to 3.6 to 3.8 MPa. The number of fringes increased dramatically in the prefailure stage at loads of 3.8 to 4.0-4.1 MPa and 4.0 to 4.1 MPa.

The shape of fringes at lower loads is not well defined, they are very thick, but they seem to be parallel to each other and form an angle of about 60°-70° with the vertical. At the loading interval 3.4 to 3.6 MPa, there is a definite kink in the otherwise smooth fringe closest to the platen opening. The kink is visible in one location as a slight semi-elliptical fringe with its centre along the platen opening. As the load increased, the kink became very definitely double; the shape of the fringes became thinner and they became parallel to each other while the angle with the vertical decreased. At 3.6 to 4.2 MPa loading the interferogram showed a clear crack, the number of fringes decreased and their shape became undefined.

At the next two interferograms, 3.5 to 4.4 and 4.4 to 4.8 MPa, just before sample failure, the shape of fringes is very definitely concentric opposite the platen opening. This concentricity is visible only up to about 2/3 of the hoop diameter, where a complete reversal of the curvature of the fringes takes place, which forms another ellipse with its centre at the outer diameter of the Hoop.

Observations from viewing direction V_2 (displacements in the X-Z plane. See fig. 5.14a-d). An even and gradual increase in the number of fringes is seen at

the initial loading stages of the experiment 2.6 to 2.8 MPa. At 3.0 to 3.2 and 3.2 to 3.4 MPa load intervals the interferograms continued to exhibit a very even pattern of fringes almost parallel to each other (see fig. 5.11a).

At 3.4 to 3.6 MPa loading a dramatic change in the fringe curvature occurs; a distinct semi-elliptical fringe forms opposite the left opening of the platens and visible micro-cracking is obvious at two locations opposite the right opening of the platens. At 3.6 to 3.8 MPa loading, the number of fringes is greatly decreased and the fringes themselves are much thicker.

In the next two interferograms the number of fringes increases greatly and they become thinner and almost parallel to each other, but almost at 90° to the previous even pattern of fringes exhibited by interferogram of 3.0 to 3.2 MPa loading.(see fig. 5.11b). A distinct double kink at the platen opening and two micro-cracks at the left side of the platen opening are clearly visible. (see fig. 5.12 V_1,V_2,V_3). At the higher load of 3.6 to 4.2 MPa the cracks on both sides of the platen opening are clearly visible while the number of fringes is greatly reduced and their thickness increased.

The last two interferograms exhibit the greatest fringe concentration before failure, with a characteristic pattern, opposite the platen opening and towards the outer diameter of the sample. The fringes describe a concentric semi-elliptical form with the centre of the ellipse somewhere along the platen opening, until about half the hoop diameter; from this point on, the fringes change their curvature completely, and while they form a semi-elliptical pattern the centre of this semi-ellipse lies somewhere at the outer diameter of the hoop (see fig.5.11c)



(a)

(b)



(c)

Fig. 5.11 Interferograms from viewing direction V_2: (a) a very even and almost horizontal pattern of fringes is exhibited at 3.0 to 3.2 MPa load, (b) the fringes acquire a different pattern and they are less dense in view of the microcracking which is seen opposite the platen opening at 3.8 to 4.0 MPa load, (c) a high concentration of fringes is built-up at the higher load of 4.4 to 4.8 MPa. The shape of fringes opposite the platen opening clearly shows the tensile and compressive regions in the hoop as well as the isotropic point (see fig. 4.10).

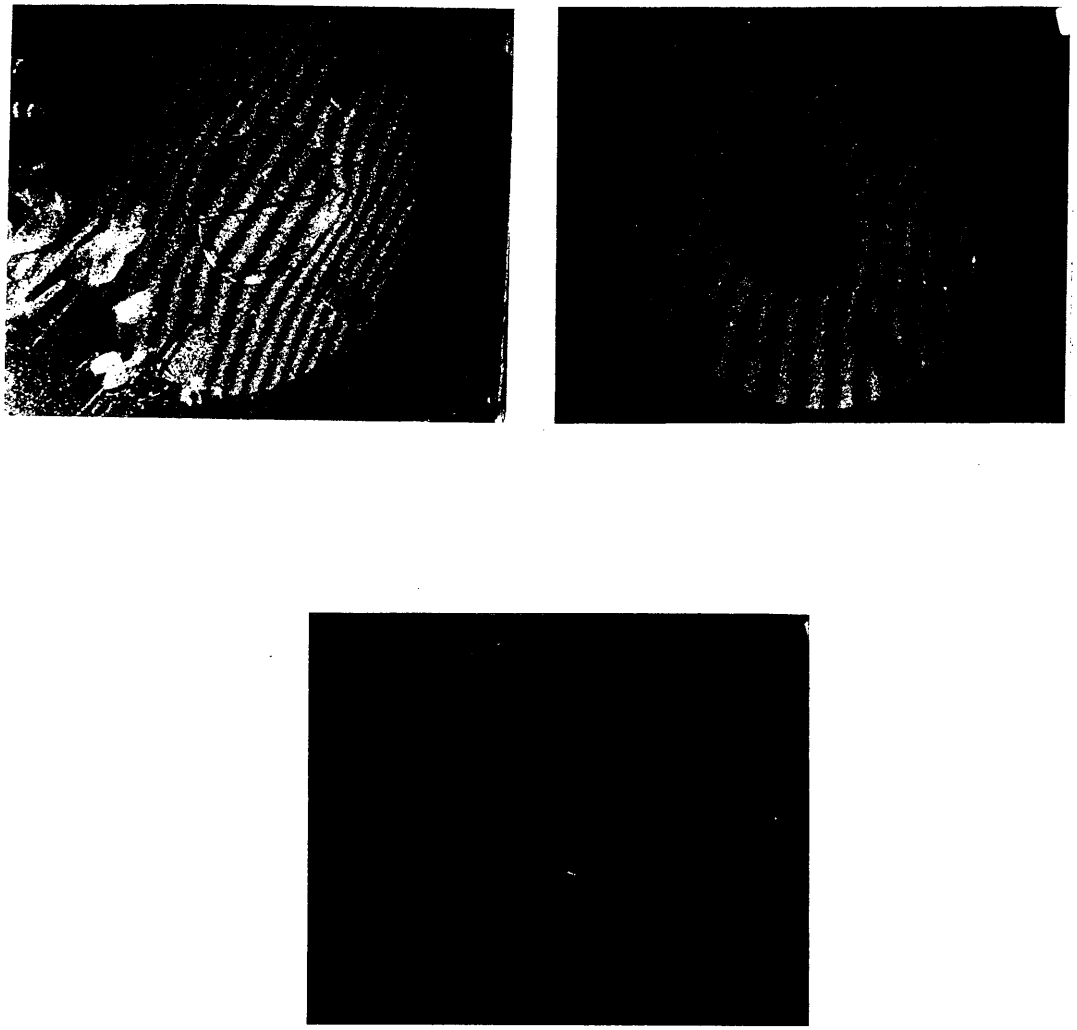


Fig. 5.12 Clockwise, the viewing directions are V_1, V_2 and V_3 of the interferogram at loading interval 3.8 to 4.0 MPa, exhibiting the density and direction of fringes as well as the kinks of the fringes.

Observations from viewing direction V_3 (displacements in the Y-Z plane. See fig. 5.14a-d). A gradual increase in the number of fringes from lower loading intervals is observed, but it is worth noting the overall denser concentration of fringes seen in this plane than in the Z and X-Z planes. The pattern of fringes is definitely a radially curved one, radiating from both sides of the platen opening (see Fig 5.13) until 3.8 to 4.0 MPa loading where there are two visible cracks. At 3.6 to 4.2 MPa loading, the number of fringes is slightly decreased and the cracks are clearly visible on both sides of the platen opening. A great increase in the density of fringes occurred at the two last loadings before sample failure. Here, a distinct change in the curvature of fringes, very similar to the one described from V_2 and V_1 observation directions, occurs.

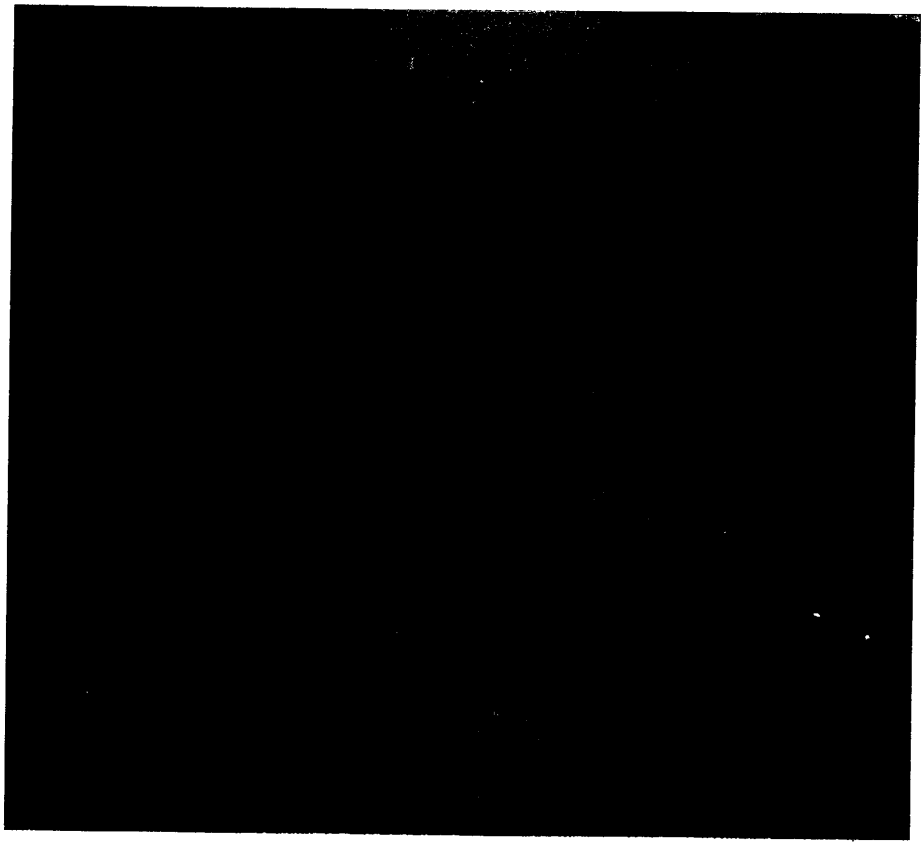


Fig. 5.13 Interferogram from V_3 at loading interval 3.4 to 3.6 MPa, showing the radial pattern of fringes opposite the platen opening.

General observations of fringes: At lower loads the fringes seem continuous through the sample and the platens. At intermediate loads the fringes on the platens appear to be completely different from the ones in the sample, indeed in some instances they differ from the one platen to the other. But at higher loads the fringes seem to be continuous from the sample through to the platens only at the top and bottom arc of the platens. At the loads just before failure, the fringes are discontinuous at the sample-platen contact and also discontinuous in the two platen halves.

If the point of observation moves from viewing direction V_1 to V_2, a small number of fringes is observed, whereas if the point of observation moves from viewing direction V_1 to V_3 the number of fringes is greatly increased. This indicates that small displacements occur in the X direction, in contrast with the greater displacements occurring in the Y direction. This agrees with the experiment, because it is at the Y direction where major displacements take place before the sample breaks opposite the platen opening and it is in the Y direction that the maximum stresses in the hoop occur. (fig.4.7)

5.3 CONCLUSIONS

It is evident from the holograms that the events of the experiment can be divided into the following stages:

(i) Initial stage (fig. 5.14a)

(ii) Intermediate or weakening stage (fig. 5.14b+c) and

(iii) Pre-failure stage (fig. 5.14d).

At the initial stage one can see the gradual and even build-up of strain expressed in the increasing number of fringes and their orderly arrangement. In decreasing order the greatest displacements occurred in the Y-Z, X-Z and Z planes. There is a strong indication that the platens and sample moved in unity and this is a significant point for future FEM modelling of the platen-hoop interface.

At the intermediate stage, the occurrence of a region that could represent a process zone is clearly evident by the first appearance of kinks in the fringes exactly opposite the platen opening. The stress release associated with this manifests itself in the dramatic reduction in the number of fringes and appearance of micro-cracks and is an interesting example of the possible adjustments which are occurring as energy is transferred from the hoop to the surfaces of cracks (as envisaged by Griffith's theory : Chapter 3).

The increase in load caused more strain to be built-up in the sample as it is seen from the increased number of fringes and their even distribution. The presence of double kinks in the fringes is a sign of crack growth and its enlargement in comparison with the first evidence. The formation of the concentric semi-elliptical pattern opposite the platen opening indicates some stress release, due to micro-fracturing, which is barely visible at this loading interval. It is important to note that two micro-fractures are visible and in this respect the hoop appears to behave symmetrically.
At the next loading stage one micro-crack is clearly seen on the interferogram (V_2 3.6 to 4.2. MPa), showing that the process of crack formation and selection has been overcome by a single fracture.

At the pre-failure stage, the number of fringes is very high despite the presence of micro-fracturing, indicating to the build-up of very high strains just before the catastrophic failure of the sample. The size of the semi-elliptical shape of fringes opposite both sides of the platen opening is increased, indicating both the enlargement of the weakening zone and the lengthening of the micro-crack.
Attention is drawn to the presence of the two semi-elliptical shape areas which lie opposite to each other, exactly opposite the platen opening and towards the outer perimeter of the sample (see fig. 5.11c). This is the strongest evidence yet obtained in a rock sample, to support the tensile and compressive regions and the presence of the isotropic point obtained from the numerical and photoelastic analyses.

An analysis of the experimental data confirms that:

(i) The formation of a zone from which a single macro-crack naturally develops- something not seen before, as all tests of crack propagation start from the end of an artificial cut.

(ii) The location of fracture, opposite the platen opening and towards the outer perimeter of the Hoop.

(iii) The isotropic point predicted from the photoelastic analysis.

(iv) The migrating of the isotropic point, as the growth of the semi-elliptical fringe pattern with increasing load shows.

(v) The evidence that can be drawn at this stage about the platen-sample contact, which is that at lower loads the two behave in unity, at the intermediate stage there is a good contact between platens and sample at the top and bottom arc of the boundary, but at the pre-failure stage there is a strong indication of slip and maybe torsion between the platens and the sample. Because the holographic method allows observations up to the fracture initiation until just before the catastrophic failure of the sample, the last fringe pattern that is available is confusing as far as the movement of the platens in relation to the hoop sample is concerned.

The method developed by I.Leifer et al, (1990) enables the components of relative displacement in the X, Y and Z directions to be obtained as well as the absolute in-plane strain between two points at a load interval. Although one of the initially stated objectives was to measure the in-plane strain in the hoop and thus, proportionally deduce the stresses, it has not been possible to do so; to achieve this more experiments and the right equipment setting are required to enable the accurate counting of fringes from a selected point P to its displaced location P'; and most importantly to identify a zero order fringe for the out-of-plane component, η_1 required in the calculations (see appendix to chapter 5)

Fig. 5.14a. Initial loading stage: This is represented by a gradual increase in the number of fringes, denoting an even and continuously increasing state of strain in the sample.

Fig. 5.14b-c Intermediate stage: This is characterised by a cyclic phenomenon of partial strain release manifesting itself in the micro-cracking, presence of kinks and reduced number of fringes, then the further build-up of strain as is evident from the increased number of fringes, their regular arrangement and their thinning.

Note: the loading at this stage was 4.0 to 4.1 MPa in anticipation of the ultimate failure of the sample, but the fringe formation for this interval was barely visible; therefore, the load was reduced to 3.6 MPa before being increased to 4.2 MPa to obtain a difference sufficient for holographic interference. In doing so, the loading sequence was interrupted and some boundary slip from relaxation of the sample was introduced.

Fig. 5.14d Pre-failure stage: this final stage, before the catastrophic failure of the sample records the highest strains, expressed in the number and thinness of fringes. The double semi-elliptical pattern of fringes opposite the platen opening is further evidence to the tensile and compressive regions predicted by the photoelastic and numerical analysis.

Facing page 164

SCHEMATIC REPRESENTATION OF FRINGES

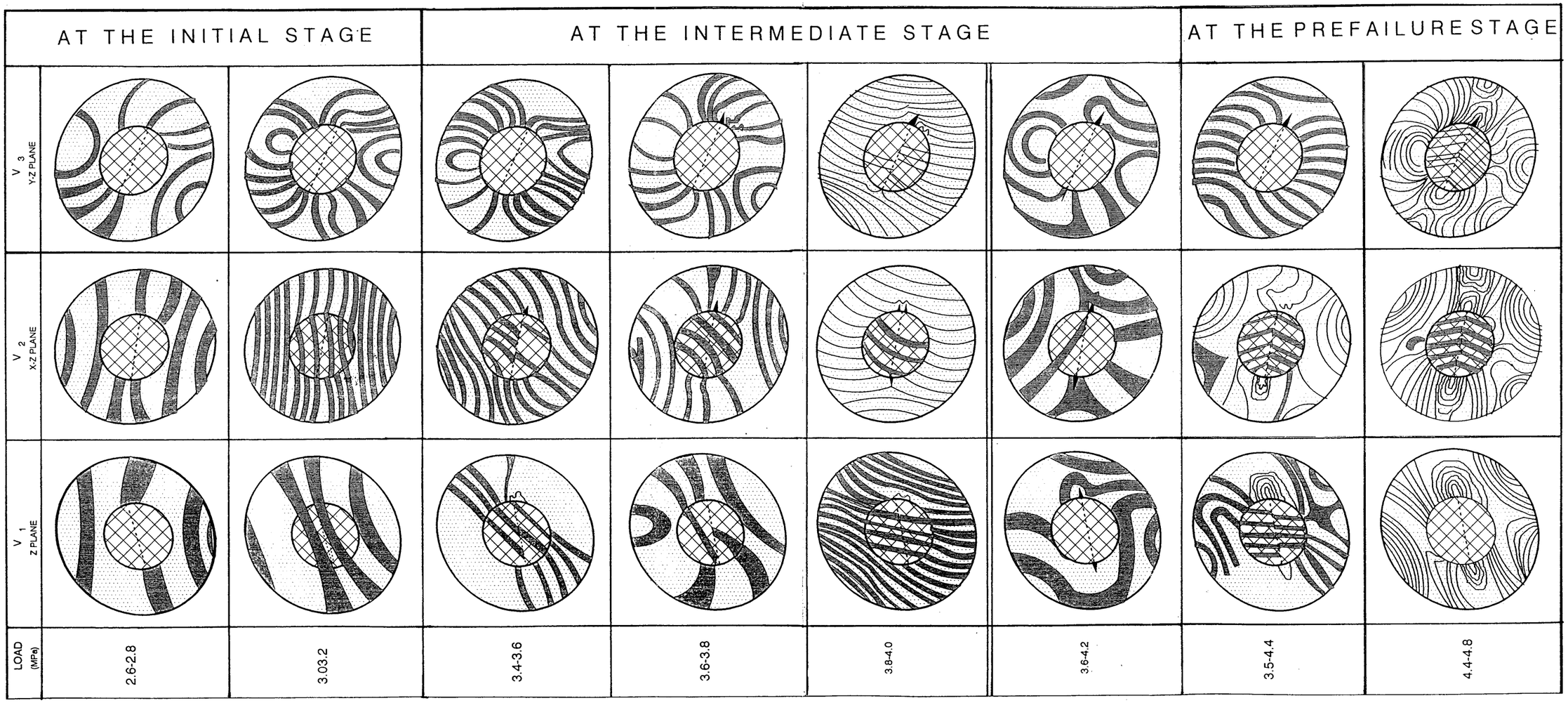


Fig. 5.14

5.3 SCANNING ELECTRON MICROSCOPY (SEM)

The use of SEM was chosen because it offers a micro-scale view and depth of field which makes it extremely attractive to the researcher for the observation of the development of fracture at the initiation and propagation stages.

Dynamic studies of material behaviour have been carried out in the SEM by several workers. Tovey (1978), applied the SEM to the study of compression of individual sand grains and the shearing of a small sample of sand by introducing a purpose-built miniature shear box. A study of statically loaded foundation materials by Aufmuth and Alezka (1976) which investigated failure in tension, bending and compression, involved alterations to the stage and door of the sample chamber of the SEM. All the above and other experiments involved in the behaviourial study of materials, involved changes to the stage in the SEM. Therefore, the Hoop Tension Test inside the SEM, was undertaken in full awareness of the difficulties which are involved to adapt this instrument for the planned experiment.

The objectives set to be achieved from the use of the SEM were the following:
(i) Investigation of boundary conditions, expressed as slip between the platens and the Hoop specimen during the experiment, at incremental loads.
(ii) Establish the location and mode of fracture initiation and propagation.
(iii) Investigate if any fracturing occurs at any other point than the predicted location.

5.3.1 The SEM and the technique

The SEM consists of an electron optical column and an electronics console. The coated samples are placed in the sample chamber in the electron optics column and evacuated to high vacuum of approximately 2×10^{-6} torr (fig. 5.15).
In the SEM the image is formed by an internally generated electron beam; this

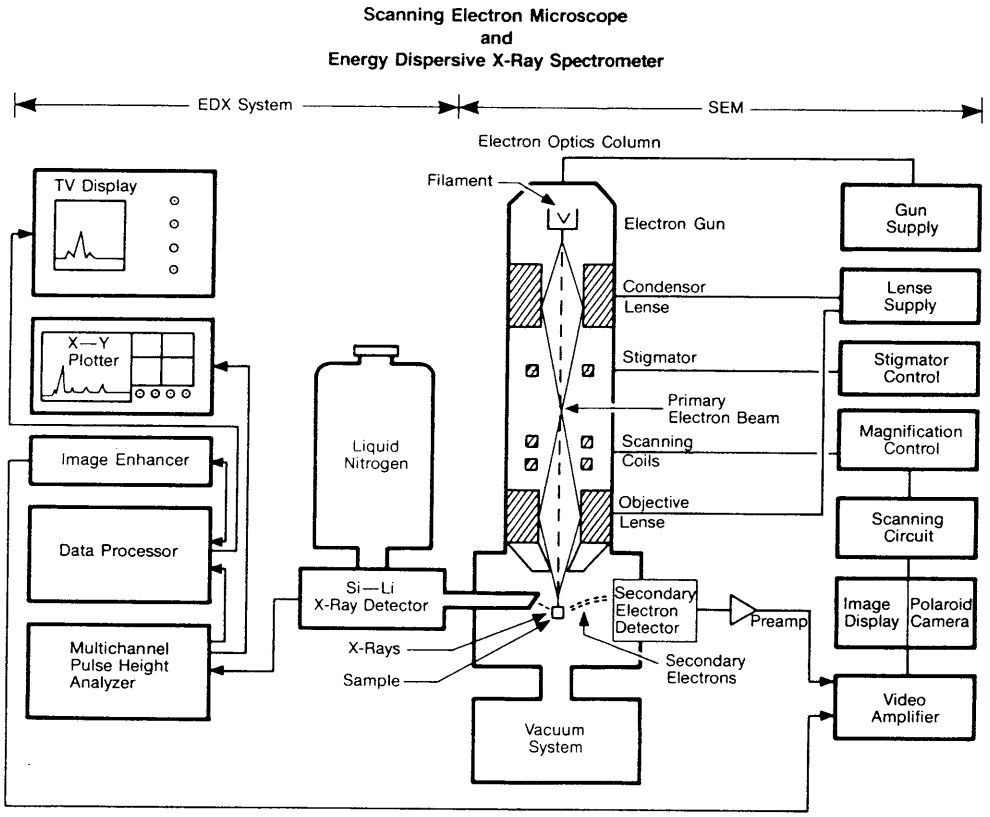


Fig. 5.15 A schematic representation of the SEM (From J.E.Welton,1984].

beam is created by heating a tungsten filament in the electron gun until this filament emits electrons. The electrons are accelerated through the column by a 5- to -30 kV accelerating voltage, they are demagnified and focused through a series of electromagnetic lenses into a finely-focused beam which bombards the sample. This beam is then scanned across a selected area of the sample. In most commercial SEMs the final diameter of the beam is typically 100 Å (1Å = 10^{-8} cm). Other components include a stigmator for controlling the shape of the beam and apertures to minimise lens defects, which in light microscopy limits resolution. The interaction of the primary electron beam with the sample produces various forms of radiation, such as secondary electrons, characteristic X-rays, auger electrons, backscatter electrons and continuous or background X-rays. All

of these reactions occur simultaneously making possible the observation and the analysis of the elemental composition of an isolated mineral in a matter of seconds. The samples are coated with a thin layer, (approximately 500 nm), of carbon, aluminium, gold or other material to give a conductive surface layer. The three-dimensional topographic image (SEI image), is formed by collecting the secondary electrons generated by the primary beam. These are low-energy electrons so only those that form near the surface are able to escape (for insulating materials such as rocks the depth at which the secondary electrons are formed is 50-500 Å). The electron beam is scanned across an area of the sample exciting secondary electrons. The irregularity of the sample surface results in varying signal strengths. A synchronised beam scanning in a cathode ray tube reflects these varying signal strengths as shades of grey, so forming an image (secondary electron image).

5.3.2 Experimental procedure

Specimens of 100 mm and 45 mm external and internal diameter respectively were used for the experiment. Load was applied from the pressure controller (GDS) from outside the SEM sample chamber and through a rigid connection from the controller to the piston inside the platens.

Alterations to equipment. To accommodate the large specimen and the hydraulic equipment necessary for the application of load, some modifications to the vacuum chamber and the stage were undertaken.

Firstly, the opening to the vacuum chamber was removed and replaced with a purpose built one, which had a feed through allowing a thin rigid pipe for the passage of hydraulic fluid. The pipe was formed into a coil at the platen's end, so as to allow some flexibility during the positioning of the sample into the vacuum chamber. All equipment non-essential for the experiment and of delicate nature was removed from the chamber; this included the backscatter, X-ray and cathodoluminiscence detectors.

Secondly, to accommodate the large specimen sample and to hold it into position, the standard stage was removed and a new one was manufactured; it comprised of a metal base plate with a post at each side. The sample was placed at the centre of the stage and while susceptible to movement, it was held in position by an o-ring positioned around the samples and posts, as shown on fig. 5.16.

Sample preparation. Sandstone and marble hoop specimens were used for the experiments, representing porous and crystalline fabric respectively. During preliminary experiments sandstone failed Hoops were used uncoated and reasonable micrographs of the fracture and their geometry were obtained. But as the object of the present exercise was to observe the development of fracture initiation and propagation, the confusion arising from the porosity of the sandstone had to be avoided. The sandstone hoops were therefore ground with loose abrasive to 1000 grade mesh, then polished to 2 microns with Cerium Oxide, before being carbon coated.

The marble hoops were also ground and polished to the same degree as sandstone, and then etched with 5% acetic acid for 10 seconds before it was carbon coated, a technique that enabled excellent grain boundary observations to be made.
The hoops were lightly taped at their perimeter so as to avoid violent scattering if the sample failed uncontrollably in the vacuum chamber. The height of the specimens was exactly equal to that of the platens, so as to avoid a "shadow" from the platens on the specimen; it was important to have a clear field of view at the platen-specimen boundary.

To achieve the set objectives it was important to observe the same points on the specimen and at the boundaries between the platens and the sample, at incremental loads. For the observation of slip, markings were drawn from the platens to the sample at selected locations as shown in fig. 5.17. Despite the alterations to the stage and by using the whole of X and Y manipulative space to move the sample along those directions, only part of the hoop sample and the platens were visible

at any time, by virtue of their size, namely the part of the marked quarter from the platen-sample boundary and towards the outer perimeter of the sample until point 0, but points 1,2,3,4 and 5 were not visible.

Acetates cut to the size of the SEM screen were used to draw several prominent features of each required position on the sample-platen boundary and of the fabric further away, enabling in this way the easy finding of the relevant position after each load application. The load line direction in relation to the bottom line of each photograph was determined to be 16° for the marble and 13° for the sandstone specimens.

An initial load was applied to provide a good contact between the platens and the sample and micrographs were taken of all relevant positions. Thereafter, incremental loads were applied and continuous scanning of the selected points was carried out; micrographs were taken which are able to convey the changes that took place during the experiments. Three marble and two sandstone samples were failed in this way.

5.3.3 Principles of observations and actual observations

The secondary electron imaging technique was employed for the experiments. The most vital observations from this exercise were the following:

(i) Increase in brightness at grain boundaries or cleavage faces, indicating localised specimen charging through cracks created in the thin coating by grain movement beneath this coating.

(ii) The visible widening of the space between separated grain boundaries.

(iii) Actual fracturing.

In marble a series of photographs at points 6,8,9,10 and 11 at x22 magnification at the initial load of 480 kPa, served as a datum for the comparison of slip between the sample and the platens. At every load increase an observation

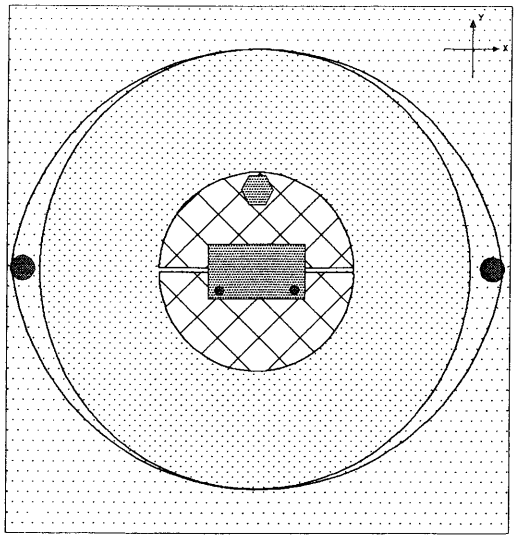


Fig. 5.16 A plan of the SEM stage with a specimen held by an o-ring

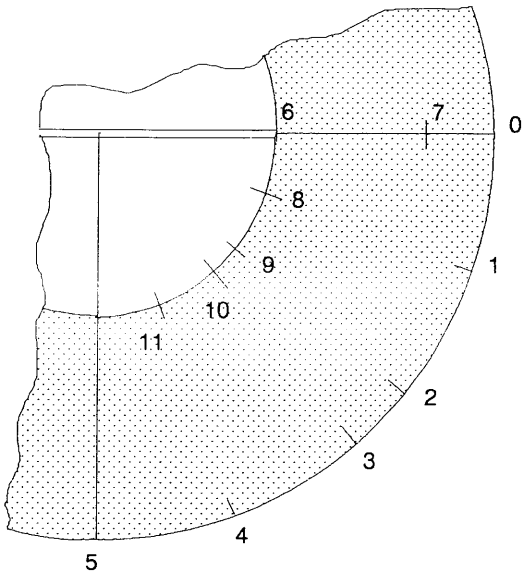
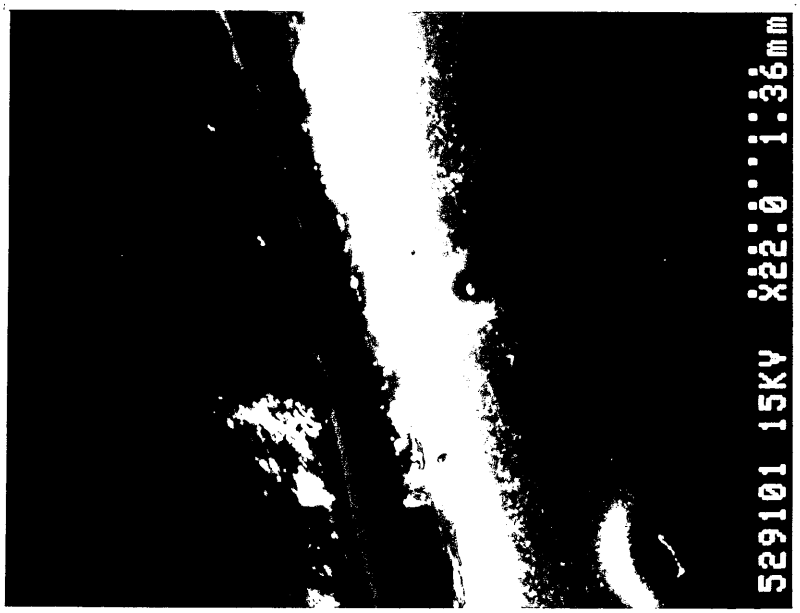


Fig. 5.17 A schematic representation of the part of Hoop specimen and platens used in the experiment. Points 0,7 and 6 were marked at 0°. Points 1 and 8 were marked at 20° clockwise from position 0. Points 2 and 9 were marked at 40° clockwise from position 0. Points 3 and 10 were marked at 50° clockwise from position 0. Points 4 and 11 were marked at 70° clockwise from position 0. Points 5 and 12 were marked at 90° from position 0.

of all points was made but no slip between platen and sample was visible; micrographs were taken at 9000 kPa for points 6,8 and 9 and at 11900 kPa and 13000 kPa for point 6. As shown by fig. 5.18a and b no slip was visible at the platen opening. The same is valid for all the other points of observation.

The dilation of the grain boundaries causes the slow break-up of the carbon coating which is expressed in the increasing brightness of those locations due to the continuous charging (see fig. 5.19a,b).

Fig. 5.20 shows the general increase in brightness closer to the platen opening and further away from it. The same is shown on fig. 5.21a and b as well as the dilation between grain boundaries and along cleavage faces; the two micrographs were taken at 11000 kPa and 13000 kPa respectively. Note that this is the location of the eventual fracture. It is clear that the development of a zone is characterised by a general and slow process of widening distance between grains, and the consequent break-up of crystals along cleavage faces. The fracturing of the marble specimens occurred at 15900 kPa, opposite the platen opening as shown by fig. 5.22a and b. The fracture seems to be a singular one, but smaller fractures are seen to run along the main one; debris which is composed of particles plucked out during the fracturing of the marble, is seen to be scattered along the fracture.

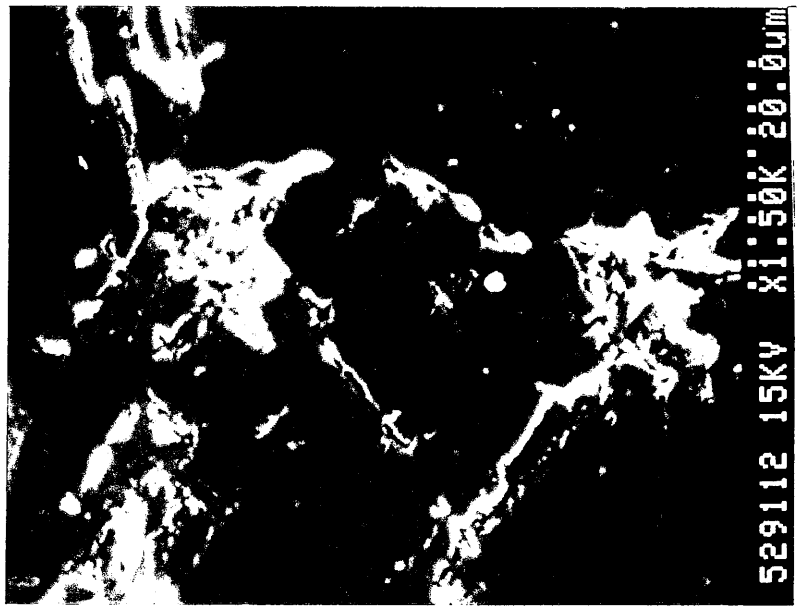


(a)

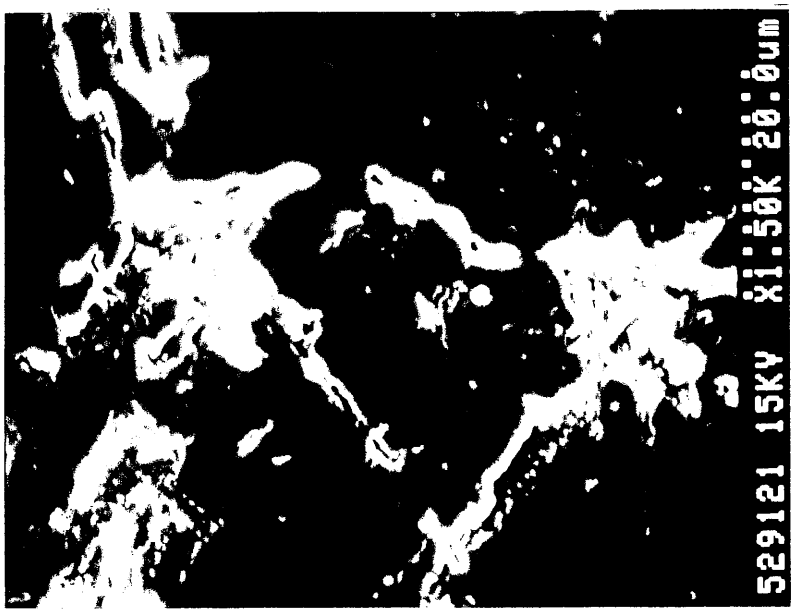


(b)

Fig. 5.18 Micrographs showing the unchanged position of platen-sample boundary opposite the platen opening at 480 kPa (a) and 13200 kPa (b). The sample failed at 15900 kPa.

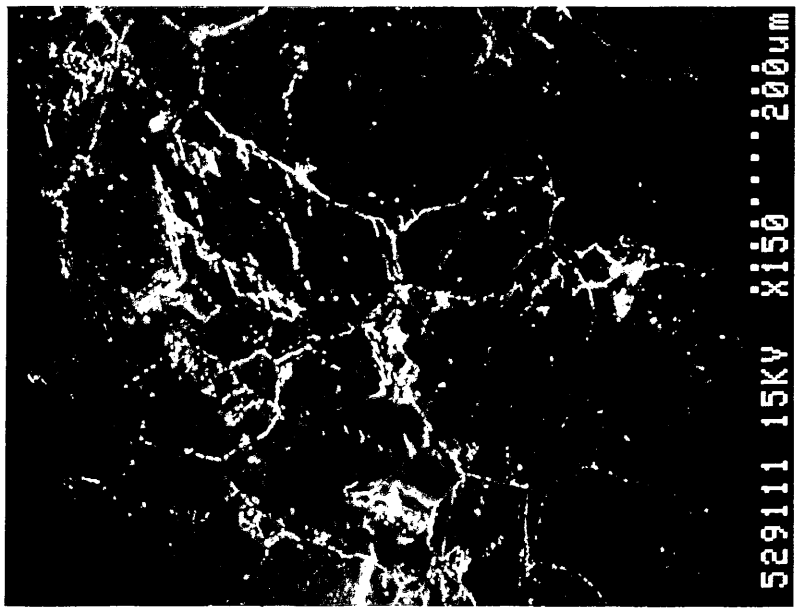


(a)

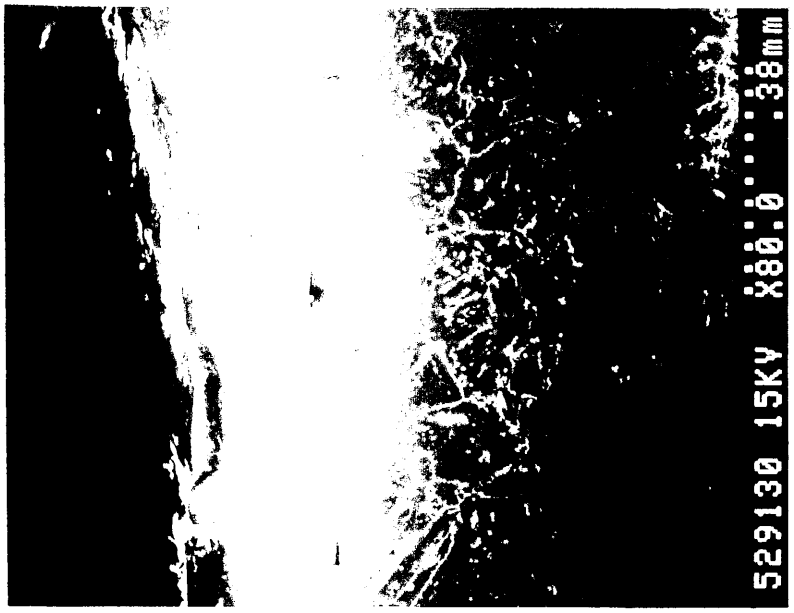


(b)

Fig. 5.19 The increasing brightness due to the break-up of the thin sample coating because of the dilation of grain boundaries; (a) 5000 kPa, (b) 9500 kPa.

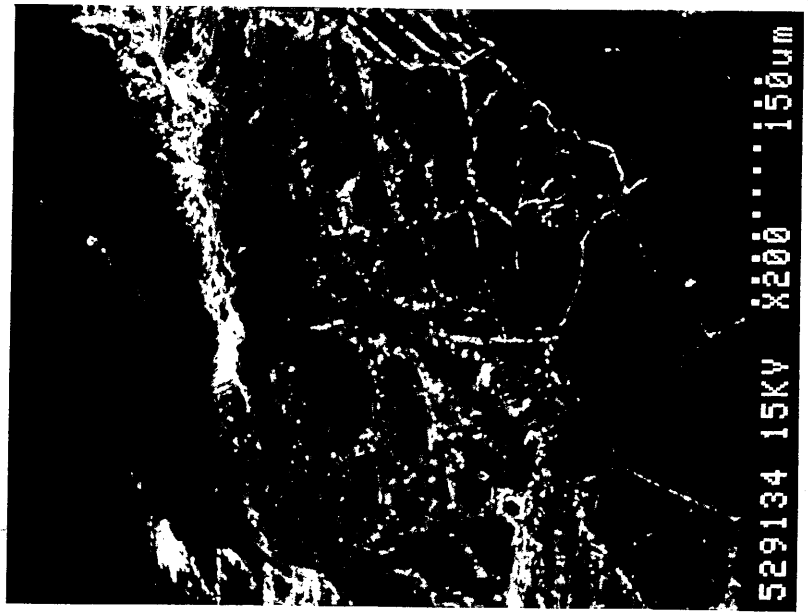


(a)

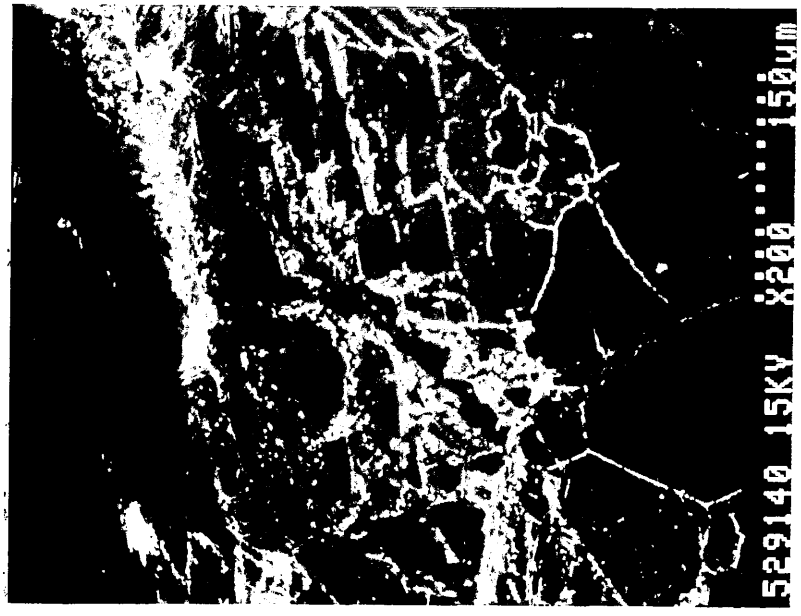


(b)

Fig. 5.20 The general increase in brightness close to the platen opening at point 6. (a) 5000 kPa and (b) 10900 kPa.



(a)



(b)

Fig. 5.21 The visible dilation of grain boundaries opposite the platen opening: load at (a) 11000 kPa and at (b) 13000 kPa.

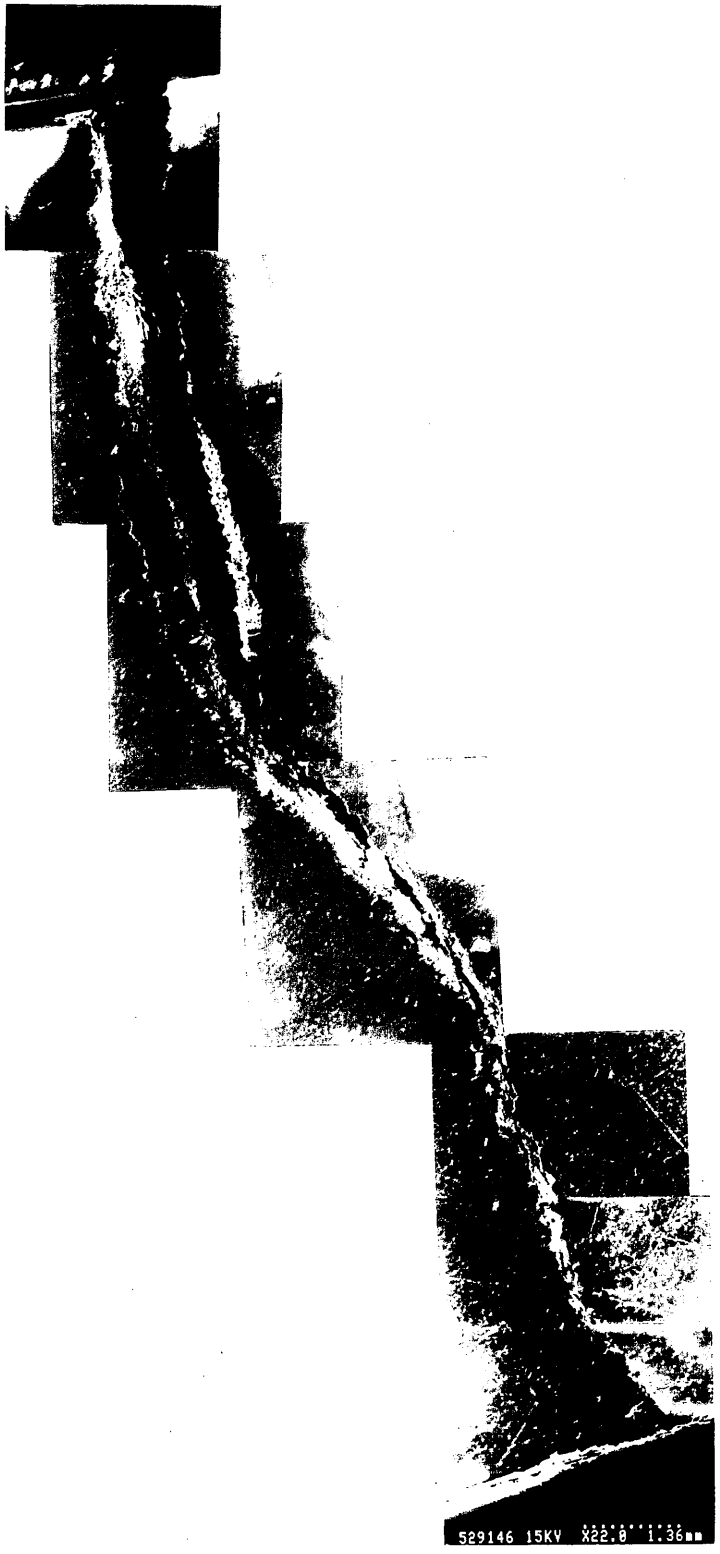


Fig. 5.22 The fracture as occurred in marble at 15900 kPa, followed from point 6 to point 0 immediately after failure occurred.

In sandstone the same procedure as for marble was followed regarding the datum for observing slip and fabric changes. The initial load applied was 1000 kPa. The markings on the platens and sample did not exhibit visible movement in respect to each other, after the incremental load applications. The gap between the platens though was visibly widened as fig. 5.23a, b, and c show at loads 1000 kPa, 5100 kPa and 6050 kPa respectively, a sign of the elasticity exhibited by the porous material before the catastrophic failure of the sample, unlike the crystalline marble. The development of a zone from which a single fracture develops is clearly observed in sandstone, expressed in the gradual brightness surrounding the grain boundaries opposite the platen opening, and extends to a distance of 2mm on each side of the pencil mark (see fig. 5.24a, b and c). The zone is made redundant by a singular macro-fracture which developed at the location opposite the platen opening and towards the outer perimeter of the sample to point 0 (fig. 5.17) at 6150 kPa. Debris consisting of quartz grains is scattered along the fracture. An examination of the fracture surfaces revealed clean surfaces with grains plucked out, an indication of the tensile mode of the fracture.

5.3.4 Conclusions

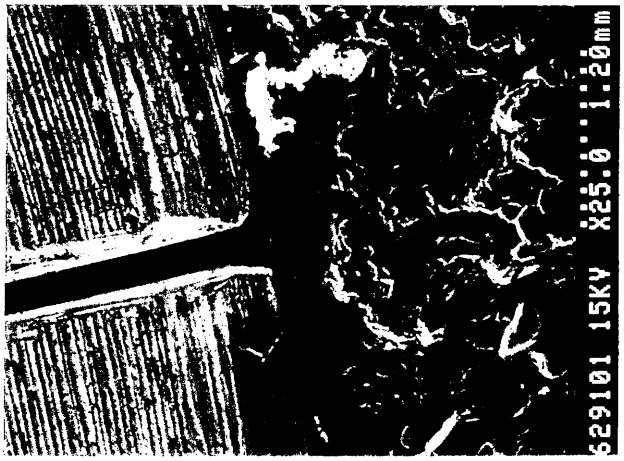
(i) As observed from both marble and sandstone samples, no slip was seen between platens and sample during loading and prior to catastrophic failure.

(ii) The development of a zone precedes macro-fracture and the catastrophic failure of the sample.

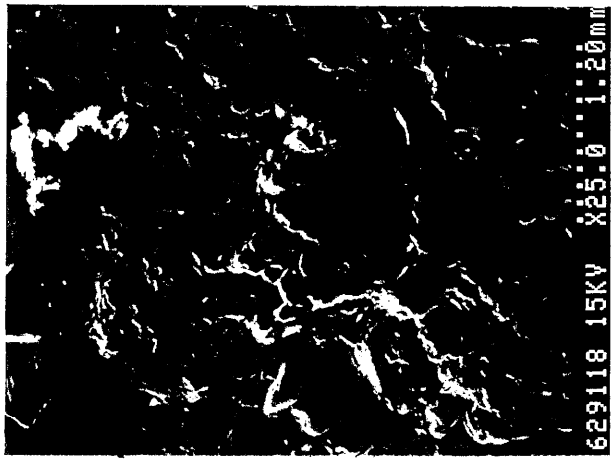
(iii) The location of the fracture is opposite the platen opening.

(iv) The failure is purely tensile as seen by the clean fracture surfaces in both the porous sandstone and the crystalline marble; particles from sandstone seemed to have been plucked out and in marble the shiny surfaces of calcite cleavage were observed. There was no sign of crushed particles or rock flour which are the evidence of shear failure: there seems to be no shear displacements opposite the platens.

(v) The sandstone is less stiff than marble. This is seen in fig. 5.23 where,



(a)

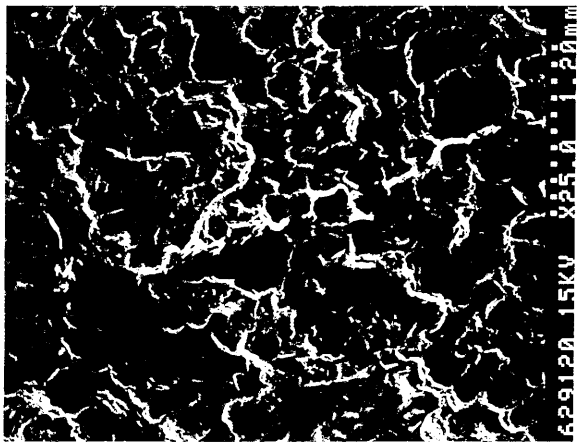


(b)

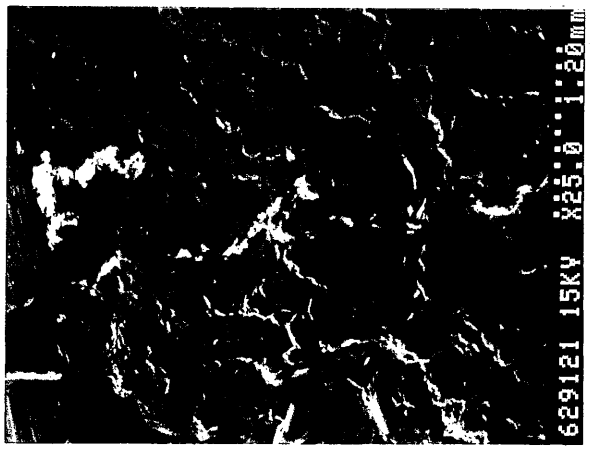


(c)

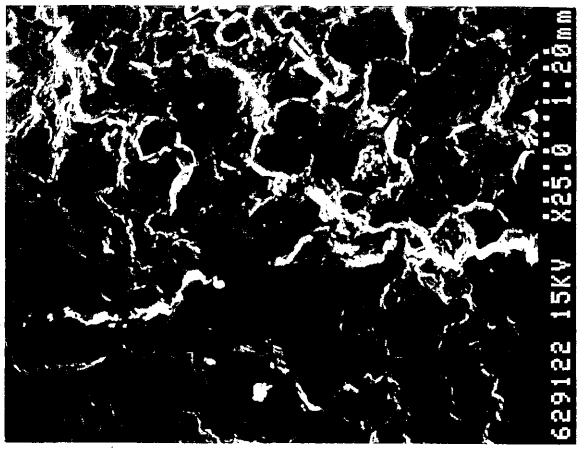
Fig. 5.23 The widening gap between the platens with increasing load before the sample failed catastrophically: (a) at 1000 kPa, (b) at 5100 kPa and (c) at 6100 kPa load.



(a)



(b)



(c)

Fig. 5.24 The development of a zone in sandstone opposite the platen opening before the catastrophic failure of the sample. (a) at 6050 kPa, (b) at 6100 kPa and (c) at 6150 kPa load.

while the gap between platens becomes wider the specimen does not fail but accommodates this increase by movement of grains; this is manifested in the brightness at grain boundaries caused by the break-up of the thin coating on the sample.

(vi) The fracture in both specimens is mostly intergranular.

(vii) The continuous observation of all selected locations did not show any micro-fracturing during load applications at any other point except opposite the platen opening.

5.4 CONCLUSIONS FROM THE THEORETICAL AND PREDICTIVE STAGE TO THE REAL PERFORMANCE OF THE HOOP TENSION TEST

A number of conclusions may be drawn from the investigations carried out and described in chapters four and five.

1 The theoretical investigations have shown that both, tensile and compressive stresses can exist in the Hoop tension test. The mathematical, finite element and photoelastic analyses have shown the stress distribution in the hoop used and the location of maximum tensile stresses opposite the platen opening. In addition, the same analyses have shown the existence of isotropic points i.e points of zero stress difference; these locations serve as cross-over points from tensile to compressive stress and vice versa. The similarity of these results obtained by three different methods is remarkably good. (see fig. 4.5, 4.7, 4.8 and 4.10).

2 The test, performed as described in 5.1, permits controlled extension of the sample and enables crack initiation to occur without the need for artificially cut stress concentrators and the consequent fracture propagation to be observed at a predictable location.

3 Rough and smooth platens used with real rock in testing with the closed loop servo-controlled machine gave very similar results allowing one to accept that these boundary conditions are not substantially influencing the results.

4 The platen-hoop boundary was investigated with the SEM. The indications are that no slip occurs for most of the period prior to failure. The same indications are obtained from the Holographic investigation, where the signs of possibly torsion or tilt of platens are present just before failure, at very high loads.

5 The Holographic investigation enabled displacements to be viewed; they clearly occurred in high concentrations opposite the platen opening. At this location the initiation of cracks is clearly visible.

6 The development of a zone from which a single fracture occurs is clearly visible during the Holographic and SEM investigations. Holography reveals the formation of this zone as kinks in the fringes and eventually as actual micro-cracks opposite the platen opening. The SEM proved an excellent way of following up a Hoop tension test; here the formation of this zone in the sandstone was expressed as loosening of grains and widening of pores, and in the crystalline marble the widening is seen along grain boundaries and along cleavage faces of calcite.

The Hoop tension test, therefore can confidently be used for the study of tensile failure in rocks because:

(i) The location of fracture initiation and propagation is predictable and the hoop can be positioned in such a way as to permit failure where it is needed.

(ii) The failure is tensile as it occurs at the location of maximum tensile stresses.

(iii) The controlled extension of the sample enables the study of a zone, from which fracture develops (a process zone), fracture initiation and fracture propagation.

(iv) Once the work of others (eg Park H., PhD. thesis 1993) has established a mathematical or other relationship between the applied load and the tensile stress, a value of ultimate strength in extension of a rock may be calculated.

PART THREE

ROCK PERFORMANCE IN EXTENSION

This part of the thesis is concerned with the performance of sandstone and marble in extension. There are two chapters; chapter 6 and chapter 7.

In chapter 6 a geological description of the rocks used is presented together with a description of their physical and mechanical properties. Results from a series of Brazilian and Direct Tension tests, conducted on these rocks for purposes of comparison of the results with those obtained from the Hoop Tension tests, are also presented.

Chapter 7 is totally devoted to the Hoop Tension tests conducted using the servo-controlled Terra-Tek machine and the GDS loading system. The influence of various parameters on the maximum pressure required for the failure of rock in the Hoop configuration is examined and the results are presented accordingly.

This part concludes with a comparison of the results obtained from conventional tensile tests and the Hoop Tension tests and a discussion on the use of the Hoop Tension test.

CHAPTER SIX

DESCRIPTION OF MATERIALS

6.0 INTRODUCTION

Two rock types have been chosen for the study of rock in extension; porous sandstone and crystalline marble. In this chapter a geological description of these rocks and their physical and mechanical properties is presented, together with an outline of the coring strategy adapted for the preparation of samples used for the Hoop tension tests and the conventional tensile tests.

6.1 DESCRIPTION OF SANDSTONE

The blocks used in this research were collected from Boles quarry, a working quarry near Penrith. The sandstone is a Permian deposit with extensive outcrops in the Penrith area of N.England. In its commonest lithology the Penrith sandstone is a reddish brown, medium to coarse grained rock, consisting from well rounded wind blown grains. This deposit is generally non-fossiliferous and is well bedded with bedding thickness varying from 0.2 to 2.0 metres.

Petrographic studies have shown that 95% of the sandstone consists of irregular quartz grains, most of which are surrounded by a thin film of haematite and illite and then by quartz overgrowth, forming an overall surface. The haematite and illite render the characteristic reddish brown colour to the rock. The remainder of the sandstone composition is made up of biotite mica and occasionally feldspar.

The sandstone used for testing was collected on two different dates from the quarry with a time difference of six months in between; therefore, some variation in its physical and mechanical properties is expected particularly as the blocks have been excavated by blasting and then hand-trimmed. Because the blocks were

not collected by the author it is regrettably not possible to relate them to natural joint sets or particular horizons.

A series of tests were conducted in the laboratory enabling the determination of the physical and mechanical properties of the sandstone the results of which are presented in table 6.1. The complete records of the sets of experiments are contained in the Appendix to chapter 6 (Tables A6.1a - A6.1f).

A search of the literature to compare these values with typical values recorded by others was unproductive as authors (Lama and Vutukuri 1978, Farmer 1983, Bell 1983) do not describe the petrology of the sandstone whose values they quote.

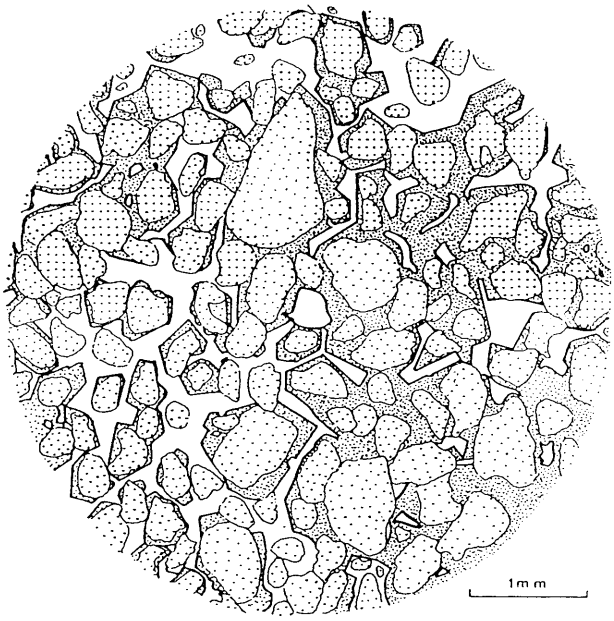


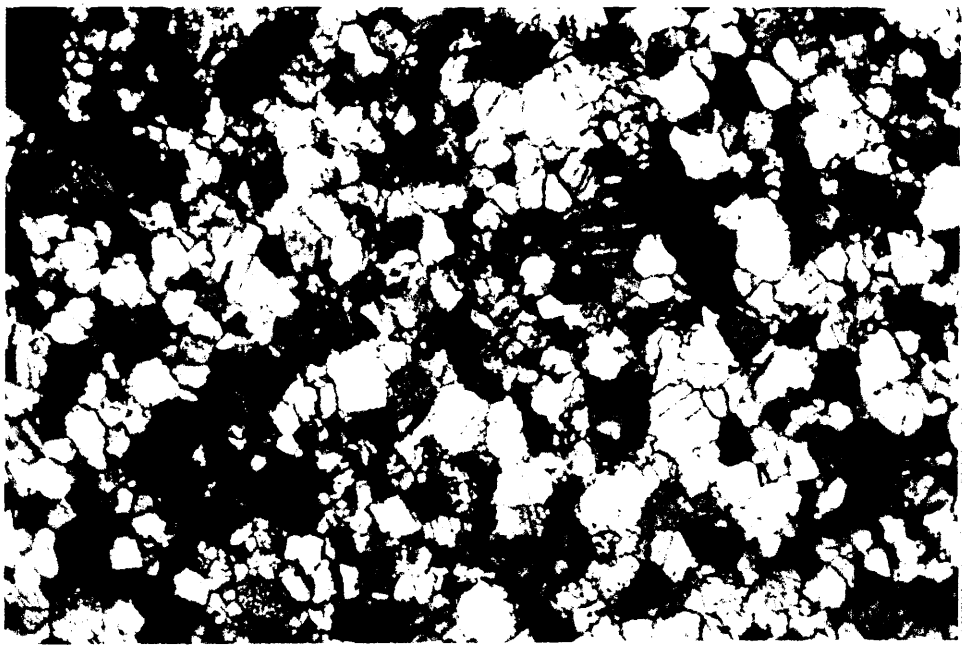
Fig.6.1 The Penrith sandstone as seen through the microscope. The irregular quartz grains, marked with light ornament, exhibit rounded boundaries which are coated with a thin film of iron oxide. The grains are surrounded by quartz cement, designated by the dense ornament; the pores are shown by the blank spaces (From S.Xu et al,1988).

6.2 DESCRIPTION OF MARBLE

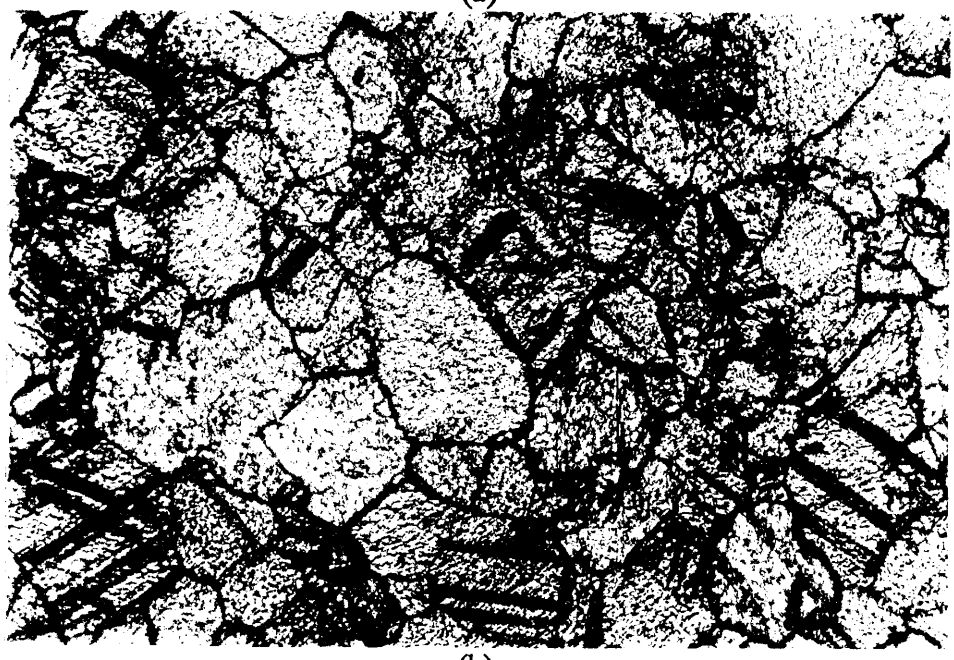
The marble used for the project is of unknown location and was purchased as two slabs. It is a fine crystalline material white in colour with thin grey wispy bands probably consisting of clay minerals. The saccharoidal fabric of the hand specimen is confirmed by the equigranular texture revealed during the study of thin sections. The microscopic examination revealed that approximately 98% of the marble consists of calcite, with the remaining being mica and traces of chlorite. The crystal boundaries are interpenetrating, unaltered and sharp. No alteration of calcite is evident except on very few crystals that appear to be speckled. The size of crystals is generally 0.5 mm.

A series of tests have been conducted in the laboratory which are shown in table 6.2. The complete record of these tests is presented in the Appendix to chapter 6 (Tables A6.2a - A6.2f).

A search of the literature to compare these values with typical values recorded by others was unproductive as authors (Lama and Vutukuri 1978, Farmer 1983, Bell 1983) do not describe the structure of marble whose values they quote.



(a)



(b)

Fig.6.2 Two photomicrographs of marble as viewed in crossed (a), and plane (b), Polars.

Table 6.1 Physical and mechanical characterization of sandstone.

TEST	LOWER VALUE	UPPER VALUE	MEAN VALUE	STANDARD DEVIATION	COEFFICIENT OF VARIATION %	UNITS
*Dry density	2.26	2.30	2.28	0.014	1.24	Kg/cm^3
*Bulk density	2.27	2.30	2.29	0.009	0.81	Kg/cm^3
*Porosity	12.76	14.65	13.64	0.54	7.99	%
Friction angle	30°	32°	31°			
*$UCS_{Sat,BLK}$	43.928	46.002	45.478	1.115	0.11	MPa
*$UCS_{Sat,GRN}$	45.758	49.029	47.458	1.339	5.64	MPa
*$UCS_{Dry,BLK}$	46.002	54.910	50.382	2.823	11.21	MPa
*$UCS_{Dry,GRN}$	45.269	55.504	51.610	4.55	17.65	MPa
*$E_{C,//to\ bed.}$	46.25	50.00	49.52	2.57	10.38	GPa
*$E_{C,\perp\ to\ bed.}$	52.63	55.00	54.09	1.04	3.84	GPa
*$E_{C,at\ 45°to\ bed}$	31.80	40.00	36.27	3.38	18.68	GPa
$E_{T,//\ to\ bed.}$	10.80	17.77	13.44	3.08	45.90	GPa
@$E_{dyn,dry,//\ to\ bed.BLK}$	11.029	13.299	12.362	1.748	28.28	GPa
@$E_{dyn,dry,//\ to\ bed.GRN}$	11.386	14.595	13.409	0.945	14.10	GPa
@$E_{dyn,sat.//\ to\ bed.BLK}$	11.98	15.17	13.60	1.05	15.39	GPa
@$E_{dyn,sat.//\ to\ bed.GRN}$	11.27	14.16	12.71	0.99	15.62	GPa
*Velocity of long. waves(P) // to bed.	2347.28	2479.33	2399.51	50.62	4.22	m/s

TEST	LOWER VALUE	UPPER VALUE	MEAN VALUE	STANDARD DEVIATION	COEFFICIENT OF VARIATION %	UNITS
4*Velocity of long.waves (P) ⊥ to bed.	1977.85	2816.59	2362.23	321.084	27.18	m/s
*Velocity of long.waves(P) at 45° to bed.	1928.07	2283.08	2087.97	122.153	11.7	m/s
*Velocity of sound waves(S) // to bed.	1477.68	1698.14	1572.84	72.35	9.20	m/s
*Velocity of sound waves(S) ⊥ to bed.	1323.31	1799.71	1613.22	172.89	21.43	m/s
*Velocity of sound waves(S) at 45°to bed.	1338.88	1572.45	1486.82	81.05	10.90	m/s

* Tests conducted according to ISRM suggested methods.

@ King, M. 1970 and 1983.

Table 6.2 Physical and mechanical characterization of marble.

TEST	LOWER VALUE	UPPER VALUE	MEAN VALUE	STANDARD DEVIATION	COEFFICIENT OF VARIATION %	UNIT
*Dry density	2.72	2.83	2.77	0.033	2.37	Kg/m^3
*Bulk density	2.72	2.84	2.78	0.035	2.51	Kg/m^3
*Porosity	3.60	6.21	4.59	0.789	34.4	$x10^{-3}\%$
*UCS_{dry}	82.415	89.111	86.112	2.887	6.71	MPa
*UCS_{sat}	71.383	80.623	76.925	3.991	10.38	MPa
@$E_{dyn,dry}$	39.200	50.170	43.041	3.33	15.45	GPa
@$E_{dyn,sat}$	58.330	63.280	60.287	1.693	5.62	GPa
*E_c	103	114	106	4.76	8.98	GPa

* Tests conducted according to ISRM, Brown, E.T. 1981

@ King, M. 1970 and 1983.

6.3 SAMPLE STRATEGY

To accommodate the number of Hoop tension tests required for this research several blocks of sandstone were used for the preparation of the samples. The hoop size was the one suggested by Xu et al (1988), of 150 mm outer and 50 mm inner diameter. As the ideas for the research were gradually focused on the investigation of an optimum hoop size it became clear that hoops of other sizes were also needed; hence, the term "class" is introduced denoting a hoop size. Four classes are defined with the detailed sizes given in table 6.3

Table 6.3 Table showing the sizes of various hoop classes.

CLASS	OUTER DIAMETER mm	INNER DIAMETER mm	RATIO
I	150	30	1:5
II	150	50	1:3
III	100	30	1:333
IV	100	50	1:2

6.4 CORING STRATEGY

The specimens for the Hoop tension tests were cored coaxially with core bits of various diameters, as will be explained later. The specimens used for the tests on the servo-controlled machine and those used on the pressure controller to investigate the effect of the rate of loading were of 150 mm outer and 50 mm inner diameter.

It was decided that a comparison of results obtained from conventional tensile tests, such as the Direct tension test and the Brazilian test, with those obtained from the Hoop tension test would be of great value in assessing the performance of the Hoop test. At the same time the idea of examining the influence of various material parameters, such as saturation and bedding, various sample parameters such as size of the hoop and its orientation, and test conditions such as smooth

and rough platens and the rate of loading, was put forward.

To make it possible to obtain an objective comparison from the conventional tensile tests and the Hoop tension tests and to examine the effect of various parameters it was important to obtain the samples as close, geographically, to each other in the block from which they are cored as possible, and to make sure that all the samples were failed in the same orientation (fig.6.3), thus limiting intrinsic variations. Two blocks of sandstone and two slabs of marble were chosen to be used.

A grid was drawn on the surface of the blocks and slabs with lines mutually perpendicular and parallel to their sides; one set of lines was black and the other green. The purpose of this was to test in orthogonal directions. Cores and hoops of different diameter ratios have been prepared from these blocks of sandstone and slabs of marble as shown in fig. 6.4 and fig. 6.5.

The cylinders have been cored coaxially and then sliced to form three Hoops with the following nomenclature: the numbers 10 and 11 represent the number of the block; numbers 1,2....7 represent the number of the cylinder and the letters a,b and c represent the layers with (a) being at the top of the block, (b) at the centre and (c) at the bottom of the block.

Detailed measurements of the hoops used for the experiments can be found in the Appendix to chapter 7 (Table A7.1a)

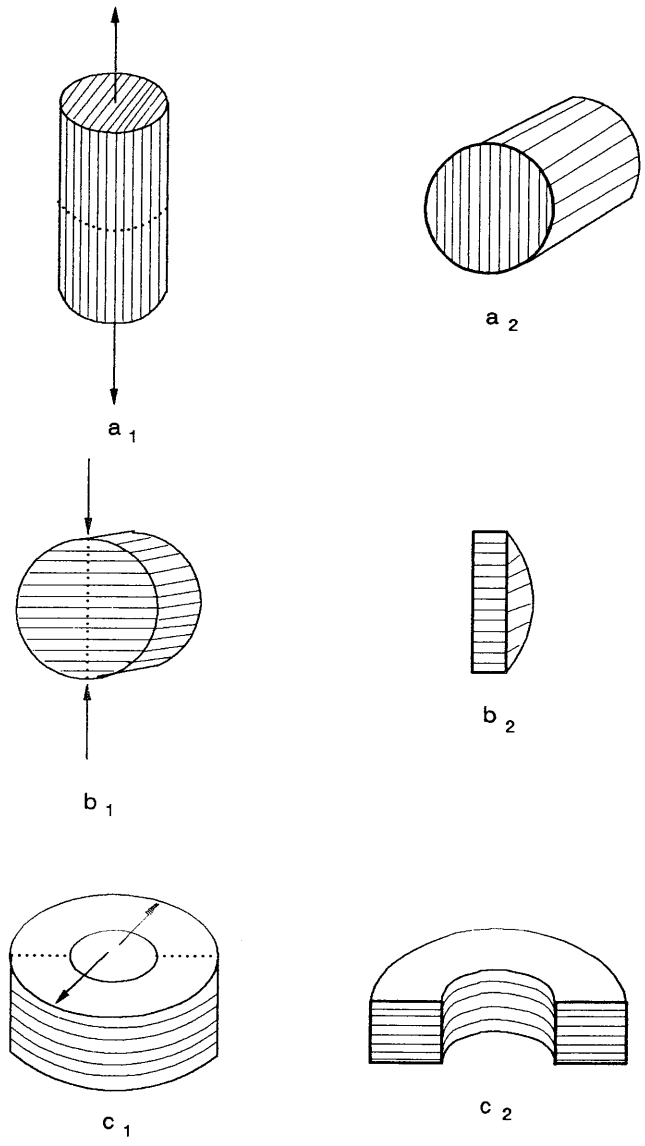
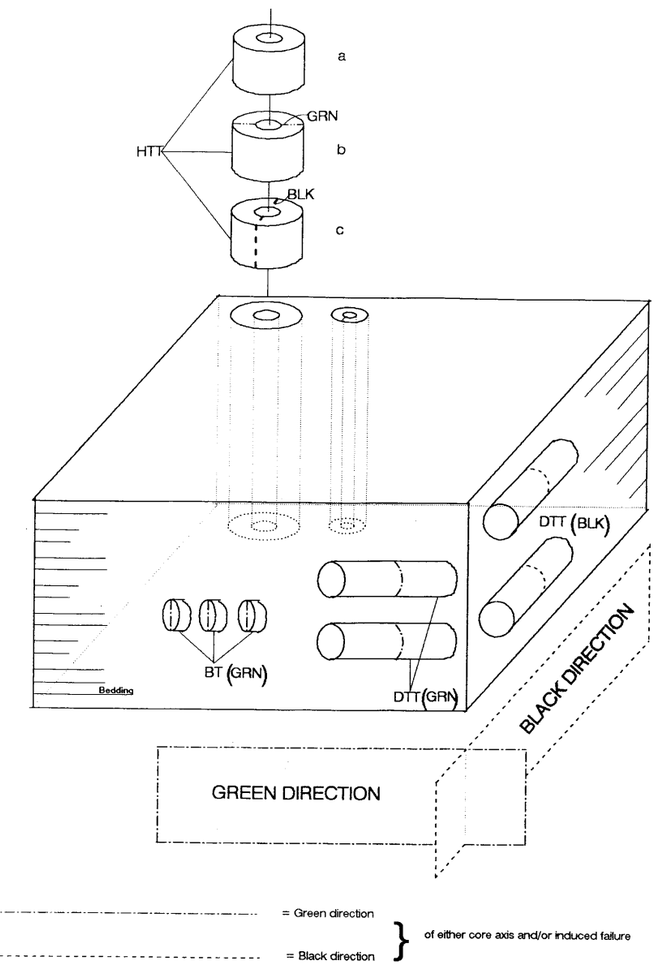
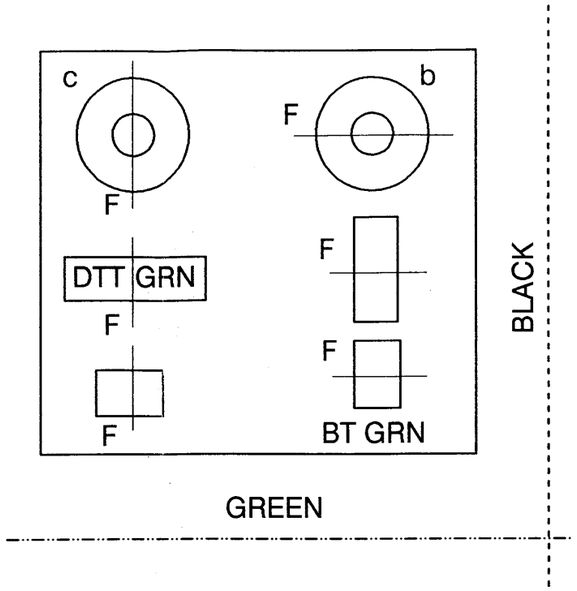


Fig. 6.3 Schematic diagram showing the relation between the direction of bedding and place of induced failure in (a_1) Direct Tension, (b_1) Brazilian and (c_1) Hoop Tension tests, and a view of the failure surface which in each case (a_2, b_2, c_2) cuts orthogonally to the plane of bedding.





Inset to fig. 6.4

A simple view in plan showing the location and failure direction (F) of hoop c and b as well as that of DTT and BT.

Fig. 6.4 Schematic drawing showing the sample orientation for Hoop (HTT), Direct (DTT) and Brazilian (BT) tension tests in respect to Green (GRN) and Black (BLK) directions in sandstone blocks. Hoop sample (c) is failed along the black direction and compared with Direct tension tests from cores drilled in the green direction, (DTT, GRN) and Brazilian tests on disks drilled in the black direction, (BT, BLK) (and not shown schematically in the figure). Hoop sample (b) is failed along the green direction and compared with Direct tension tests from cores drilled in the black direction (DTT, BLK) and Brazilian tests on disks drilled in the green direction.

The marble slabs were marked with a similar grid as that used for the sandstone blocks, but the nomenclature adapted was slightly different as the thickness of the slabs permitted only one Hoop to be cored at any location. Thus the Roman numbers I,II.III and IV represent the class of samples related to the diameter ratio, the number that follows is the serial number of a sample within a particular class.

Tables with the detail measurements of the Hoops used for the experiments can be found in the Appendix to chapter 7 (Table A7.1b).

Cores for Direct tension and Brazilian tests were prepared as shown in fig. 6.3 and fig. 6.4 and failed in such a way as to coincide with the failure direction in the Hoop. Disks for the BT were sliced to the appropriate thickness from cores prepared for the DTT.

Note: The thickness of marble slabs did not permit the suggested diameter of 54 mm for the DTT; therefore, a diameter of 38 mm was used with the ratio of diameter to length (1:2.5) being observed.

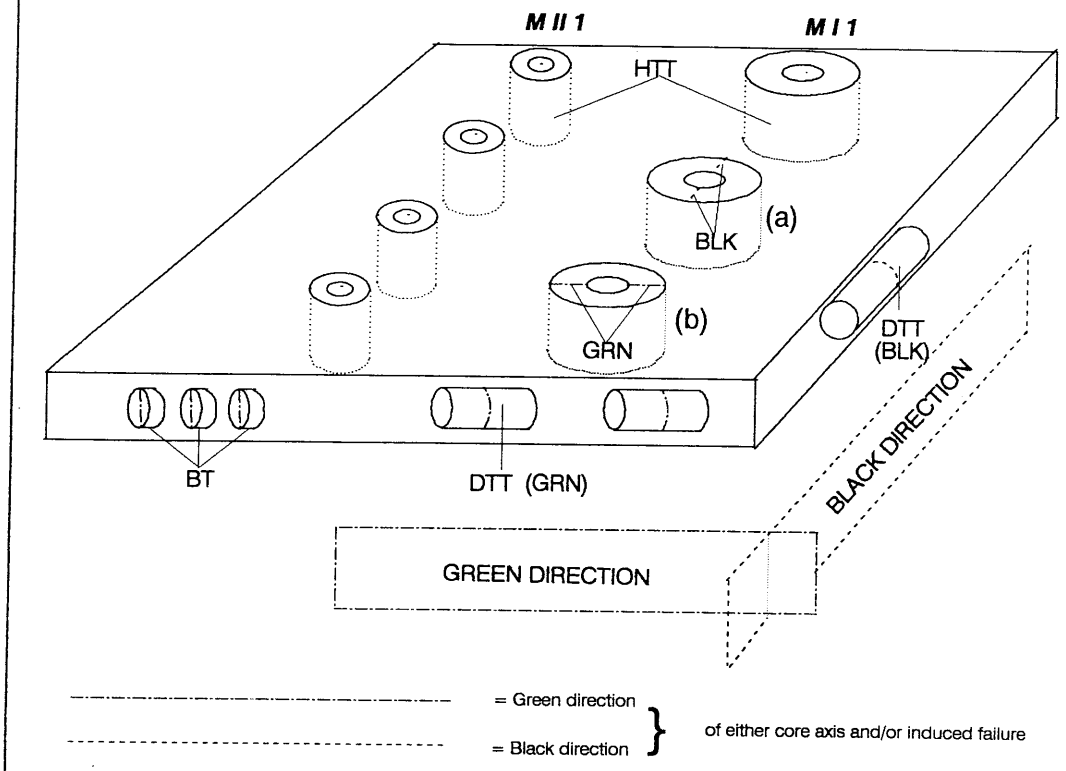
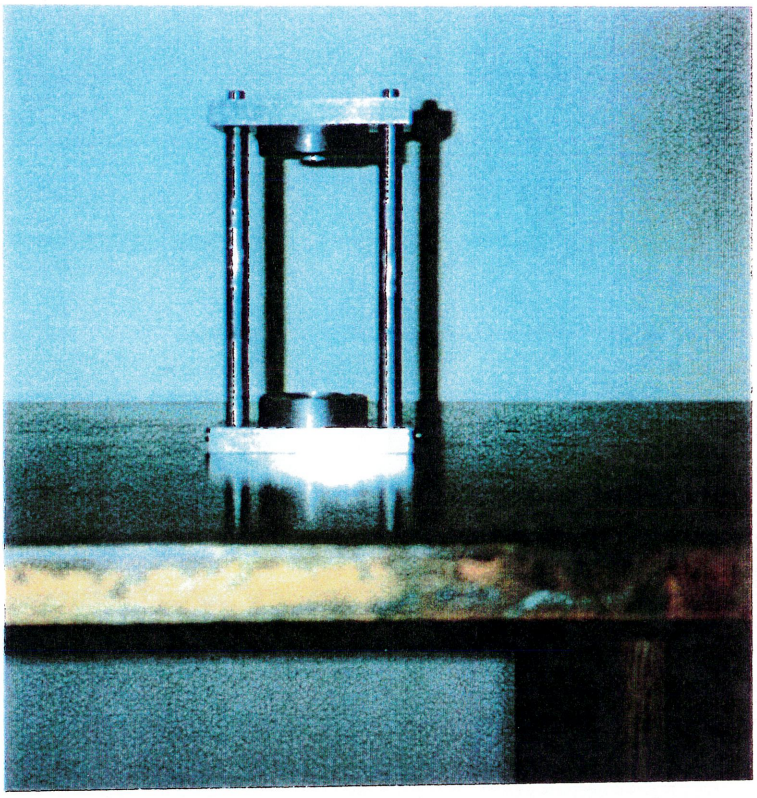


Fig. 6.5 A schematic drawing showing the sample orientation for Hoop (HTT), Direct (DTT) and Brazilian (BT) tension tests in respect to Green and Black directions in marble slabs. Hoop sample (a) is failed along the black direction and compared with Direct tension tests from cores drilled in the green direction (DTT, GRN) and Brazilian tests on disks drilled in the black direction (BT, BLK) (and not shown schematically in the figure). Hoop sample (b) is failed along the green direction and compared with Direct tension tests on cores drilled in the black direction (DTT,BLK) and Brazilian tests on disks drilled in the green direction.

6.5 CONVENTIONAL TENSILE TESTS

The most widely used tensile tests are the Direct tension and the Brazilian tests. The most credible of the two is the DTT. The BT is used as an index for the tensile strength (Hudson,1974). Both tests have been conducted according to ISRM recommendations (Brown,1981) with slight variations which are described below. In addition, Fracture Toughness tests have been conducted on sandstone according to ISRM suggested methods (Int. J. Rock Mech. Min. Sci. & Geomech. Abstr. Vol.25, No 2, pp73-96, method I, level I chevron bend, no displacement measurement).

In the course of experimental investigations regarding the DTT some difficulties were encountered during the sample preparation. According to the ISRM, platens of diameter either equal to or 2 mm larger than the core diameter are to be cemented to the specimen ends. The platens were prepared to ISRM specifications and epoxy resin was used as cement: it was found difficult to locate the core at the centre of the platens as the cement prior to hardening acted as a viscous layer which permitted the centrally placed platen to drift from its original location to one slightly off centre. Several attempts were made to construct a rig to help locate the core exactly in the centre of the platens, the final version of which is shown in fig. 6.6a and b. The platens were screwed to the top and bottom plates of the rig, positioned at right angles to the length of the rig (and length of the core) so that the platens were held orthogonal to the core thus eliminating any bending during testing. The bottom plate is permanently fixed to the two cylindrical supports, while the top one slips down along the cylindrical supports; there was provision for minor variations in the core length. The platens were manufactured to provide a 1 mm lip around their perimeter, an additional precaution to centrally locate the core. This lip has four equally spaced grooves for uniformly draining the excess cementing material by radial flow thus preventing non-radial flow in the viscous layer of unset resin from causing movement of the platen once the platen is placed on the sample. The inner surface



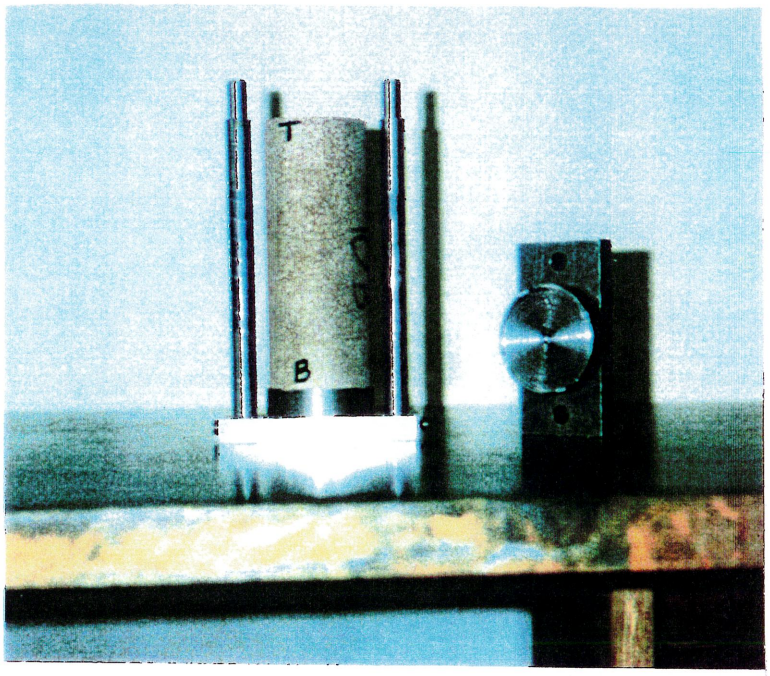


Fig. 6.6 Two photographs showing the rig manufactured for positioning the core at the centre of the platens.

of the platens had circular grooves for a better contact between core and platen at the cementing interface. The object of the above described alteration was to avoid any misalignment of the core with the end platens and consequently misalignment with the application of the uniaxial tensile load. The method proved to be successful. The results of the DTT both for the sandstone and marble are presented in Table 6.4 and 6.5 respectively.

In the Brazilian test, the disk was held between flat platens; at the point of contact between platen and sample a section of soft wood was inserted; in this manner the curved loading jaws were replaced and the soft wood at the contact point provided an arc of contact of approximately 10° during the load application, as required. Informed practitioners have long found that this is to be preferred over ISRM recommendations. The results of the BT for sandstone and marble are presented in table 6.6 and 6.7 respectively.

The number of cores used for the Fracture Toughness experiments were prepared from the same block and the core axis was parallel to bedding; all the tests were conducted in oven dry condition. The results are presented in Table 6.8

The DTT were carried out on an AVERY frame machine 6000 lbf range with a 4000 lb ring. The BT and Fracture Toughness tests were carried out on an ESH frame machine. Both machines have been calibrated prior to testing. The certificates of calibration are included in the Appendix to chapter 6.

Table 6.4(a) Direct Tension tests on oven dry sandstone.

SAMPLE NO	PARALLELISM $\alpha°$	HEIGHT mm	DIAMETER mm	AREA $x10^{-3}$ m^2	LOAD N	TENSILE STRENGTH MPa
BLK 1	0.006	139.24	53.68	2.26	2446.52	1.08
BLK 2	0.0005	134.20	54.46	2.33	5023.49	2.16
BLK 3	0.015	138.24	53.60	2.26	2068.42	0.92
BLK 4	0.005	138.24	53.60	2.26	1725.90	0.77
BLK 5	0.001	140.60	54.46	2.34	3202.72	1.37
GRN 2	0.0003	138.64	53.24	2.23	2686.73	1.21
GRN 3	0.005	135.90	53.32	2.23	2379.80	1.07
GRN 4	0.004	138.40	53.36	2.24	1934.98	0.87
GRN 5	0.004	138.90	53.48	2.25	2268.59	1.01
GRN 6	0.006	139.50	53.32	2.23	2686.73	1.20

Mean $_{BLK}$:1.26
Standard deviation $_{BLK}$:0.49
Coefficient of variation $_{BLK}$:78.08%

Mean $_{GRN}$:1.07
Standard deviation $_{GRN}$:0.126
Coefficient of variation $_{GRN}$:23.6%

BLK and GRN denote the direction of core axis in respect to the block.

Table 6.4 (b) Direct Tension tests on saturated sandstones.

SAMPLE NO	PARALLELISM α°	HEIGHT mm	DIAMETER mm	AREA $x10^{-3}$ m^2	LOAD N	TENSILE STRENGTH MPa
BLK 6	0.002	133.78	54.16	2.20	2135.15	0.93
BLK 7	0.002	134.26	54.48	2.33	2846.86	1.22
BLK 8	0.004	134.98	54.26	2.31	2446.52	1.06
BLK 9	0.005	139.26	53.64	2.59	934.13	0.361
BLK 10	0.003	132.30	54.54	2.33	2446.52	1.05
BLK 11	0.006	138.64	53.64	2.26	1823.77	0.807
BLK 12	0.011	139.30	53.64	2.26	1734.81	0.768
GRN 7	0.002	133.86	53.44	2.24	2713.41	1.21
GRN 8	0.005	133.64	53.68	2.26	2535.49	1.12
GRN 9	0.005	133.98	54.02	2.29	2824.62	1.23
GRN 10	0.005	136.36	53.50	2.25	2579.97	1.15
GRN 11	0.002	134.20	53.82	2.28	2357.56	1.04
GRN 12	0.002	133.84	53.44	2.24	2139.59	0.95

Mean $_{BLK}$:0.973
Standard deviation $_{BLK}$:0.157
Coefficient of variation $_{BLK}$:32.28%

Mean $_{GRN}$:1.12
Mean $_{GRN}$:0.048
Coefficient of variation $_{GRN}$:8.5%

BLK and GRN denote the direction of core axis in respect to the block.

Table 6.5 Direct Tension tests on oven dry marble.

SAMPLE No	PARALLELISM α°	HEIGHT mm	DIAMETER mm	AREA $X10^{-3}$ m^2	LOAD N	TENSILE STRENGTH MPa
BLK 1	0.006	97.3	37.7	1.11	3825.47	3.45
BLK 2	0.003	95.7	37.3	1.09	2335.32	2.14
BLK 3	0.005	96.9	37.5	1.11	3380.65	3.07
BLK 4	0.001	97.0	37.6	1.11	6828.02	6.15
BLK 5	0.003	95.5	37.3	1.04	4225.81	4.06
BLK 6	0.005	97.1	37.7	1.11	1801.53	1.62
BLK 8	0.004	97.1	37.6	1.11	4448.22	4.01
BLK 9	0.004	97.4	37.8	1.11	3736.50	3.37
BLK 10	0.003	97.0	37.5	1.10	2668.93	2.43
GRN 1	0.005	97.0	37.5	1.10	2837.96	2.58
GRN 2	0.002	96.5	37.3	1.09	3024.79	2.78
GRN 4	0.002	96.9	37.5	1.10	2246.35	2.04
GRN 5	0.002	96.4	37.5	1.10	5604.76	5.09
GRN 6	0.001	95.9	37.5	1.10	3202.72	2.91
GRN 8	0.003	96.6	37.4	1.10	1779.29	4.93
GRN 9	0.004	96.9	37.5	1.10	5426.83	4.93
GRN 10	0.003	96.9	37.2	1.09	4626.15	4.24

$Mean_{BLK}$:3.37
$Std.dev_{BLK}$:1.255, COV_{BLK}:74.52%

$Mean_{GRN}$:3.27
$Std.dev_{GRN}$:1.24, COV_{GRN}:75.86%

Table 6.6 (a) Brazilian test results on oven dry sandstones.

SAMPLE No	DIAMETER (D) mm	THICKNESS (t) mm	LOAD (P) N	TENSILE STRENGTH (σ) MPa
BLK 1	54.56	27.33	10002.8	4.27
BLK 2	54.63	29.18	10738.3	4.28
BLK 3	54.63	27.84	10738.3	4.49
BLK 4	54.56	28.73	10297.0	4.18
BLK 5	54.51	28.93	10076.4	4.06
GRN 6	54.53	26.29	7796.3	3.46
GRN 7	54.53	27.66	10738.3	4.53
GRN 8	54.53	29.21	12135.7	4.85
GRN 9	54.53	28.93	10738.3	4.33
GRN 10	54.48	28.02	10885.4	4.54

Mean $_{BLK}$:4.26
Standard deviation $_{BLK}$:0.148
Coefficient of variation $_{BLK}$:6.95%

Mean $_{GRN}$:4.34
Standard deviation $_{GRN}$:0.47
Coefficient of variation $_{GRN}$:21.65%

Table 6.6 (b) Brazilian tests on saturated sandstones.

SAMPLE No	DIAMETER (D) mm	THICKNESS (t) mm	LOAD (P) N	TENSILE STRENGTH MPA
BLK 1	54.59	27.66	8311.2	3.50
BLK 2	54.61	25.78	8458.3	3.82
BLK 3	54.66	27.18	7060.8	3.02
BLK 4	54.48	27.23	7722.8	3.31
BLK 5	54.69	28.75	7281.5	2.95
GRN 6	54.66	28.25	8016.9	3.30
GRN 7	54.46	28.40	8237.6	3.39
GRN 8	54.51	27.97	7355.0	3.01
GRN 9	54.51	28.22	7796.3	3.22
GRN 10	54.53	28.45	8899.6	3.65

Mean $_{BLK}$:3.32
Standard deviation $_{BLK}$:0.322
Coefficient of variation $_{BLK}$:19.4%

Mean $_{GRN}$:3.314
Standard deviation $_{GRN}$:0.211
Coefficient of variation $_{GRN}$:12.73%

Table 6.7 (a). Brazilian tests on oven dry marble.

SAMPLE No	DIAMETER (D) mm	THICKNESS (t) mm	LOAD (P) N	TENSILE STRENGTH MPA
BLK 1	54.20	24.14	22809.6	11.09
BLK 2	54.30	28.34	17047.8	7.05
BLK 3	54.28	28.34	17047.8	7.05
BLK 4	54.25	28.39	17463.6	7.21
BLK 5	54.27	28.39	17463.6	7.21
BLK 8	54.21	28.57	13840.2	5.68
BLK 9	54.26	28.34	21502.8	8.89
BLK 13	54.27	28.38	15206.4	6.28
BLK 14	54.28	28.04	21562.2	9.01
GRN 6	54.17	28.19	18651.6	7.77
GRN 7	54.18	28.31	17998.2	7.46
GRN 10	54.09	28.01	16929.0	7.11
GRN 11	54.20	28.21	15562.8	6.47
GRN 12	54.22	28.23	15325.2	6.37

Mean $_{BLK}$:7.72, Std. dev$_{BLK}$:1.56, COV $_{BLK}$:40.55% Mean $_{GRN}$:7.04, Std. dev.$_{GRN}$:0.49, COV$_{GRN}$:13.92%

Table 6.7 (b). Brazilian tests on saturated marble.

SAMPLE No	DIAMETER (D) mm	THICKNESS (t) mm	LOAD (P) N	TENSILE STRENGTH MPA
BLK 3	54.27	28.41	19839.6	8.18
BLK 4	54.25	28.28	23106.6	9.58
BLK 5	54.36	28.39	22690.8	9.35
BLK 6	54.30	27.75	13305.6	5.62
BLK 8	54.33	28.37	23344.2	9.63
BLK 9	54.35	28.35	17107.2	7.06
BLK 10	54.30	28.44	20077.2	8.27
BLK 11	54.31	28.39	22690.8	9.36
BLK 13	54.35	28.31	13662.0	5.65
GRN 1	54.10	28.15	17998.2	7.52
GRN 2	54.21	28.14	22928.4	9.56
GRN 7	54.12	28.06	24116.4	10.10
GRN 12	54.25	28.44	15384.6	6.34
GRN 14	54.27	28.31	19720.8	8.16

Mean $_{BLK}$:8.08, Std.dev$_{BLK}$:1.51, COV$_{BLK}$:37.38%. Mean $_{GRN}$:8.34, Std. dev$_{GRN}$:1.34, COV$_{GRN}$:32.13%

Table 6.8. Fracture Toughness results on oven dry sandstone.

SAMPLE	DIAMETER D mm	SPAN S mm	a_0 mm	Θ°	VOLT (LOAD)	LOAD KN	TEST DURATION sec	FRACTURE TOUGHNESS $MN/m^{1.5}$
A	37.68	125.5	5.4	90	0.12	0.252	4	0.350
B	37.57	125.5	5.4	90	0.05	0.105	5	0.148
C	37.87	125.5	5.4	90	0.08	0.168	8	0.236
D	37.61	125.5	5.4	90	0.10	0.210	9	0.295
E	37.73	125.5	5.4	90	0.07	0.147	10	0.204
F	37.70	125.5	5.4	90	0.06	0.126	7	0.175

Mean: 0.234
Standard Deviation: 0.071
COV: 61.27%

CHAPTER SEVEN

INVESTIGATIONS USING HOOP TENSION TESTS

7.0 INTRODUCTION

In this chapter a series of experiments, using the HTT, on sandstone and marble, will be presented together with their analysis. The purpose of conducting these experiments was to:

(i) evaluate the performance of the HTT in real situations,

(ii) measure the strength of material in extension, and

(iii) examine the influence of various parameters on the HTT.

Bearing in mind that what is understood by the term "tensile strength" of a rock and whether this is a material property or not, remains a debatable issue (see chapter one), there remains nevertheless, beyond the theoretical debates of what tensile strength is, the necessity to quantify the strength of material in extension. Two approaches seem to hold potential for this determination:

(1) the strength of materials approach and

(2) the work involved in failure.

The former originates from the understanding that a fracture or failure occurs when a computed tensile stress exceeds either a stated or perceived tensile strength of a given material (2.1.4) and the latter from the theory of LEFM and the concept of energy (3.2).

If the first approach is to be adopted for the determination of the strength of a rock in extension, the tensile stress in the Hoop configuration is required. Although the mathematical and Finite Element analyses (4.2) and Photoelasticity (4.3) show the location of the maximum tensile stress opposite the platen opening and the distribution of that stress, to date a clear understanding of the magnitude of this stress is not yet available even though parallel theoretical studies on this

very subject are underway.

As a simplification and purely for calculation, and comparison purposes with other tensile tests, the maximum Force at failure was divided by the total failure area of the Hoop to obtain the "ultimate strength" of material in extension.

As a reasonably accurate measure for work can be obtained from the plots of load against displacement measured along the load line, a measure of "work to failure" was used; futhermore the data obtained can also be used for other analyses when more is known in the theoretical field. This work is done to the hoop and is concentrated at the innermost boundary of the hoop, at what seems to be a near perfect contact between platens and hoop and is then transferred to the hoop itself, as evidenced in the Holographic investigations (5.2)

7.1 RESULTS OBTAINED FROM THE GDS PRESSURE CONTROLLER

From the GDS pressure controller three values can be measured viz. pressure, volume and time. The values of Pressure and Volume change can be used to give the values of Force and Displacement: an explanation of the mechanics of these calculations can be found in the Appendix to chapter 7 (Appx 7.2). Therefore, the values obtained from the GDS are Force and Displacement. No other information is available to assist with the interpretation of this data except the point of ultimate failure of the specimen. Consequently the problem presented is how to interpret these values.

Many tests have been conducted on the GDS with sandstone and marble and all the data obtained can be represented by a typical curve, consisting of four basic components, as shown in fig. 7.1.

Experience obtained during testing on the GDS shows that a finite pressure is required to overcome the inertia of the system, this being the compressibility of

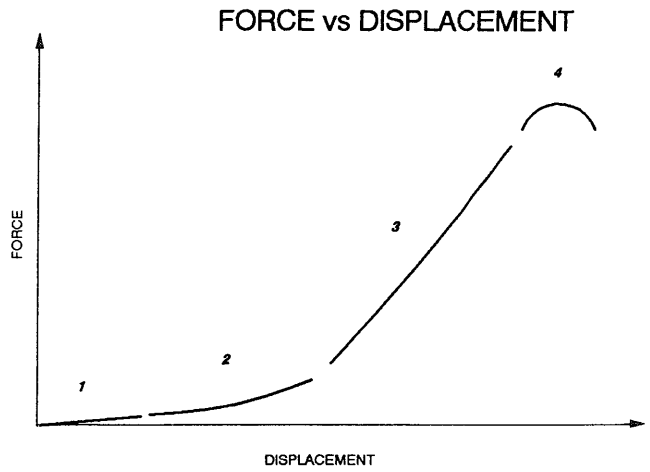


Fig.7.1 A schematic representation of a typical Force vs Displacement curve obtained when testing using a GDS system.

seals in the pressure controller and the friction of the piston within the platens of the hoop, including any minute displacement the piston may require to mate with its loading face inside the platens. This is thought to be the phase of testing which dominates the segment marked 1 on the typical curve in fig. 7.1. This part of the curve is also seen on the curves obtained when checking the equipment (fig. A7.3).

This passes into a period where the stiffness of the system increases in a non linear fashion from very soft to the stiffness approaching that of the sample; this is thought to represent the progressive contact between the platens and the inner surface of the Hoop, probably causing local crushing of protruding grains or minor irregularities, i.e effects dominated by the platen-Hoop bedding-in. This is

thought to be the second basic component of the typical curve, marked 2 and shown in fig. 7.1. This is substantiated by holograms obtained from initial loads up to 34 MPa.(5.2). The stiffness increases, becomes equal to that of the sample, up to its approach to yield, and is represented by the linear segment marked 3 of the typical curve of fig. 7.1. This part has been seen during Holographic investigations where the linear behaviour of sandstone was detected at loads 34-36 MPa, where loading and unloading took place (5.2). SEM observations showed no fabric change in sandstone between loads 1000-5000 MPa; the same was observed in marble between loads 1000-10000 MPa (5.3).

The fourth basic component of the curve in fig. 7.1 is represented by the yield and the ultimate failure of the sample and, sometimes depending on the material, by some component of the post-failure response of the hoop. The yield may be thought of as reflecting the formation of the process zone preceding failure; this is evident in the Holographic investigation at the intermediate and pre-failure stages shown in fig. 5.14b+c and 5.14d respectively. The SEM analysis also points out to the presence of the process zone both in sandstone and in marble as may be seen in fig. 5.24 and fig. 5.21.

7.1.1 Suggestions for the qualitative interpretation of the obtained curves

As mentioned above, Work will be considered for the quantitative interpretation of a GDS test. To calculate work from a plot of load vs displacement an area needs to be defined, which raises the question of which Force and which Displacement to use for the purpose. As it is not known which force and displacement to best use for the analysis of a material strength in extension, several variations and combinations of these parameters were considered, as shown in fig. 7.2a, b and c.

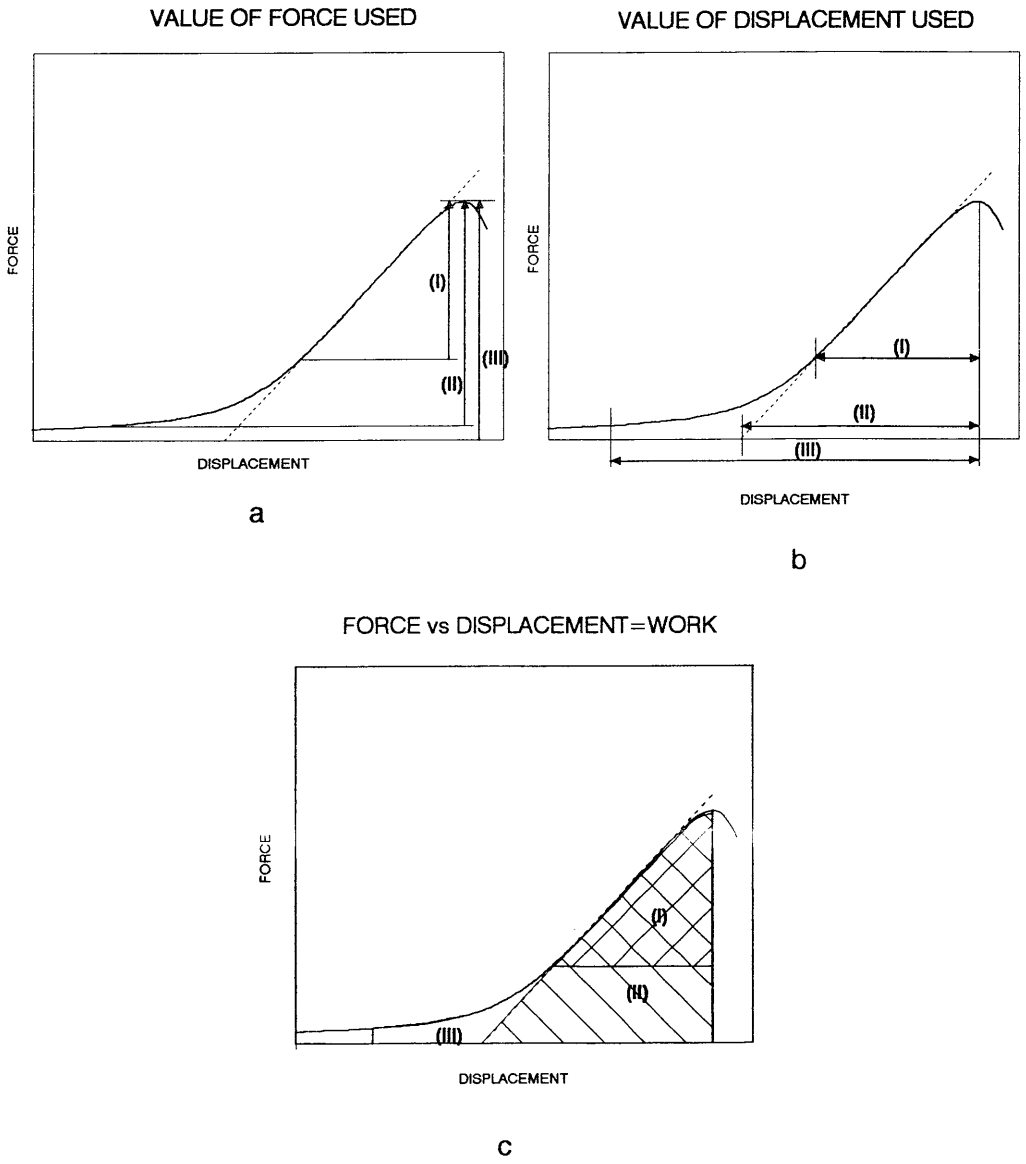


Fig. 7.2 A schematic representation of the value of Force (a), the value of Displacement (b) and the Work (c) used for calculations.

Force: (fig. 7.2a)

F_i, was used out of interest and because it represents just the linear portion of the curve including yield up to failure.

F_{ii}, was used because it represents the behaviour of the material from bedding-in to failure; this seems the most correct part of the curve to consider for calculations.

F_{iii}, was used out of interest because there may have been some component in the initial section of the load-displacement plot which did contribute to failure.

Displacement: (fig. 7.2b)

D_i, was used out of interest

D_{ii}, was used out of interest and because it represents the displacement corresponding to the extrapolated linear part of the sample behaviour including yield.

D_{iii}, was used because it seemed to be the most complete.

Work: (fig. 7.2c).

W_i, represents the work done by the sample from the beginning of its linear range and includes yield up to failure, ($W_i=F_iD_i$).

W_{ii}, represents the work done as described above for W_i but the linear portion of the curve is extended until it meets axis X, ($W_{ii}=F_{iii}D_{ii}$).

W_{iii}, represents the work done from the time of the bedding-in of platens into the sample until failure. This seems to represent the total amount of work involved in the failure of the sample, ($W_{iii}=F_{iii}D_{iii}$).

7.2 INFLUENCE OF THE RATE OF LOADING

Having decided to quantify the data in this way, it was possible to consider various aspects of the Hoop test with respect to the behaviour of sandstone and marble in extension. The first of these is the response of the material to the rate of loading.

To investigate the influence of the rate of loading on the work required to cause failure in extension, samples from one block were used. The indexing and location of samples is shown in fig. 7.3.

All the samples were tested in oven dry condition. Smooth platens were used for all the experiments. Where the platens did not fit well into the annulus initial pressure was applied to provide a good fit before the experiment was started. This is reflected on the obtained curves where Force does not originate from zero. The samples were tested at three different rates of loading as will be explained later. The grouping of samples for each rate of loading was such as to represent as uniform properties as possible within the sandstone block; hence, the influence of bedding was avoided because the samples used for the comparison of one rate were obtained from the same layer.

The samples from the top layer of the block marked with "a" at the end of their nomenclature i.e 9Aa, 9Ba, 9Ca, 9Da, 9Ea and 9Fa were tested at a continuous loading rate such that the sample failed within five minutes from the beginning of load application. This rate was chosen to be comparable with that for the

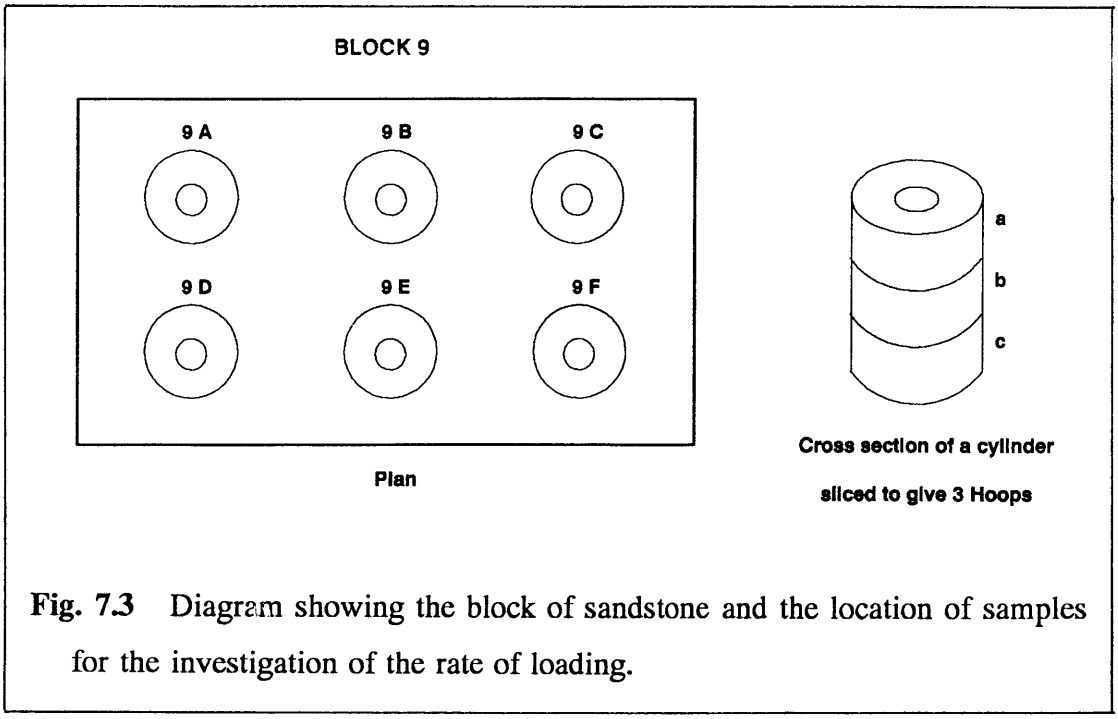


Fig. 7.3 Diagram showing the block of sandstone and the location of samples for the investigation of the rate of loading.

Direct Tension tests, (ISRM Suggested methods, E.T.Brown, 1987). Failure of the samples occurred within 1.35 to 4.5 minutes. This was classified as " suggested rate of loading", and is called the ISRM rate. Five samples were tested at this rate, sample 9Fa broke soon after the experiment was started and no data was registered.

Samples from the middle layer of the block, marked with "b", i.e 9Ab, 9Bb, 9Cb, 9Db, 9Eb and 9Fb were tested at a continuous rate of loading such that failure occurred within 0.65 to 0.88 minutes; this was classified as "fast rate of loading". Sample 9Cb broke soon after the experiment started so no data was collected.

Samples from the lower layer of the block marked with "c" i.e 9Ac, 9Bc, 9Cc, 9Dc, 9Ec, and 9Fc were tested at a continuous rate of loading such that failure occurred within 21.22 to 52.40 minutes from the beginning of loading; this is called the "slow rate of loading".

The results acquired from the samples used to investigate the influence of the rate of loading, calculated as suggested in fig. 7.2, are presented in Table A7.1a, b and c and their respective plots, both in Appendix 7.2.
It must be noted that the values for Work $_{(iii)}$ are lower than they should be if one strictly follows the instructions of fig. 7.2c; the reason is that due to the initial pressure which was applied to the platens until a perfect contact was achieved between platens and sample before the experiment was started, the curves used for analysis were incomplete as far as segment 1, and partly segment 2, of fig. 7.1 are concerned. This is true for all the tests conducted on the GDS.

Work was plotted vs Time on Semi-logarithmic and Linear scales and the results are shown in fig. 7.4 and fig. 7.5 respectively. The numerical values are shown in table 7.1.

Table 7.1 Results obtained from experiments on the influence of the rate of loading.

SAMP	WORK Nm			TIME sec		
	(i)	(ii)	(iii)	(i)	(ii)	(iii)
		ISRM		rate		
9Aa	0.9916	1.7612	1.845	79.7	103.4	138.4
9Ba	0.7533	1.4915	1.579	154.1	214.4	270.3
9Ca	0.6460	1.3220	1.406	36.1	50.1	100.8
9Da	1.1810	1.9547	2.040	35.8	48.1	100.8
9Ea	0.7903	1.665	1.914	71.2	100.4	184.9
AVE	0.8725	1.639	1.757	75.38	103.3	159.0
M.D	0.1711	0.186	0.211	33.22	44.44	54.85
COV	34%	22.7%	24.0%	88.1%	86.1%	69.0%
		Fast		rate		
9Ab	1.2321	2.274	2.401	24.7	30.7	40.6
9Bb	1.1444	2.201	2.318	23.7	31.6	39.0
9Db	1.4729	2.499	2.598	26.14	33.11	40.5
9Eb	0.9084	1.885	2.031	20.17	28.86	51.9
9Fb	0.9461	2.120	2.290	21.5	31.4	52.5
AVE	1.1408	2.196	2.328	23.24	31.12	44.9
M.D	0.1709	0.175	0.137	1.84	1.09	5.84
COV	29.95%	15.9%	11.81%	15.8%	7.0%	26.0%
		Slow			rate	
9Ac	0.7744	1.524	1.622	709.9	991.6	1273
9Bc	0.962	1.843	1.940	1863.6	2562	3144
9Cc	0.7585	1.432	1.535	732.2	995.8	1275
9Dc	1.1263	1.894	1.997	862.9	1115	1345.7
9Ec	1.0049	1.849	1.968	803.3	1075	1953.6
9Fc	0.9705	1.858	1.958	687.9	737.8	1754
AVE	0.9328	1.733	1.837	943.3	1246	1791
M.D	0.1170	0.1702	0.172	340.1	438.5	431.1
COV	25.08%	19.64%	18.8%	72.11%	70.4%	48.1%

AVE = average, M.D = mean deviation, COV = coefficient of variation

It is important to point out the spread of values within one group of the rate of loading as well as the spread of values within the combinations of the same

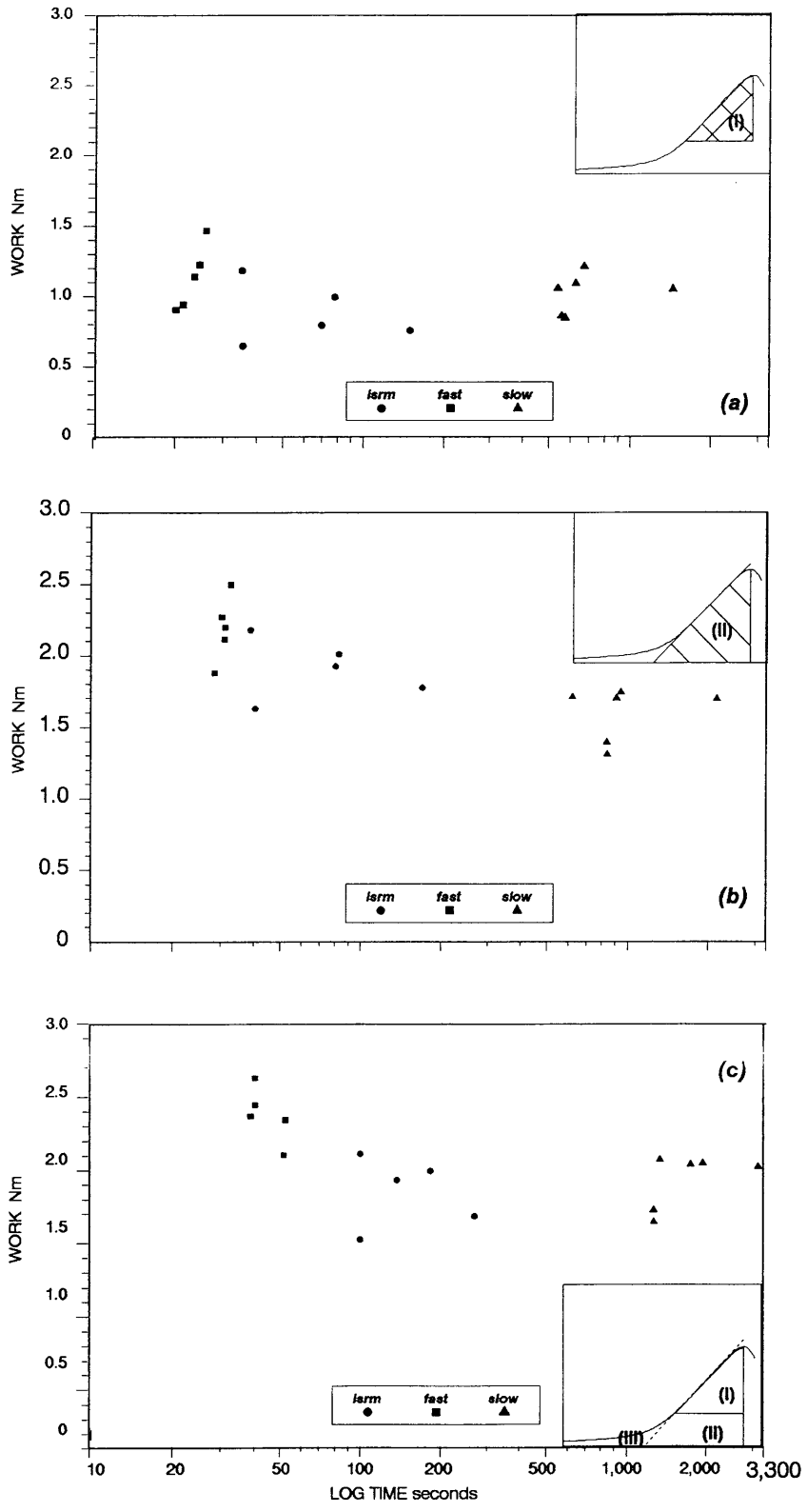


Fig. 7.4 Semi-logarithmic plots of (a) $Work_{(i)}$, (b) $Work_{(ii)}$ and (c) $Work_{(iii)}$ for the three rates of loading (common time axis).

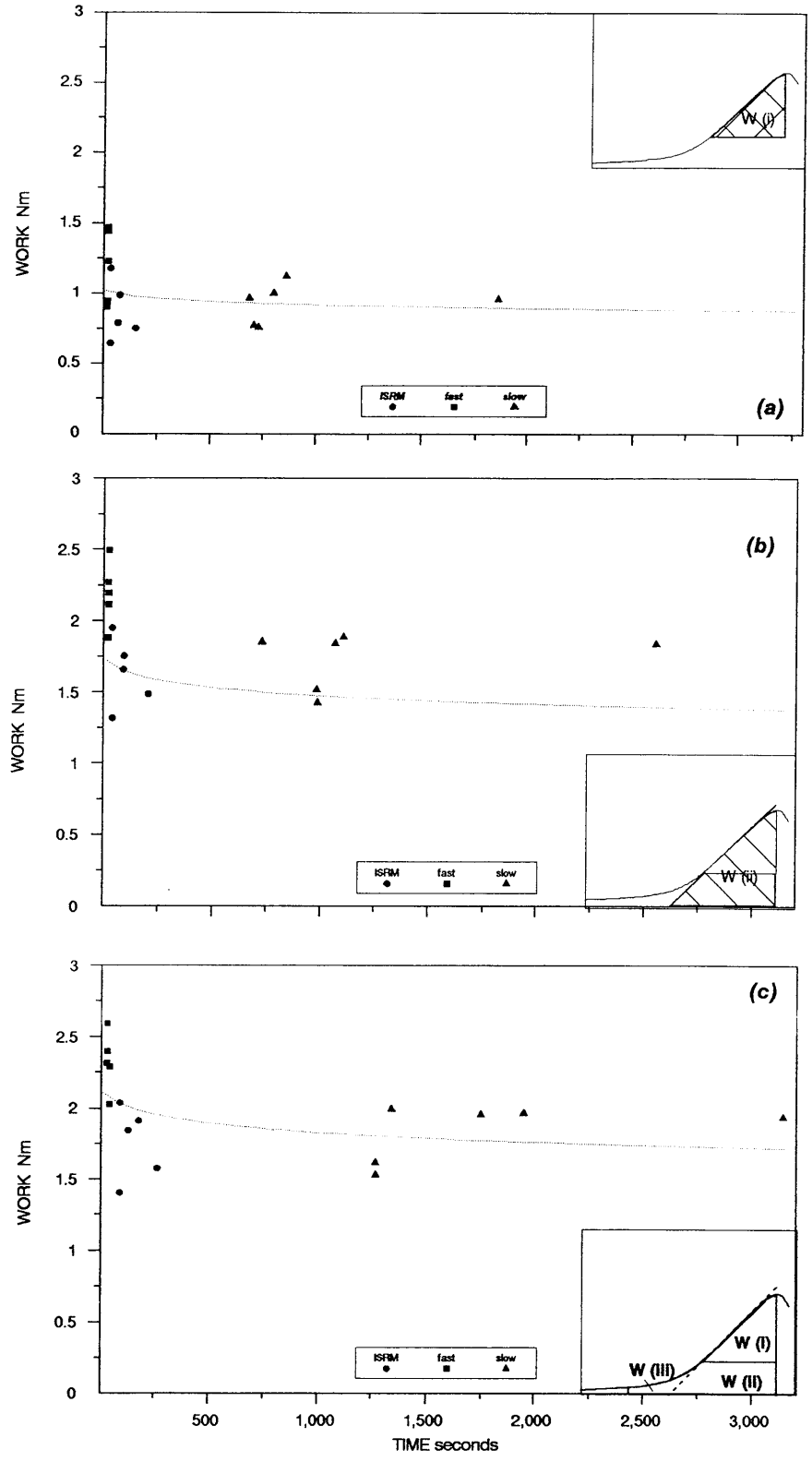


Fig. 7.5 Linear plots of (a) $Work_{(i)}$, (b) $Work_{(ii)}$ and (c) $Work_{(iii)}$ with logarithmic regression, showing the influence of the rate of loading (common time axis).

group. (See Table 7.1). The Fast rate appears to have the smallest spread with the ISRM and the Slow rates following in ascending order. The mean deviation of Time varies by an order of magnitude between the Fast and the ISRM rates and by two orders of magnitude with that of the slow rate.

The analysis of the semi-logarithmic plots for Work vs Time and the numerical results show the following:
For $Work_{(i)}$ vs $Time_{(i)}$, fig.7.4a and table 7.1, the input of Work required for the failure of the sample is greatest for the fast rate of loading (ave 1.14 Nm), less for the Slow rate (ave 0.93 Nm) and smallest for the ISRM rate (average 0.87 Nm). For $Work_{(ii)}$ vs $Time_{(ii)}$, fig.7.4b, a greater input of work is needed to induce failure of the samples loaded at the Fast rate (average 2.19 Nm), in comparison with the Work input required when the sample is loaded at the Slow rate (average 1.73 Nm) and that necessary to fail the sample at the ISRM rate (average 1.64 Nm).

The same pattern is repeated for the results of $Work_{(iii)}$ vs $Time_{(iii)}$, fig. 7.4c and table 7.1, where the input required for the failure of the sample loaded at the Fast rate is greatest, at average 2.33 Nm, compared to that needed when the sample is loaded at a Slow rate, at average 1.84 Nm, and that required when the sample is loaded at the ISRM rate, which is smallest, at average 1.76 Nm.

Considering table 7.1 the COV was calculated between the average values of the three rates of loading and the results are presented in table 7.2.
From this table it is seen that the greatest variation in the average values is between the fast and the ISRM rates, while the smallest variation exists between the slow and the ISRM rates.

Considering that the time of failure of samples tested at the ISRM rate varied by 10.8% and the same time for the slow rate varied by 84.7%, and that the COV for work between these two rates is 3.31% to 6.67%, a rate of constant loading that will induce failure to the sample within 5-10 minutes from the beginning of load

Table 7.2 Results show the COV between the average values of the three variations of work at the three rates of loading.

Difference between	Work (i)	COV	Work (ii)	COV	Work (iii)	COV
Fast-Slow	1.14-0.93	20.3%	2.20-1.73	23.9%	2.33-1.84	23.5%
Fast-ISRM	1.14-0.87	26.9%	2.20-1.64	29.2%	2.33-1.78	26.8%
Slow-ISRM	0.93-0.87	6.7%	1.73-1.64	5.34%	1.84-1.78	3.31%

COV = coefficient of variation

application seems to be correct for obtaining reproducible values of work for hoop sizes of class II.

From the above it can be concluded that the test seems to be sensitive to the rate of loading i.e the duration of the test. However, as the rate of loading is reduced, this sensitivity is also reduced and probably below some critical rate of loading the Work required to induce failure tends to a constant value. (fig. 7.5a, b and c).

The implications of knowing the influence of the rate of loading on the work required to induce failure of the sample are considerable. The Hoop test in the laboratory may give an indication for the energy input required to fail rock in quarries and other projects involved with blasting (fast rate-higher energy values), in rock bolting (ISRM rate) and long term measurements of in-situ tests (slow rate).

7.3 INFLUENCE OF VARIOUS OTHER PARAMETERS ON THE BEHAVIOUR OF MARBLE AND SANDSTONE

After the investigations of the response of sandstone to the rate of loading, using the HTT, several other parameters and their influence were examined using

sandstone and marble. These parameters were the sensitivity of a rock failed in extension to orientation of the fracture in respect to the blocks and slabs from which the samples were prepared (6.4), the saturation, the size of the Hoops and the roughness of the testing platens. The testing was carried out mainly on the GDS pressure controller.

The Hoops used for these experiments were prepared as described in detail in 6.4, fig. 6.3 and fig. 6.4. Twenty marble Hoops were tested, five of each class, I, II, III and IV. Regrettably, one of these samples, (M9/S1), failed soon after the experiment was started and therefore no results were obtained; two other samples, M3/S2 and M5/2, failed partially before failing catastrophically ; this is reflected on the obtained curves, which are presented together with the rest in Appendix 7.3. The shape of these two curves is such that did not permit an interpretation of the results as described in 7.1 and fig.7.2.

In addition to marble, twenty four sandstone hoops were also tested; six samples of class I, four samples of class II, five samples of class III and eight samples of class IV. Two samples failed soon after the experiments were started without permitting collection of results; these were sample 10 5b of class II and 10 2a of class IV.

Both work and "ultimate strength in extension" were used for interpreting the results obtained from experiments conducted on the GDS. The values of Work (ii) were used because, as pointed out, the curves used for the analysis were not always furnishing the total amount of Work (iii) used, and because it was thought that Work (ii) is more representative of the work expended purely by the sample, without the influence of other parameters reflected in segment 2 of the curve in fig. 7.1. Furthermore, as means to normalize the values of work for reasons of comparison and understanding, these values were divided by the total failure area of the hoop, as shown in fig. 7.6, resulting in work per unit area (Nm/m^2). The maximum force from each experiment was also divided by the same total failure

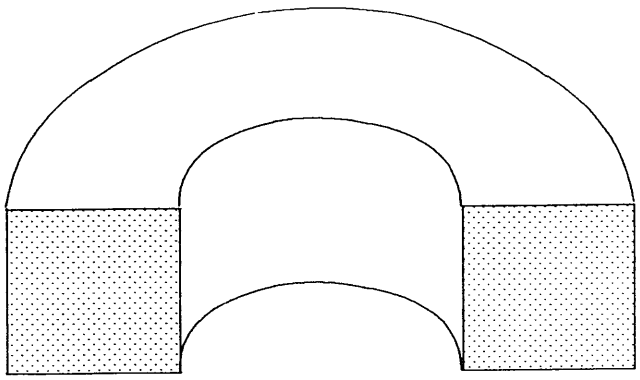


Fig. 7.6a Diagram showing (stipled), the total failure area in a Hoop tension test.

area resulting in "ultimate strength at failure, in extension" (MPa).

A note on failure.

The majority of samples tested with the HTT failed as predicted, opposite the platen opening. However a smaller number (9Da, 9Fc, 106a, 107a, 107b, 107c and 6f2) failed in addition to the two predicted locations, in a third location as shown in fig. 7.6b. The failure of the sample in this third location has taken place during testing with the GDS and the Terra-Tek. The location from where the piston emerges was marked routinely on each sample prior to testing; there seems to be no relationship between the position of the piston and the location of this occasional third fracture. As far as it was possible to have visibly assessed the order in which the three fractures were formed it can be said that all three are fast fractures and the third fracture seems to have no influence on the results of ultimate strength obtained from the tests; this may be an indication that the third fracture was formed immediately after the two fractures opposite the platen opening. Although the stresses associated with the third fracture have not been analyzed, it is suspected that they are related to the tensile stress that would result from the collision of compressional waves travelling around the hoop from the fast fractures propagating at either inner diameter of the hoop. This third fracture is

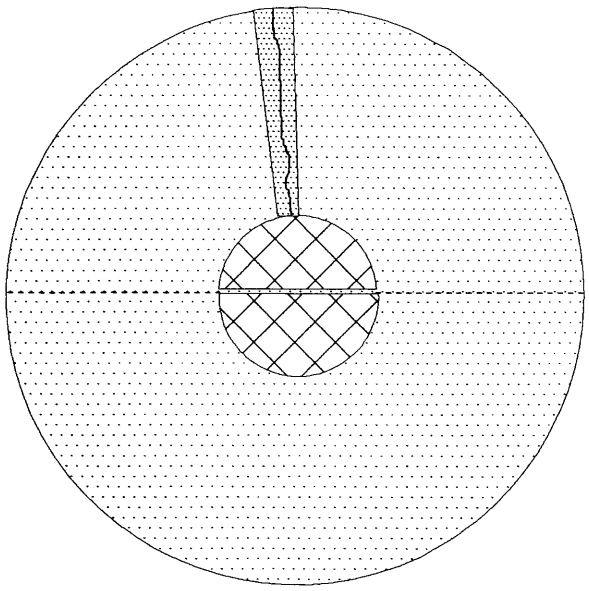


Fig.7.6b Diagram showing the location of the third fracture in a hoop. The shaded area illustrates the range within which the fracture took place. This location could have been on either side of the platens.

thought to form in tension as it has the same features on the surface as the surfaces formed in tension by the hoop.

The results obtained are now reported. As will be discussed later, the behaviour of rock in extension was found to be most sensitive to sample condition (as indicated by the form of natural veins studied in Chapter 2) and unfortunately the number of tests conducted was limited by the samples available.

7.3.1 The behaviour of marble

The numerical results of Work (ii) and stress obtained from the marble hoops are presented in tables 7.3 and 7.4 respectively. These values are plotted vs the ratio

of hoop diameter and are shown in fig.7.7a and b respectively.

The effect of orientation. The hoops have been prepared and marked in such a way as to fracture at locations which were parallel to the original sides of the slabs from which they were cored and are mutually perpendicular (fig. 6.5). Therefore, the hoops were tested so that they failed either in the "green" or the "black" directions. Samples available for this comparison are: M2/S2, M4/S2, M5/S2 of class I, and M2/S2, M4/S2 of class III.
If values of work are used (table 7.3) the COV varies from 10% to 28%; if values of "ultimate strength in extension" are used the COV varies from 2.75% to 80%. This can also be seen in fig. 7.7a and b. With such spread of values in such few comparisons one can hardly see any trend.

The effect of saturation. The hoop samples tested in saturated condition have been immersed in water under vacuum of less than 800 Pa for a period of 6 hours (ISRM Suggested methods, E.T.Brown, 1987). The suggested time is at least one hour but in view of the low porosity of marble it was thought safer to prolong this period of saturation. Before the platens were inserted into the annulus, the samples were surface-dried with tissue. The samples tested in dry condition, have been dried in a thermostatically controlled oven at 105° C overnight, cooled and kept in a desiccator until testing.

The results show that the "ultimate strength in extension" at failure, is greater in the saturated samples and that greater amount of work is required to fail saturated than dry samples. (see fig.7.7a and b and Table 7.4). This obviously is contrary to the general belief of material weakening when saturated, therefore sample identification and cross-checking with computer file numbering was carried out, leaving no doubt about the truthfulness of this finding. One of the two following explanations may be offered for this behaviour:
(a) The extremely low porosity and interpenetrating grain boundaries of marble may have prevented all the voids within the sample from being saturated thus

Table 7.3 Results showing the $Work_{(ii)}$ required to fail the marble hoop samples.

CLASS	BSS	BSD	GSS	GSD	BRS	BRD	GRS	GRD
I	16885 (M2/S2)	8966 (M3/S2)	13887 (M4/S2) 12731 (M5/S2)	1519 (M1/S1)				
II		1991 (M3/S2)			3210 (M2/S2)	1662 (M5/S2)	3554(M4/S2)	1655 (M1/S2)
III	8355 (M11/S1) 6520 (M8/S1) 6095 (M10/S1)			3219 (M7/S1)				
IV					869 M2/S2 878 (M4/S2)			512 (M1/S2)

The values have been obtained by dividing the $Work_{(ii)}$ by the total failure area of the hoop samples.

Class I= (150/30) 1:5 BSD=Black Smooth Dry BRD=Black Rough Dry
Class II= (150/50) 1:3 BSS=Black Smooth Saturated BRS=Black Rough Saturated
Class III= (100/30) 1:333 GSS=Green Smooth Saturated GRS=Green Rough Saturated
Class IV= (100/50) 1:2 GSD=Green Smooth Dry GRD=Green Rough Dry

Table 7.4 Results showing the "ultimate strength in extension" of the marble hoop samples.

CLASS	BSS	BSD	GSS	GSD	BRS	BRD	GRS	GRD
I	2.475 (M2/S2)	1.586 (M3/S2)	2.235 (M4/S2) 1.061 (M5/S2)	0.6692 (M1/S1)				
II		1.327 (M3/S2)			1.620 (M2/S2)	1.169 (M5/S2)	1.6651 (M4/S2)	1.192 (M4/S2)
III	2.300(M11/S1) 1.995 (M8/S1) 2.053 (M10/S1)			1.446 (M7/S1)				
IV					1.133 (M2/S2) 1.098 (M4/S2)			0.826 (M1/S2)

The values have been obtained by dividing the max. force by the total h op failure area.

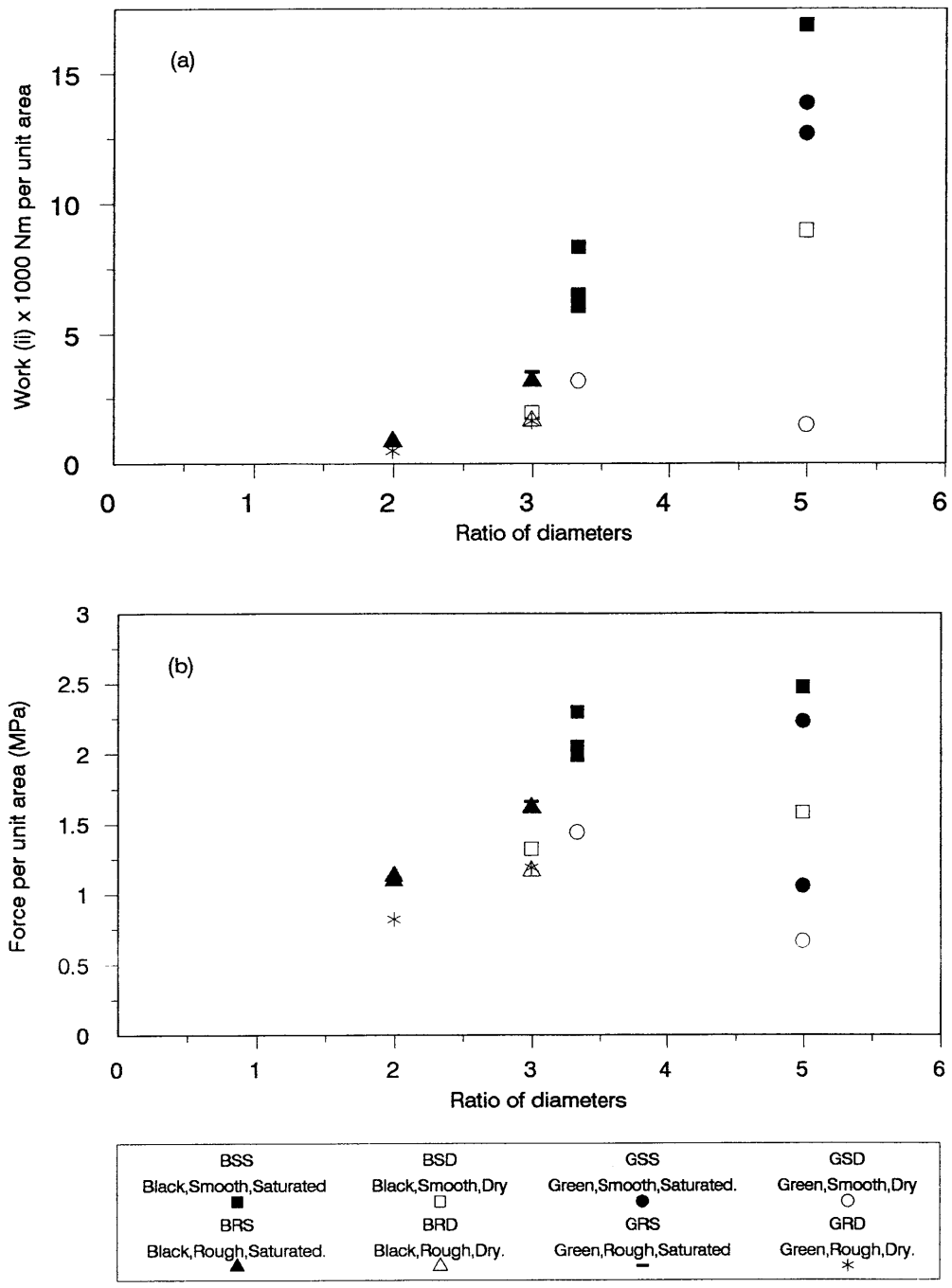


Fig. 7.7 Plots showing (a) the work per unit area and (b) the "ultimate strength in extension" experienced by hoops of various diameters in marble at failure.

leaving a partially saturated condition within the sample. Such condition will have air-water interfaces defined by menisci which are capable of providing a cohesion by virtue of their surface tension.

(b) The speed with which fracture occurs causes the present pore water to fill a larger volume, so creating a meniscus within the crack and negative pore pressure, which has the effect of increasing the strength of the material, thus this could effect the absolute values which were obtained close to the peak. The same phenomenon was detected in low porosity granites during dynamic tests (prof. M. King private communication).

The effect of hoop size. In an attempt to investigate the effect of the ratio of the outer to the inner diameter of the hoop and hoping to establish an optimum size, four classes of specimens were prepared (6.4), partly influenced by the availability of coring bits; class IV has a ratio of 2, not a representative ratio as this should be more than 2 (Jaeger and Hoskins, 1966).

Referring to fig. 7.7a and b, it is prominent that on average, more work is required to fail a sample of a greater diameter ratio than the work required to do the same for a specimen of a smaller ratio. This is quite agreeable with SEM observations (5.3), where the fracture initiates from the inner to the outer diameter; in a specimen of greater diameter ratio this fracture path becomes longer and hence more work input is required. It must be noted that the values of ratio 1:5 exhibit considerable spread, but the lowest value is a result of a sample cored from slab 1 whereas all the other samples were prepared from slab 2.

The effect of roughness of loading platens. Only platens of 50 mm diameter were available in both smooth and knurled surface exterior; therefore, the testing and comparison were limited to samples of 1:3 and 1:2 ratios, i.e to class II and IV respectively.

The one pair of results available for this comparison is M2/S2, M5/S2 of class II and it shows that more work is required to fail a sample with rough platens. Pair

M3/S2, M5/S2 of class IV, failed in a fashion that did not permit interpretation of results (see respective curves in appx 7.4).

Conclusions about the behaviour of marble in extension, using the hoop tension test. From the above discussion of the results obtained from the testing of marble using the HTT, two trends are seen and can be reported with some degree of confidence:

(a) The saturated marble seems to be stronger than the oven dry, and

(b) The greater the diameter ratio the more work is required to fail a sample.

The effects of orientation of fracture and roughness of platens are inconclusive due to the limited number of samples involved in the comparison.

7.3.2 The behaviour of sandstone

Sandstone specimens have been tested with the GDS pressure controller and a smaller number with the Terra-Tek servo-controlled machine. First, an analysis of the results obtained from the GDS will be presented, followed by a section on the Terra-Tek results.

The specimens used with the GDS were prepared from blocks 10 and 11 as described in 6.3 and 6.4. The numerical results, interpreted as discussed in 7.1.1, and their corresponding curves are presented in Appendix to chapter 7 (Appx 7.5). The results obtained from the testing on the GDS, expressed as Work (ii) per unit area and "ultimate strength in extension" are presented in Tables 7.5 and 7.6 respectively. The same results of work and "ultimate strength in extension" have been plotted vs the ratio of diameters, the plots of which are shown in fig. 7.8a and b respectively.

The influence of bedding. Bearing in mind that the hoops have been prepared from different layers of each block (a, b and c, see fig. 6.4), whenever possible a comparison of results within the same layer was carried out, with the purpose

of establishing the homogeneity of the material. For samples prepared from block 11, if "ultimate strength in extension" is considered, the COV varies from 4 to 7%, and if work is considered, the COV varies between 1% and 5%. For samples prepared from block 10, the COV varies from 9 to 13% and up to 28% (with one exception where the COV is 42%), if "ultimate strength in extension" and work are considered, respectively. A comparison of results from the same cylinder but across layers (for example 106a and 106b), and from different cylinders across layers, was also carried out. Block 11 exhibits a COV of 1.45% and 5.3% if "ultimate strength in extension" and work are considered respectively. Block 10 exhibits a COV of 7 to 18% and up to 28% if "ultimate strength in extension" and work are considered respectively. Visually the hoops prepared from different layers display some grain variation and possibly this is associated with porosity which in turn influences the overall strength of the material. Despite the variations, to be able to continue with the investigation on the influence of the other parameters, the assumption that the material is homogeneous has to be made.

The influence of orientation. The hoop samples were marked with black and green lines denoting the relationship of their position to the block from which they were cored (fig. 6.4). The fracture in the hoops was induced in such a way as to coincide with either the black or the green directions. Four pairs of results were available for this comparison: 111c/112c, 104c/105c, 102c/101c and 107b/107c (see table 7.5 and 7.6). In three of these pairs the strength of material is higher when the samples failed at the green direction. The COV varies from 13.4 to 43.4% and from 4.9 to 43.4% if work and "ultimate strength in extension" are considered respectively. The considerable variation in the values obtained and the small number of comparisons available, are insufficient to lead to any conclusions about a trend on the influence of the orientation in testing.

The influence of saturation. The samples which have been tested both in saturated and oven dry condition have been treated in the same way as the marble samples described earlier (7.3.1). The samples of which the values of work and "ultimate strength in extension" have been used for the comparison between the

Table 7.5 Results showing the $Work_{(ii)}$ required to fail the sandstone hoop samples.(Nm/m^2).

CLASS	LAYER	BSS	BSD	GSS	GSD	BRS	BRD	GRS	GRD
I	a		2128 (1 11a) 1957 (11 2a)						
	b	1485 (11 1b) 1470 (11 2b)							
	c		1937 (11 1c)		2226 (11 2c)				
II	a							297 (10 4a) 358 (10 5a)	
	b						560 (10 4b)		
	c	155 (10 4c)		241 (10 5c)					

CLASS	LAYER	BSS	BSD	GSS	GSD	BRS	BRD	GRS	GRD
III	a	468 (10 6a) 720 (10 7a)							
	b	789 (10 6b)			812 (10 7b)				
	c		533 (10 7c)						
IV	a		227 (10 1a) 224 (10 3a)						
	b							146 (10 2b) 124 (10 3b) 122 (10 1b)	
	c						216 (10 2c)	176 (10 3c)	172 (10 1c)

1 The values have been obtained by dividing the $Work_{(ii)}$ by the total hoop failure area.

2 "Layer" Denotes the location of the samples in respect to the block from which the hoops were cored.

Table 7.6 Results showing the ultimate strength in extension of the sandstone hoop samples.

CLASS	LAYER	BSS	BSD	GSS	GSD	BRS	BRD	GRS	GRD
I	a		0.8361 (11 1a) 0.7812 (11 2a)						
	b	0.6909 (11 1b) 0.6635 (11 2b)							
	c		0.7970 (11 1c)		0.837 (11 2c)				
II	a							0.3683 (10 4a) 0.4159 (10 5a)	
	b						0.5157 (10 4b)		
	c	0.1986 (10 4c)		0.3105 (10 5c)					

CLASS	LAYER	BSS	BSD	GSS	GSD	BRS	BRD	GRS	GRD
III	a	0.4553 (10 6a) 0.4987 (10 7a)							
	b	0.5769 (10 6b)			0.5858 (10 7b)				
	c		0.5114 (10 7c)						
IV	a		0.3362 (10 1a) 0.3768 (10 2a)						
	b							0.3128 (10 2b) 0.2737 (10 3b) 0.2465 (10 1b)	
	c						0.3502 (10 2c)	0.3169 (10 3c)	0.3120 (10 1c)

1 The values have been obtained by dividing the max. force by the total hoop failure area.

2 "Layer" denotes the location of the samples in respect to the block from which the hoops were cored.

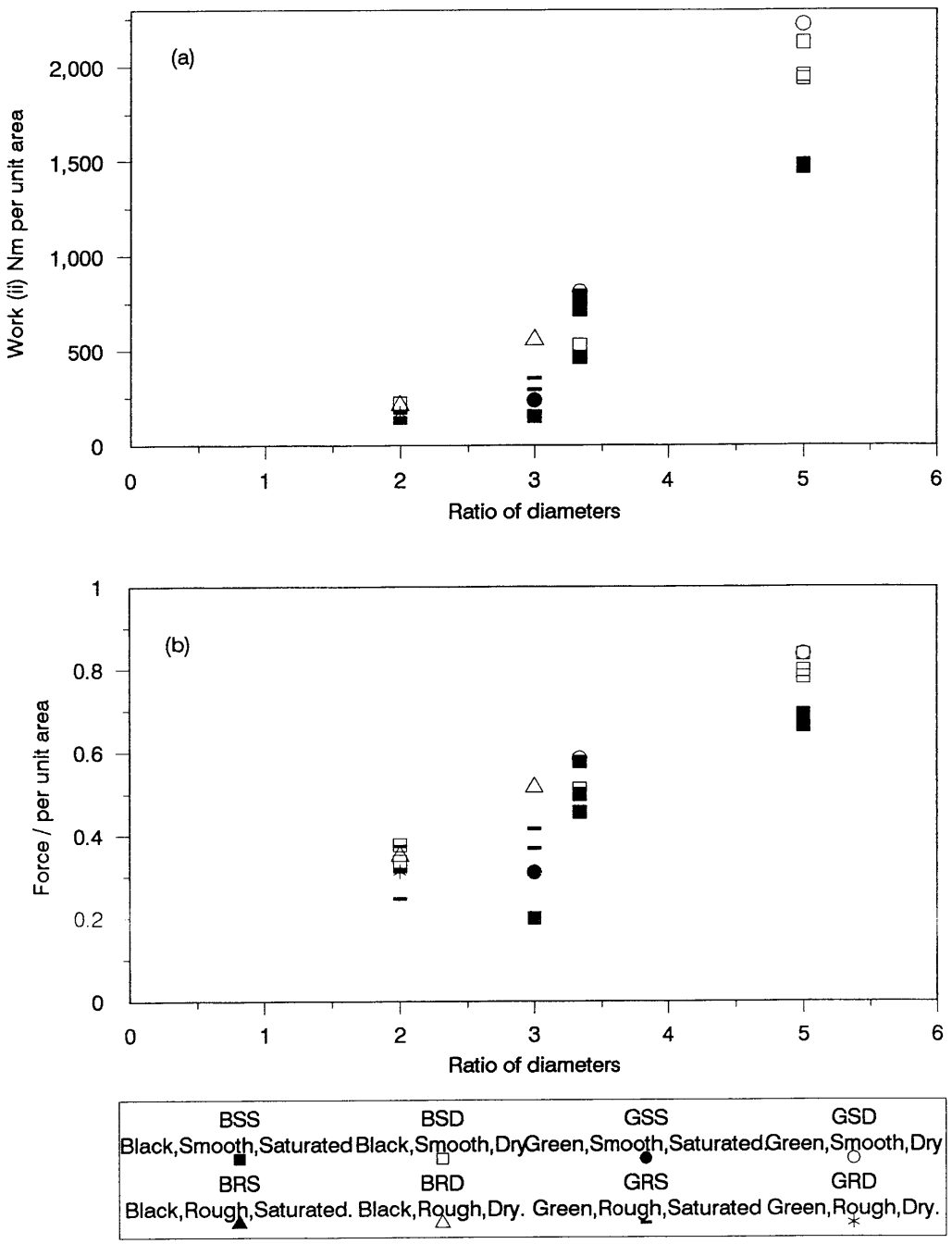


Fig. 7.8 Plots showing (a) the work consumed per unit area, and (b) the "ultimate strength in extension", experienced by hoops of various diameter ratios in sandstone at failure.

dry and saturated condition, together with the COV are presented in table 7.7. The values of the samples originating from block 11 are consistently higher for the dry ones; hence, the values of dry and saturated samples have been averaged and the COV calculated. The values of the samples originating from block 10 are not persistently higher for dry samples as one would expect; therefore the comparison of values has been carried out not only on averaged values but also on a one to one basis.

An examination of fig. 7.8a and b shows that for samples of class I and II (ratios 1:5 and 1:3 respectively), dry samples have consistently higher values than those for saturated samples, but the same is not true for values of samples belonging to class III and IV (ratios 1:333 and 1:2) respectively. Out of the total number of comparisons though only three show that the saturated samples are stronger than the dry ones; these cases show a low COV between the dry and saturated values, except for one (106b/107c). As the comparison is done for samples not originating from the same layer, one may explain this seeming difference with variability in porosity originating from different grain size; this might have caused problems with saturation and hence the unexpected discrepancies in strength when the material was saturated. Since doing this work, analysis of the distribution of compressive and tensile stresses in the hoop has advanced (Park, H. PhD thesis in preparation) which shows that the diameter ratios used for the present experimental work results in the tensile and compressive regions in the hoop as seen in the photoelastic and holographic work. The work by H.Park (PhD. thesis, in preparation) demonstrates that there is a ratio of diameters beyond which no compression exist within the hoop opposite the opening of the platens. In general terms the inside diameter of the hoop should be as close as possible to the outside diameter of the hoop for uniform tension to be developed along the line opposite the platen openings. In the tests conducted for this research the areas of the hoop dominated by extension of pores will be areas where negative pressures might be expected and here saturated samples might be expected to be stronger. Ratios greater than the ones which place the hoop completely into tension will have

positive pore pressure at their outer compressive regions and negative pore pressure close to the platens, therefore there, will be pore pressure gradients in the sample, the effects of which are unknown but the greater the area of compressive stress along the diameter of the hoop the greater will be the volume of the water with positive pore pressure, and under these circumstances it will not be surprising for saturated samples to be weaker than dry samples.

The effect of hoop size. An examination of the curves in fig. 7.8a and b shows that on average more work or a higher "ultimate strength in extension" is required to fail a sample of greater diameter ratio; if the values for each class are averaged regardless of conditions of testing an indication is obtained from both the work and "ultimate strength in extension" values that there is an increase in the values as the ratio of diameters increases. The same is true for marble (7.3.1).

Table 7.7 Results on the influence of saturation of sandstone.

CONDITION	BSS	BSD	COV% (WORK)	>	COV% (STRESS)	>
SAMPLE	111b	111a				
	112b	112a				
		111c				
AVE			30.39	D	17.22	D
SAMPLE	106a	107c	13.0	D	11.6	D
	107a	107c	29.8	S	2.51	D
	106b	107c	38.7	S	12.04	S
AVE			21.1	S	0.21	D
CONDITION	GRS	GRD				
SAMPLE	102b	101c	16.35	D	0.0001	S
	103b	101c	32.4	D	13.08	D
	101b	101c	34.0	D	23.46	D
	103c	101c	2.3	S	1.56	S
AVE			19.1	D	8.18	D

D = dry, S = saturated, BSS = black smooth saturated, BSD = black smooth dry, GRS = green rough saturated, GRD = green rough dry

The effect of roughness. Two sets of comparison are available for the examination of the effect that smooth and rough loading platens have on the sandstone; the first set involves three samples: 104a / 105a in GRS and 105c in GSS. If the values of the samples in the same experimental condition (GRS) are

averaged and compared with the value of the sample in GSS the COV is 23.23% and 30.43% for "ultimate strength in extension" and work respectively, with the values being greater for smooth platens. The second set also involves three samples: 101a 103a in BRD and 102c in BSD. If the same method as described above is followed the COV is 1.78% and 4.3% for "ultimate strength in extension" and work respectively, with the values being greater for smooth platens. With the COV being so low in one case it is difficult to decide on any trend on the basis of only one comparison.

Conclusions about the behaviour of sandstone. With so many parameters considered and so few comparisons for each parameter available, the degree of confidence about the conclusions is low: the effect that rough or smooth platens or the effect of the orientation of testing is inconclusive. Based on the results in this study the sandstone seems to be weaker when saturated. There is an indication that the greater the diameter ratio of the hoop the more work is required to fail a sample, a fact that has been noticed also in marble. The effect that the bedding has on the behaviour of sandstone must be one totally influenced by material properties.

7.4 THE TERRA-TEK TESTING

This part of the experimental investigation has been conducted on the servo-controlled, Terra-Tek, system (5.1.1). As this comprised the preliminary stage of the investigation, the number of tests is small and the variability of test conditions is considerable. All the hoops used were cored from one sandstone block and belonged to size class II; the detailed measurements of these hoops together with the corresponding plots are presented in Appendix 7.5. The plots represent the mean stress vs displacement: the stress is called mean because it is calculated as the force acting on the total failure area of the hoop as shown in fig. 7.6a.

$$\sigma = \frac{F}{(OD - ID)\,H} \qquad (7.1)$$

The displacement is measured in four locations: two are measured at each side of the platen opening, and two at each central point of the expected location of fracture, on the sample (see fig. 5.2). Therefore, the results for each sample are plotted as mean stress vs each one of these four displacements. In most cases the two plots of stress vs displacement of platens on the sample are very similar to each other; the plots of stress vs displacement of platens are not always similar to each other because the platens sometimes rotated slightly before they opened in tension; these "anomalies" are reflected on the obtained plots.

The samples tested on the servo-controlled system consisted of: (a) five specimens tested with rough loading platens, four in dry and one in saturated condition, (b) two specimens tested with smooth loading platens one of each in dry and saturated condition and (c) three specimens which belonged to a series devoted to determine the location, on the stress-displacement curve, of the fracture initiation (5.1.1); the curves from these three samples are not complete, except for one, because the test was ended for the specimens to be X-rayed.

7.4.1 Quantitative interpretation of results

In the absence of a formula to calculate the tensile strength of a material in the hoop configuration (7.2.1), the acquired results from the testing on the Terra-Tek were interpreted in terms of mean stress and work as was done for the tests conducted on the GDS. The work was measured for three sections as shown in fig. 7.9.

Work$_{(i)}$ represents the area under the linear part of the curve.

Work$_{(ii)}$ represents the area from yield to maximum force applied during the experiment.

$\mathbf{Work}_{(iii)}$ represents the area from maximum force to the end of the test.

Because testing with this system enables the post peak component of the stress-displacement curve to be obtained, it was thought useful to compare the amount of work done prior to and after the maximum load sustainable by the sample;

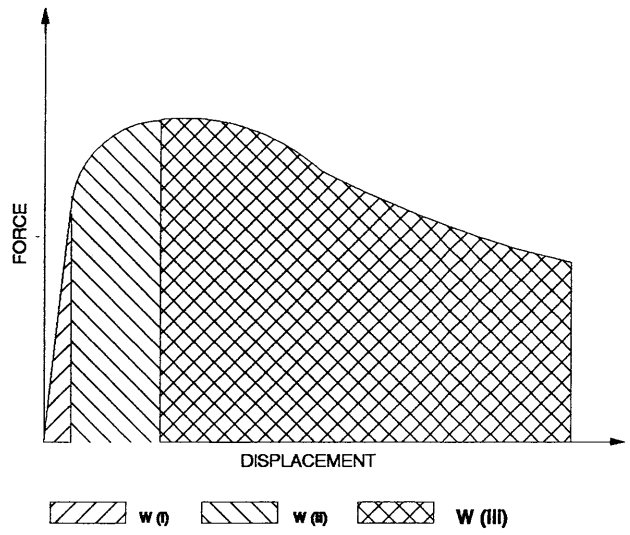


Fig. 7.9 A schematic representation of the suggested three variations of work, considered in the Terra-Tek testing.

therefore, $\text{Work}_{(i)}$ and $\text{Work}_{(ii)}$ were combined and the ratio of this to $\text{Work}_{(iii)}$ was calculated. The results as work, mean stress and ratio of pre-maximum and post-maximum work as well as the test conditions are presented in table 7.8.

It was noticed that the experiments conducted with the rough loading platens were not successful except one; they failed uncontrollably soon after they reach maximum stress, although the values of maximum stress are quite comparable among themselves.

Table 7.8 Results obtained from the closed loop servo-controlled, Terra-Tek testing system.

SAMPLE	CONDITION TESTED	MEAN STRESS MPa	WORK (i) x 10^{-4} Nm	WORK (ii) x 10^{-4} Nm	WORK (iii) x 10^{-4} Nm	RATIO OF WORK *
6a1	RD	0.56	132.95	1861.25		
6e1	RD	0.63	133.12	1597.44		
6c2	RD	0.63	122.08	2807.84	7080.64	0.41
6d2	RD	0.62	186.11	1240.72		
6f2	RS	0.38	154.22	616.86	3007.22	0.26
* 6f1	SS	0.32	135.71	1221.39	2985.68	0.45
6e2	SD	0.48	135.27	3111.26	6222.52	0.26
6c3	SD,X-R	0.49	122.62	1348.8		
6d3	SD,X-R	0.53	119.27	2623.98	2862.53	
* 6f3	SD,X-R	0.55	264.64	2646.4	8336.16	0.35

The work for the samples marked with * has been calculated on the basis of one stress vs sample displacement plot, the more "complete".

* = the work up to maximum stress/work from maximum stress to ultimate failure.

The values of the mean stress of the samples tested with rough loading platens have been considered together and the average and COV of these values has been calculated. The same was done for the samples tested with smooth loading platens and in a dry condition; the two samples tested in a saturated condition, one with rough and one with smooth loading platens, also have been considered in the same way. The results are presented in table 7.9

Table 7.9 A simplified table of results obtained from testing with the Terra-Tek.

CONDITION TESTED	NUMBER OF SAMPLES	STANDARD DEVIATION	AVERAGE	COV %
RD	4	0.03	0.61	9.56
SD	3	0.03	0.52	11.3
SS, RS	2	0.03	0.35	17.14

RD = rough dry, SD = smooth dry, SS = smooth saturated, RS = rough saturated.

7.5 CONCLUSIONS

From the above presented and analyzed experimental work it is clear that in the investigation of the performance of sandstone and marble in extension, one can consider two issues: (a) the ultimate strength of the materials, expressed as tensile strength in the Brazilian and Direct and tension tests and (b) the load vs deformation of the materials in extension, expressed as the force-displacement curves obtained for both porous sandstone and crystalline marble, in Hoop tests conducted on the Terra-Tek and GDS testing systems. The similarities and differences between the sample behaviour as revealed using these results and the contribution of the Hoop tension test to an understanding of the behaviour of rock in extension will now be considered.

7.5.1 Ultimate strength

The results from the tests conducted in extension, including BT, DTT, HTT and Fracture Toughness (due to the lack of material this test was conducted only on

sandstone), are summarised in composite tables 7.10(a) and 7.11(a) for marble and sandstone respectively. As is seen on these tables, the results acquired using the orientation of testing i.e Black and Green and the Smooth and Rough loading platens in the HTT has been preserved in the reporting. But as mentioned in the previous analysis (7.3.1 and 7.3.2) the effect that these two parameters have on the results is inconclusive; therefore, the division of results based on these parameters is here removed and for reasons of comparison these results are regrouped in tables 7.10(b) and 7.11(b) for marble and sandstone respectively. In addition, a third version of these tables (7.10c and 7.11c), contains a ratio of ultimate strength obtained from BT/DTT, BT/HTT, DTT/HTT and HTT/DTT for marble and sandstone. The values used to calculate these ratios are the mean values and those pertaining to HTT were considered per class (as class indicates the hoop size).

From the values presented in table 7.10(b) two observations made about marble previously (7.3.1) are reconfirmed, namely that the ultimate saturated strength is greater than the dry one and that the greater the hoop size the stronger the material seems to be, with one exception. The calculated ratios of ultimate strength among the various tension tests, show that the greatest values are obtained from BT/HTT with those of DTT/HTT, BT/DTT and HTT/DTT following in descending order: table 7.10(c).

Table 7.11(b) allows a reconfirmation of the previous conclusions that the dry sandstone seems to be stronger than the saturated one but only marginally so, and that the hoop size affects the strength of the material, i.e the greater the hoop size the stronger the material appears to be. The calculated ratios of the ultimate strength are highest for BT/HTT, with those obtained from BT/DTT and DTT/HTT following in descending order: table 7.11(c).

Table 7.10(a) Composite table of ultimate strength results on tension tests in marble.

TEST	OR/CL/CON		LOWER VALUES		UPPER VALUES		MEAN VALUES		STD DEV		COV %		No OF SAMPLES		UNIT
			DRY	SAT	DRY	SAT	DRY	SAT	DRY	SAT	DRY	SAT	DRY	SAT	
BT		GRN	6.37	6.34	7.77	10.1	7.04	8.34	0.49	1.34	13.9	32.1	5	5	MPa
		BLK	5.68	5.65	11.1	9.63	7.72	8.08	1.56	1.51	40.6	37.4	9	9	
DTT		GRN	2.04	-	5.09	-	3.64	-	1.24	-	75.9	-	8	-	MPa
		BLK	1.62	-	6.15	-	3.37	-	1.26	-	74.5	-	9	-	
HTT	I	BS	-	-	-	-	1.59	2.48	-	-	-	-	1	1	MPa
		GS	-	1.06	-	2.24	-	1.65	-	0.59	-	71.2	-	2	
		BS	-	-	-	-	-	-	-	-	-	-	-	-	
		GS	-	-	-	-	0.67	-	-	-	-	-	1	-	
	II	BS	-	-	-	-	1.33	-	-	-	-	-	1	-	
		BR	-	-	-	-	1.17	-	-	-	-	-	1	-	
		BR	-	-	-	-	-	1.62	-	-	-	-	-	1	
		GR	-	-	-	-	1.19	-	-	-	-	-	1	-	
		GR	-	-	-	-	-	1.67	-	-	-	-	-	1	
	III	BS	-	1.99	-	2.3	-	2.12	-	0.02	-	1.65	-	3	
		GS	-	-	-	-	1.45	-	-	-	-	-	-	1	
	IV	BR	-	1.10	-	1.13	-	1.12	-	0.02	-	3.14	-	2	
		GR	-	-	-	-	0.83	-	-	-	-	-	1	-	

OR/CL/CON = orientation/class/condition

Table 7.10(b) Simplified composite table of ultimate strength results on tension tests in marble.

TEST		LOWER VALUES		UPPER VALUES		MEAN VALUES		STD DEV		COV %		No OF SAMPLES		UNIT
		DRY	SAT	DRY	SAT	DRY	SAT	DRY	SAT	DRY	SAT	DRY	SAT	
BT		5.68	5.65	11.1	10.1	7.38	8.21	1.79	1.23	48.5	30.0	14	14	MPa
DTT		1.52	-	6.15	-	3.52	-	1.22	-	69.4	-	17	-	MPa
HTT	I	0.67	1.06	1.59	2.481.67	1.13	1.92	0.46	0.62	81.0	64.1	2	3	
	II	1.17	1.62	1.33	2.30	1.23	1.64	0.07	0.02	11.3	2.74	3	2	
GDS	III	-	1.99	-	1.13	1.45	2.12	-	0.13	-	12.5	1	3	MPa
	IV	-	1.10	-		0.83	1.12	-	0.02	-	3.14	1	2	

Class I = (150/30), 1:5
II = (150/50), 1:3
III = (100/30), 1:333
IV = (100/50), 1:2

Table 7.10(c) The ratios among the various tension tests in marble.

RATIO	CL	DRY	SAT	RATIO	CL	DRY	SAT
HTT/ DTT GDS	I	0.32	-	DTT/ HTT GDS	I	3.12	-
	II	0.35	-		II	2.86	-
	III	0.41	-		III	2.43	-
	IV	0.23	-		IV	4.26	-
BT/ DTT		2.10	-	BT/ HTT GDS	I	6.54	4.27
					II	6.00	5.00
					III	5.10	3.88
					IV	8.93	9.94

Table 7.11(a) Composite table of ultimate strength results on tension tests on sandstone.

TEST	OR/CL/CON		LOWER VALUE		UPPER VALUE		MEAN VALUE		STD DEV		COV %		No OF SAMPLES		UNIT
			DRY	SAT	DRY	SAT	DRY	SAT	DRY	SAT	DRY	SAT	DRY	SAT	
BT	GRN		3.46	3.01	4.9	3.65	4.34	3.31	0.47	0.21	21.7	12.7	5	5	MPa
	BLK		4.06	2.95	4.5	3.82	4.26	3.32	0.15	0.32	6.95	19.7	5	5	
DTT	GRN		0.87	0.95	1.2	1.23	1.07	1.12	0.13	0.05	23.6	8.5	5	6	MPa
	BLK		0.77	0.77	2.2	1.22	1.26	0.97	0.49	0.16	78.1	32.3	5	6	
HTT	I	BS	-	0.66	-	0.69	-	0.68	-	0.01	-	3.99	-	2	MPa
		BS	0.78	-	0.8	-	0.81	-	0.02	-	5.73	-	-	3	
		GS	-	-	-	-	0.84	-	-	-	-	-	-	1	
	II	BS	-	-	-	-	-	0.2	-	-	-	-	-	1	
		BR	-	-	-	-	0.52	-	-	-	-	-	1	-	
		GS	-	-	-	-	-	0.31	-	-	-	-	-	1	
		GR	-	0.37	-	0.42	-	0.39	-	0.02	-	12.1	-	2	
GDS	III	BS	-	0.46	-	0.58	-	0.51	-	0.05	-	19.7	-	3	
		BS	-	-	-	-	0.51	-	-	-	-	-	1	-	
		GS	-	-	-	-	0.59	-	-	-	-	-	1	-	
	IV	BS	0.34	-	0.4	-	0.36	-	0.02	-	11.4	-	2	-	
		BR	-	-	-	-	0.35	-	-	-	-	-	1	-	
		GR	-	0.25	-	0.32	-	0.29	-	0.03	-	20.2	-	4	
		GR	-	-	-	-	0.31	-	-	-	-	-	1	-	

TEST	OR/CL/CON		LOWER VALUE		UPPER VALUE		MEAN VALUE		STD DEV		COV %		No OF SAMPLES		UNIT
HTT	II	R	0.56	-	0.6	-	0.61	-	0.03	-	9.6	-	4	-	MPa
T-T		R	-	-	-	-	-	0.38	-	-	-	-	-	1	
		S	0.48	-	0.6	-	0.51	-	0.03	-	11.2	-	4	-	
		S	-	-	-	-	-	0.32	-	-	-	-	-	1	

T-T = Denotes Terra-Tek testing

Table 7.11(b) Simplified composite table of ultimate strength results on sandstone.

TEST		LOWER VALUE		UPPER VALUE		MEAN VALUE		STD DEV		COV %		No OF SAMPLES		UNIT
		DRY	SAT	DRY	SAT	DRY	SAT	DRY	SAT	DRY	SAT	DRY	SAT	
BT		3.46	2.95	4.85	3.82	4.30	3.32	0.35	0.27	16.30	16.29	10	10	MPa
DTT		0.77	0.77	2.19	1.23	1.17	1.05	0.37	0.15	63.67	28.42	10	12	MPa
HTT GDS	I	0.78	0.66	0.84	0.69	0.81	0.68	0.02	0.01	6.00	3.99	4	2	MPa
	II	-	0.20	-	0.42	0.52	0.32	-	0.08	-	50.17	1	4	
	II	0.51	0.46	0.59	0.58	0.55	0.51	0.04	0.05	14.58	19.72	2	3	
	IV	0.34	0.25	0.38	0.32	0.36	0.29	0.02	0.03	11.54	20.21	4	4	
T-T		0.48	0.32	0.63	0.38	0.56	0.35	0.06	0.03	20.19	17.14	8	2	MPa
FR T		0.15	-	0.35	-	0.23	-	0.07	-	61.27	-	6	-	

FR T= Fracture toughness measured in $MN/m^{1.5}$ T-T= Terra-Tek testing

Table 7.11c The ratios among the various tension tests on sandstone.

RATIO	CL	DRY	SAT	RATIO	CL	DRY	SAT
HTT/DTT GDS	I	0.70	0.65	BT/DTT	-	4.30	3.17
	II	0.44	0.31				
	III	0.47	0.49				
	IV	0.28	0.30				
HTT/DTT T-T	II	0.48	0.33	BT/HTT GDS	I	5.29	4.89
					II	8.34	10.26
					III	7.84	6.50
					IV	12.99	10.68
DTT/HTT GDS	I	1.43	1.54	BT/HTT T-T	II	7.68	9.48
	II	2.26	3.23				
	III	2.13	2.05				
	IV	3.52	3.37				
DTT/HTT T-T	II	2.08	2.99				

GDS = Testing with the GDS pressure controller
T-T = Testing with Terra-Tek.
CL = class, size of the hoop

Table 7.10(d). Illustration of the position of the ratios relative to each other and the difference of values of ultimate strength in crystalline and porous materials.

RATIOS	MARBLE		SANDSTONE	
	RANGE	DIFFERENCE	RANGE	DIFFERENCE
BT/HTT	5.1-8.43	3.83	5.29-13.0	7.71
DTT/HTT	2.43-4.26	1.83	1.43-3.52	2.09
BT/DTT	2.10		4.30	
HTT/DTT	0.23-0.41	0.18	0.28-0.70	0.42

Table 7.10(d) illustrates the position of the ratios to each other and the difference of values of ultimate strength that each records. The greatest difference by far occurs in the porous material and it is interesting to speculate why this should be. The porous sandstone will (a) have two fundamental differences to the marble i.e its pores will contain a variety of crack "tips" (as each pore becomes the end of the crack) having different radius of curvature and thus each pore will lead to a different microvalue of fracture toughness. (b) The strain energy that may be stored within the porous material will be located in the grains and their cement; as seen from chapter 5, failure in sandstone occurs in the cement and thus, the amount of stored energy available for release will be the smaller amount stored in the cement rather than the larger amount stored in the grains. It is therefore, not surprising to find that the porous material exhibits a large range of values in response to the test methods used, lithological variations not withstanding.

With the crystalline material fractures are obliged to travel along grain boundaries that are in atomic contact with their neighbour, and through grains via cleavage; thus, any stored energy within the crystalline material will be mobilized during failure. If the release of this energy is capable of overwhelming the progress of the test, eg as occurs in fast fracture, then the difference between samples tested might not be so great as in each test, by whatever method, the stored strain energy becomes the dominant factor in failing the sample rather than the test method being employed.

The other noticeable point about table 7.10(d) is how well the values obtained from the DTT and HTT compare when seen with the other ratios. This is not surprising because for the hoops tested the greater part of their failure surface lay in a zone of tension. Interestingly, area per area, the area of the DTT is within 80% of the area of the HTT of class IV , diameter ratio 1:2. The hoop test has many practical advantages over the DTT when it comes to testing particularly on matters of alignment and platen performance and the ratios shown in table 7.10(d) raise the interesting question of which test gives a better value of tensile

strength, bearing in mind that tensile strength is not a material property (Hudson, 1970), but a function of sample size and shape.

Thus, the conclusion of greatest potential significance concerning the ultimate strength of rock in extension seems to be that it is a parameter which may be very much influenced by stored strain energy and the way it is released, and the HTT seems to be very sensitive to it.

7.5.2 Load vs deformation in extension

Because the concept of ultimate strength values is, at the moment, of limited relevance, and the testing equipment enabled force-displacement curves to be obtained, the work done was measured in the Hoop tests and therefore failure described by this measure can be examined.

If one accepts that the initiation of failure starts at the appearance of the yield on the force-displacement curve, then the work required for this failure initiation can be calculated; furthermore, the work involved in the propagation of failure can also be measured.

The Terra-Tek equipment enabled some "complete" stress-displacement plots to be obtained and therefore the work involved to yield, (W_i), the work involved from this failure initiation to maximum stress, (W_{ii}) and from there to post-maximum, (W_{iii}), were measured (fig. 7.9). From table 7.8 it is clear that the work required for the initiation of failure is an order of magnitude smaller than the work required to propagate it; from the "complete" curves it is also seen that the work input required to bring the maximum stress to ultimate failure is at least twice that necessary to take the sample to its peak stress. The amount of this work is of course a function of the hoop size.

The Hoop tension test thus allows the work input required for the failure

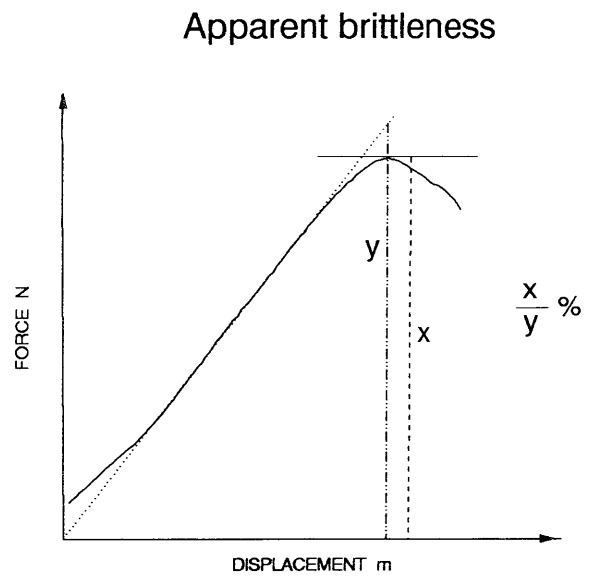
initiation, failure propagation and eventually catastrophical failure of the sample, to be quantified although the significance of these results are not yet fully understood.

The curves obtained from GDS are not as complete as the ones acquired from the Terra-Tek in relation to the post-peak behaviour, but a lot of pre-failure information can be extracted from them.

Considering that the investigation of the performance of rock in extension was conducted on two different materials, porous sandstone and crystalline marble, it is useful to examine the brittleness of these materials, their stiffness, the ratio of $Work_{(i)}$ / $Work_{(ii)}$ (see fig. 7.2) as well as the pre-failure and post-failure behaviour of the rocks and the way these attributes manifest themselves on the curves of load vs displacement.

(a) Apparent brittleness is introduced and schematically shown in fig. 7.10a; it represents the drop from the extended linear portion of the curve to the actual maximum force reached by the sample expressed as a percentage.
(b) Stiffness is expressed as the slope of the curve and is shown schematically in fig. 7.10b.
(c) The ratio of $W_{(i)}/W_{(ii)}$ expressed as a percentage; a comparison with $Work_{(iii)}$ is not always possible because, as mentioned earlier (7.4) the GDS curves did not always start from zero (see figures in A7.4).

The results of the above mentioned apparent brittleness, stiffness and ratio of work are presented below in tables 7.11(a) and 7.12(a) for marble and sandstone respectively; a summary of the results is presented in tables 7.11(b) and 7.12(b) respectively for marble and sandstone.



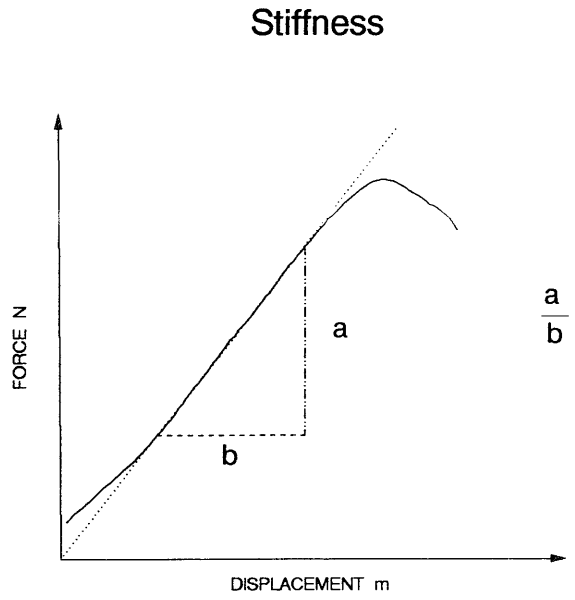


Fig. 7.10 Schematic representation of apparent brittleness and stiffness of marble and sandstone tested with the GDS system.

Table 7.12(a) Results of apparent brittleness, stiffness and ratio of work on marble

CL	CON	SAMPLE	APPARENT BRITTLENESS	STIFFNESS	$W_{(i)}/W_{(ii)}$
I	DRY	M1	100	0.82	46.43
		M3	98	0.88	47.39
	SAT	M2	100	1.02	47.38
		M4	100	0.97	50.90
		M5	98	0.92	54.52
II	DRY	M1	99	2.1	46.7
		M3	99	2.1	69.3
		M5	100	2.0	63.8
	SAT	M2	100	2.0	60.6
		M4	100	1.9	60.8
III	DRY	M7	98.3	0.96	57.6
	SAT	M8	98	0.87	69.23
		M10	100	0.99	63.82
		M11	100	0.95	59.16
IV	DRY	M3	98	1.5	33.79
	SAT	M2	99	1.8	40.74
		M4	100	1.7	51.48

CON = Condition of testing, CL = Class, hoop size, SAT = Saturated

Table 7.13(a) Results of apparent brittleness, stiffness and ratio of work on sandstone.

CL	CON	SAMPLE	APPARENT BRITTLENESS	STIFFNESS	$W_{(i)}/W_{(ii)}$
I	DRY	11 2A	99	1.0	68.1
		11 2C	99	1.0	68.9
		11 1A	99	1.0	
		11 1C	97	1.0	79.5
	SAT	11 2B	99	0.99	81.6
		11 1B	97	1.1	65.2
II	DRY	10 4B	93	1.5	61.5
	SAT	10 4A	92	1.4	62.6
		10 4C	91	0.8	33.3
		10 5A	93	1.4	57.1
III	DRY	10 7B	98	0.84	56.0
		10 7C	96	0.98	51.4
	SAT	10 6A	93	0.89	51.7
		10 6B	97	0.80	64.5
		10 7B	95	0.70	54.6
IV	DRY	10 1A	94	0.73	29.3
		10 1C	91	0.99	48.4
		10 2C	87	1.04	48.4
		10 3A	93	0.97	31.3
	SAT	10 1B	92	0.82	38.0
		10 2B	91	1.02	50.7
		10 3B	92	0.92	44.2
		10 3C	92	0.94	48.0

CON= Condition of testing, CL= Class, hoop size, SAT= Saturated.

An examination of the respective tables for marble reveals that its apparent brittleness is higher in the saturated samples of all hoop sizes. The ratio of work is also greater for the saturated samples of all classes. The stiffness though does not follow the same pattern; the mean values of dry and saturated samples differ very little among them and the samples of class II have higher stiffness in dry condition whereas the samples of class I and class IV present the opposite situation.

Table 7.12(b) A summary of results of table 7. 12(a) for marble with mean values, Std. Dev. and COV.

QUALITY	CL	LOWER VALUE		UPPER VALUE		MEAN VALUE		STD DEV		COV %		No OF SAMPLES	
		DRY	SAT	DRY	SAT	DRY	SAT	DRY	SAT	DRY	SAT	DRY	SAT
APP BRIT	I	98	98	100	100	99	99.33	1	0.94	2.02	1.90	2	3
	II	99	100	100	100	99.33	100	0.47	0	0.94	0	3	2
	III	-	98	-	100	98.3	99.33	-	0.94	-	1.90	1	3
	IV	-	99	-	100	98	99.5	-	0.5	-	1.00	1	2
STIF	I	0.82	0.92	0.88	1.02	0.85	0.97	0.03	0.04	7.02	8.42	2	3
	II	2.00	1.9	2.1	2.00	2.07	1.95	0.05	0.05	4.55	5.13	3	2
	III	-	0.87	-	0.99	0.96	0.94	-	0.05	-	10.6	1	3
	IV	-	1.7	-	1.8	1.5	1.75	-	0.05	-	5.71	1	2
$W_{(i)}/W_{(ii)}$	I	46.43	47.38	47.39	54.52	46.91	50.93	0.48	2.91	2.05	11.5	2	3
	II	46.7	60.6	69.3	60.8	59.93	60.7	9.62	0.1	32.1	0.33	3	2
	III	-	59.16	-	69.23	57.6	64.07	-	4.11	-	12.8	1	3
	IV	-	10.74	-	51.48	33.79	46.11	-	5.37	-	23.3	1	2

APP BRIT = apparent brittleness, STIF = stiffness

When only one sample was tested in a given condition and therefore no lower or upper value were available, the result for that sample was entered into the "Mean value" column; this can be seen also in the "No of samples" column as well where the number 1 stands.

Table 7.13(b) A summary of results of table 7.13(a) for sandstone with mean values, Std. Dev. and COV.

QUALITY	CL	LOWER VALUE		UPPER VALUE		MEAN VALUE		STD DEV		COV %		No OF SAMPLES	
		DRY	SAT	DRY	SAT	DRY	SAT	DRY	SAT	DRY	SAT	DRY	SAT
APP BRIT	I	97	97	99	99	98.5	98	0.87	1	1.76	2.04	4	2
	II	-	91	-	93	93	92	-	0.71	-	1.54	1	4
	III	96	93	98	97	97	95	1	1.63	2.06	3.44	2	3
	IV	87	91	94	92	91.25	91.75	2.68	0.43	5.88	0.94	4	4
STIF	I	1	0.99	1	1.1	1	1.05	0	0.06	0	10.5	4	2
	II	-	0.8	-	1.4	1.5	1.23	-	0.25	-	40.6	1	4
	III	0.84	0.70	0.98	0.89	0.91	0.80	0.07	0.08	15.4	19.4	2	3
	IV	0.73	0.82	1.04	1.02	0.93	0.93	0.12	0.07	25.7	15.4	4	4
$W_{(i)}/W_{(ii)}$	I	63.0	65.2	79.5	81.6	69.88	73.4	6.00	8.2	17.2	22.3	4	2
	II	-	33.3	-	62.6	61.5	47.63	-	12.5	-	52.4	1	4
	III	51.4	51.7	56.0	64.5	53.7	56.93	2.3	5.47	8.57	19.3	2	3
	IV	29.3	38.0	48.4	50.7	39.35	45.23	9.08	4.77	46.1	21.1	4	4

APP BRIT= Apparent brittleness, STIF= Stiffness, CL= Class, hoop size.

When only one sample was tested in a given testing condition (either dry or saturated) and therefore no lower and upper value are available, the result was entered in the "mean value" column; this can be seen also in the "No of samples" column where the number 1 stands.

The tables relevant to sandstone show that the apparent brittleness of sandstone is higher in dry samples except those of class IV where the values are approximately the same. It is worth noting that samples of class I feature values very close to those characterizing marble and are higher than the rest of sandstone samples; the reader is reminded that these samples have been prepared from the same block, which is different from the one from which the other samples have been cored. The values obtained from the rest of the samples reveal, in general, lower numbers of apparent brittleness. The ratio of work is higher for saturated samples except for those of class II where the opposite is true. The values of stiffness pertaining to dry and saturated samples are very similar to each other and hence no conclusion can be drawn that either dry or saturated samples are stiffer.

A comparison of values obtained from marble and sandstone shows that the apparent brittleness of marble is higher than that of sandstone, an observation which is also clear from the plots (A7.3 and A7.4) and the way the material fails. The stiffness, generally, seems also to be higher in marble. The comparison among the mean values of ratio of work indicate that the dry sandstone possesses higher values than the dry marble, while for the saturated rocks the opposite is valid except for specimens of class II.

Table 7.13(c) Range of values and their differences for apparent brittleness, stiffness and ratio of work $W_{(i)}/W_{(ii)}$.

QUALITY	MARBLE		SANDSTONE	
	RANGE	DIFFERENCE	RANGE	DIFFERENCE
APP BRIT	98-100	2	91-99	8
STIF	0.87-2.0	1.13	0.7-1.4	0.7
W_i/W_{ii}	10.7-69.2	58.5	33.3-81.6	48.3

Table 7.13(c) illustrates the range of values of apparent brittleness (APP BRIT), stiffness (STIF) and the ratio of work (i) to work (ii) (W_i/W_{ii}), obtained and their differences; once again it can be seen that the crystalline material cannot be controlled as easily as the porous material and the differences in apparent

brittleness are much smaller than in porous material, not withstanding sample differences. Furthermore, although the work required to propagate a failure (W_i/W_{ii}), shows differences which are greater for crystalline material than for porous material, the work required to propagate a fracture through porous material seems to be consistently greater than that required for crystalline material, i.e the porous material requires work to be put into it to propagate a failure whereas the crystalline material seems to have reserves of stored strain energy sufficient to do the work of crack propagation for it.

It seems quite clear that in terms of load-deformation in extension the Hoop tension test has advantages over the Direct tension test and other tests in the ease with which load-deformation data can be obtained, the experimental arrangement being unaffected by such problems as the adhesion between platens and specimen in a DTT and the lack of uniformity in deformation occurring within the sample of a DTT.

(d) Pre-failure behaviour. The sandstone curves obtained from the GDS testing can clearly be divided into two groups: The first group is represented by the curves of samples belonging to class I and have been prepared from block 11. The displacement increases linearly at an identical slope (stiffness) for the dry samples and with minor variations to this slope for the saturated samples; a very short gradual increase to non-linearity (yield) is abruptly interrupted by the sample failure for both the dry and saturated samples (fig 7.11a). The second group of sandstone samples is represented by the samples of class II, III and IV which have been prepared from the same block. These curves do not appear to be characterized by a consistent stiffness neither within the dry or saturated groups of samples. The non-linear part of the curve is generally longer than that shown by the samples prepared from block 11 (fig.7.11b and figures in A7.2)

The pre-failure behaviour of marble seems more eventful; there are exceptions to the smooth linear displacement increase; in samples of all classes some curves

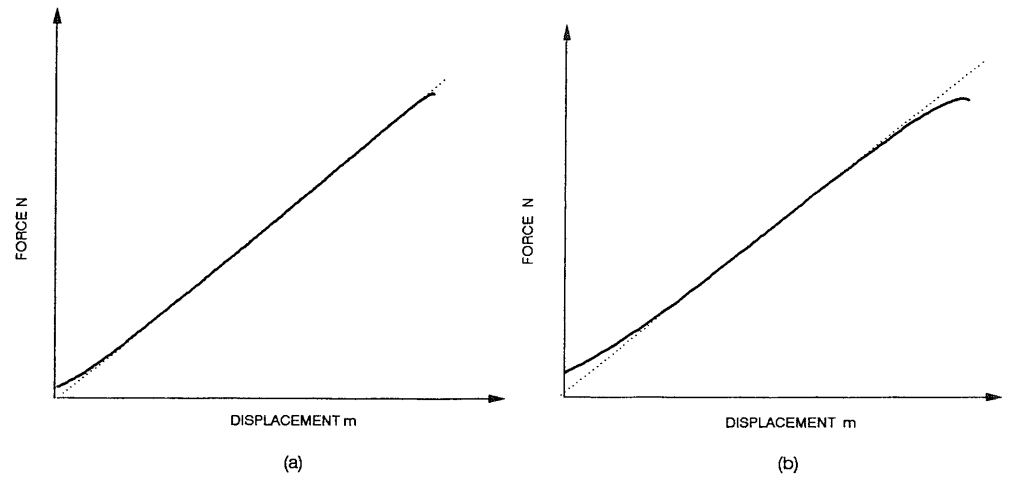


Fig. 7.11 Diagram showing the pre-failure behaviour of sandstone: (a) shows the short yield before failure and (b) the more gradual yield before failure.

display a "pop-in" which is a sudden crack extension and arrest (fig.7.12a and A7.3) probably caused by a failure along grain boundaries that coincide with cleavage. Some curves extend linearly and seem to follow a concave path before failure (fig.7.12b), and in one particular case (sample M4 class II) the curve possesses a peculiar form as shown in fig.7.12c; two more samples (M3 and M5 of class IV, A7.3) show a big drop in force before they continue increasing until failure. The yield part on the marble curves is almost absent, the failure is quite brittle.

(e) Post-peak behaviour. In general, sandstone curves contain some post-peak element except the ones of relatively high brittleness. The shape of the post-peak element is either comparable with the yield part of the curve (almost like a mirror image) or it is quite steep. The curve of sample 10 1b, class IV seems to lower naturally after it reached the maximum and then again continued to rise (A7.2).

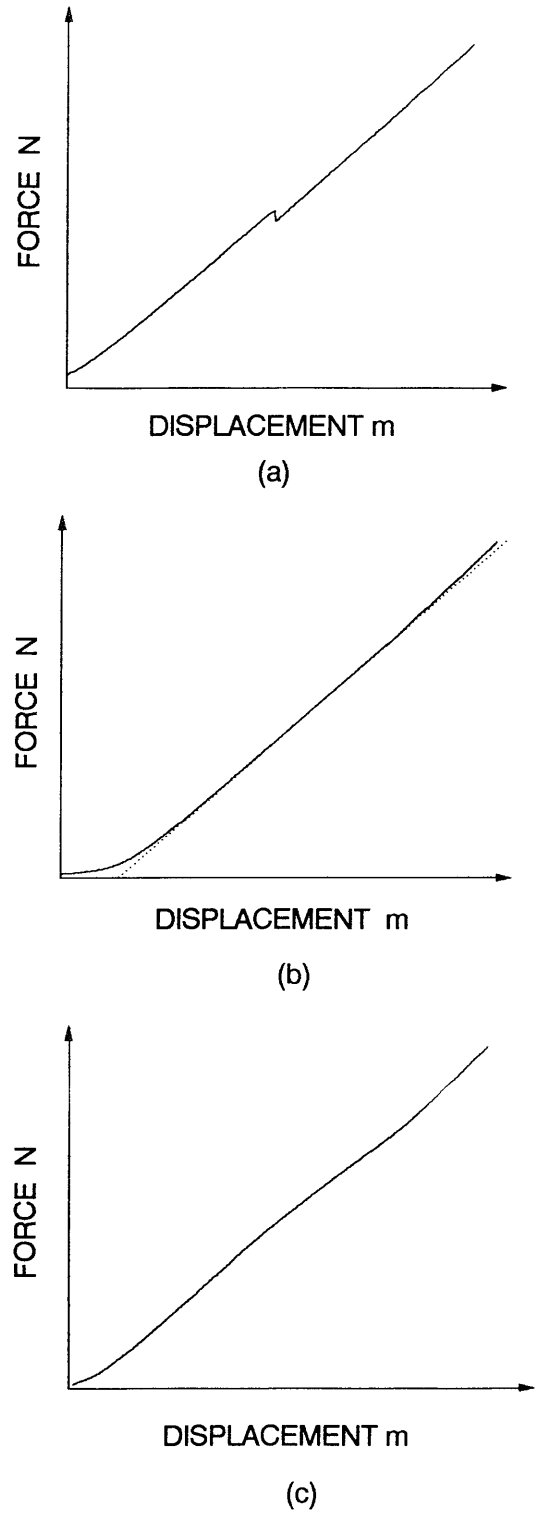


Fig. 7.12 Diagrams showing the pre-failure behaviour of marble: (a) illustrates the "pop-in", (b) the concave upwards shape of the displacement and (c) the peculiar form that the curve obtained sometimes.

The marble does not show any post-peak behaviour as it failed very quickly without the GDS testing response time being able to cope.

All the above discussion is evidence of the sensitive behaviour of material in extension, which has made it difficult to interpret results obtained from rock specimens which have been assessed visually for their similarity, based on experience which comes from failure in compression.

There is no doubt that the HTT enables the behaviour of rock in extension to be easily investigated, and this is an area which requires much more investigation before it is fully understood and compared with the compressional behaviour of rock, with which we are more familiar. It is of utmost importance to mention that until a knowledge of the mechanisms of failure in extension is achieved attempts to model rock failure in direct or indirect tension are not justified. Without an understanding of physical mechanisms, statistical and finite element models become abstract and complex as they are adapted to account for all the available data.

Had the sensitivity of failure of rock in extension, coupled with the sensitivity of the hoop tension test, been suspected at the time the specimens were collected and prepared a rather different process of selection would have been used and a different programme of testing would have been followed.

Far greater use would have been made of geophysical characterization of the samples tested because it would have been appreciated that appearance, under close inspection, and indices based on compression, would be insufficient. Secondly, samples would have been nested more closely to avoid problems with lithological variations which have created uncertainty; eg. the hoops for the HTT would have been close to samples destined for DTT etc. Thirdly, a far more restrictive testing programme would have been adopted because from any one block sufficient samples could be obtained to support only limited test options.

PART FOUR

This part is devoted solely to conclusions concerning the soundness of the Hoop tension test for investigating behaviour of rock in extension, the observed behaviour of rock in extension including the different behaviour of porous and crystalline materials and suggestions for future research.

CHAPTER EIGHT

CONCLUSIONS

8.0 Introduction

At the onset of this research two objectives were defined: to improve an understanding of the Hoop tension test, to an extent that would allow this to become the method for investigating the extensional behaviour of rock, and to apply this tension test to investigate the behaviour of rock in extension.

What has been achieved in relation to the set objectives in the course of this research has been analyzed in the preceding chapters in parts II and III. In these concluding remarks the results and findings which enabled the HTT, and its application to testing rock specimens, to be viewed with confidence, as well as the actual behaviour of these rocks in extension will be summarised.

8.1 SOUNDNESS OF THE HOOP TENSION TEST FOR INVESTIGATING THE BEHAVIOUR OF ROCK IN EXTENSION

The analyses which resulted from the Mathematical, Finite Element and Photoelastic investigations about the hoop reveal that there are clearly tensile and compressive regions in the hoop of dimensions tested. Neither the photoelastic experiments nor the FEM, which until recently was in its infancy for the hoop, gave clear or definite enough information about the behaviour of the hoop at the locations which lie 90° to the platen opening i.e along the load line; nevertheless, it was apparent that there was a compressive region on the load line because of the way with which the platens open when loaded. Further studies currently in progress, (Park, D. PhD thesis in preparation), using the PC based COSMOS program have shown that indeed there exist compressive stresses in the hoop at the locations which are adjacent to the platens and at a certain point these

compressive stresses pass through an isotropic point and cross over to become tensile. The compressive and tensile regions in the hoop, therefore, schematically resemble the diagram of fig. 8.1: compression is in the Y direction.

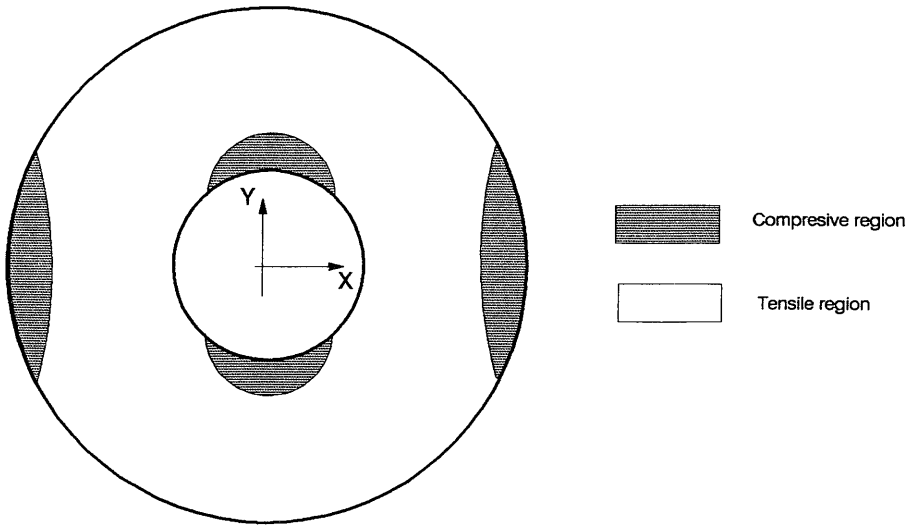


Fig. 8.1 Diagrammatic representation of the tensile and compressive regions in the hoop.

Therefore, theoretically, there exists enough evidence for the test to be confident in the belief that the stresses in the hoop are dominated by tension and that the predominant displacements are extensional. The Holographic and SEM studies have shown experimentally that the fracture initiates and propagates opposite the platen opening, at the location where the maximum tensile stresses prevail. Careful examination of the fracture faces of failed rock specimens indicate that the failure is tensile. Consequently, there cannot be any doubt about the Hoop tension test providing a value of the ultimate strength of the hoop in extension.

The advantages of the HTT over other traditional methods used for tensile testing are several: ease of specimen preparation and easy alignment, absence of adhesive bonding which may corrupt the deformation behaviour of a specimen, ability of the hoop to accommodate the testing of intrinsic mechanical anisotropy such as

bedding, schistosity and tectonically induced mineral fabric, and the ease to test relative to direction of in-situ stresses. It is interesting to mention that the HTT has been used in France by the BRGM (internal report 623 RP BRG 90-016) to test schists. In these experiments it was verified how useful and how sensitive the HTT may prove to be in measuring the ultimate strength of material in extension, relevant to inherent anisotropy of rock. In addition the HTT enables the study of stiffness of the rock in extension in any chosen direction. This is possible because the curves obtained provide the load and displacement values. From the same curves the work required to induce failure in extension in any chosen direction, as a substitute at the moment for tensile stress because it cannot yet confidently be defined for reasons mentioned earlier, can easily be obtained. If these advantages of the HTT are coupled with the confidence originating from the theoretical and experimental investigations of the hoop about the location and mode of failure of the sample, then the value of the HTT in measuring the ultimate strength of material in extension becomes clear. The only shortcoming of the test is that, to date, the theoretical studies have not provided the means to relate the load applied (to induce failure) to the maximum tensile stress which obviously causes the failure of the specimen to occur. Studies on this topic are continued by others.

8.2 OBSERVED BEHAVIOUR OF THE ROCK IN EXTENSION

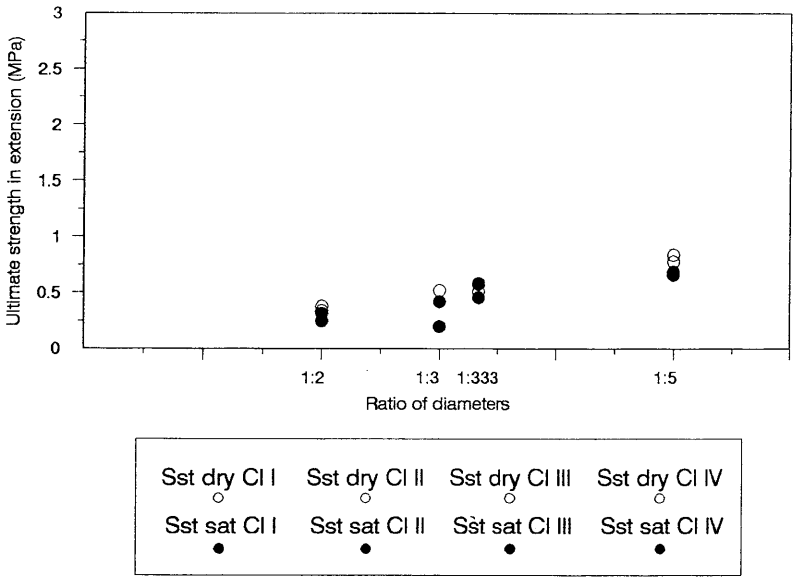
Our experience with rock testing is that gained from the tests which generate compression; what appears to be a uniform material in compression is not so in extension. This is important because it implies that our concept of rock behaviour is significantly incomplete. The tests carried out in the course of this research aimed to contribute to our knowledge of how rock behaves in extension.

The ultimate strength of material in tension is much lower than that of compression. This is seen from the values of UCS where the average value for dry sandstone is ≈51 MPa whereas the ultimate strength of the dry sandstone

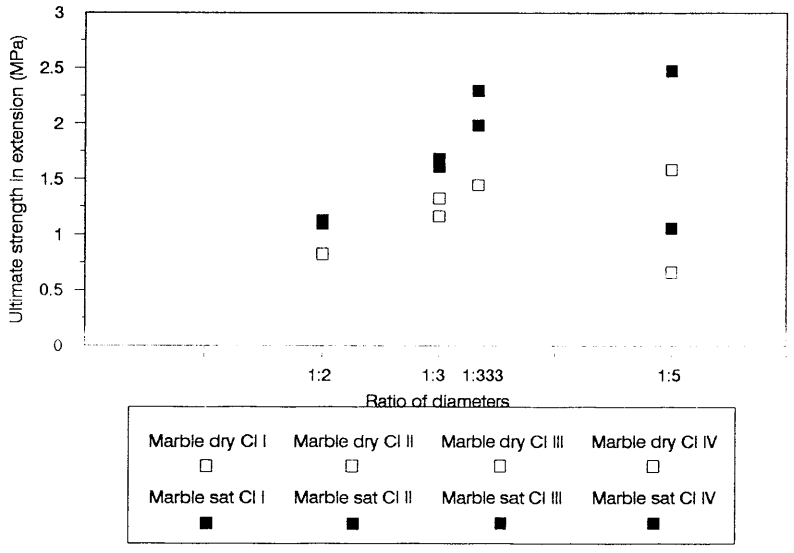
≈1.2 MPa; the same values for saturated sandstone is ≈46 MPa, 0.45 MPa and ≈1 MPa for UCS, ultimate strength in extension and DTT respectively. The dry marble values are ≈86 MPa, ≈1 MPa and ≈3 MPa for UCS, ultimate strength in extension from the HTT and DTT respectively; the values for saturated marble obtained from UCS and HTT tests are ≈77 MPa and ≈2 MPa respectively. The Young's modulus of elasticity measured in dry sandstone cores prepared to be tested parallel to bedding was ≈46 GPa in compression and ≈11 GPa in tension. It is worth mentioning that the dynamic Young's modulus measured in dry sandstone was ≈11 GPa. The differences in the values measured in compression and tension are considerable. It is important to mention here that E values measured in compression are quite routinely adopted in numerical modelling to investigate situations where the rock behaves in extension; it is clear, in view of the considerable difference between the values of E measured in compression and in extension, that this practice has to be reconsidered.

The speed of testing is an influential factor on the results of ultimate strength of rock in extension. Our investigations have shown that fast testing yielded high values, but as the rate of loading slowed down, the results for ultimate strength exhibited a tendency to stabilize; an indication that the test tends to become less sensitive to the speed of testing beyond a certain limit.

The influence of saturation on the rock specimens tested exhibits some unusual results. The sandstone becomes weaker when saturated, as illustrated by the results of UCS and HTT, although the extensional results show only a marginal difference between the dry and saturated samples (fig. 8.2a). However, the results obtained from marble using the HTT exhibit the opposite (fig. 8.2b), although those obtained from the UCS tests are as expected i.e the saturated marble is weaker than the dry. The explanations of negative pressures and surface tensions in the minute flaws of marble are thought to be the explanation to this strange behaviour.



(a)



(b)

Fig. 8.2 Plots of ultimate strength of material in extension vs ratio of diameters of (a) saturated and dry sandstone and (b) marble to illustrate the range of difference between the saturated and dry results, as well as the range of difference within results obtained from the same testing conditions. The plots also show the strength of the rocks in relation to hoop dimensions.

The ratio between the inner and outer diameter of the hoop has an influence on the ultimate strength of the hoop. This influence is the same for the porous sandstone and crystalline marble (fig. 8.2). It is clear that in the HTT the smaller the ratio of diameters the weaker the material appears to be; this is logical since the path that the fracture has to travel is shorter. In the porous material there is a smaller difference in the ultimate strength among the classes of hoops tested than in the crystalline material. The results obtained from the same class of hoops which have been tested in the same conditions from sandstone exhibit a very good correlation; the same is valid for the marble samples except for those that belong to class I (1:5)

8.3 DIFFERENCES BETWEEN CRYSTALLINE AND POROUS ROCKS

The failure in marble and sandstone was expressed in quite different manner. Perhaps the most important difference and one from which other expressions of non-similarity among the two materials originate, is the way that the stored strain energy is released. In the sandstone this energy is likely to be present in both the grains and cement: as SEM investigations have shown the fracture propagates mainly in the cement which (volume for volume with grains) is likely to possess a smaller amount of stored strain energy. This smaller amount of energy is easier to control during testing and hence the sandstone exhibits smaller values of apparent brittleness. Because this smaller amount of stored energy cannot sustain the fracture propagation, once it has been initiated, a greater amount of work is required to provide for this task. On the other hand, marble, being a crystalline material of very low porosity is likely to possess a greater amount of stored strain energy in its crystals, which are in contact with each other. When a fracture initiates and propagates through marble, it does so along grain boundaries and via cleavage faces, as seen in the SEM micrographs. When the fracture propagates a considerable amount of stored energy could be released, which may overwhelm the test, which in turn becomes difficult to control. This may be a reason why the apparent brittleness is high; the amount of work required to provide the fracture

with the appropriate amount of energy to propagate is not so great, in comparison with sandstone, because the grains themselves provide part of this energy.

In general, both in compression and in extension, marble appears to be "stronger" than sandstone. Of course the strength of a porous rock lie in the quality of grains and cement, the state of weathering and porosity among other factors. The sandstone used in this research, as described in detail in chapter six, consists of quartz grains, is cemented by the same material, its porosity is not high and it is unweathered, being freshly quarried. Marble, consists of calcite, which is a soft mineral, which has been metamorphosed, meaning that it has been exposed to high temperatures and pressures that have welded the grains together and possibly provided the stored energy. This stored energy which is likely to be present in the crystals of marble requires an equally great amount of work to be input to separate these grains and initiate a fracture, and once a fracture is initiated the amount of stored energy which is released is proportionally high and able, with little help, to sustain the propagation.

8.4 FUTURE WORK

In conclusion to this research, a few suggestions for continuing the investigations on the Hoop tension test are presented.

To define a way to connect the load applied to induce failure with the maximum tensile stress acting opposite the platen opening, which presumably is the cause for fracture initiation, is of paramount importance. Investigations are continuing towards this direction using FEM.

Up to now the analysis has been two-dimensional because this was the simplest way to start the theoretical explorations but, in view of the thickness of the hoop specimens, it will be more realistic to adopt a three-dimensional analysis.

Concurrently with the theoretical studies a few parameters must experimentally be investigated in more detail than has been done in the course of this research (or have not been investigated at all).

(i) The effect of parallelism has not been investigated in the present research; the maximum angle with the horizontal is reported for each hoop specimen for future use. This probably will be best examined in a combination of 3-dimensional FE model and experimental work.*

(ii) The thickness of the hoop is another parameter that has not been contemplated; this also will be better explored in a combination of FE modelling with experimental verification in a three-dimensional analysis.*

(iii) The rate of loading can be investigated further; the range of each rate must be kept at a small interval so as to establish that rate at which the experiment becomes less sensitive to the rate of loading.*

(iv) A closer study of diameter ratios must be conducted; this will be enormously helped by a numerical model simulation, because initial studies have shown that there may be an optimum diameter ratio where the compressive region at the outer part of the hoop, opposite the platen opening, ceases to exist (H.Park, PhD. thesis in preparation, University of London, 1993).*

(v) The HTT can be used to study more closely the behaviour of crystalline and porous rocks of all types, including soluble rocks such as limestones and evaporites.

(vi) It may be interesting to investigate the fracture propagation with mineral fluids i.e simulate the genesis of a natural fracture.

(vii) It would also be possible to study the effect of different fluid chemistries on fracture propagation.

*** Note:** A programme of study for points (i) to (iv) is presented as a supplement on p352 to p359.

REFERENCES

Adams, M. and Sines, G. 1978 "Crack extension from flaws in a brittle material subjected to compression" *Tectonophysics*, **49**, 97-118.

Alder, H.L., Roessler, E.B. 1977 "*Introduction to probability and statistics*" 6th ed.

Arthuton, R.S. Wadge, A.J. "Country around Penrith" *Geological survey of Great Britain, England and Wales.*

Atkinson, B.K. and Meredith, P.G. 1989 "The theory of subcritical crack growth with applications to minerals and rocks" *"Fracture Mechanics of Rock"* ed. by Atkinson,B.K. Academic Press Ltd.

Attewell, P.B. and Farmer, I.W. 1976 "*Principles of Engineering Geology*" Chapman & Hall.

Aufmuth, R.E. and Alezka, J.C., 1976 "Scanning Electron Microscope Investigation of Statically Loaded Foundation Materials", *Bulletin of the Assoc. of Engineering Geologists*, **XIII**, (2) 137-150.

Barber, D.J. and Meredith, P.G. 1990 (edited by), "*Deformation Processes in Minerals, Ceramics and Rocks*", Publ. by Union Hyman.

Bell, F.G. 1983 "*Fundamentals of Engineering Geology*", Butterworths.

Bieniawski, Z.T. 1972 "Propagation of Brittle Fracture in Rock", *10th Symposium Rock Mechanics*, A.I.M.E, New York, 409-427.

Bieniawski, Z.T. 1967 "Mechanisms of brittle fracture of rock: "Part 1 "Theory of the fracture process" *Int. J. Rock Mech. Min. Sci. & Geomech. Abstr.*, **4** 395-406.

Bieniawski, Z.T. 1967 "Mechanisms of brittle fracture of rock: Part II "Experimental studies" *Int. J. Rock Mech. Min. Sci. & Geomech. Abstr.* **4** 407-423.

Bieniawski, Z.T. 1967 "Mechanisms of brittle fracture of rock: Part III "Fracture in tension and long-term loading" *Int. J. Rock Mech. Min. Sci. & Geomech. Abstr.* **4** 425-430.

Boresi, A.P., Sidebottom, O.M., Seely, F.B., Smith. J.O. 1978 "*Advanced*

Mechanics of Materials" 3rd Ed., John Wiley and Sons.

Brown, E.T. 1987 (editor) "Rock characterization Testing and Monitoring" *ISRM Suggested methods*. Pergamon press.

Bruno, M.S. and Nakagawa, F.M. 1991 "Pore Pressure Influence on Fracture Propagation in Sedimentary Rock" *Int. J. Rock Mech. Min. Sci. & Geomech. Abstr.* **28, 4** 261-273.

British Standards Institute, BS 5930, 1981 "Code of Practice for Site Investigations" (formerly CP200L).

Burdekin, F.M. and Stone, D.E.W., 1966 "The crack opening displacement approach to fracture mechanics" *Yielding, Journal of Strain Analysis*, **1** 145-153.

Carpinteri, A.J. 1982 *J. Struct. Div. ASME* **108** ST4 833-848.

Coker, E.G., Filon, L.N.G., Jessop, H.T.A. 1974 "*Treatise on photoelasticity*" Cambridge University Press.

Colback, P.S.B and Wild, B.L. 1965 "The influence of moisture content on the compressive strength of rock" *Proc. 3rd Canadian Symposium on Rock Mechanics*, Toronto.

COSMOS (Version 1.52) Finite Element System, developed by Structural Research and Analysis Corporation, Santa Monica, California, U.S.A.

Dawes, M.G. 1980 "The COD design curve" *Advances in Elasto-Plastic Fracture Mechanics*" ed. Larsson, L.H. Applied Science Publishers, London, 279-300.

De La Cruz,R.V. 1978 "Modified Borehole Jack Method for Elastic Property Determination in Rocks" *Int. J. Rock Mech. Min. Sci. & Geomech., Abstr.* **10** 221-239.

Dugdale, D.C. 1960 *J. Mech. Phys. Solids* **8** 100-104.

Ebdon, D. 1985 *"Statistics in geography"* 2nd edition, Blackwell.

Einstein, H.H., Dershowitz,W.S. 1990 "Tensile and shear fields - a view" *Engineering Geology*, **29** 149-172.

Ennos, A.E. and Virdee, M.S. 1982 "Application of reflection Holography to deformation measurement problems" *Experimental Mechanics* **22** 202-209.

Ewalds, H.L. and Wanhill, R.J.H. 1986 "*Fracture Mechanics*" Co publication

Edward Arnold and Delftse Uitgevers Maatschappij 3rd imprint . First published 1984.

Fairhurst, C. "On the validity of the Brazilian test for brittle materials" *Int. J. Rock Mech. Min. Sci. & Geomech. Abstr.* **1** 535-546.

Farmer, I.W. 1983 "*Engineering Behaviour of Rocks*" 2nd ed., Chapman & Hall.

Fyfe, W., Price, N.J. and Thompson, A.B. 1978 "*Fluids in the Earth's crust*" Amsterdam, Elsevier.

Goodman, R.E., Van, K.T., and Heuzé, F.E. 1968 "Basic and Applied Rock Mechanics" Chapter 19 523-543 *Proc.10th Symposium on Rock Mechanics,* University of Texas, Austin.

Griffith, A.A. 1924 "The theory of rupture" *Proc.1st International Congress for Applied Mechanics.* Delft, 53-63 Addison Wesley publishing Company.

Hardy, M.P., Hudson, J.A. and Fairhurst, C. 1973 "The failure of rock beams Part I-Theoretical studies" *Int. J. Rock Mech. Min. Sci. & Geomech. Abstr.* **10** 53-67.

Hartog, den J.P. 1952 "*Advanced Strength of Materials*" McGraw Hill Book Company.

Hecht, E. 1987 "*Optics*" 2nd ed.

Hoek, E. 1964 "Fracture of Anisotropic Rock" *Journal of South African Inst. of Min. Metall.* **64** (10) 510-518.

Howarth, D.F. 1987 "The effect of pre-existing microcavities on mechanical rock performance in sedimentary and crystalline rocks" *Int. J. Rock Mech. Min. Sci. & Geomech. Abstr.* **24**, (4) 223-233.

Hudson, J.A. 1970 "A critical examination of indirect tensile strength tests for brittle rocks" *PhD thesis, University of Minessota.*

Hudson, J.A., Hardy, M.P and Fairhurst, C. 1973 "The failure of rock beams Part II-Experimental studies" *Int. J. Rock Mech. Min. Sci. & Geomech. Abstr.* **10** 69-82.

Hutchinson, J.W. 1979 "*Non Linear Elastic Fracture Mechanics*" Technical Univ. of Denmark, Department of Solid Mechanics, Copenhagen.

Hustrulid, W.A. 1976 "An analysis of the Goodman Jack" *19th U.S. Symp. on*

Rock Mech. **10** 221-239.

Ingraffea, A.R. 1987 "Theory of crack initiation and propagation in rock" in "*Fracture mechanics of Rock*" ed. by Atkinson,B.K. academic press.

Ingraffea, A.R. and Gerstle, W.,Gergely, P. and Saouma, V.J. 1984 *Struct. Div. ASCE,* **110**, 881-890.

Ingraffea, A.R., and Gerstle, W. 1984 "*Application of fracture mechanics to cementitious composites*" ed.by Shah,S.P. Martinus Nijhoff, The Hague, 171-209.

Irwin, G.R. 1958 "*Fracture encyclopedia of Physics*" ed. by S. Fluge Springer Verlag, Berlin 551-589.

Irwin, G.R. 1960 "Plastic zone near a crack and Fracture Toughness" *7th Sagamore Conference* Paper IV-63.

ISRM Commission on Testing Methods 1988 Suggested Methods for Determining the Fracture Toughness *Int. J. Rock Mech. Min. Sci. and Geomech. Abstr.*, 25 (2) 73-96.

Jaeger, J.C. and Cook, N.G.W. 1976 "*Fundamentals of Rock Mechanics*" 2nd ed.

Jaeger, J.C. and Hoskins, E.P. 1966 "Stresses and Failure in Rings Loaded in Diametral Tension or Compression" *Brit. Jour. of Appl. Phys.* **17** 685-692.

Jessop, H. and Harris, F.C. 1960 "*Photoelasticity: Principles and Methods*", Dover Publications Inc. New York.

John, S.J., Al-Samahiji, D.C., de Freitas, M.H., Cosgrove, J.W., Clarke, B.A., Loe,N., Tang,H. 1991, "Stress analysis of a unidirectionally loaded hoop specimen *"Proc. 7th International Congress on Rock Mechanics*, 513-518 Aachen, Germany.

Jones, R. and Wykes, C. 1983 "*Holographic and Speckle Interferometry*" Cambridge University Press.

Jöreskog, K.G., Klovan, J.E. and Reyment, R.A. 1976 "*Geological Factor Analysis*".

King, M.S. 1970 "Static and dynamic elastic moduli of rocks under pressure. *Proc. 11th U.S Symposium on Rock Mech.* 329-351 Berkeley .

King, M.S. 1983 "Static and dynamic elastic properties of rocks from the

Canadian shield" *Int. J. Rock Mech. & Geomech. Abstr.* **20** 237-241.

Koch Jr., G.S. and Link, R.F. 1971 "*Statistical Analysis for Geological Data*"

Kranz, R.L. 1979 "Crack-crack and crack-pore interactions in stressed graphite" *Int.J.Rock Mech. Min. Sci. & Geomech. Abstr.* **16** 37-47.

Kuske, A. and Robertson, G. 1974 "*Photo-elastic Stress Analysis*" Publ. by J.Wiley and Sons.

Labuz. J.F., Shah, S.P., Dowding, C.H. 1985 "Experimental Analysis of crack propagation in graphite" *Int. J. Rock Mech. & Geomech. Abstr.* **22** (2), 85-98.

Lajtai, E.Z., Carter, B.J. and Ayari, M.L. 1989 "The fracture of rocks and the science of Fracture Mechanics" *Int. J. Rock Mech. Min. Sci.& Geomech. Abstr.*

Lama, R.D. and Vutukuri, V.S. 1978 (1st print) "*Handbook on Mechanical Properties of Rocks*", **II** Transtech Publications.

Laqueche, H., Rouseau, A., Valentin, G. 1986 "Crack propagation under Mode I and II loading in slate schist" *Int. J. Rock Min. Sci. & Geomech. Abstr.* **23** (5) 347-354.

Leifer, I., McKenzie, W.M.C., Leask, J.D. 1990 "Holographic interferometry, a novel experimental technique for the testing of brickwork" *Proc. 9th International conference on Experimental Mechanics,* Copenhagen, **4** 1551-1563.

Ljunggren, C., **Amadei, B. and Stephansson, O.,** 1988 "Use of the Hoek and Brown failure criterion to determine in-situ stresses from hydraulic fracturing measurements" 133-142, *CARE (Conference on Applied Rock Engineering)* The Institution of Mining and Metallurgy and the Department of Mining Engineering, University of Newcastle upon Tyne.

Shuzo Takemoto ed. 1989 "Laser Holography in Geophysics" John Wiley and Sons.

Maji, A.K. and Wang, J.L. 1992 "Experimental study of fracture processes in Rock" *Rock Mechanics and Rock Engineering* **25** 25-47.

Matsuki, K., Hasibuan, S.S. and Takahashi, H. 1991 "Specimen Requirements for Determining the Inherent Fracture Toughness of Rocks According to ISRM Suggested Methods" *Int. J. Rock Min. Sci. & Geomech. Abstr.* **28** (5) 365-374.

McLintock, F.A. and Irwin, G.R. 1965 "Plasticity aspects of fracture toughness testing and its applications" *ASTM* STP **381** 84-113 Philadelphia.

McClintock, F.A. and Walsh, J.B. "Friction on Griffith cracks in rock under pressure" *Proc. 4th U.S. Nat.Congr. Appl. Mech.* University of California, Berkeley (CA).

Millmore, S.and Allsop, J.A. 1978 "A qualitative investigation of holographic interferometry techniques applied to the measurement of the general displacement field" *Strain* **14** 106-111.

Olsson, W.A. and Peng, S.S 1976 "Microcrack nucleation in marble" *Int. J. Rock Mech. Min. Sci. & Geomech. Abstr.* **13** 53-59.

Ostle, B. 1963 *"Statistics in Research"* 2nd ed. Iowa State University Press.

Park, H. 1993, *PhD. thesis* in preparation, provisional title "Behaviour of rock in extension".

Peng, S. 1975 "A note on the fracture propagation and time dependent behaviour of rocks in uniaxial compression" *Int. J. Rock Mech. Min. Sci.& Geomech. Abstr.* **12** 125-127.

Peterson, P.E. "Crack growth and development of fracture zones in plain concrete and similar materials" *Report TVBM-1006, Div. of Build. Lund Institute of Tech., Sweden.*

Ramsay, J.G. and Huber, M.I. 1983 *"The techniques of Modern Structural geology"* **1** *"Strain analysis"* Academic press.

Price, N.J. and Cosgrove, J.W. 1990 *"Analysis of Geological Structures"* Cambridge University Press.

Pollard, D.D. and Aydin, A. 1988 *"Progress in understanding jointing over the past century"* Geological Society of America Bulletin 100 1181-1204

Pollard, D.D. and Segall, P. "Theoretical displacements and stresses near fractures in rock: with applications to faults, joints, veins, dikes and solution surfaces" *"Fracture Mechanics of Rock"* 1987 ed. by Atkinson,B.K. Academic Press Inc. (London) Ltd.

Rice, J.R., Sorensen, E.P. "Continuing crack tip deformation for plain strain crack growth in elastic-plastic solids." *Journal of Mechanics and Physics of*

Solids **26** 163-186.

Roberts, A., Hawkes, I. 1963 "The determination of in-situ stress and strain using photoelastic techniques" *"Principles in the field of Geomechanics"* 14th Symposium of the Austrian Regional Group of the International Society for Rock Mechanics Salzburg ed. by Müller in cooperation with Fairhurst,C.

Sangha, G.M., Talbot, G.J., Dhir, R.K. 1974 "Microfracturing of a sandstone in uniaxial compression" *Int. J. Rock Mech. Min. Sci & Geomech. Abstr.* **11** 139-150.

Scholle, P. 1979 "A colour illustrated guide to constituents, textures, cements, porosities of sandstone and associated rocks" *AAPG memoir 2Y U.S. Geological Survey.*

Schuhann, W. and Dubas, M. 1979 *"Holographic Interferometry"*, Springer-Verlag Berlin Heidelberg New York.

Secor, D. "Mechanics of natural extension functioning at depth in the Earth's crust". *Geol. Surv.* Paper Can., Pap. **68** 52.

Shell Tallus Oils. 2nd ed.1967, *Shell International Petroleum Company.*

Sprunt, E.S. and Brace, W.F. 1974 "Direct observations of microcavities in crystalline rocks" *Int. J.Rock Mech. Min. Sci.& Geomech. Abstr.* **11** 139-150.

Stewart, I. and Monaghan, B.G., 1988 "Hydraulic Fracturing stress measurements at two sides in Leicestershire, United Kingdom" *CARE (Conference on Applied Rock Engineering)*, 221-233. The Institute of Mining and Metallurgy and the Department of Mining Engineering, University of Newcastle upon Tyne.

Taiju Tsuboi 1989 "Optical principles of holographic interferometry" *"Laser Holography in Geophysics"* Ed. by S.Takemoto John Wiley and Sons.

Takemoto, S. 1986 "Application of laser holographic techniques to investigate crustal deformation *Nature* **322** 49-51.

Tapponier, P. and Brace, W.F. 1976 "Development of stress-induced microcracks in Westerley granites" *Int.J.Rock Mech. Min. Sci. & Geomech. Abstr.* **13** 103-112.

Tovey, N.K. 1978 "A scanning electron microscope study of the liquefaction

potential of sand grains" *"Scanning Electron Microscopy in the study of sediments, a symposium"* ed. by Whalley,W.B. Geo Abstracts England.

Timoshenko, S.P., Goodier, J.N. *"Theory of Elasticity"* 3rd edition McGraw Hill International editions.

Xu,S., de Freitas, M.H. and Clarke, B.A. 1988 "The measurement of tensile strength of rock" *Proc. of the ISRM Symposium Rock Mechanics and Power Plants* Madrid Spain 125-132.

Waugh "A preliminary electron microscope study of the development of authigenic silica diagenesis in the Penrith sandstone. *Proc. Yorkshire Geol. Soc.* **35** 59-69.

Waugh "Petrology, provenance and silica diagenesis of the Penrith sandstone (Lower Permian) of North-West England *J. Sediment. Petrol.* **40** 1226-1240.

Wells, A.A. 1962 "Unstable crack propagation in metals:damage and fast fracture" *Proc. of the crack propagation Symposium* Granfield, The College of Aeronautics **1** 210-230.

Welton, J.E. 1984 *SEM Petrology Atlas* Chevron Oil Field Research Co. Pub.by AAPG Tulsa Oklahoma.

Yamada, S.E., Schatz J.F., Abou-Sayed, Jones, A.H. 1981 "Elasto-plastic behaviour of porous rocks under undrained conditions" *Int. J. Rock Mech. Min. Sci. & Geomech. Abstr.* **18** 177-179.

APPENDIX TO CHAPTER FIVE

In this appendix some basic information about laser light is given.

In addition a short account of the principles of Holographic Interferometry are highlighted so as to compliment the information given in chapter 5.

Finally the mathematical analysis, adopted by I.Leifer et al, and used for this research, is presented.

Laser Amplification by Stimulated Emission of Radiation

Each atom (as in solid, liquid and gas) is composed of a nucleus and electron cloud and possesses a certain amount of internal energy; each atom tends to maintain its lowest energy configuration known as the **ground state.** Each atom can also exist in well-defined configurations corresponding to higher energies than the ground state; these states are called the **excited states.**

In a conventional light source, such as the tungsten lamp, energy is pumped into the reacting atoms within the filament, a fact that raises these atoms into excited states. Each atom then drops back spontaneously to the ground state, emitting the absorbed energy in the form of a randomly directed photon. Atoms in this kind of source radiate essentially independently; the photons in the emitted stream bear no phase relationship with each other and the light is incoherent varying in phase from point to point and from moment to moment.

If an incident photon impinges on an atomic system and is energetic enough it may be absorbed by an atom thus raising it to an excited state. As early as 1917 Einstein pointed out that an excited atom can revert to a lower state through photon emission via two distinctive mechanisms: in one instance the atom emits energy spontaneously, while in the other the emission is triggered by the presence of electromagnetic radiation of the proper frequency. This process is known as **stimulated emission** and is the key to the operation of the LASER. In both situations the emerging photon carries off the energy difference ($h\mu_{if}$) between the initial state ε(i) and the final state ε(f).

$$h\mu_{if} = \epsilon_i - \epsilon_f \qquad \text{(A5.1)}$$

(where $_i$ and $_f$ are energies of initial and final state respectively).

For an incident electromagnetic wave to trigger an excited atom into stimulated emission, it must have frequency μ_{if}. A remarkable feature of this process is that

the emitted photon is in phase with, has the polarization of, and propagates in the same direction as the stimulating radiation. Thus, the emitted photon is said to be in the same radiation mode as the incident wave and tends to add to it increasing its flux density.

However, since most of the atoms are ordinarily in the ground state, stimulated emission is less likely. But if population inversion is to take place, a process by which a substantial percentage of the atoms can somehow be excited into an upper state leaving the lower state empty, then an incident photon of the proper frequency can trigger an avalanche of stimulated photons all in phase. The initial wave of stimulated photons will continue to build as long as there are no dominant competitive processes, such as scattering, and provided the population inversion can be maintained. In effect if energy is supplied to sustain the population inversion a beam of light can be extracted after sweeping across the active medium.

Speckle effect. An observation about laser light is that it has a granular appearance on reflection from a diffuse surface. The spatially coherent light scattered from such a surface fills the surrounding region with a stationary interference pattern.

The detailed explanation of the principle of Holographic Interferometry.

Holographic Interferometry is a linear process in time and is based on two or more optical waves that can be recorded and then reconstructed simultaneously, resulting in an interferogram. Therefore, the sum, difference, or even time average of a sequence of waves can be formed. For example, at some time t_1 an unstressed holographic system can be used to reconstruct an optical wave whose complex amplitude in the hologram plane is $U_{1(x,y)}$. At time t_2 a second wave, $U_{2(x,y)}$, from the same but now stressed system can be recorded on the same photographic plate. The process is simply holographic double exposure; the plate

is first exposed to $U_{1(x,y)}$ together with a reference wave $U_{R(x,y)}$ and then to $U_{2(x,y)}$ together with $U_{R(x,y)}$. When the hologram formed by developing this plate is illuminated by $U_{R(x,y)}$, the complex amplitude of the reconstructed wave will be proportional to

$$[U_{1(x,y)} + U_{2(x,y)}] \tag{A5.2}$$

and the irradiance will be proportional to

$$I_{(x,y)} = [U_{1(x,y)} + U_{2(x,y)}]^2 \tag{A5.3}$$

In applications to interferometry, $U_1 = U_{0(x,y)}$ represents the light scattered or transmitted to the hologram plane by some object and $U_2 = U'_{0(x,y)}$ represents light from the same object after it has been slightly deformed or changed in some manner. Slight deformation or changes of the object primarily affect the phase of U'_0, thus

$$U_{0(x,y)} = a_{(x,y)} \exp[-i\phi_{(x,y)}] \tag{A5.4}$$

and

$$U_{0(x,y)} = a_{(x,y)} \exp\{-i[\phi_{(x,y)} + \delta\phi_{(x,y)}]\} \tag{A5.5}$$

The irradiance of the reconstructed wave from equation (A5.4) becomes

$$I_{(x,y)} = |a_{(x,y)} \exp\{-i[\phi_{(x,y)} + \delta\Phi_{(x,y)}]\}|^2 = 2a^{2(x,y)}\{1 + \cos[\delta\phi_{(x,} \tag{A5.6}$$

where:

$2|a_{(x,y)}|^2$ - represents the light from the image of the object

$[-i\Phi_{(x,y)}]$ - describes the fringes

$\delta\Phi_{(x,y)}$ - is the change in optical phase due to the change in object position

between exposures.

$a_{(x,y,z)}$ - real amplitude of the light wave.

$\Phi_{(x,y,z)}$ - phase of the light wave.

$\delta\Phi$ - difference in phase of light wave.

i - angle of incidence.

Equation (A5.6) represents the irradiance of the object modulated by a fringe pattern.

Note: The analysis refers to fig. 5.6 in chapter 5.

Dark fringes are contours of constant values of $\delta\Phi$ which are odd-integer multiples of π. Bright fringes are contours of constant values of $\delta\Phi$ which are even-integer multiples of π. In various applications $\delta\Phi$may be related to physical qualities such as displacement, rotation, strain, bending moment, vibrational concentration, electron density or stress.

The uniqueness of holographic interferometry for many applications is based on the following key properties:

(i) High information content

(ii) Division of amplitude in time

(iii) Permanent recording of events

(iv) Temporal filtering

The information content of holograms can be sufficiently high to permit the recording and reconstruction of fine details of a complicated wave with great fidelity. A permanent record of optical waves is extremely useful for the study of transient events. Holographic interferograms can be recorded instantaneously and studied later by reconstruction. Temporal filtering refers to the formation of interferograms representing one temporal frequency component of a time-varying wave.

Interferograms have a fine structure which is a speckle pattern. The speckles in the region of dark fringes are, on the average, darker than those in regions recognised as bright fringes. The speckle pattern conveys information about the displacement and deformation of the object between exposures. Localisation occurs where $U_{0(x,y,z)}$ and $U'_{0(x,y,z)}$ are most closely matched. At such locations the corresponding speckle patterns I_0 and I'_0 nearly match and overlap, and U_0 and U'_0 differ only by a large scale variation in phase. This position can be found if it is specified that the phase difference for light scattered by P and P' must be equal to that for all the neighbouring corresponding points such as M and M' (M and M' are points on an object in the unstressed and stressed states respectively).

Speckle is not possible to eliminate from the interferograms for the following reasons: (i) If the object is deformed between exposures, strain caused by the change in the microscopic contour of the surface, deforms the scattered waves in such a way that U_0 and U'_0 do not match precisely even at locations where the fringes are localised.

(ii) The finite viewing aperture will sample slightly different portions of the waves leaving the neighbourhood of P and P' and hence U_0 and U'_0 will not match perfectly in the image. This effect causes an apparent decrease in fringe visibility at large strains.

(iii) Light is always scattered by the grains in the photographic emulsion in which the hologram is recorded.

Mathematical analysis of the Single Beam Reflection Holographic Interferometry used in this research.

The analysis can be conducted if a point P on the surface of the object is considered, which undergoes displacement d, due to deformation between two exposures of the reflection interferogram. It is assumed that the displacement is small enough for the illumination and viewing angles to be considered unchanged for the displaced image of P (P'). Point P is illuminated by laser from a direction

ID, which makes angles α, γ and θ with the plane axes X, Y, and Z respectively and when viewed from viewing angles V_1, V_2 and V_3 makes angles β_i, ε_i and ϕ_i (i=1-3) with the three axes (fig 5.8)

Displacement d, has components u, v and w in the X, Y and Z directions respectively. The path difference, Δ, for the original and displaced points P and P' respectively, with unit illumination vector K_I and unit viewing vector K_V is given by

$$\Delta = d(K_I - K_V) = \eta\lambda \qquad \text{(A5.7)}$$

where η=fringe order and λ=wave length

Another useful variation of the above equation is given by Millmore and Allsopp:

$$\eta\lambda = u(\cos\alpha + \cos\beta) + v(\cos\gamma + \cos\epsilon) + w(\cos\theta + w\cos\phi) \qquad \text{(A5.8)}$$

For viewing direction V_1 (Fig. 5.8a)

$$\eta_1\lambda = u(\cos\alpha + \cos\beta) + v(\cos\gamma + \cos\epsilon_1) + w(\cos\theta + \cos\phi_1) \qquad \text{(A5.9)}$$

but $\beta=\pi-\alpha$, $\varepsilon_1=\pi-\gamma$ and $\eta_1=\theta$

therefore,

$$\eta_1\lambda = w(2\cos\theta) \qquad \text{(A5.9a)}$$

$$w = \eta_1 \frac{\lambda}{2\cos\theta} \qquad \text{(A5.9b)}$$

For viewing direction V_2 (Fig. 5.8b) $\beta_2=\alpha$, $\varepsilon_2=\pi-\gamma$ $\phi_2=\theta$

therefore,

$$\eta_2\lambda = 2u\cos\alpha + 2w\cos\theta \qquad \text{(A5.10)}$$

and by substituting w from equation (A5.9b)

$$u = \frac{\lambda(\eta_2 - \eta_1)}{2\cos\alpha} \qquad \text{(A5.11)}$$

In the same way, the displacement component v for viewing direction V_3 is determined, where $\beta_3=\pi-\alpha$, $\varepsilon_3=\gamma$, $\phi_3=\theta$ and therefore

$$\eta_3\lambda = 2v\cos\gamma + 2w\cos\theta \qquad \text{(A5.12)}$$

and by substituting w from equation (A5.9b)

$$v = \frac{\lambda(\eta_3 - \eta_1)}{2\cos\gamma} \qquad \text{(A5.13)}$$

where η_1, η_2, and η_3 are the fringe orders at point P for viewing directions V_1, V_2 and V_3 respectively.

Thus the three components of displacement (w, u, v) of point P can be determined; but, whereas the u and v displacement components of in-planes X-Z and Y-Z respectively can be determined by simply counting fringes between the different viewing directions, the out-of-plane displacement w, can only be determined if a zero order fringe is observed (η_1).

Consider a point P' as the position of point P which has undergone displacement d' with displacement components w', u' and v'. The displacement components can be determined by

$$w' = \frac{\eta_1' \lambda}{2\cos\theta} \tag{A5.14}$$

$$u' = \frac{\lambda (\eta_2' - \eta_1')}{2\cos\alpha} \tag{A5.15}$$

$$v' = \frac{\lambda (\eta_3' - \eta_1')}{2\cos\gamma} \tag{A5.16}$$

where η'_1, η'_2 and η'_3 are the fringe orders for P' for viewing directions V_1, V_2 and V_3 respectively.

Deducing the displacement components of P' from the displacement components of P

$$w - w' = \frac{\lambda (\eta_1 - \eta_1')}{2\cos\theta} \tag{A5.17}$$

$$u - u' = \frac{\lambda [(\eta_2 - \eta_2') - (\eta_1 - \eta_1')]}{2\cos\alpha} \tag{A5.18}$$

$$v - v' = \frac{\lambda [(\eta_3 - \eta_3') - (\eta_1 - \eta_1')]}{2\cos\gamma} \tag{A5.19}$$

where, $(\eta_1-\eta_1')$, $(\eta_2-\eta_2')$ and $(\eta_3-\eta_3')$ are the number of fringes counted from P to P' as viewed from V_1, V_2, and V_3 respectively.

If P and P' are separated by x and y in the X and Y directions respectively, the x-component of the average strain between P and P' is given by equation

$$\frac{u-u'}{x} = \frac{\lambda\left[(\eta_2-\eta_2')-(\eta_1-\eta_1')\right]}{2x\cos\alpha} \qquad \text{(A5.20)}$$

and the Y-component of the average strain between P and P' is given by equation

$$\frac{v-v'}{y} = \frac{\lambda\left[(\eta_3-\eta_3')-(\eta_1-\eta_1')\right]}{2y\cos\gamma} \qquad \text{(A5.21)}$$

Above, it has been demonstrated how with this technique we are able to determine the three components of relative displacement and the two components of the in-plane strain, by counting fringes between P and P' in the three viewing directions V_1, V_2 and V_3.

Note: The above analysis refers to fig. 5.7 in chapter 5.

APPENDIX TO CHAPTER SIX

This appendix contains information about the physical and mechanical characteristics of sandstone and marble.

Table A6.1a contains information on the tests conducted for the determination of bulk density, dry density and porosity of sandstone.
Table A6.1b contains the measurements of the sandstone cores, drilled at different angles to the bedding, and used for the determination of the longitudinal (P) waves and the transverse (S) waves. Table A6.1c contains the results of the tests conducted on the P and S waves.
Table A6.1d contains the measurements of the cores, drilled in the "black" and "green" directions, and used for the tests on the dynamic elastic moduli. Tables A6.1e and A6.1f contain the results of the tests on E_{dyn} and P_{dyn} on oven dry and saturated sandstone respectively.

Tables A6.1g and A6.1h contain the results of the tests conducted for the determination of the unconfined compressive strength (UCS) on oven dry and saturated sandstone respectively.

Table A6.2a contains the results of tests used for the determination of bulk density, dry density and porosity of marble. Table A6.2b contains the measurements of cores used for the determination of the elastic moduli of marble. Tables A6.2c and A6.2d contain the results of the tests for the determination of E_{dyn} and P_{dyn} on oven dry and saturated marble respectively. Tables A6.2e and A6.2f contain the results of the tests conducted to determine the UCS of oven dry and saturated marble respectively.

The calibration conducted for the AVERY and ESH frame machines prior to testing for the DTT and BT are also included.

Table A6.1a Tests for the characterization of sandstone

SAMPLE No	CONTAINER + SAMPLE A g	CONTAINER + SAMPLE DRY B g	CONTAINER EMPTY C g	MASS OF SOLIDS M_s=B-C g	MASS OF WATER M_w=A-B g	MASS SUBMERGED (sam+cont) D g	MASS OF CONTAINER SUBMERGED E g
6e3	153.21	152.61	8.02	144.59	0.60	347.30	257.40
6e4	143.38	142.14	7.91	134.23	1.24	341.16	257.40
6e1	149.89	149.38	8.05	141.33	0.51	345.26	257.40
6c2	150.57	150.45	8.08	142.37	0.12	345.92	257.40
6c3	160.20	159.92	7.89	152.03	0.28	351.92	257.40
6c4	155.52	155.12	7.90	147.22	0.40	348.96	257.40
5a1	155.02	154.27	8.00	146.27	0.75	348.37	257.40
5a2	154.66	154.19	7.98	146.21	0.47	348.35	257.40
5a3	155.84	155.54	7.89	147.65	0.30	349.23	257.40
5a4	157.49	157.32	7.99	149.33	0.17	350.30	257.40

Table A6.1a(cont.) Tests for the characterization of sandstone

SAMPLE No	MASS OF SAMPLE SUBMERGED M_{sub}=D-E g	MASS SATURATED g	BULK VOLUME cm_3	BULK DENSITY g/cm_3	DRY DENSITY g/cm_3	VOLUME OF VOIDS cm_3	POROSITY %
6e3	89.90	153.28	63.57	2.28	2.27	8.71	13.70
6e4	83.76	142.89	59.30	2.28	2.26	8.69	14.65
6c1	87.86	150.07	62.39	2.27	2.26	8.77	14.05
6c2	88.52	150.46	62.12	2.29	2.29	8.11	13.06
6c3	94.52	160.44	66.11	2.30	2.30	8.44	12.76
6c4	91.56	156.20	64.83	2.28	2.27	9.01	13.89
5a1	90.97	155.11	64.33	2.29	2.27	8.87	13.78
5a2	90.95	155.12	64.36	2.28	2.27	8.94	13.89
5a3	91.83	156.49	64.85	2.28	2.28	8.87	13.67
5a4	92.90	157.70	64.99	2.30	2.30	8.39	12.92

The water temperature at the time of the experiment was 25.5 C°; the water density at this temperature = 0.997078

Table A6. 1b. Details of cores used for the measurement of longitudinal (P) waves and transversed sound (S) waves.

Sample No	Parallelism α°	Height m	Diameter m	Mass Kg	Volume x10^{-5} m3	Density Kg/m^3
$\perp_{\text{to bed}}$1	0.005	0.0766	0.0378	0.1948	8.5961 1	2266.1
2	0.002	0.0753	0.0378	0.1922	8.4839 9	2265.4
3	0.003	0.0760	0.0379	0.193	8.5739 7	2250.9
4	0.002	0.0759	0.0378	0.192	8.5175 6	2254.2
5	0.002	0.0764	0.0380	0.194	8.6646 4	2238.9
6	0.004	0.0770	0.0378	0.1964	8.6410 0	2272.9
//$_{\text{to bed}}$1	0.008	0.0744	0.0377	0.1886	8.3051 1	2270.8
2	0.005	0.0740	0.0377	0.1892	8.2604 6	2290.4
3	0.002	0.0749	0.0375	0.1898	8.2724 5	2294.4
4	0.002	0.0745	0.0375	0.1894	8.2282 7	2301.8
5	0.0003	0.075	0.0375	0.1909	8.2834 9	2304.5
6	0.003	0.0757	0.0377	0.1935	8.4502 3	2289.8
45°to bed.1	0.001	0.0747	0.0377	0.1893	8.3386 0	2270.2
2	0.0008	0.0748	0.0378	0.1895	8.3941 2	2257.5
3	0.0003	0.0742	0.0377	0.1888	8.2827 8	2279.4
4	0.0005	0.0750	0.0376	0.1909	8.3277 3	2292.3
5	0.001	0.0755	0.0376	0.1918	8.3832 5	2287.9
6	0.008	0.0764	0.0375	0.1915	8.4381 2	2269.5

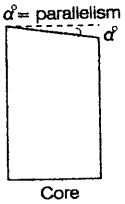


Table 6.1c. P and S wave velocity measured on oven dry sandstone.

Sample	Arrival time P μs	Arrival time S μs	Δt_P μs	Δt_S μs	Vel. V_P m/s	Vel. V_S m/s
$\perp$ 1	33.625	51.125	28.12	42.56	2724	1800
2	38.00	55.0	32.5	46.44	2317	1622
3	38.00	52.75	32.5	44.19	2338	1720
4	43.87	60.87	38.38	52.31	1978	1451
5	32.63	51.88	27.12	43.31	2817	1764
6	44.00	66.75	38.5	58.19	2000	1323
// 1	36.00	52.38	30.5	43.81	2439	1698
2	36.88	57.0	31.38	48.44	2359	1528
3	37.38	59.25	31.88	50.69	2350	1478
4	36.25	56.75	30.75	48.19	2423	1546
5	35.75	54.5	30.25	45.94	2479	1633
6	37.75	57.25	32.25	48.69	2347	1555
at 45°	43.87	60.5	38.38	51.94	1947	1438
2	40.12	56.5	34.63	47.94	2160	1560
3	38.0	55.75	32.5	47.19	2283	1572
4	41.25	59.38	35.75	50.82	2098	1476
5	41.25	57.75	35.75	49.19	2112	1535
6	45.13	65.63	39.63	57.06	1928	1339

"Zero arrival times" for S, $t_0 = 8.5625\ \mu s$ and for P, $t_0 = 5.5\ \mu s$; these values are deducted from the total time, hence $\Delta t = t - t_0$

Table A6. 1d. Details of sandstone cores used for the measurement of E_{dyn} and Poisson's ratio.

SAMPLE No	PARALLELISM	HEIGHT	DIAMETER	VOLUME	MASS DRY	DENSITY DRY	MASS SATURATED	DENSITY SATURATED
	α°	m	m	$x10^{-5}$ m^3	Kg	Kg/m^3	Kg	Kg/m^3
BLK 1	0.0030	0.0760	0.0374	8.349	0.1884	2,257.1	0.19940	2,388.3
BLK 2	0.0008	0.0760	0.0372	8.260	0.1843	2,231.2	0.19612	2,374.3
BLK 3	0.0050	0.0765	0.0373	8.359	0.1896	2,267.9	0.20048	2,398.4
BLK 4	0.0759	0.0759	0.0372	8.249	0.1884	2,284.4	0.19934	2,416.5
BLK 5	0.0020	0.0760	0.0373	8.305	0.1887	2,272.8	0.19969	2,404.5
BLK 6	0.0050	0.0756	0.0372	8.217	0.1831	2,228.5	0.19435	2,365.2
BLK 7	0.0003	0.0758	0.0373	8.283	0.1844	2,226.9	0.19685	2,376.6
BLK 8	0.0050	0.0759	0.0373	8.294	0.1880	2,266.8	0.19898	2,399.0
BLK 9	0.0040	0.0759	0.0372	8.249	0.1889	2,289.6	0.19963	2,420.0
BLK 10	0.0008	0.0756	0.0370	8.129	0.1865	2,294.6	0.19750	2,429.6
GRN 11	0.0030	0.0758	0.0370	8.150	0.1837	2,254.4	0.19523	2,395.5
GRN 12	0.0020	0.0758	0.0375	8.372	0.1854	2,215.5	0.19726	2,356.2
GRN 13	0.0040	0.0762	0.0370	8.193	0.1889	2,305.2	0.20008	2,442.1
GRN 14	0.0030	0.0759	0.0373	8.294	0.1883	2,270.9	0.19950	2,4053
GRN 15	0.0008	0.0760	0.0371	8.216	0.1883	2,292.2	0.19948	2,427.9
GRN 16	0.0003	0.0761	0.0370	8.182	0.1884	2,302.8	0.19935	2,436.4
GRN 17	0.0005	0.0763	0.0373	8.337	0.1881	2,255.7	0.19912	2,388.4
GRN 18	0.0010	0.0762	0.0373	8.327	0.1889	2,268.7	0.19981	2,399.5
GRN 19	0.002	0.0768	0.0373	8.392	0.1875	2,234.3	0.19894	2,370.6
GRN 20	0.0030	0.0764	0.0373	8.348	0.1880	2,254.3	0.19938	2,388.4

Table A6. 1e. Results for E_{dyn} and P_{dyn} on oven dry sandstone samples.

SAMPLE No	P WAVES Arrival time μs	S WAVES Arrival time μs	ΔtP μs	ΔtS μs	Velocity of P waves m/s	Velocity of S waves m/s	Edyn GPa	Pdyn
BLK 1	36.625	55.000	31.062	46.437	2,446	1,637	13.238	0.094
BLK 2	37.625	59.250	32.062	50.687	2,370	1,499	11.697	0.167
BLK 3	39.000	59.000	33.437	50.437	2,288	1,517	13.200	0.108
BLK 4	35.750	56.875	30.187	48.313	2,514	1,571	13.299	0.180
BLK 5	38.875	60.125	33.313	51.563	2,281	1,474	11.270	0.142
BLK 6	39.500	57.500	33.937	48.937	2,228	1,545	11.029	0.037
BLK 7	37.625	55.750	32.063	47.188	2,364	1,606	12.303	0.072
BLK 8	37.625	59.875	32.063	51.312	2,367	1,479	11.696	0.180
BLK 9	37.625	55.750	32.062	47.188	2,367	1,608	12.683	0.072
BLK 10	36.875	54.750	31.312	46.187	2,414	1,637	13.208	0.074
GRN 11	38.750	59.000	33.188	50.438	2,284	1,503	11.386	0.118
GRN 12	35.625	55.375	30.062	46.812	2,521	1,619	13.342	0.149
GRN 13	34.875	54.750	29.312	46.187	2,600	1,650	14.595	0.163
GRN 14	36.125	56.125	30.563	47.563	2,483	1,559	12.961	0.175

SAMPLE No	P WAVES Arrival time μs	S WAVES Arrival time μs	ΔtP μs	ΔtS μs	Velocity of P waves m/s	Velocity of S waves m/s	Edyn GPa	Pdyn
GRN 15	36.125	56.125	30.562	47.563	2,487	1,565	13.161	0.172
GRN 16	36.50	55.000	29.937	46.437	2,542	1,600	13.813	0.172
GRN 17	36.625	56.125	31.062	47.563	2,456	1,579	12.905	0.148
GRN 18	34.50	53.875	28.937	45.312	2,633	1,668	14.700	0.165
GRN 19	36.250	56.50	30.687	47.937	2,503	1,565	12.903	0.179
GRN 20	34.750	53.750	29.187	45.187	2,618	1,645	14.319	0.174

Cores have been tested with a 10 kg weight.

Arrival times for P_0 = 5.5625 μs and for S_0 = 8.5625 μs; these are considered the "zero times" and are deducted from the arrival times for Pand S waves. Hence, tS = S - S_0 and tP = P - P_0.

Table A6.1f. Results for E_{dyn} and P_{dyn} on saturated sandstone samples

SAMPLE No	P WAVES Arrival time μs	S WAVES Arrival time μs	ΔtP μs	ΔtS μs	Velocity of P waves m/s	Velocity of S waves m/s	Edyn GPa	Pdyn
BLK 1	31.250	59.000	25.687	50.437	2,959	1,507	14.37	0.325
BLK 2	29.750	61.000	24.187	52.437	3,142	1,449	13.61	0.365
BLK 3	39.000	60.250	33.437	51.687	2,288	1,480	11.98	0.140
BLK 4	29.000	58.500	23.437	49.937	3,238	1,520	15.17	0.359
BLK 8	36.750	60.750	31.187	52.187	2,434	1,454	12.40	0.223
BLK 9	30.000	62.000	24.437	53.437	3,106	1,420	13.35	0.368
BLK 10	30.250	59.750	24.687	51.187	3,062	1,477	14.29	0.344
GRN 12	30.750	60.750	25.187	52.187	3,009	1,452	13.39	0.348
GRN 13	30.000	64.500	24.437	55.937	3,118	1,460	14.16	0.359
GRN 14	29.500	62.000	23.937	53.437	3,171	1,420	13.33	0.375
GRN 15	33.500	66.500	27.937	57.937	2,720	1,312	11.27	0.348
GRN 16	29.500	65.500	23.937	56.937	3,179	1,337	12.128	0.393
GRN 18	29.500	63.750	23.937	55.187	2,622	1,381	11.969	0.226

"Zero arrival times" for S waves S_0 = 8.5625 μs and for P waves P_0 = 5.5625 μs

The tests have been conducted with a 10 kg weight. The coupling material was "SWC", Shear Wave Coupling from Parametrics, 221 Crescent st. Waltham, Mass. 02154 USA.

Table A6.1g Unconfined compressive strength on oven dry sandstones

SAMPLE No	DIAMETER m	AREA $x10^{-3}$ m^2	LOAD KN	UNCONFINED COMPRESSIVE STRENGTH MPa
BLK 1	0.0374	1.0986	55	50.064
BLK 2	0.0372	1.0869	50	46.002
BLK 3	0.0373	1.0927	60	54.910
BLK 4	0.0372	1.0869	55	50.602
BLK 5	0.0373	1.0927	55	50.334
GRN 11	0.0370	1.0752	50	46.503
GRN 12	0.0375	1.1045	50	45.269
GRN 13	0.0370	1.0752	60	55.803
GRN 14	0.0373	1.0927	60	54.910
GRN 15	0.0371	1.0810	60	55.504

Table A6.1h Unconfined compressive strength on saturated sandstones

BLK 6	0.0372	1.0869	50	46.002
BLK 7	0.0373	1.0927	48	43.928
BLK 10	0.0370	1.0752	50	46.503
GRN 15	0.0371	1.0810	53	49.029
GRN 17	0.0373	1.0927	50	45.758
GRN 20	0.0373	1.0927	52	47.588

Table A6. 2a Tests for the characterization of marble

SAMPLE No	MASS BEFORE DRYING (A) g	MASS AFTER DRYING (B) M_s g	MASS OF WATER (A-B) M_w g	MASS SUBMERGED (SAM+CONT) C g	MASS OF CONTAINER SUBMERGED D g	MASS OF SAMPLE SUBMERGED (C-D) g	MASS SATURATED M_{sat} g
1	229.68	229.65	0.03	727.22	580.95	146.27	229.96
2	230.40	230.48	0.02	727.30	580.95	146.35	230.90
3	226.96	226.94	0.02	726.07	580.95	145.12	227.29
4	229.70	229.68	0.02	727.80	580.95	146.85	230.06
5	229.20	229.20	0.00	727.82	580.95	146.87	229.51
6	235.32	235.29	0.03	730.50	580.95	149.55	235.63
7	229.80	229.78	0.02	729.12	580.95	148.17	230.31
8	233.39	233.35	0.04	730.61	580.95	149.66	233.78
9	229.24	229.22	0.02	729.02	580.95	148.07	229.60
10	226.38	226.33	0.03	728.10	580.95	147.15	226.82

Table A6. 2a(cont) Tests for the characterization of marble

SAMPLE No	BULK DENSITY g/cm^3	DRY DENSITY g/cm^3	BULK VOLUME cm^3	VOLUME OF VOIDS cm^3	POROSITY x10^{-3} %
1	2.74	2.74	83.84	0.31	3.70
2	2.72	2.72	84.70	0.42	4.96
3	2.76	2.76	82.32	0.35	4.26
4	2.76	2.76	83.35	0.38	4.57
5	2.77	2.77	82.79	0.31	3.75
6	2.73	2.73	86.23	0.31	3.60
7	2.79	2.79	82.29	0.51	6.21
8	2.77	2.77	84.27	0.39	4.64
9	2.81	2.81	81.68	0.38	4.66
10	2.84	2.83	79.81	0.44	5.52

The water temperature at the time of the experiments was 20° C; the density of the water at this temperature = 0.998206

Table A6. 2b Details of Marble samples used for E_{dyn} and P_{dyn}.

SAMPLE No	PARALLELISM	HEIGHT	DIAMETER	VOLUME	MASS DRY	DENSITY DRY	MASS SATURATED	DENSITY SATURATED
	α°	m	m	$x10^{-5}$ m^3	Kg	Kg/m^3	Kg	Kg/m^3
4	0.006	0.0768	0.0373	8.39	0.2297	2,738.4	0.23006	2,742.7
5	0.003	0.0768	0.0375	8.47	0.2292	2,703.5	0.22951	2,707.1
6	0.004	0.0776	0.0377	8.66	0.2353	2,717.7	0.23563	2,721.5
7	0.002	0.0763	0.0377	8.51	0.2298	2,699.4	0.23031	2,706.3
8	0.008	0.0763	0.0377	8.77	0.2334	2,661.3	0.23378	2,665.7
9	0.006	0.0754	0.0375	8.32	0.2292	2,754.8	0.22960	2,759.6
10	0.007	0.0758	0.0373	8.28	0.2264	2,734.9	0.22682	2,740.0

Table A6. 2c. Results for E_{dyn} and P_{dyn} on oven dry marble samples

Sampl No	P WAVES Arrival time	S WAVES Arrival time	ΔtP	ΔtS	Velocity of P waves	Velocity of S waves	E_{dyn}	P_{dyn}
	μs	μs	μs	μs	m/s	m/s	GPa	
4	21.375	36.375	18.000	29.875	4266.660	2570.711	43.980	0.240
5	22.000	36.375	18.625	29.875	4123.490	2570.711	42.080	0.182
6	22.875	38.000	19.500	31.500	3979.487	2463.492	39.200	0.189
7	22.000	35.125	18.625	28.625	4096.644	2665.502	43.270	0.133
8	23.125	36.875	19.750	30.375	3959.494	2574.486	39.900	0.134
9	20.000	34.000	16.625	27.500	4535.338	2741.818	50.170	0.212
10	22.125	35.375	18.750	28.875	4042.667	2625.108	42.690	0.135

"Zero arrival times" for S_0 = 6.500 μs and P_0 = 3.375 μs

Table A6. 2d. Results for E_{dyn} and P_{dyn} on saturated marble samples

Samp No	P WAVES Arrival time μs	S WAVES Arrival time μs	ΔtP μs	ΔtS μs	Velocity of P waves m/s	Velocity of S waves m/s	E_{dyn} GPa	P_{dyn}
4	16.750	32.375	13.500	25.875	5689.000	2968.000	63.280	0.312
5	16.750	33.125	13.500	26.625	5689.000	2884.000	59.620	0.327
6	17.250	33.375	14.000	26.875	5543.000	2887.000	59.580	0.314
7	17.000	33.000	13.750	26.500	5549.000	2879.000	58.900	0.316
8	17.250	32.500	14.000	26.000	5586.000	3030.000	62.360	0.293
9	17.250	32.500	14.000	26.000	5386.000	2900.000	59.940	0.296
10	17.000	33.125	13.750	26.625	5513.000	2847.000	58.330	0.318

Cores have been tested with a 10 kg weight.

"Zero arrival times" for S waves S_0 = 6.500 μs and for P waves P_0 = 3.25 μs.

Table A6. 2e Unconfined compressive strength on oven dry marble

SAMPLE No	DIAMETER m	AREA $x10_{-3}$ m2	LOAD KN	UNCONFINED COMPRESSIVE STRENGTH MPa
7	0.0377	1.1163	92	82.415
8	0.0378	1.1222	100	89.111
9	0.0375	1.1045	98	88.728
10	0.0373	1.0927	92	84.195

Table A. 6.2f Unconfined compressive strength on saturated marble

4	0.0373	1.0927	78	71.383
5	0.0375	1.1045	87	78.769
6	0.0377	1.1163	90	80.623

INSTRUMENT CALIBRATION

Date : 4/7/89

Calibration of : RDP 100 KLBF LOAD CELL ON ESH RAM TO COUNTERWEIGHT

Base plug / location : ESH FRAME

Amplifier location : ESH LOAD

Balance position : -5.90 v @ 9.38 SETTING

Gain / LVDT or Pot. :

Reading	500 RANGE v	DIVS		
1	-5.80	0		
2	-4.98	14.1		
3	-3.42	32.8		
4	-2.50	45		
5	-1.75	54.9		
6	-0.59	70.2		
7	+0.59	85.8		
8	+1.39	96.2		
9	+2.60	112.0		
10	+4.46	136.9		
11	+5.30	147.8		
12	+6.13	158.9		
13	+7.39	175.4		
14	+8.45	189.2		
15	+9.08	197.3		
16	+7.76	180.7		
17	+3.04	118.7		
18	-2.29	48.1		
19		0.5556 KN/div		
20	-3.90	26.6		
21	-5.80	0.0		
22				
23				
24				
25				

Calibration factors : 13.2379 divs/v | 7.3550 KN/v

Coeff. of correlation r : 0.99997

CONVERSIONS :

Linear : 1 inch = 25.4 mm
Pressure : 1 psi = 6894.76 Pa 1 kgf/cm² = 98.066 kPa 10 Bar = 1 MPa
Force : 1 lbf = 4.4482 N 1 tonf = 9.96402 kN

Linear regression by least squares fit technique

AVERY frame 6000 lbf range vs 4000 lbf ring - 13.7.89

Data no.	-----	READING ON AVERY (LBF) x values	DIVS. ON LOAD RING DIAL y values
1	-----	0	0
2	-----	200	78
3	-----	400	152
4	-----	400	155
5	-----	600	232
6	-----	800	309
7	-----	800	312
8	-----	1000	393
9	-----	1200	470
10	-----	1200	470
11	-----	1400	556
12	-----	1600	628
13	-----	1600	630
14	-----	1800	712
15	-----	2000	785
16	-----	2000	786
17	-----	2200	860
18	-----	2400	939
19	-----	2400	941
20	-----	2600	1019
21	-----	2800	1100
22	-----	2800	1100
23	-----	3000	1180
24	-----	3200	1261
25	-----	3200	1261
26	-----	3400	1342
27	-----	3600	1423
28	-----	3600	1423
29	-----	3800	1502
30	-----	0	2

This data yields the following linear model :

y = 0.3949196 x + -3.149963

with a correlation coefficient 'r' of : 0.9999739

and a standard deviation in y of : 3.235438

and a 99% confidence interval about y of : +/- 1.521072×10^{-1}
a 95% confidence interval about y of : +/- 1.157787×10^{-1}
a 90% confidence interval about y of : +/- 0.9717138×10^{-1}
(assuming a normal distribution in y about mean y)

0.3949196 DIVS/LB READ ON AVERY

BUT WE HAVE 11.3743 N/DIV

$\therefore$ $0.3949196 \times 11.3743 = 4.491934$ N/LB READ ON AVERY

$\therefore$ READING ON AVERY IN LBF $\times$ 4.491934 = LOAD IN N

($\therefore$ 4.44822 N/LBF $\therefore$ AVERY IS UNDER-READING SLIGHTLY)

APPENDIX TO CHAPTER SEVEN

This appendix contains the results obtained from testing with the GDS loading system and the closed loop servo-controlled (Terra-Tek) machine. Since it contains a lot of information, to assist in its future use, it has been divided into six sections, Appx7.1- to 7.6.

Appx 7.1 contains tables A7.1a and A7.1b with the measurements of sandstone and marble hoops respectively, used with the GDS. Table A7.1c contains the measurements of sandstone hoops used with the Terra-Tek.

Appx 7.2 summarizes the mechanics of the calculations which enabled the volume change of the GDS to be interpreted as displacement along the load line direction, as well as the curves obtained prior to, and after the testing which illustrate the satisfactory level of reproducible performance provided by the GDS; in addition an example of a spread sheet is included.

Appx 7.3 contains the curves obtained from hoops used for the investigation of the rate of loading and table A7.2 shows the numerical results of force, displacement, and work obtained from these curves.

Appx 7.4 contains the curves acquired from marble hoop samples tested with the GDS and table A7.3 summarizes the numerical values of force, displacement and work obtained from these curves.

Appx 7.5 contains the curves obtained from sandstone hoops tested with the GDS and table A7.4 summarizes the numerical results of force, displacement and work obtained from these curves. The results of Appx 7.4 and Appx 7.5 have been used in the analysis of the influence of orientation, saturation, hoop size and roughness of platens.

Appx 7.6 contains the curves of the sandstone hoops tested on the Terra-Tek.

Table A7. 1a Details of sandstone Hoop samples used with the GDS machine in oven dry and saturated condition.

SAMPLE No.	INTERNAL DIAMETER (mm)	EXTERNAL DIAMETER (mm)	CLASS	THICKNESS (mm)	PARALLELISM ° (α°)	TOTAL FAILURE AREA ($x10^{-3}$) m^2	HOOP VOLUME ($x10^{-4}$) m^3
9 Aa	47.86	150.83	II	48.63	0.23	5.01	7.8
9 Ab	47.79	150.84	II	49.38	0.27	5.08	7.9
9 Ac	47.82	150.85	II	48.64	0.21	5.01	7.8
9 Ba	47.91	150.88	II	50.39	0.17	5.19	8.1
9 Bb	47.88	150.84	II	49.36	0.17	5.08	7.9
9 Bc	47.85	150.84	II	49.14	0.30	5.06	7.9
9 Ca	47.85	150.85	II	41.37	0.38	4.23	6.6
9 Cb	47.90	150.86	II	44.81	0.21	4.61	7.2
9 Cc	47.78	150.83	II	44.48	0.09	4.58	7.2
9 Da	48.04	150.87	II	49.96	0.99	5.14	8.0
9 Db	47.93	150.91	II	49.05	0.21	5.05	7.9
9 Dc	47.84	150.90	II	48.81	0.20	5.03	7.8
9 Ea	47.77	150.85	II	42.72	0.16	4.4	6.9
9 Eb	47.75	150.81	II	46.58	0.30	4.8	7.5
9 Ec	47.69	150.88	II	49.96	0.38	5.15	7.9
9 Fa	47.84	150.86	II	48.83	0.78	5.03	7.8
9 Fb	47.82	150.82	II	48.36	1.08	4.98	7.7
9 Fc	47.75	150.87	II	47.16	1.00	4.86	7.6

SAMPLE No.	INTERNAL DIAMETER (mm)	EXTERNAL DIAMETER (mm)	CLASS	THICKNESS (mm)	PARALLELISM (α°)	TOTAL FAILURE AREA ($x10^{-3}$) m^2	HOOP VOLUME ($x10^{-4}$) m^3
7 Aa	47.90	150.74	II	44.70	0.72	4.59	7.2
7 Ab	47.75	150.87	II	49.30	0.57	5.08	7.9
7 Ac	47.66	150.81	II	46.51	0.55	4.80	7.5
7 Ba	47.87	149.92	II	43.00	0.29	4.39	6.8
7 Bb	47.67	150.75	II	45.55	0.32	4.70	7.3
7 Bc	47.58	150.82	II	43.28	0.37	4.47	7.0
7 Ca	48.72	150.70	II	49.06	0.38	5.00	7.9
7 Cb	48.37	150.78	II	35.77	0.57	3.66	5.7
7 Cc	48.67	150.80	II	50.41	0.55	5.15	8.1
7 Da	45.01	150.90	II	45.16	0.49	4.78	7.4
7 Ea	49.47	150.87	II	44.81	0.50	4.54	7.2
7 Ec	49.33	150.05	II	48.29	0.49	4.90	7.7
7 Fa	49.32	150.80	II	44.21	0.44	4.49	7.1
7 Fb	48.86	150.95	II	44.45	0.38	4.54	7.1
7 Ga	49.19	149.33	II	49.84	0.38	4.99	7.8
7 Gb	48.76	150.74	II	48.35	0.38	4.93	7.7
7 Gc	48.82	150.85	II	50.67	0.42	5.17	8.1
7 Ha	47.73	150.79	II	48.85	0.32	4.98	7.7
7 Hb	47.58	150.77	II	49.17	0.33	5.07	7.9
7 Hc	47.53	150.78	II	50.40	0.35	5.2	8.1

SAMPLE No.	INTERNAL DIAMETER (mm)	EXTERNAL DIAMETER (mm)	CLASS	THICKNESS (mm)	PARALLELISM * (α°)	TOTAL FAILURE AREA ($x10^{-3}$) m^2	HOOP VOLUME ($x10^{-4}$) m^3
10 1a	47.63	101.50	IV	53.89	0.54	2.90	3.4
10 1b	47.65	101.53	IV	52.63	0.61	2.84	3.3
10 1c	47.73	101.51	IV	54.23	0.67	2.92	3.4
10 2a	47.35	101.48	IV	51.38	0.69	2.78	3.3
10 2b	47.46	101.47	IV	51.35	0.76	2.77	3.2
10 2c	47.66	101.43	IV	51.29	0.77	2.76	3.2
10 3a	47.51	101.38	IV	52.35	0.80	2.82	3.3
10 3b	47.71	101.29	IV	52.16	1.19	2.79	3.3
10 3c	47.57	101.61	IV	52.59	1.12	2.84	3.3
10 4a	47.53	150.77	II	52.00	0.99	5.37	8.4
10 4b	47.65	150.74	II	52.65	0.98	5.43	8.5
10 4c	47.73	150.73	II	51.99	0.71	5.35	8.4
10 5a	47.28	150.75	II	51.09	0.37	5.29	8.2
10 5b	47.39	150.76	II	50.63	0.77	5.23	8.2
10 5c	47.54	150.70	II	52.74	0.38	5.44	8.5
10 6a	30.73	101.32	III	52.55	1.35	3.71	3.9
10 6b	30.82	101.28	III	51.72	1.12	3.64	3.8
10 6c	30.87	101.11	III	51.01	1.26	3.58	3.7
10 7a	30.74	101.40	III	52.47	1.03	3.71	3.9
10 7b	30.79	101.35.	III	52.03	0.95	3.67	3.8

SAMPLE No.	INTERNAL DIAMETER (mm)	EXTERNAL DIAMETER (mm)	CLASS	THICKNESS (mm)	PARALLELISM * (α°)	TOTAL FAILURE AREA ($x10^{-3}$) m^2	HOOP VOLUME ($x10^{-4}$) m^3
10 7c	30.83	101.19	III	51.85	1.12	3.65	3.9
11 1a	30.28	150.74	I	50.28	0.37	6.06	8.61
11 1b	30.30	150.78	I	52.50	0.44	6.32	8.99
11 1c	30.33	150.74	I	51.43	0.99	6.19	8.80
11 2a	30.37	150.73	I	51.79	0.89	6.23	8.86
11 2b	30.45	150.72	I	52.66	0.86	6.33	9.01
11 2c	30.50	150.70	I	52.37	0.95	6.29	8.96

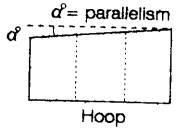


Table A7. 1b Details of marble hoops used for testing with the GDS pressure controller

SAMPLE No.	INTERNAL DIAMETER (mm)	EXTERNAL DIAMETER (mm)	CLASS	THICKNESS (mm)	PARALLELISM * (α°)	TOTAL FALIURE AREA ($x10^{-5}$) m^2	HOOP VOLUME ($x10^{-4}$) m^3
I M 1/S1	30.43	150.98	I	46.18	0.77	5.57	7.93
I M 2/S2	30.42	151.16	I	46.30	0.75	5.59	7.97
I M 3/S2	30.70	151.10	I	46.09	0.88	5.55	7.92
I M 4/S2	30.59	151.38	I	44.44	0.77	5.37	7.67
I M 5/S2	30.33	150.96	I	45.85	1.02	5.53	7.88
II M 1/S2	48.20	151.13	II	47.78	0.75	4.92	7.7
II M 2/S2	48.22	150.85	II	48.75	0.85	5.00	8.9
II M 3/S2	48.24	151.10	II	46.80	1.02	4.81	7.54
II M 4/S2	48.20	149.25	II	47.03	0.84	4.75	7.37
II M 5/S2	48.25	151.29	II	48.72	0.71	5.02	7.87
III M 7/S1	31.70	94.82	III	46.28	0.83	2.92	2.9
III M 8/S1	31.48	94.84	III	46.48	0.74	2.94	2.9
III M 9/S1	31.64	94.84	III	45.81	0.76	2.89	2.9
III M10/S1	31.70	94.52	III	46.13	0.82	2.89	2.9
III M11/S1	31.59	94.73	III	46.84	0.89	2.96	2.9
III M12/S1	31.72	94.58	III	46.31	0.78	2.91	2.9

SAMPLE No.	INTERNAL DIAMETER (mm)	EXTERNAL DIAMETER (mm)	CLASS	THICKNESS (mm)	PARALLELISM * (α°)	TOTAL FALIURE AREA ($x10^{-3}$) m^2	HOOP VOLUME ($x10^{-4}$) m^3
IV M 1/S2	**48.34**	**101.45**	**IV**	**45.63**	**0.63**	**2.42**	**2.85**
IV M 2/S2	**48.14**	**101.28**	**IV**	**47.08**	**1.13**	**2.50**	**2.93**
IV M 3/S2	**45.74**	**101.35**	**IV**	**46.64**	**0.95**	**2.59**	**3.00**
IV M 4/S2	**48.18**	**101.59**	**IV**	**46.59**	**0.86**	**2.49**	**2.93**
IV M 5/S2	**48.24**	**101.21**	**IV**	**47.96**	**0.80**	**2.54**	**2.98**

Table A7.1c Details of sandstone hoops used with the Terra-Tek

SAMPLE	INTERNAL DIAMETER mm	EXTERNAL DIAMETER mm	CLASS	THICKNESS mm	PARALLELISM * α°	TOTAL FAILURE AREA $x10^{-4}$ m^2	HOOP VOLUME $X10^{-4}$ m^3
6a1	58.375	150.72	II	49.525	0.057	4.57	7.51
6e1	58.21	150.725	II	49.515	0.046	4.58	7.52
6c2	58.20	150.705	II	45.43	0.226	4.20	6.70
6d2	58.225	150.673	II	46.13	0.243	4.26	7.00
6f2	58.685	150.675	II	49.64	0.030	4.57	7.51
6f1	58.408	150.735	II	50.53	0.084	4.67	7.66
6e2	58.245	150.70	II	50.30	0.049	4.65	7.63
6c3	58.19	150.67	II	45.585	0.167	4.20	6.70
6d3	58.245	150.715	II	44.37	0.171	4.26	6.70
6f3	58.235	150.785	II	49.205	0.019	4.57	7.51

Appx 7.2

As mentioned in 5.1.2 the equipment and software when used together are capable of providing measurements of three parameters; time, pressure and volume change.

Platens of two different diameters and containing pistons of also two different diameters were used. For the piston of 25.4 mm diameter contained in the 50 mm diameter platens, it was calculated that for 1 mm displacement 506.7 mm^3 of volume is required to be displaced; for the piston of 20.1 mm diameter and contained in platens of 30 mm diameter 317.3, mm^3 of volume is required to be displaced for 1 mm displacement. Hence, depending on the size of platens used, numbers 506.7 and 317.3 are considered to be constants and the volume change for every measurement in the test is divided by this constant to obtain the displacement in mm. This is the displacement resulting from the application of pressure along the load line and is the displacement of one half of the platens in relation to the other. A typical result of raw data is shown in Fig.A7.1

The volume change is obtained in negative values (compression of the oil reservoir results in increasing pressure). In some tests, because of the initial position of the piston, the values of displacement start from negative at the origin and become positive later. For reasons of presentation and further calculations it was necessary to plot the results of displacement to start from zero (0) displacement expressed in meters; hence the conversion of Volume change was done by (0.001/506.7075) and by adjusting the initial volume to equal 0.

The Force is required in Newtons and it is calculated from the obtained values of Pressure. (F= P x A, where A is the area of the piston). As Pressure is given in KPa, F=P x 0.5067075 N). The resultant plot of Force vs Displacement is shown in Fig.A7.2

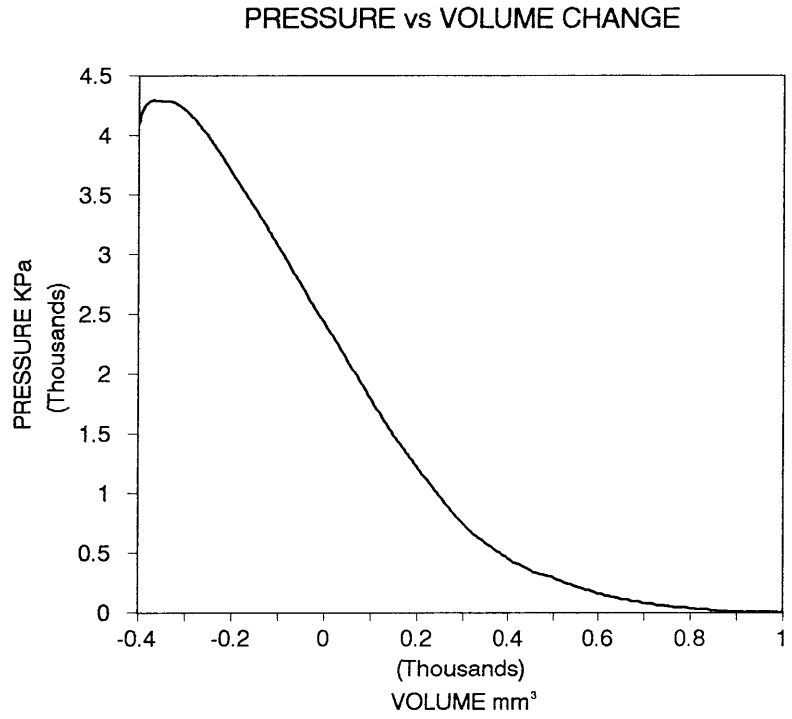


Fig. A7.1 A typical result of data as obtained from the GDS

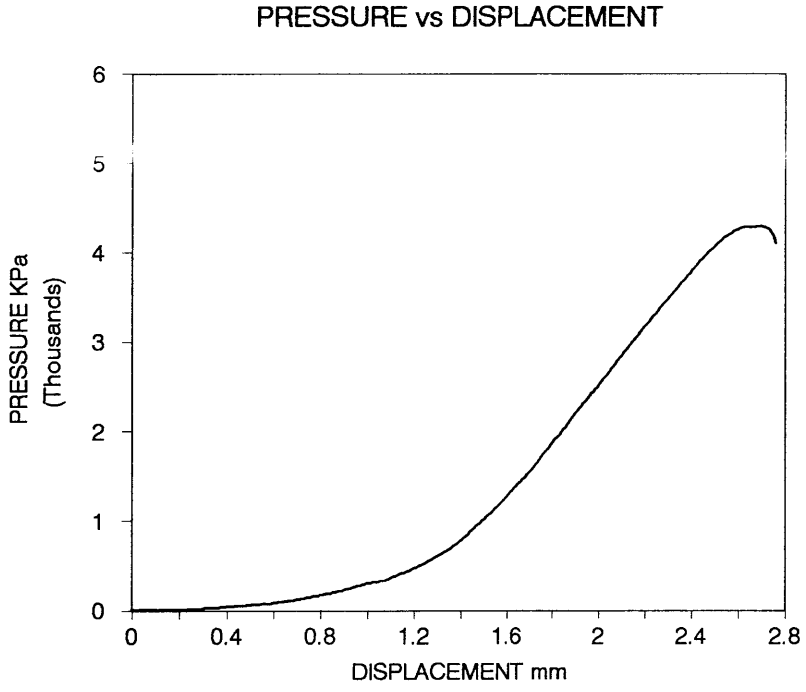


Fig. A7.2 Plot of Force vs Displacement after adjustment of results.

All precautions have been taken to ensure that no air bubbles were entrapped in the oil by de-airing it under pressure and then filling the oil reservoir in the pressure controller as per manufacturer's instructions. A rigid and as short as possible connection was provided to connect the GDS to the piston contained in the platens. Fig. A7.3a and b shows curves obtained when the system was tested before and after the testing was completed. This was obtained with the platens held between the jaws of a vice while pressure was applied to the system. It is important to draw the attention of the reader to the almost identical curves, a proof of the extremely satisfactory condition of the equipment during the whole period of testing.

Comparing the curves of fig. A7.2 and fig. A7.3 a distinct similarity is clear at their initial and at their elastic parts.

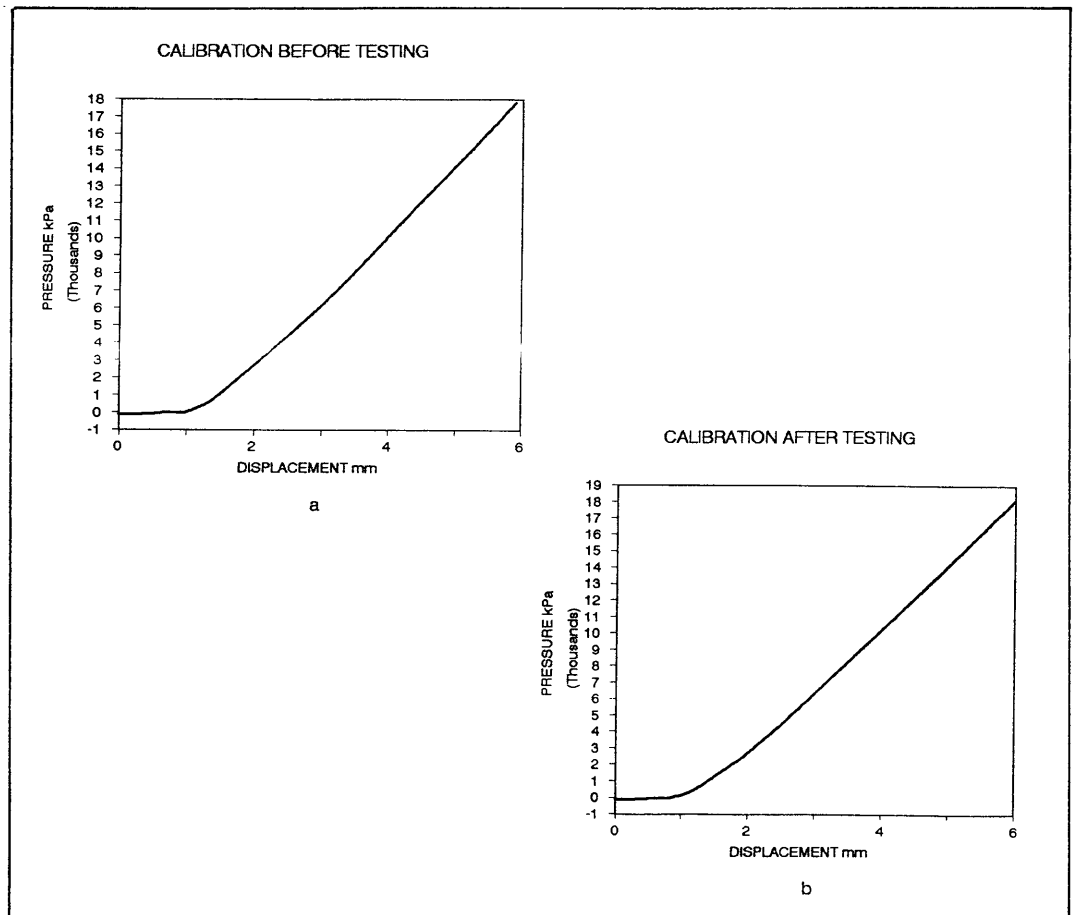


Fig. A7.3 calibration of the GDS (a) prior to testing and (b) after testing.

An example of a typical spread sheet of results obtained from the GDS is included at the end of this section of the appendix.

The hydraulic oil used was "Shell Tallus oil No 41". Its properties are presented below:

Properties and calculations concerning the hydraulic oil used in the GDS loading system

Shell Tellus Oil

$$Compression = \frac{V_o - V}{V_o} \qquad \text{(A7.1)}$$

where V_o = original volume at atmospheric pressure, V = volume at a given pressure P.

Compression may be also expressed through density:

$$Compression = \frac{\varrho - \varrho_o}{\varrho} \qquad \text{(A7.2)}$$

where ϱ_o = density of oil at atmospheric pressure, ϱ = density at pressure P

Isothermal compression: that which takes place when the oil is compressed isothermally

Isentropic compression: that which takes place when the oil is compressed isentropically (adiabatically) (entropy = not constant temperature). In practice, compression may approximate to one or the other or fall in between the two.

Bulk modulus of elasticity: of a fluid is a measure of its resistance to reduction in volume under pressure.

Tangent modulus:

$$k = -V\frac{\partial p}{\partial V} \tag{A7.3}$$

Compressibility: is the reciprocal of bulk modulus

$$\frac{1}{k} = \frac{1}{V}\left(\frac{\partial V}{\partial P}\right) \tag{A7.4}$$

Elasticity of vessels: some allowance has to be made for the elastic expansion of the containing vessels (including pipe work). An approximate value of the in-situ bulk modulus of an oil in a typical hydraulic system may be obtained by reducing the actual bulk modulus by 25%.

Effect of entrained air: oil normally contains 8 to 9% by volume of dissolved air. The only satisfactory way of dealing with this situation is to remove the entrained air, preferably by bleeding it out of the system; if this is impossible, air may be disposed by holding the system at high pressure until the air has dissolved.

Viscosity of a fluid: a physical measure of its internal resistance to flow by shear.

The values relevant to Shell Tallus Oil No 41, which was used in the GDS, are as follows:

At 20 to 22 C° and at atmospheric pressure:

Isothermal compression: 0.008 at 12.5 MPa

Isentropic compression: 0.007 at 12.5 MPa

Isentropic secant bulk modulus: $k_s = 1.92 \times 10^3$ kg/cm^3

Isothermal secant bulk modulus: $k_T = 1.68 \times 10^3$ kg/cm^3

Specific gravity: 0.79

Kinematic viscosity: 300 centistokes

Compressibility $1/(1.92 \times 10^3)$ kg/cm^3 (isentropic) and $1/(1.68 \times 10^3)$ kg/cm^3

An example of a typical spread sheet of results obtained from the GDS.

OVEN DRY SST

SAMPLE 9AA NUM_RDGS 230

RDGS	TIME SECONDS	PRESSURE KPa	VOLUME mm3	DISPLACEMENT METERS	FORCE NEWTONS
1	0	174	-631	0.000000	88.1671
2	0.7	174	-635	0.000008	88.1671
3	1.3	180	-639	0.000016	91.2073
4	2	187	-644	0.000026	94.7543
5	2.6	191	-649	0.000036	96.7811
6	3.3	194	-653	0.000043	98.3013
7	4	204	-657	0.000051	103.3683
8	4.6	210	-662	0.000061	106.4086
9	5.3	218	-667	0.000071	110.4622
10	5.9	225	-671	0.000079	114.0092
11	6.6	230	-676	0.000089	116.5427
12	7.3	238	-680	0.000097	120.5964
13	7.9	245	-686	0.000109	124.1433
14	8.6	254	-690	0.000116	128.7037
15	9.2	257	-694	0.000124	130.2238
16	9.9	263	-699	0.000134	133.2641
17	10.5	271	-704	0.000144	137.3177
18	11.2	274	-708	0.000152	138.8379
19	11.9	284	-712	0.000160	143.9049
20	12.5	291	-717	0.000170	147.4519
21	13.2	300	-722	0.000180	152.0123
22	13.8	305	-727	0.000189	154.5458
23	14.5	313	-731	0.000197	158.5994
24	15.2	320	-736	0.000207	162.1464
25	15.8	329	-740	0.000215	166.7068
26	16.5	336	-746	0.000227	170.2537
27	17.1	345	-750	0.000235	174.8141
28	17.8	351	-754	0.000243	177.8543
29	18.5	358	-759	0.000253	181.4013
30	19.1	367	-764	0.000262	185.9617
31	19.8	375	-768	0.000270	190.0153
32	20.4	384	-772	0.000278	194.5757
33	21.1	391	-777	0.000288	198.1226
34	21.8	399	-782	0.000298	202.1763
35	22.4	403	-787	0.000308	204.2031
36	23.1	411	-791	0.000316	208.2568
37	23.7	417	-796	0.000326	211.2970
38	24.4	426	-800	0.000334	215.8574
39	25	432	-805	0.000343	218.8976
40	25.7	438	-810	0.000353	221.9379
41	26.4	447	-814	0.000361	226.4983
42	27	452	-819	0.000371	229.0318
43	27.7	460	-824	0.000381	233.0854
44	28.3	464	-829	0.000391	235.1123
45	29	468	-833	0.000399	237.1391
46	29.7	476	-837	0.000407	241.1928
47	30.3	479	-842	0.000416	242.7129

48	31	480	-847	0.000426	243.2196
49	31.6	481	-852	0.000436	243.7263
50	32.3	487	-856	0.000444	246.7666
51	33	494	-860	0.000452	250.3135
52	33.6	504	-865	0.000462	255.3806
53	34.3	512	-870	0.000472	259.4342
54	34.9	520	-874	0.000480	263.4879
55	35.6	529	-879	0.000489	268.0483
56	36.3	538	-884	0.000499	272.6086
57	36.9	550	-889	0.000509	278.6891
58	37.6	560	-893	0.000517	283.7562
59	38.2	567	-897	0.000525	287.3032
60	38.9	580	-902	0.000535	293.8904
61	39.6	591	-907	0.000545	299.4641
62	40.2	603	-912	0.000555	305.5446
63	40.9	615	-916	0.000562	311.6251
64	41.5	628	-920	0.000570	318.2123
65	42.2	640	-925	0.000580	324.2928
66	42.8	654	-930	0.000590	331.3867
67	43.5	669	-934	0.000598	338.9873
68	44.2	682	-939	0.000608	345.5745
69	44.8	697	-943	0.000616	353.1751
70	45.5	712	-949	0.000628	360.7757
71	46.1	727	-953	0.000635	368.3764
72	46.8	741	-957	0.000643	375.4703
73	47.5	759	-962	0.000653	384.5910
74	48.1	774	-967	0.000663	392.1916
75	48.8	790	-971	0.000671	400.2989
76	49.4	808	-976	0.000681	409.4197
77	50.1	825	-980	0.000689	418.0337
78	50.8	844	-985	0.000699	427.6611
79	51.4	862	-990	0.000708	436.7819
80	52.1	880	-995	0.000718	445.9026
81	52.7	901	-999	0.000726	456.5435
82	53.4	921	-1003	0.000734	466.6776
83	54.1	938	-1008	0.000744	475.2916
84	54.7	960	-1013	0.000754	486.4392
85	55.4	981	-1017	0.000762	497.0801
86	56	1003	-1022	0.000772	508.2276
87	56.7	1022	-1027	0.000782	517.8551
88	57.3	1042	-1032	0.000791	527.9892
89	58	1062	-1036	0.000799	538.1234
90	58.7	1087	-1041	0.000809	550.7911
91	59.3	1109	-1045	0.000817	561.9386
92	60	1130	-1050	0.000827	572.5795
93	60.6	1153	-1055	0.000837	584.2337
94	61.3	1179	-1060	0.000847	597.4081
95	62	1201	-1063	0.000853	608.5557
96	62.6	1224	-1068	0.000862	620.2100
97	63.3	1249	-1073	0.000872	632.8777
98	63.9	1277	-1078	0.000882	647.0655
99	64.6	1304	-1082	0.000890	660.7466
100	65.3	1330	-1087	0.000900	673.9210
101	65.9	1356	-1092	0.000910	687.0954
102	66.6	1386	-1096	0.000918	702.2966
103	67.2	1411	-1100	0.000926	714.9643
104	67.9	1436	-1105	0.000935	727.6320
105	68.6	1464	-1110	0.000945	741.8198
106	69.2	1492	-1115	0.000955	756.0076
107	69.9	1522	-1119	0.000963	771.2088

108	70.5	1549	-1123	0.000971	784.8899
109	71.2	1578	-1128	0.000981	799.5844
110	71.8	1605	-1133	0.000991	813.2655
111	72.5	1634	-1138	0.001001	827.9601
112	73.2	1661	-1142	0.001008	841.6412
113	73.8	1687	-1146	0.001016	854.8156
114	74.5	1715	-1151	0.001026	869.0034
115	75.1	1747	-1156	0.001036	885.2180
116	75.8	1773	-1160	0.001044	898.3924
117	76.5	1804	-1165	0.001054	914.1003
118	77.1	1833	-1170	0.001064	928.7948
119	77.8	1862	-1174	0.001072	943.4894
120	78.4	1891	-1178	0.001080	958.1839
121	79.1	1918	-1183	0.001089	971.8650
122	79.8	1946	-1188	0.001099	986.0528
123	80.4	1974	-1193	0.001109	1000.241
124	81.1	2005	-1197	0.001117	1015.949
125	81.7	2033	-1202	0.001127	1030.136
126	82.4	2063	-1206	0.001135	1045.338
127	83.1	2091	-1211	0.001145	1059.525
128	83.7	2122	-1216	0.001155	1075.233
129	84.4	2150	-1220	0.001162	1089.421
130	85	2179	-1225	0.001172	1104.116
131	85.7	2212	-1230	0.001182	1120.837
132	86.3	2239	-1235	0.001192	1134.518
133	87	2271	-1239	0.001200	1150.733
134	87.7	2301	-1243	0.001208	1165.934
135	88.3	2331	-1248	0.001218	1181.135
136	89	2364	-1253	0.001228	1197.857
137	89.6	2399	-1257	0.001235	1215.591
138	90.3	2430	-1262	0.001245	1231.299
139	91	2463	-1266	0.001253	1248.021
140	91.6	2495	-1271	0.001263	1264.235
141	92.3	2529	-1276	0.001273	1281.463
142	92.9	2557	-1280	0.001281	1295.651
143	93.6	2588	-1285	0.001291	1311.359
144	94.3	2619	-1290	0.001301	1327.067
145	94.9	2655	-1295	0.001310	1345.308
146	95.6	2682	-1299	0.001318	1358.990
147	96.2	2711	-1303	0.001326	1373.684
148	96.9	2744	-1308	0.001336	1390.405
149	97.6	2775	-1313	0.001346	1406.113
150	98.2	2807	-1317	0.001354	1422.328
151	98.9	2838	-1322	0.001364	1438.036
152	99.5	2869	-1326	0.001372	1453.744
153	100.2	2902	-1331	0.001381	1470.465
154	100.8	2933	-1336	0.001391	1486.173
155	101.5	2963	-1340	0.001399	1501.374
156	102.2	2997	-1345	0.001409	1518.602
157	102.8	3027	-1349	0.001417	1533.804
158	103.5	3056	-1354	0.001427	1548.498
159	104.1	3086	-1359	0.001437	1563.699
160	104.8	3115	-1363	0.001445	1578.394
161	105.5	3145	-1368	0.001454	1593.595
162	106.1	3176	-1373	0.001464	1609.303
163	106.8	3205	-1377	0.001472	1623.998
164	107.4	3236	-1382	0.001482	1639.705
165	108.1	3266	-1386	0.001490	1654.907
166	108.8	3298	-1391	0.001500	1671.121
167	109.4	3328	-1396	0.001510	1686.323

168	110.1	3359	-1400	0.001518	1702.030
169	110.7	3390	-1405	0.001528	1717.738
170	111.4	3423	-1409	0.001535	1734.460
171	112.1	3454	-1415	0.001547	1750.168
172	112.7	3485	-1419	0.001555	1765.876
173	113.4	3514	-1423	0.001563	1780.570
174	114	3549	-1428	0.001573	1798.305
175	114.7	3579	-1433	0.001583	1813.506
176	115.3	3611	-1437	0.001591	1829.721
177	116	3642	-1442	0.001601	1845.429
178	116.7	3671	-1446	0.001608	1860.123
179	117.3	3703	-1451	0.001618	1876.338
180	118	3729	-1456	0.001628	1889.512
181	118.6	3757	-1460	0.001636	1903.700
182	119.3	3786	-1465	0.001646	1918.395
183	120	3815	-1469	0.001654	1933.089
184	120.6	3844	-1474	0.001664	1947.784
185	121.3	3873	-1479	0.001674	1962.478
186	121.9	3904	-1483	0.001681	1978.186
187	122.6	3934	-1488	0.001691	1993.387
188	123.3	3959	-1493	0.001701	2006.055
189	123.9	3987	-1497	0.001709	2020.243
190	124.6	4014	-1502	0.001719	2033.924
191	125.2	4045	-1506	0.001727	2049.632
192	125.9	4067	-1511	0.001737	2060.779
193	126.6	4092	-1516	0.001747	2073.447
194	127.2	4117	-1521	0.001756	2086.115
195	127.9	4146	-1525	0.001764	2100.809
196	128.5	4168	-1529	0.001772	2111.957
197	129.2	4189	-1534	0.001782	2122.598
198	129.8	4211	-1539	0.001792	2133.745
199	130.5	4233	-1543	0.001800	2144.893
200	131.2	4254	-1548	0.001810	2155.534
201	131.8	4272	-1553	0.001820	2164.654
202	132.5	4293	-1558	0.001829	2175.295
203	133.1	4310	-1562	0.001837	2183.909
204	133.8	4328	-1566	0.001845	2193.030
205	134.5	4340	-1571	0.001855	2199.111
206	135.1	4354	-1576	0.001865	2206.204
207	135.8	4370	-1581	0.001875	2214.312
208	136.4	4381	-1585	0.001883	2219.886
209	137.1	4385	-1589	0.001891	2221.912
210	137.8	4384	-1594	0.001901	2221.406
211	138.4	4386	-1599	0.001910	2222.419
212	139.1	4386	-1603	0.001918	2222.419
213	139.7	4380	-1608	0.001928	2219.379
214	140.4	4367	-1612	0.001936	2212.792
215	141.1	4354	-1618	0.001948	2206.204
216	141.7	4341	-1622	0.001956	2199.617
217	142.4	4317	-1626	0.001964	2187.456
218	143	4287	-1631	0.001974	2172.255
219	143.7	4249	-1636	0.001983	2153.000
220	144.3	4200	-1640	0.001991	2128.172
221	145	4132	-1645	0.002001	2093.715
222	145.7	4072	-1649	0.002009	2063.313
223	146.3	4018	-1654	0.002019	2035.951
224	147	3636	-1659	0.002029	1842.388
225	147.6	1926	-1664	0.002039	975.9186
226	148.3	818	-1668	0.002047	414.4867
227	149	512	-1672	0.002054	259.4342

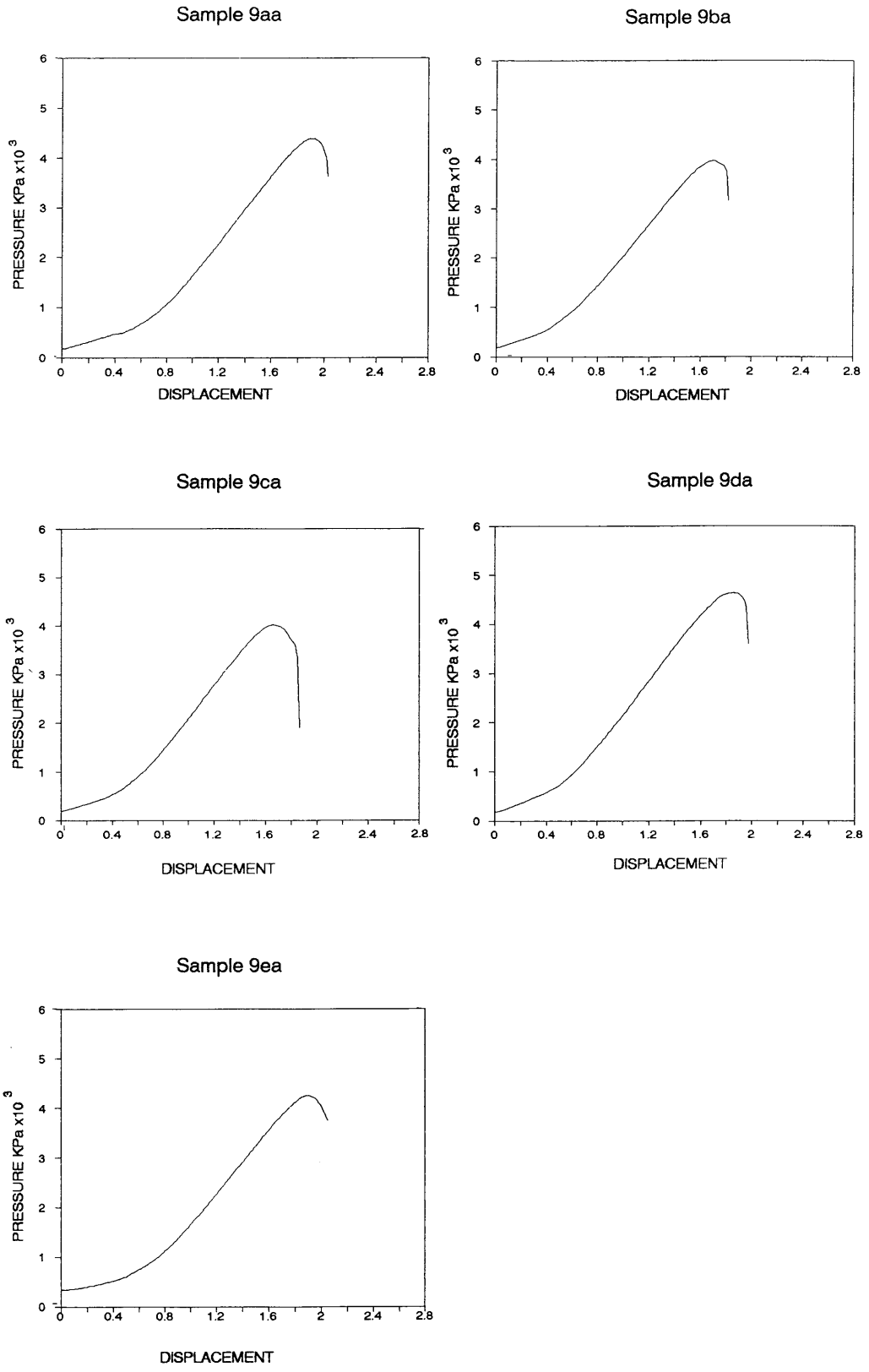


Fig. A7. 4 Curves obtained from samples loaded at the ISRM rate of loading

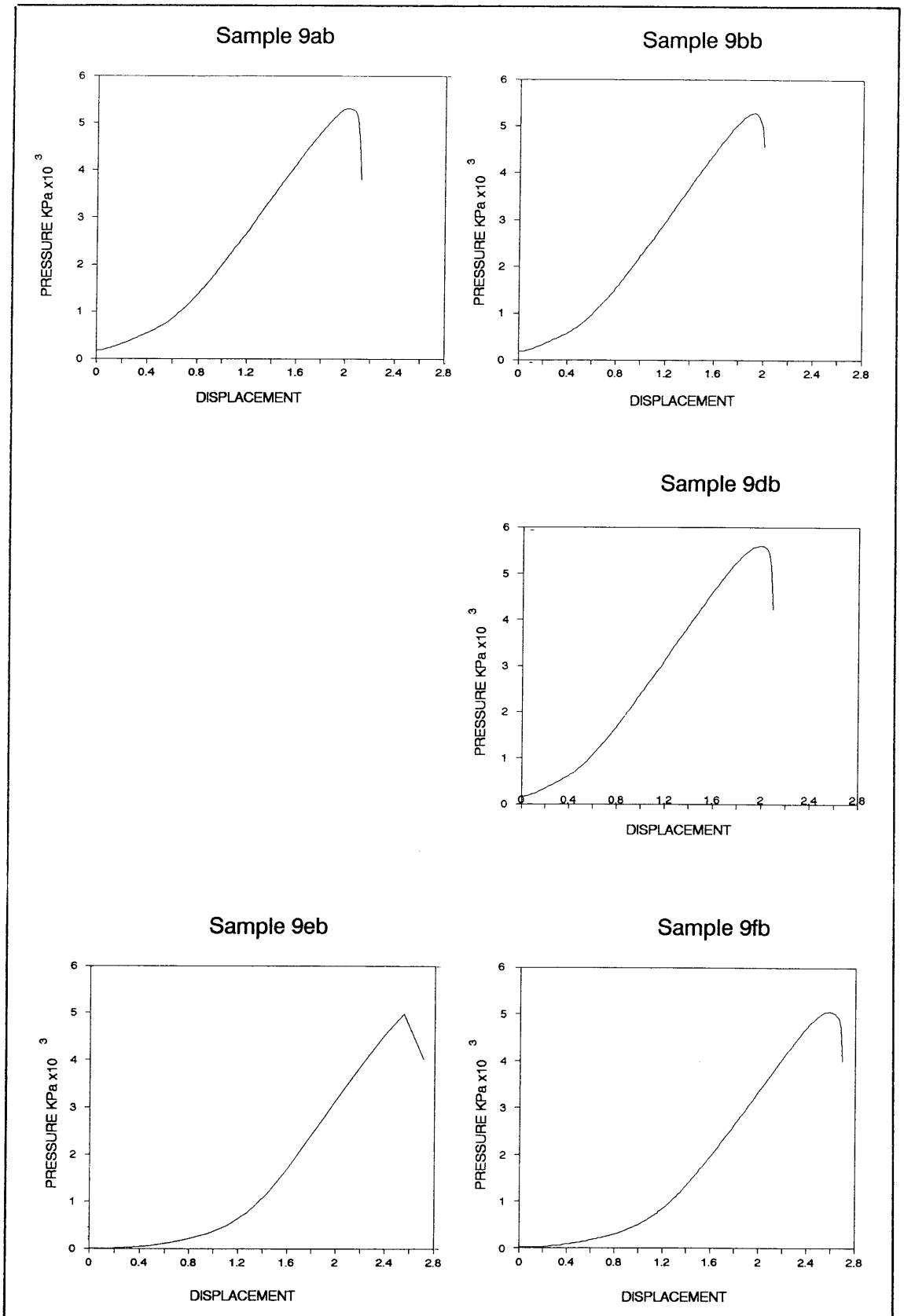


Fig. A7. 5 Curves obtained from samples loaded at the fast rate of loading

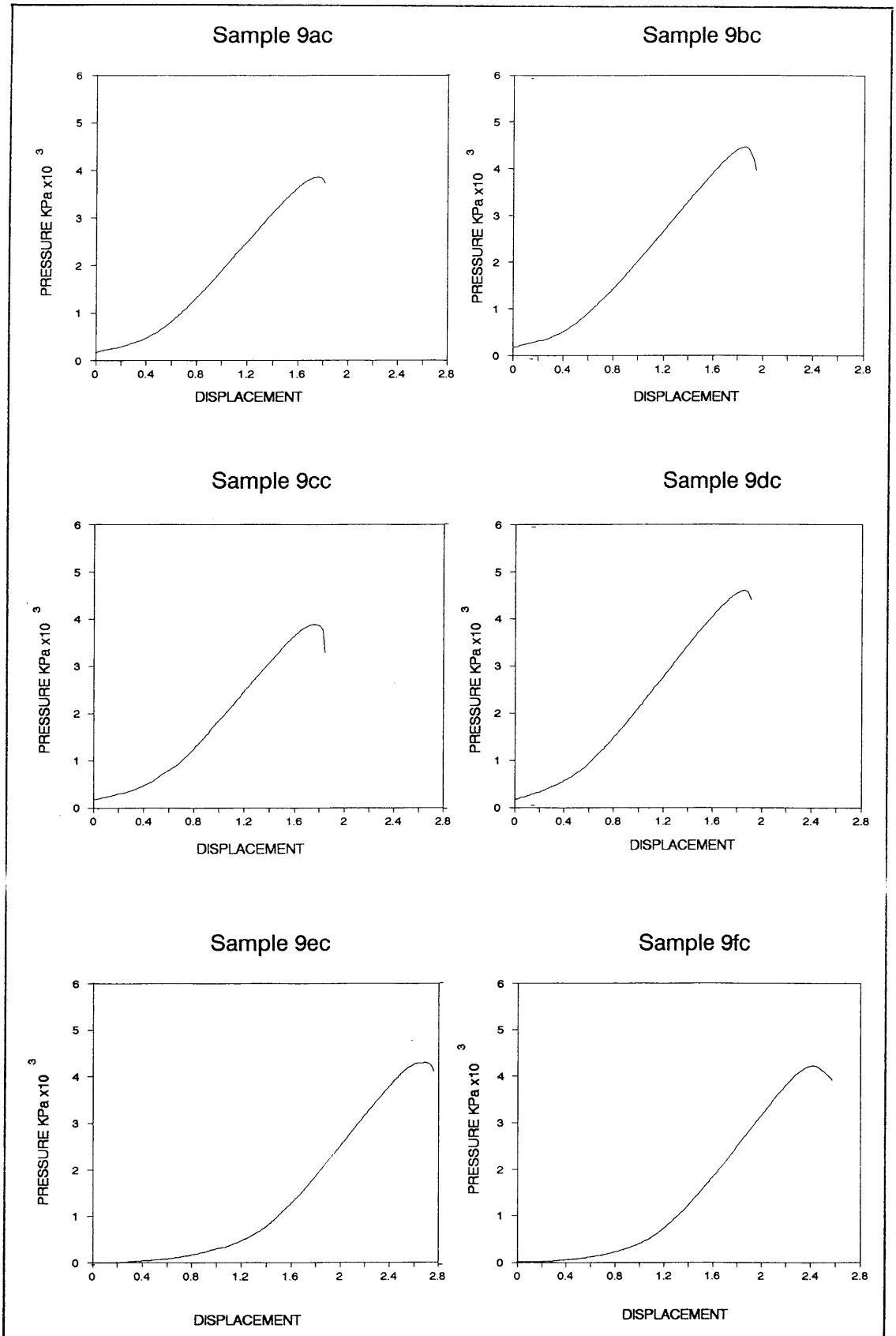


Fig. A7. 6 Curves obtained from samples loaded at the slow rate of loading

Table A7.2 Results obtained from the three rates of loading

ISRM RATE

SAMPLE	9Aa	9Ba	9Ca	9Da	9Ea	9Fa
FORCE N	1666.6700	1399.9986	1399.9986	1766.6649	1433.3319	
	2133.3300	1933.3314	1899.9981	2233.3311	2016.6646	
	2233.3300	2033.3313	1999.9980	2333.3310	2133.3312	
LOAD LINE	0.00111	0.0009768	0.0009324	0.0011988	0.000999	
DISPLACEM.	0.00146	0.0013764	0.0012876	0.0014985	0.001443	
m	0.00195	0.0017538	0.0016428	0.0019092	0.0022644	
WORK Nm	0.99160	0.75332	0.64602	1.18104	0.79032	
	1.76124	1.49147	1.32201	1.95471	1.66537	
	1.84556	1.57953	1.40637	2.04018	1.91364	

FAST RATE

SAMPLE	9Ab	9Bb	9Cb	9Db	9Eb	9Fb
FORCE N	1933.3314	1899.9981		2099.9979	1733.3316	1683.3316
	2566.6641	2599.9974		2733.3306	2499.9975	2533.3308
	2666.664	2666.6640		2816.66385	2533.3308	2583.3307
LOAD LINE	0.0011988	0.0011322		0.0012765	0.000999	0.0010434
DISPLACEM.	0.0016317	0.0015651		0.0016764	0.0014319	0.0015762
m	0.0020535	0.0019425		0.001998	0.0021312	0.0022977

SAMPLE	9Ab	9Bb	9Cb	9Db	9Eb	9Fb
	1.2321	1.14441		1.47297	0.90835	0.9460911
WORK Nm	2.27402	2.2008		2.49861	1.88515	2.11991
	2.40093	2.31809		2.59777	2.03093	2.29011

SLOW RATE

SAMPLE	9Ac	9Bc	9Cc	9Dc	9Ec	9Fc
	1366.6653	1599.9984	1566.6651	1766.6649	1566.6651	1599.9984
FORCE N	1899.9981	2199.9978	1883.33145	2249.99775	2133.3312	2133.3312
	1966.6647	2283.3310	1966.6647	2333.3310	2199.9978	2168.6610
LOAD LINE	0.0010101	0.00111	0.000999	0.0011766	0.0011322	0.000999
DISPLACEM	0.0014319	0.0015429	0.0013764	0.001554	0.0015429	0.0014319
m	0.0017982	0.001887	0.001776	0.001887	0.002109	0.001998
K	0.77441	0.9620	0.7585	1.12628	1.00492	0.97051
WORK Nm	1.52394	1.8426	1.43153	1.89366	1.84852	1.85777
	1.62161	1.94028	1.53476	1.99652	1.96766	1.95841

APPX 7.4

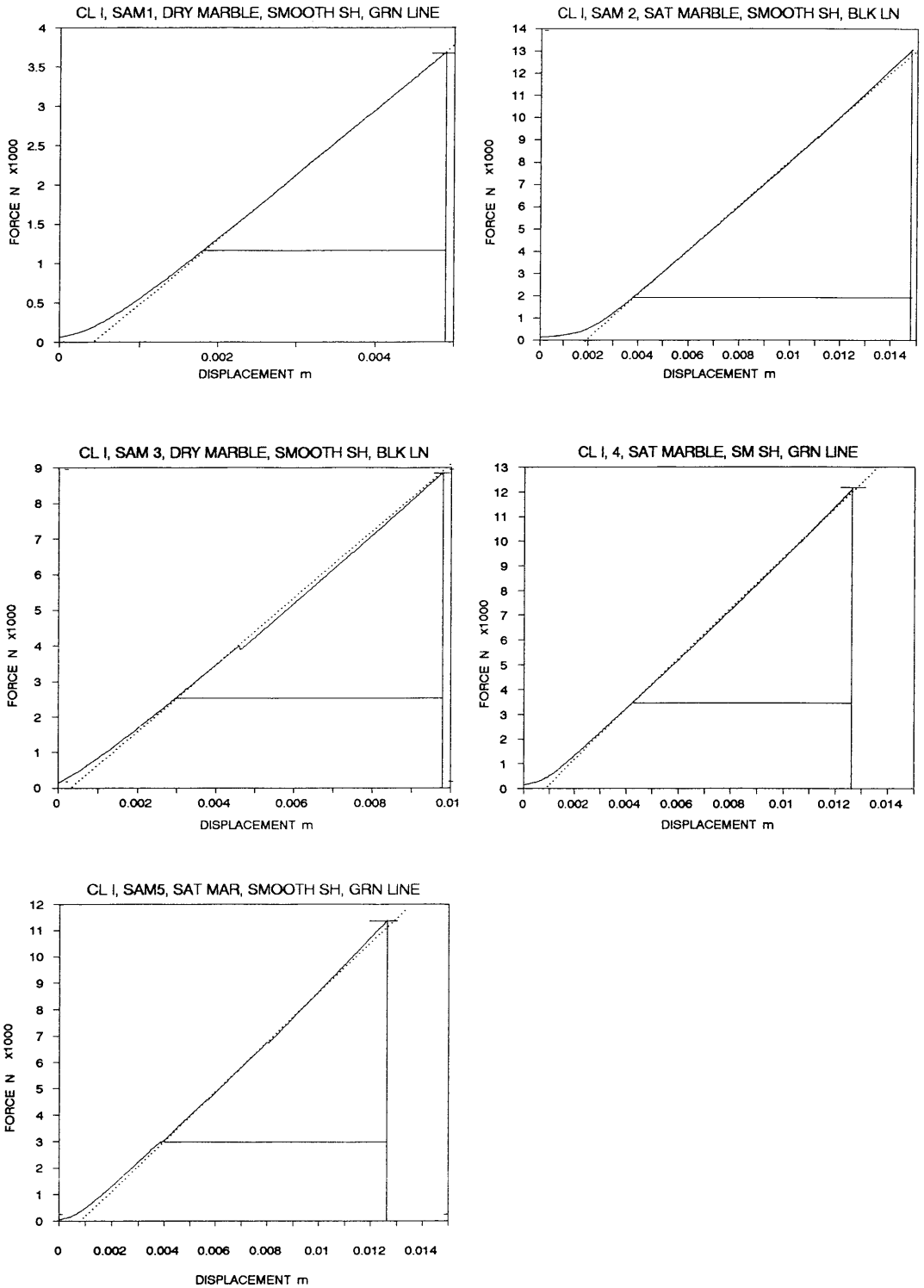


Fig. A7. 7 Curves obtained from marble hoops of class I

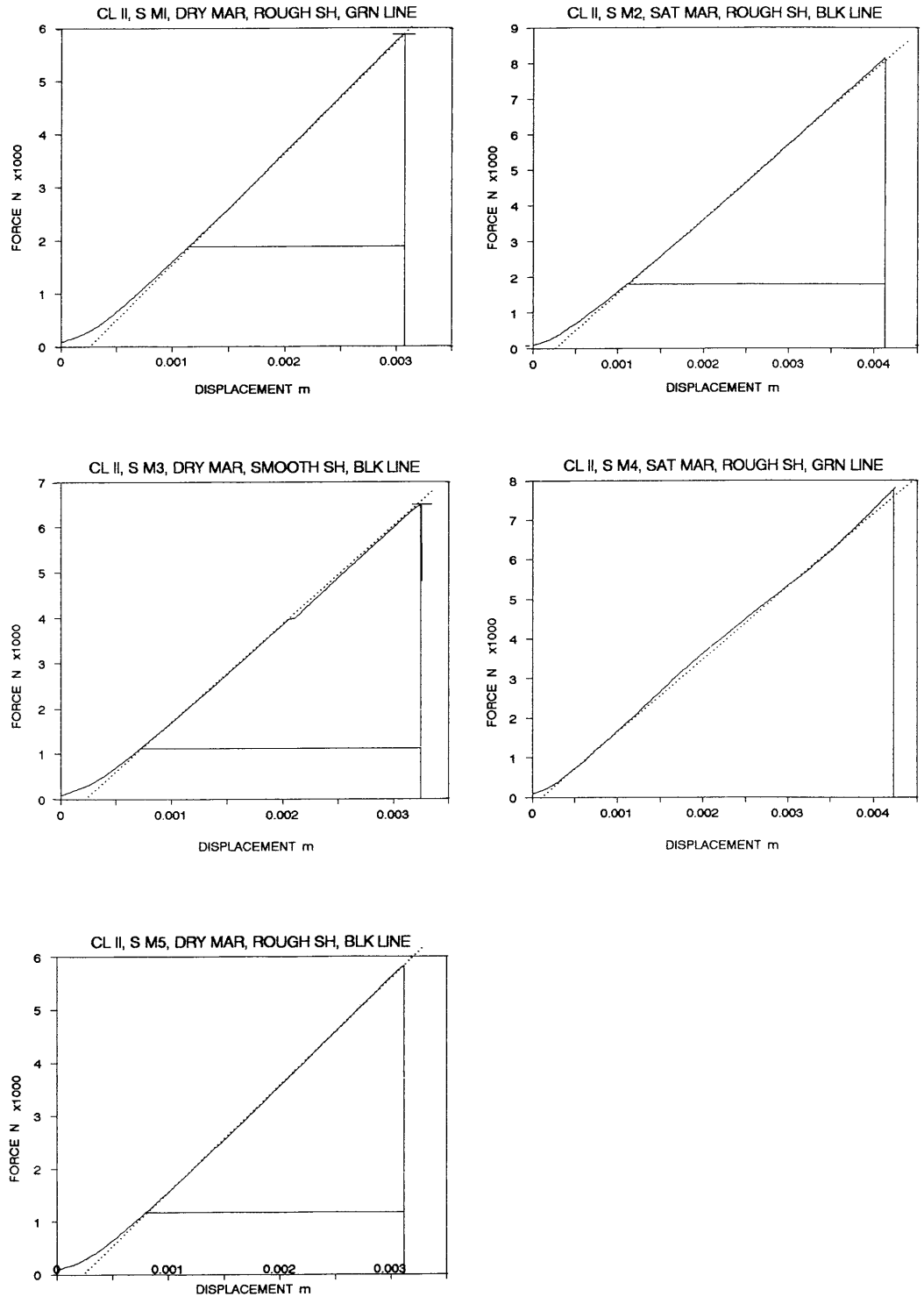


Fig. A7. 8 Curves obtained from marble hoops of class II

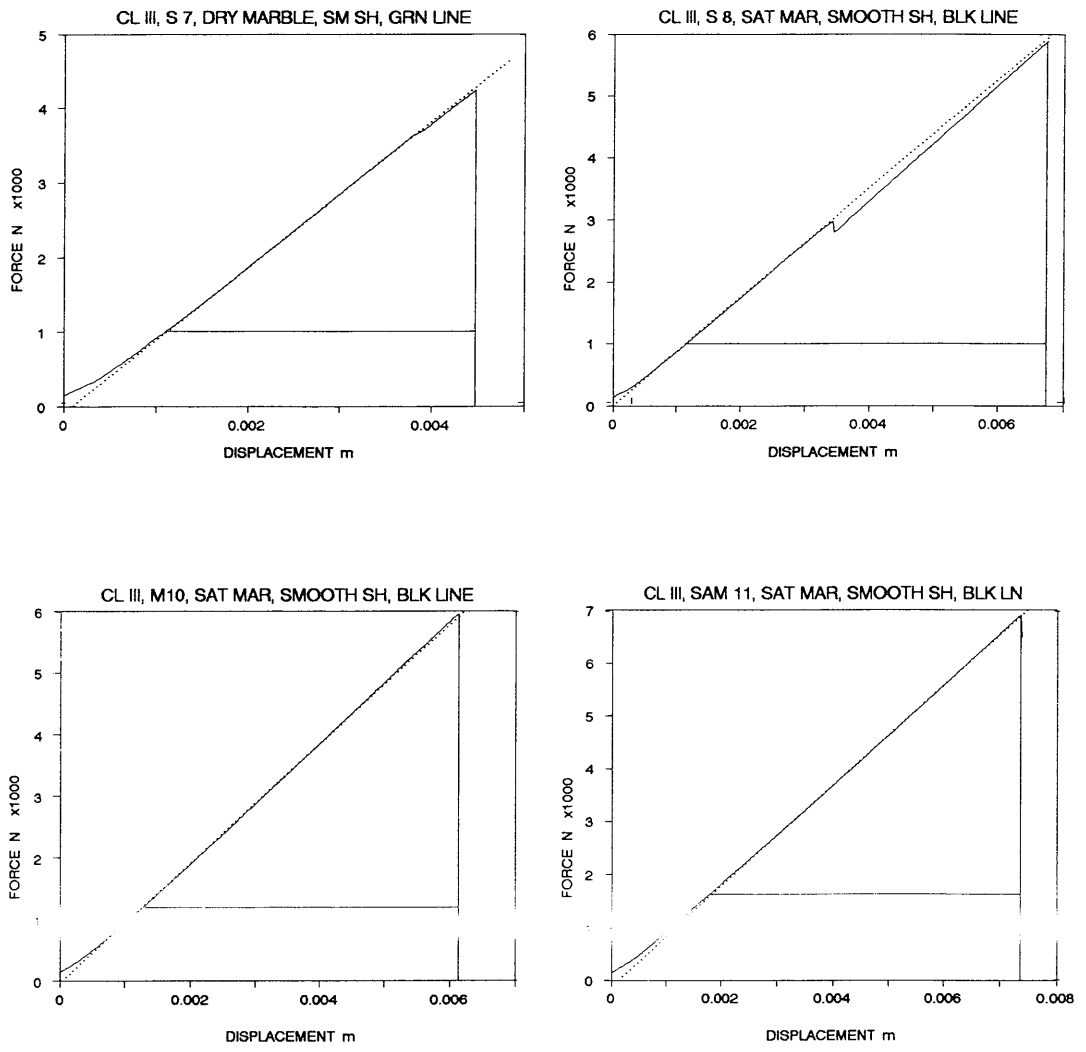


Fig. A7. 9 Curves obtained from marble hoops of class III

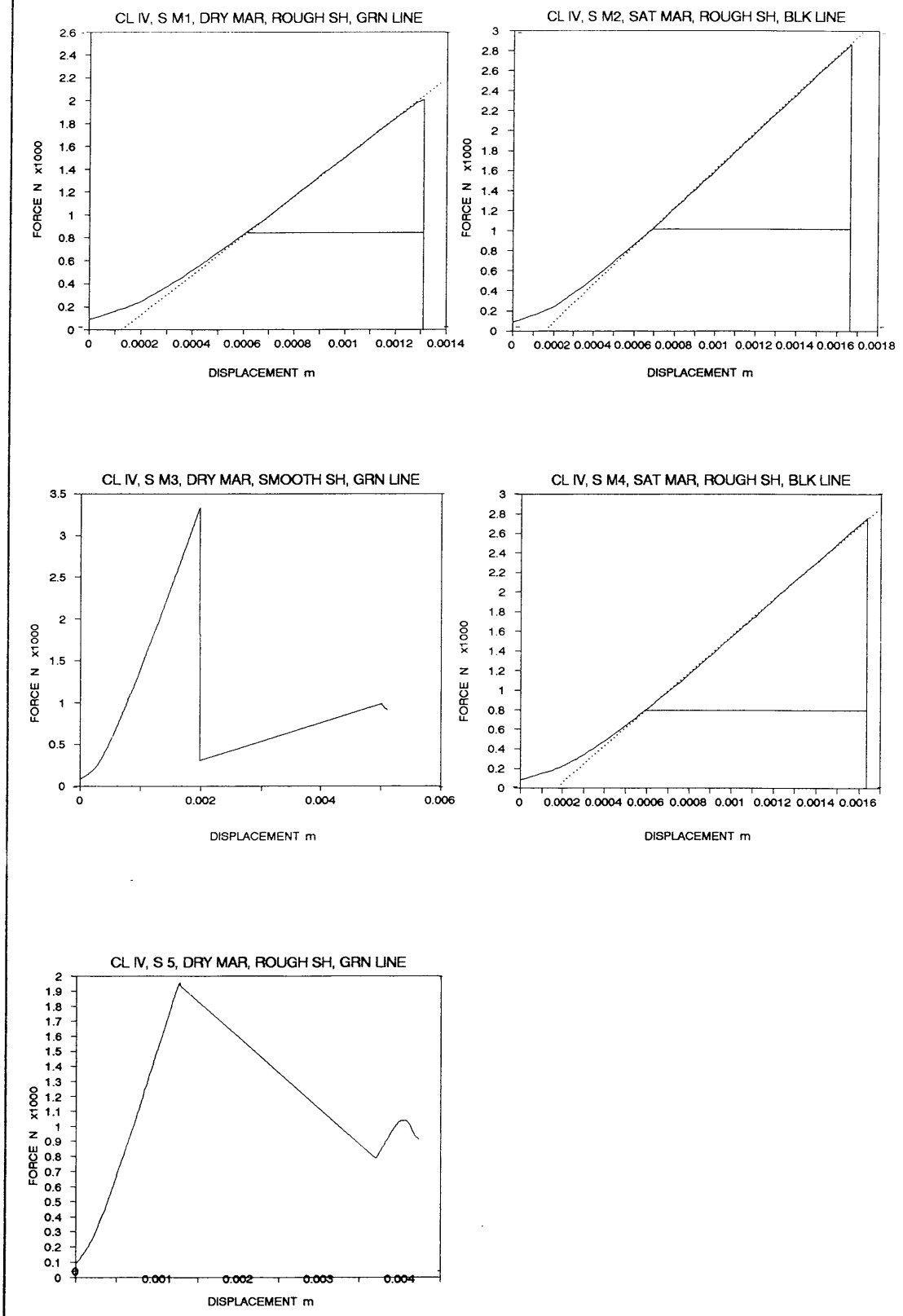


Fig. A7. 10 Curves obtained from marble hoops of class IV

Table A7. 3 Results used for the investigation of the influence of orientation, saturation, hoop size and roughness of platens in marble

	SAMPLE	M1/S1	M2/S2	M3/S2	M4/S2	M5/S2
	CONDITION	GSD	BSS	BSD	GSS	GSS
CLASS I	FORCE Newton	2545.45	11833.332	6500	8571.43	8399.979
			13499.999			
		3727.27	13833.332	8800	11999.999	11333.305
	DISPLAC meters	0.0030872	0.0011567	0.00736	0.088536	0.0091372
		0.00454	0.01428	0.00954	0.124236	0.0124236
			0.01556			
	WORK Nm	3.929	68.85	23.58	37.959	38.384
		8.461	94.39	49.76	74.571	70.400
		8.543	95.02			

CLASS II	SAMPLE	M1/S2	M2/S2	M3/S2	M4/S2	M5/S2
	CONDITION	GRD	BRS	BSD	GRS	BRD
	FORCE Newton	3999.999	6300	5307.692	6181.818	4666.667
		5866.666	8100	6384.615	7909.091	5866.667
	DISPLAC meters	0.0019032	0.003083	0.0025	0.003292	0.002281
		0.0027768	0.003958	0.003	0.00425	0.002844
	WORK Nm	3.8062	9.733	6.634	10.273	5.323
		8.1449	16.052	9.577	16.905	8.342
		8.2385	16.169	9.635		
CLASS III	SAMPLE	M7/S1	M8/S1	M10/1	M11/S1	
	CONDITION	GSD	BSS	BSS	BSS	
	FORCE Newton	3222.222	4866.667	4733.33	5230.769	
		4222.222	5866.667	5933.33	6807.692	
	DISPLAC meters	0.003364	0.005563	0.00475	0.0055	
		0.004455	0.006625	0.005938	0.007143	
	WORK Nm	5.414	13.273	11.242	14.385	
		9.399	19.171	17.615	24.313	

	SAMPLE	M1/S2	M2/S2	M4/S2
	CONDITION	GRD	BRS	GSD
CLASS IV	FORCE Newton	1142.857	1800	2133.33
		2000.000	2833	2733.33
	DISPLAC meters	0.0007333	0.0009833	0.00125
		0.00124	0.001533	0.0016
	WORK Nm	0.419	0.885	1.333
		1.240	2.172	2.187
			2.228	2.235

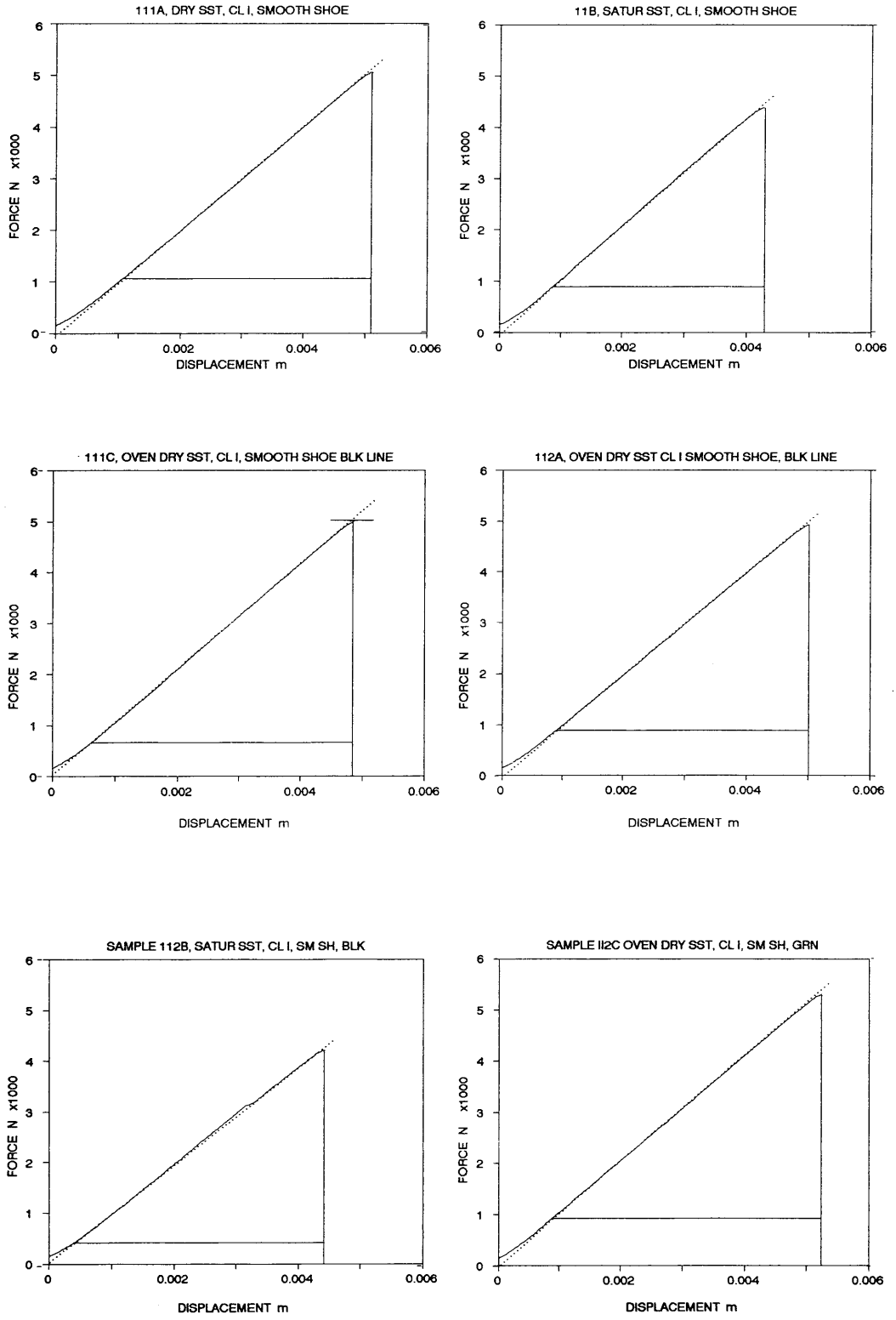


Fig. A7. 11 Curves obtained from sandstone hoops class I.

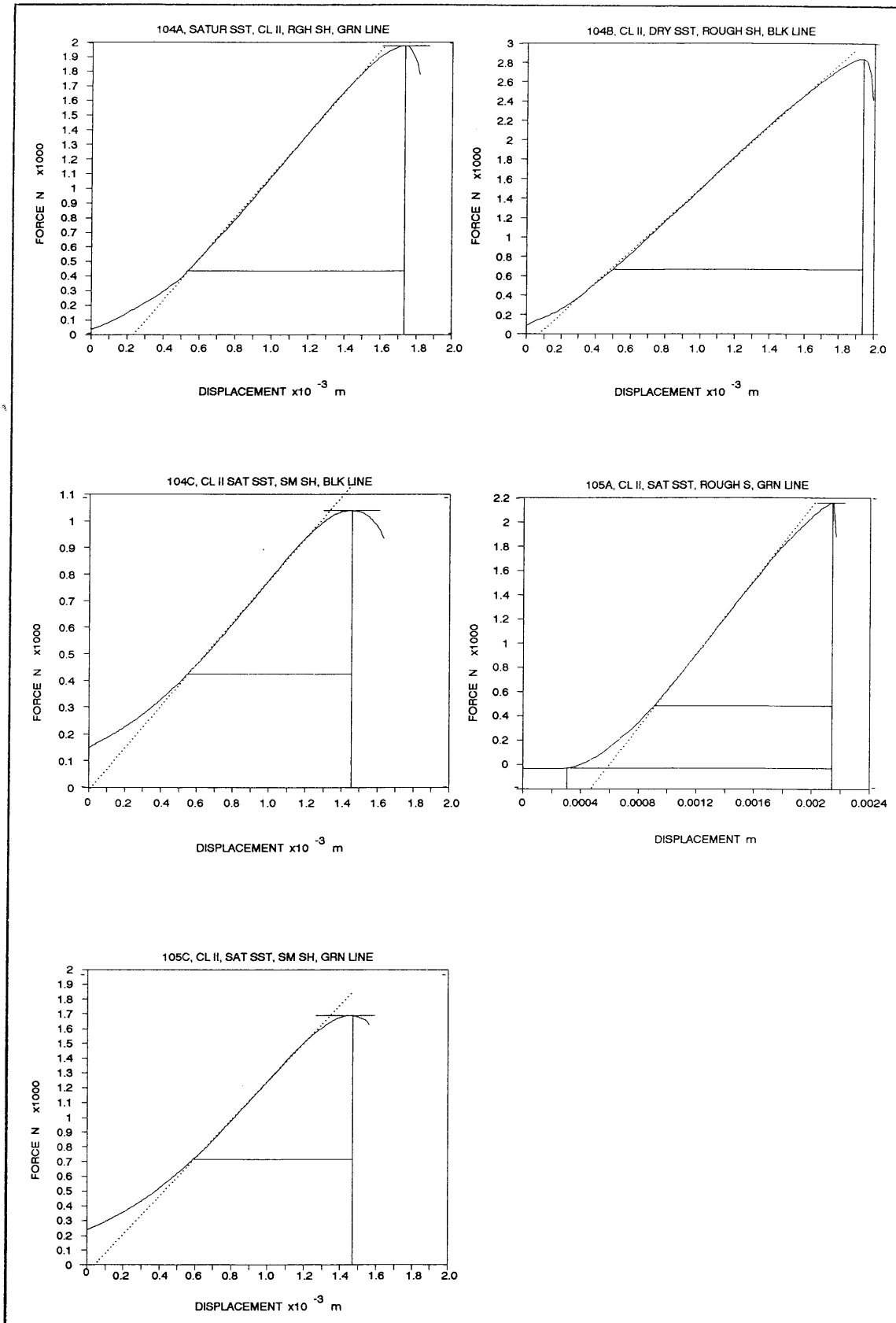


Fig. A7.12 Curves obtained from sandstone hoops class II.

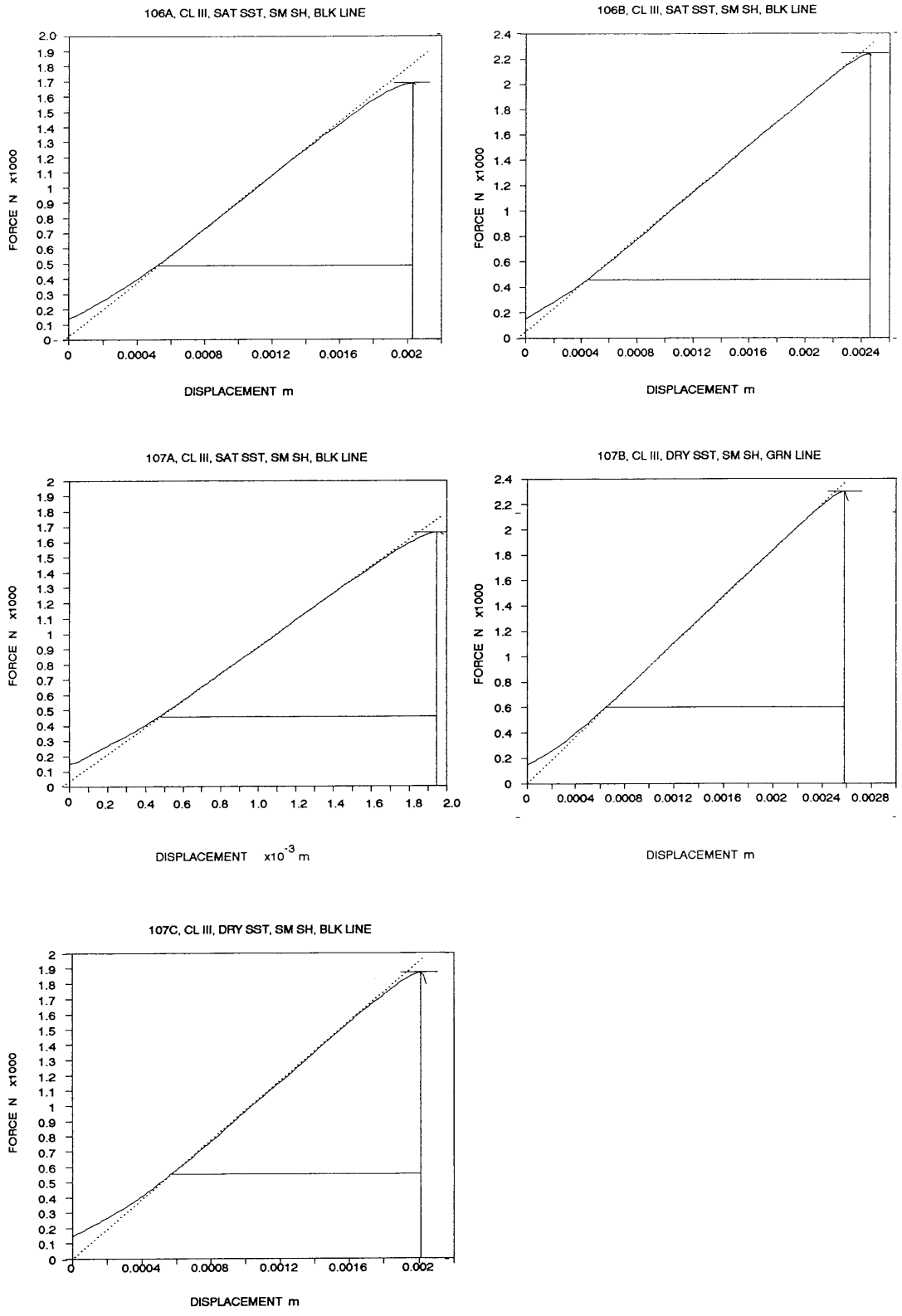


Fig. A7. 13 Curves obtained from sandstone hoops class III.

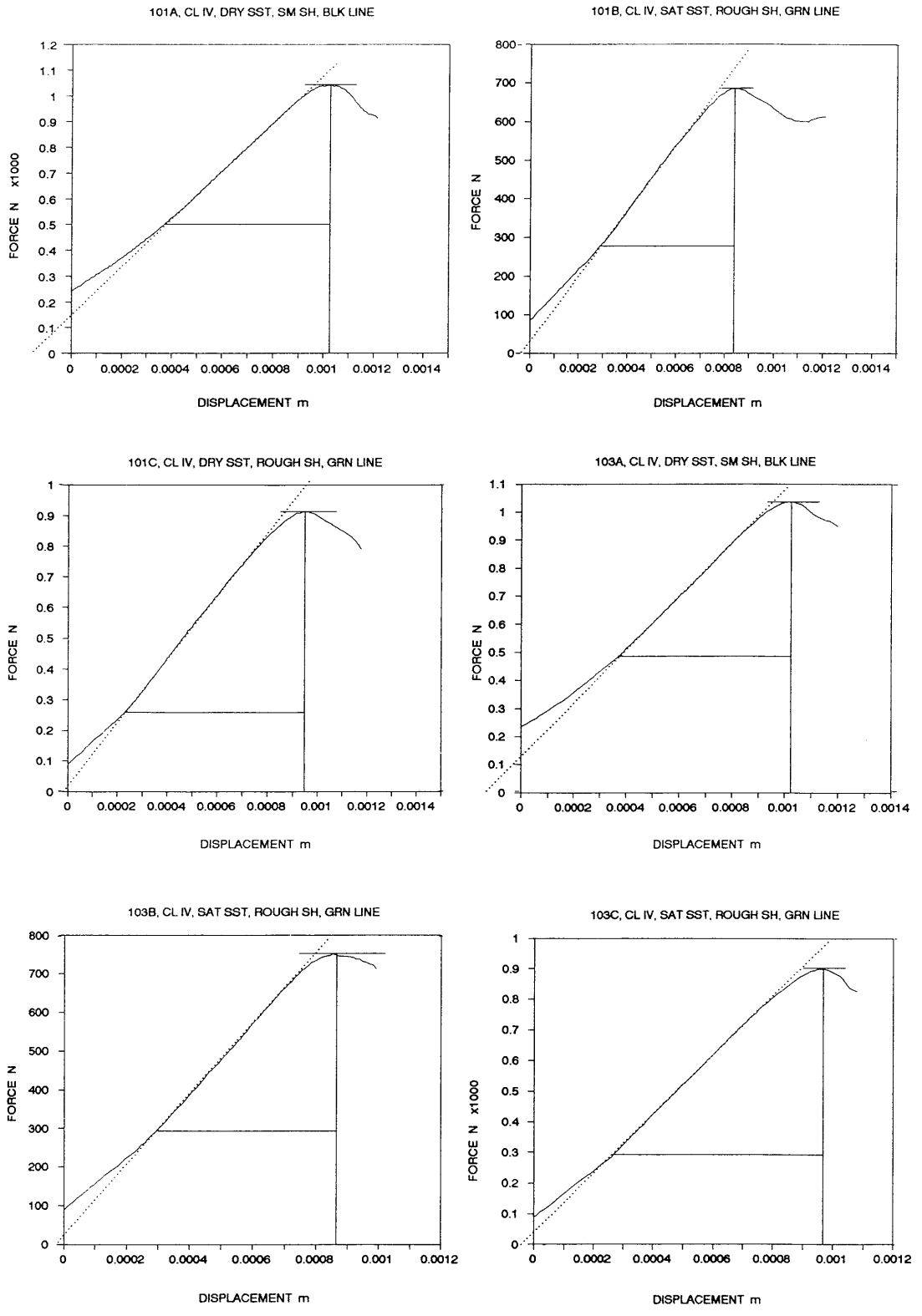


Fig. A7. 14 Curves obtained from sandstone hoops class IV.

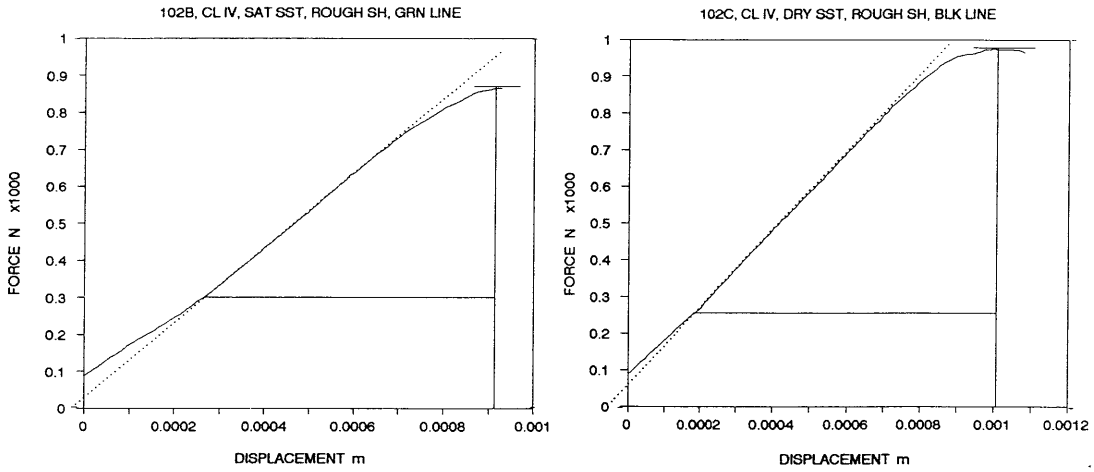


Fig. A7.14 Curves obtained from sandstone hoops class IV

Table A7. 4 Results used for the investigation of the influence of orientation, saturation, Hoop size and roughness of platens in sandstone.

	SAMPLE		11 1a	11 1b	11 1c	11 2a	11 2b	11 2c
	CONDITION		BSD	GSS	BSD	BSD	BSS	GSD
CLASS I	FORCE N	i	4000	3466.66	4400	4033.33	3800	4400
		ii						
		iii	5066.62	4366.66	4933.33	4866.66	4200	5266.66
	DISPL m	i	0.004	0.003405	0.00427	0.004054	0.004107	0.004324
		ii	0.00503	0.0042702	0.00486	0.004956		0.005189
		iii					0.004551	
	WORK Nm	i	8.130	6.1225	9.5296	8.307	7.599	9.650
		ii	12.897	9.3873	11.9927	2.194	9.308	14.004
		iii						
	SAMPLE		10 4a	10 4b	10 4c	10 5a	10 5b	10 5c
	CONDITION		GRS	BRD	BSS	GRS		GSS
CLASS II	FORCE N	i	533.33	2166.45	625	1575		947.78
						2075		
		iii	1977.78	2800.00	1062.5	2200		1689.0
	DISPL m	i	0.0012	0.0016	0.000909	0.00127		0.000891
		ii	0.00151	0.0020	001455	0.00171		0.00144
		iii				0.00247		

		i	1.000	1.8698	0.2759	1.082		0.4917
	WORK Nm	ii	1.596	3.040	0.8282	1.896		1.3115
		ii				1.966		
	SAMPLE		10 6a	10 6b		10 7a	10 7b	10 7c
	CONDITION		BSS	BSS		BSS	GSD	BSD
		i	1200	1675		1350	1587.5	1310.98
	FORCE N	ii						
CLASS III		iii	1689	2100		1850	2150	1866.48
		i	0.00152	0.00215		0.002025	0.002028	0.00146
	DISPL m	ii	0.00208	0.00268		0.00275	0.002714	0.00202
		iii						
		i	0.8981	1.852		1.4581	1.6693	1.000
	WORK Nm	ii	1.7380	2.873		2.6712	2.9814	1.947
		iii						
	SAMPLE		10 1a	10 1b	10 1c	10 3a	10 3b	10 3c
	CONDITION		BSD	GRS	GRD	BSD	GRS	GRS
		i	500	418	655.49	562.5	463.64	611.11
	FORCE N	ii						
CLASS IV		iii	975	700	911.02	1062.5	763.64	900.0
		i	0.0006864	0.000572	0.0007579	0.00065	0.0005772	0.000722
	DISPL m	ii	0.001258	0.0009295	0.001015	0.00115	0.0009102	0.00103
		iii						

	i	0.1905	0.1321	0.2424	0.20	0.1525	0.2403
WORK Nm	ii	0.6502	0.3475	0.5013	0.64	0.3454	0.5003
	iii						

SAMPLE			10 2b	10 2c
CONDITION			GRS	BRD
CLASS IV	FORCE N	i	566.61	722.15
		ii		
		iii	866.58	966.57
	DISPL m	i	0.000654	0.0008436
		ii	0.000954	0.0001088
		iii		
	WORK Nm	i	0.205	0.2883
		ii	0.404	0.596
		iii		

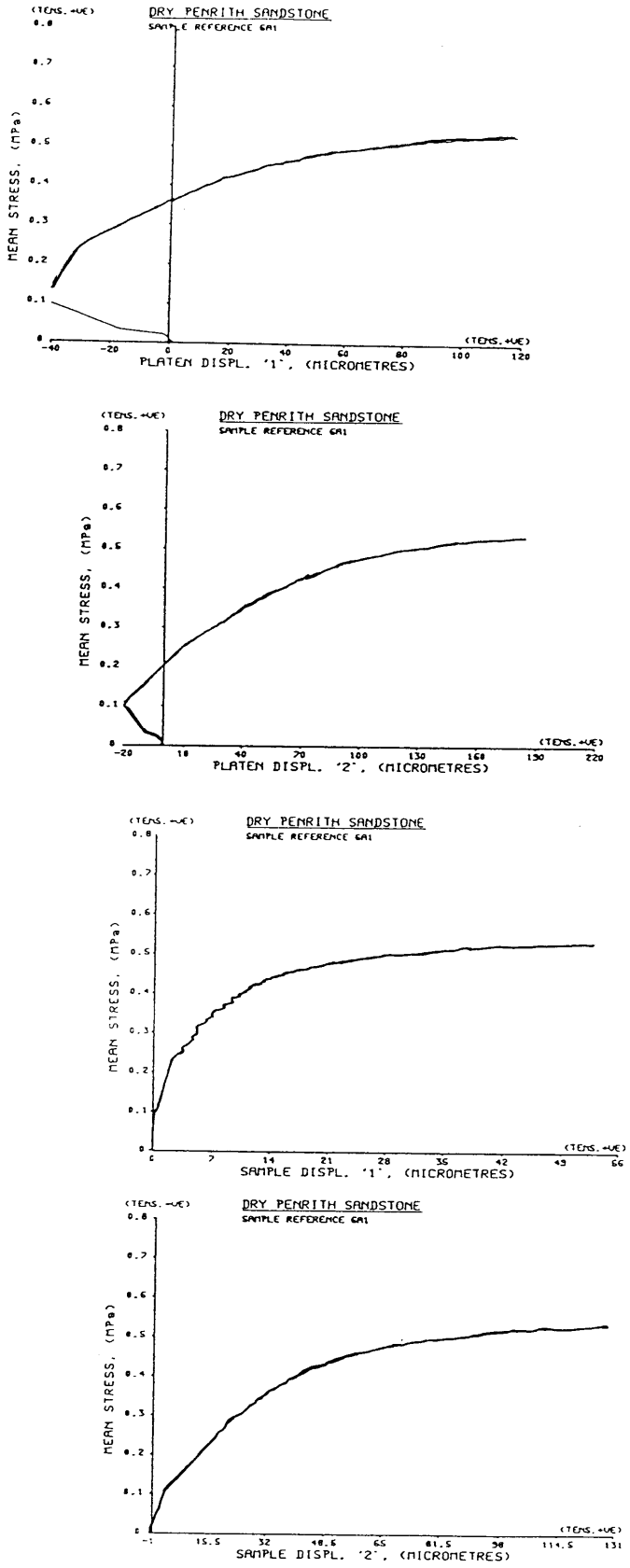


Fig. A7.15 Curves obtained from testing with the Terra-Tek (sample 6a1)

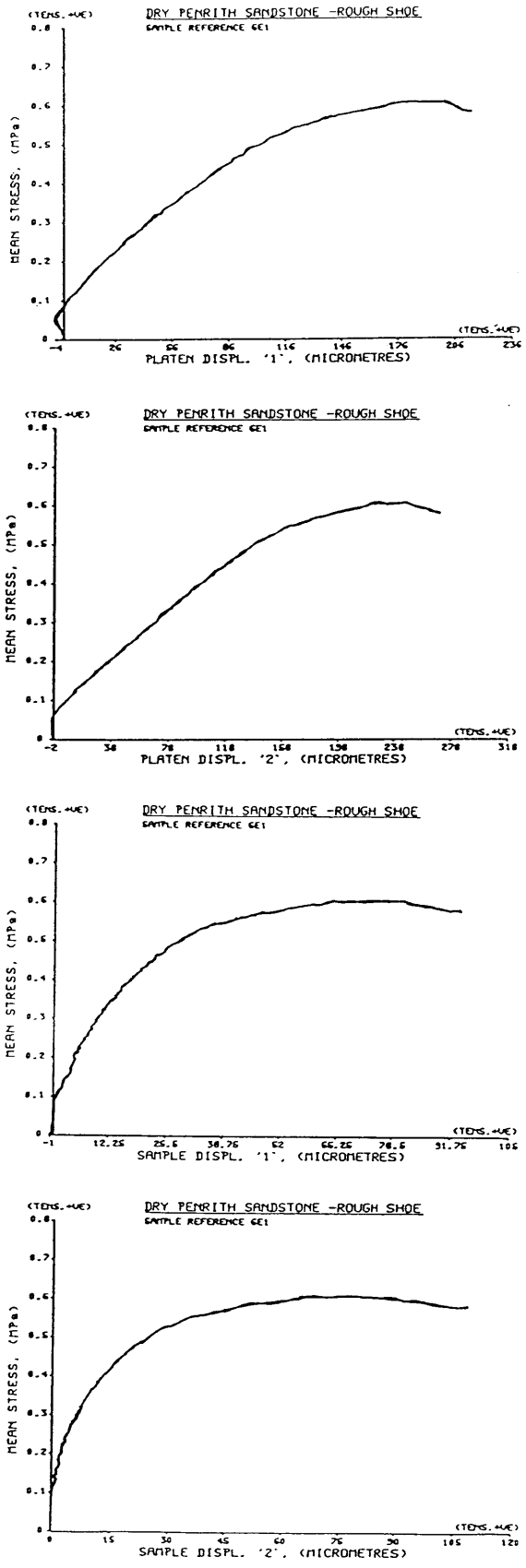


Fig. A7. 16 Curves obtained from testing with the Terra–Tek (sample 6e1)

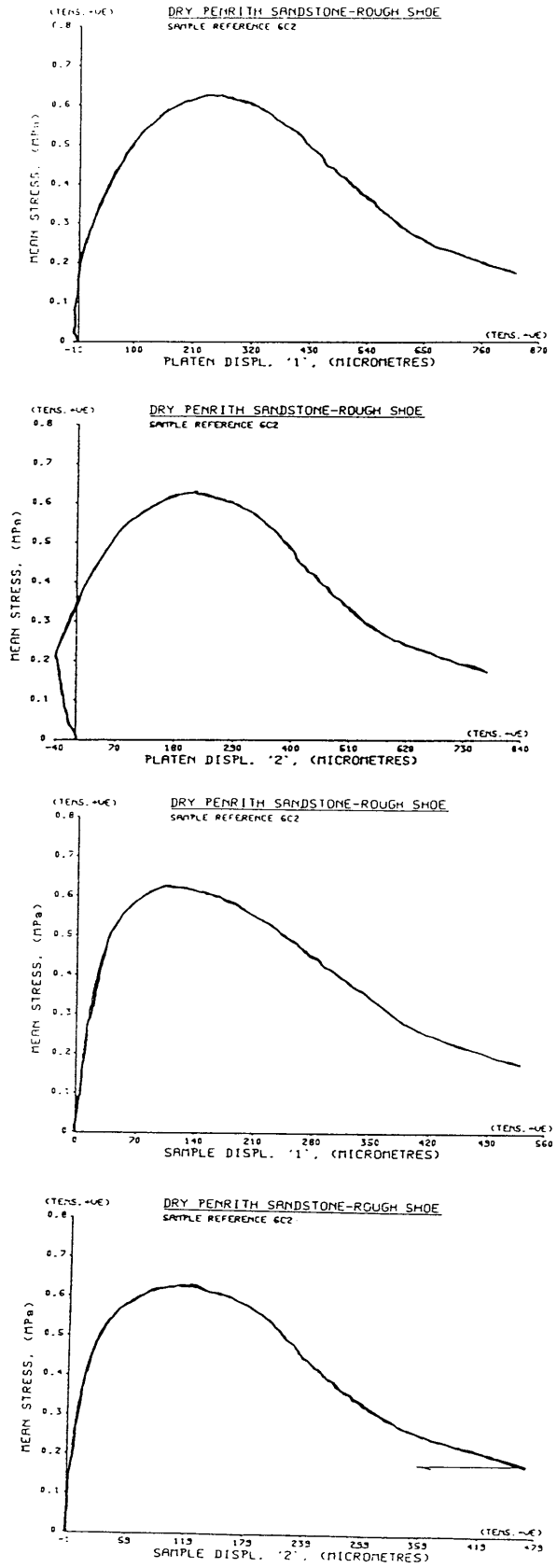


Fig. A7. 17 Curves obtained from testing with the Terra-Tek (sample 6c2)

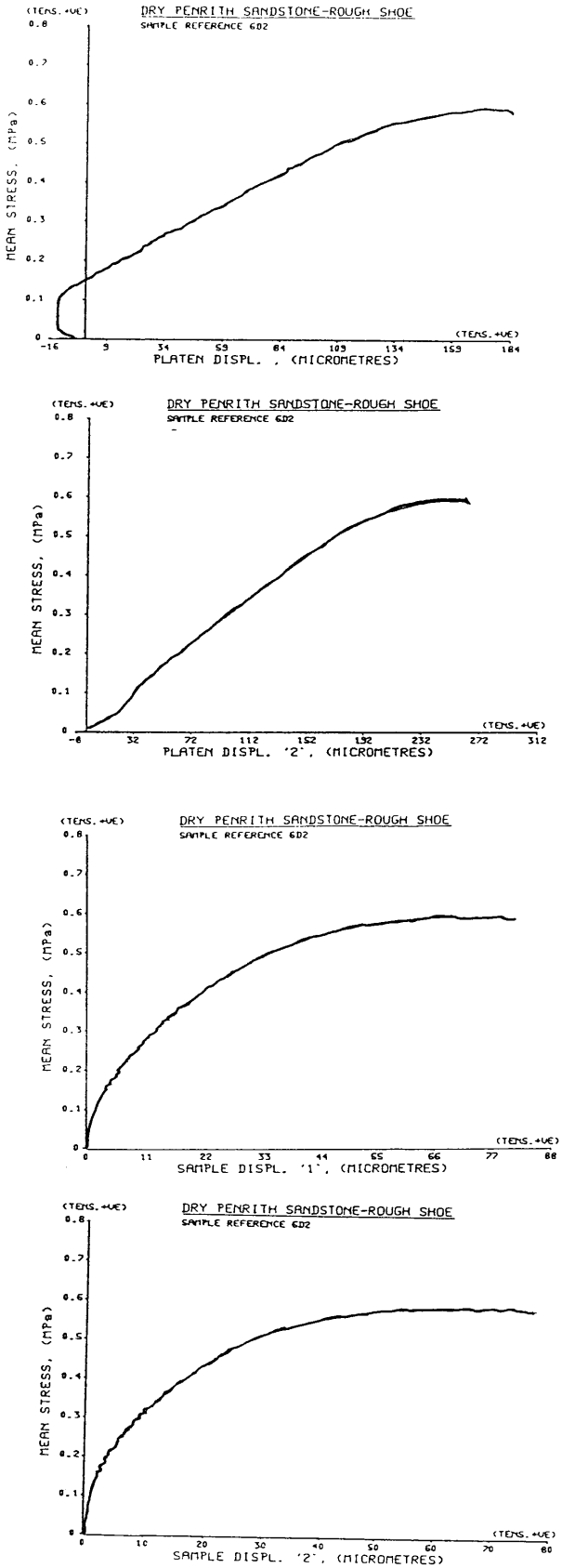


Fig. A7. 18 Curves obtained from testing with the Terra-Tek (sample 6d2)

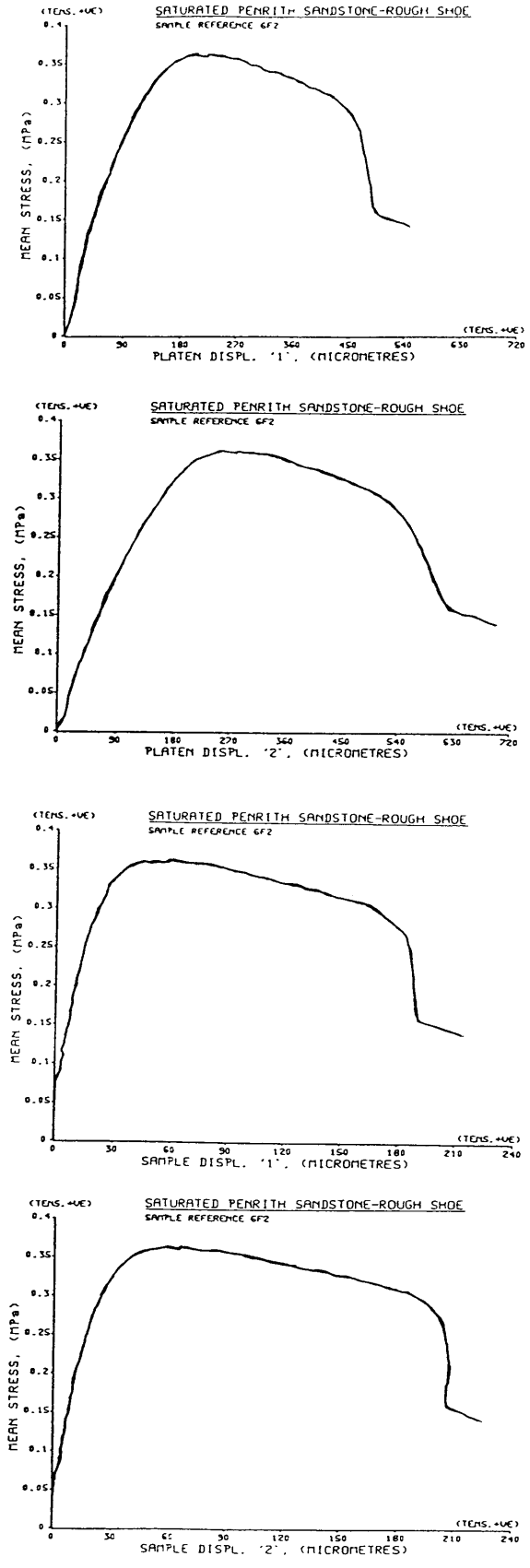


Fig. A. 19 Curves obtained from testing with the Terra-Tek (sample 6f2)

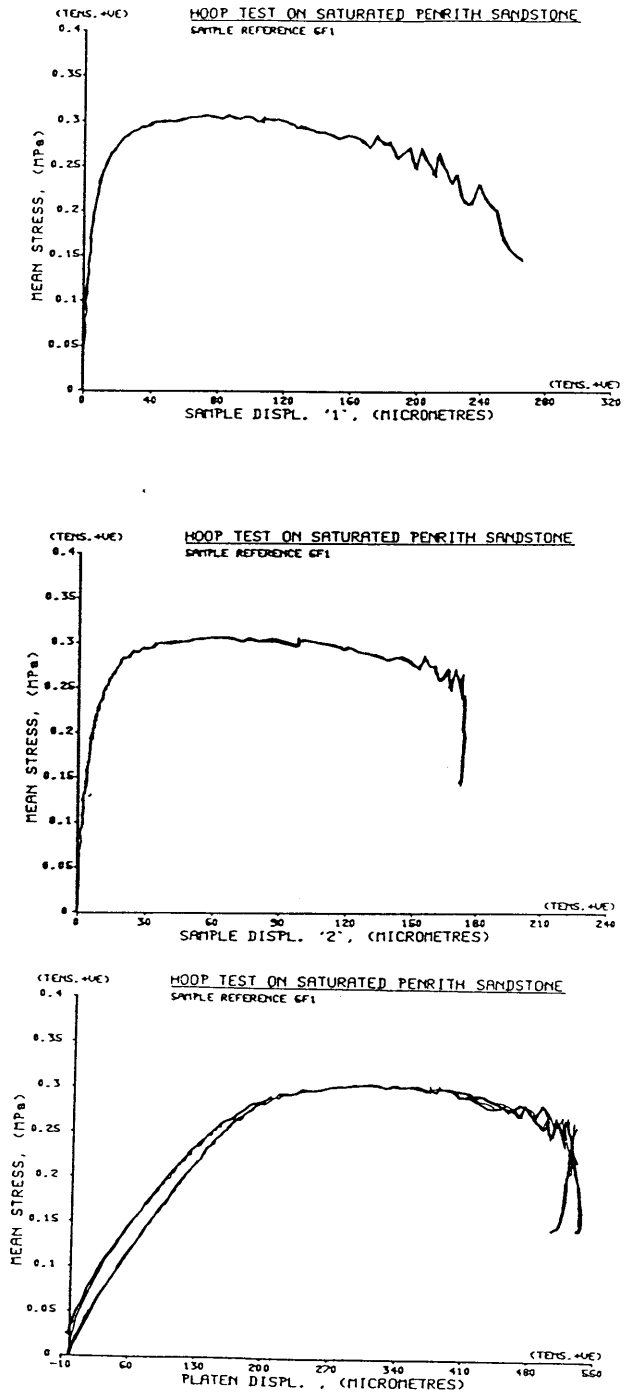


Fig. A7. 20 Curves obtained from testing with the Terra-Tek (sample 6f1)

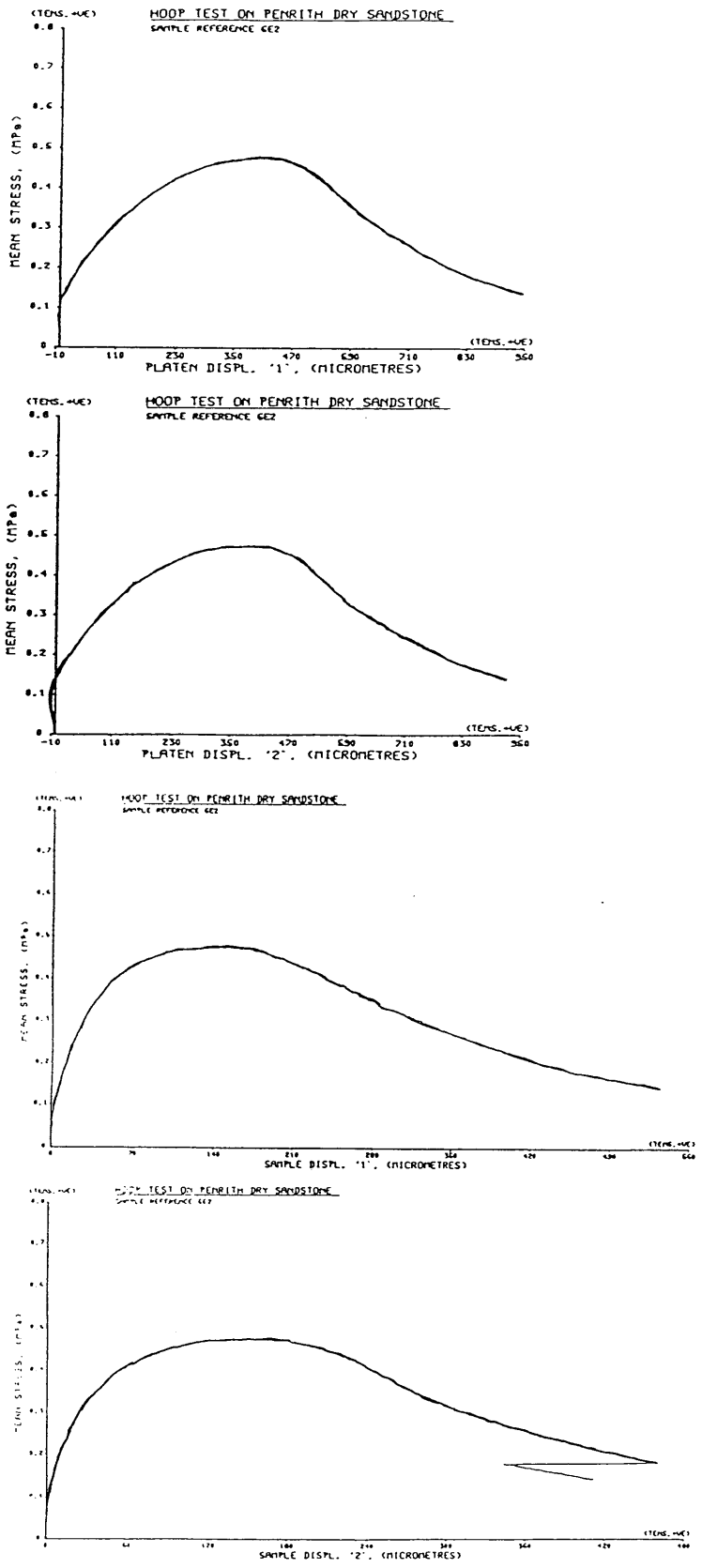


Fig. A7. 21 Curves obtained from testing with the Terra-Tek (sample 6e2)

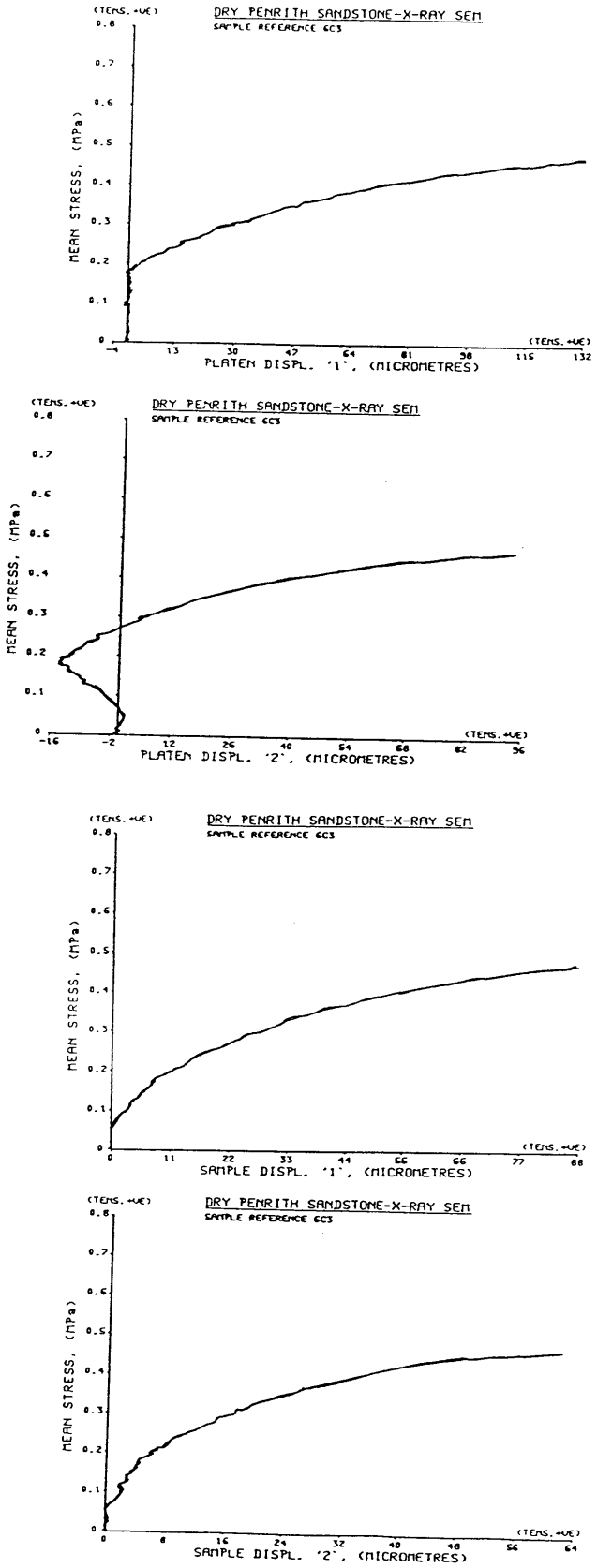


Fig. A7. 22 Curves obtained from testing with the Terra-Tek (sample 6c3)

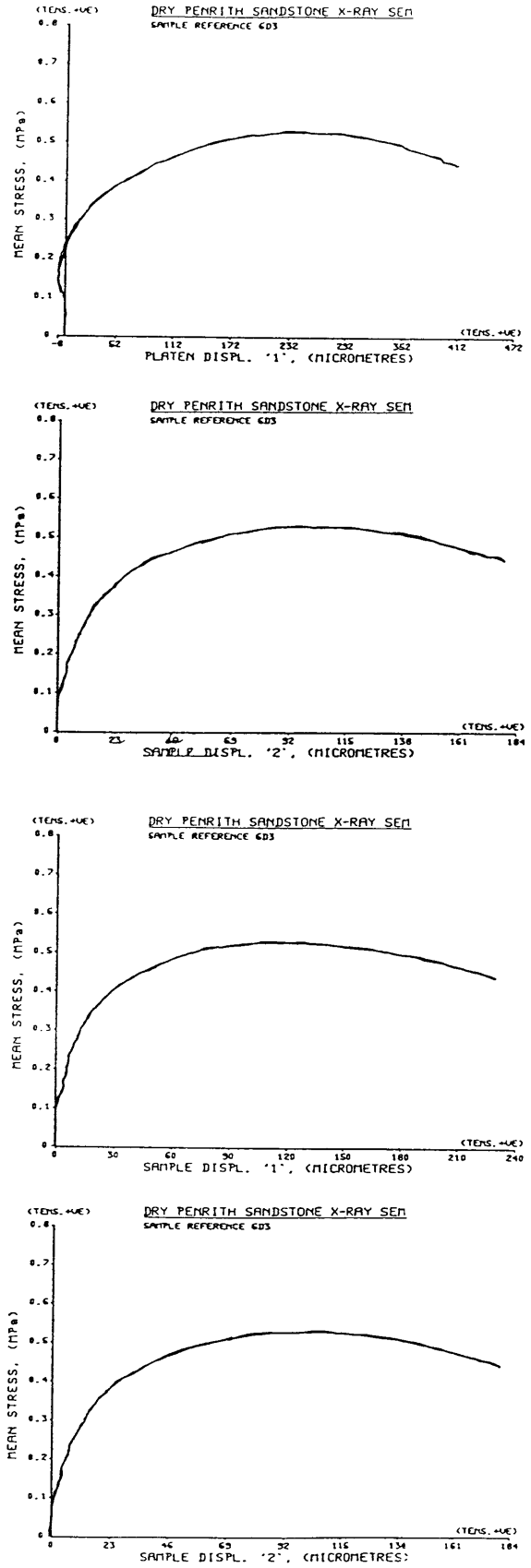


Fig. A7. 23 Curves obtained from testing with the Terra-Tek (sample 6d3)

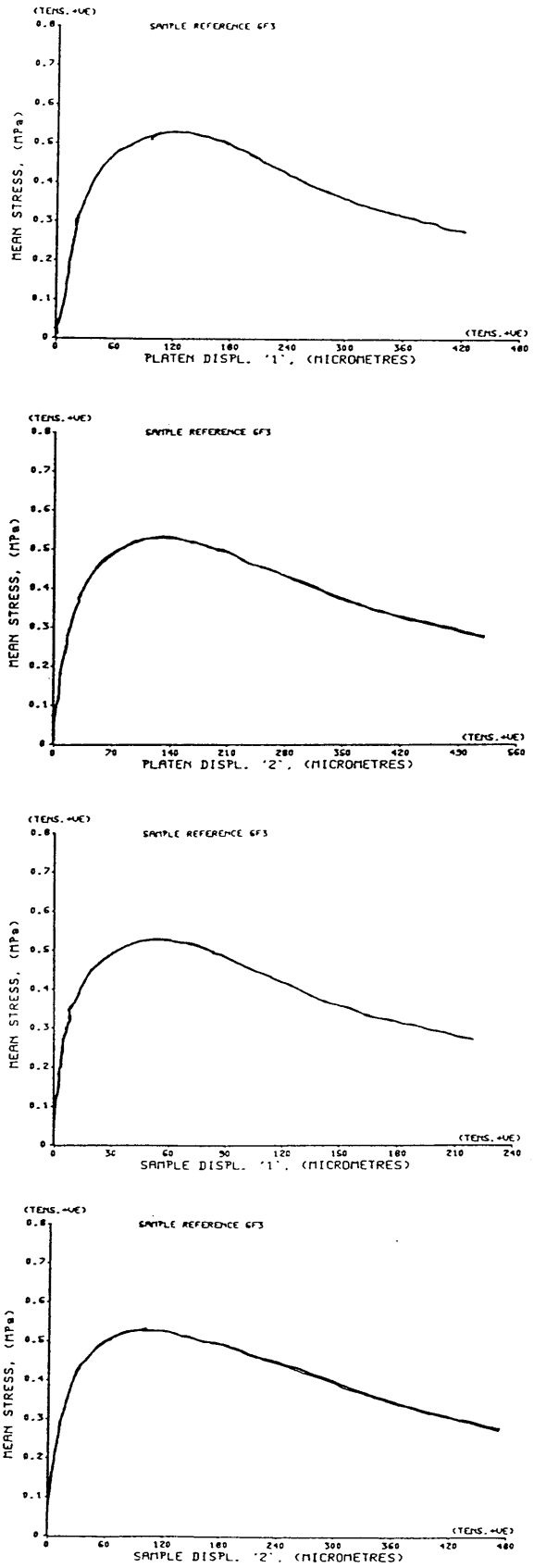


Fig. A7. 24 Curves obtained from testing with the Terra-Tek (sample 6f3)

GENERAL APPENDIX TO THE THESIS

FORMULAE USED FOR CALCULATIONS

$$Bulk\ \ volume\ (V) = \frac{M_{sat} - M_{sub}}{\varrho_w}$$

$$Bulk\ density = \frac{M_s + M_w}{V}$$

$$Dry\ density = \frac{M_s}{V}$$

$$Porosity\ (n) = \frac{V_v}{V}$$

Where: M_{sat} = mass saturated, M_{sub} = mass submerged,

M_s = mass of solids, M_w = mass of water,

V_v = volume of voids, V = bulk volume, ϱ = density, ϱ_w = density of water

$$Unconfined\ Compressive\ Strength\ (UCS) = \frac{L}{A}$$

$$Tensile\ strength\ \sigma = \frac{0.636P}{Dt}$$

$$for\ \ BT$$

$$Tensile\ strength\ \sigma = \frac{L}{A}$$

$$for\ \ DTT$$

Where: P = load at failure, A = area of sample, D = diameter of sample,

t = thickness of sample.

$$V_p = \frac{L}{t}, \qquad V_s = \frac{L}{t}$$

$$E_{dyn} = \varrho\, V_s^2 \left[\frac{3V_p^2 - 4V_s^2}{V_p^2 - V_s^2} \right]$$

$$\nu_{dyn} = \left[\frac{V_p^2 - 2V_s^2}{2\,(V_p^2 - V_s^2)} \right]$$

Where: V_p = velocity of P waves, V_s = velocity of S waves, t = time, ϱ = density of rock, E_{dyn} = dynamic Young's modulus of elasticity, ν_{dyn} = dynamic Poisson's ratio, L = length of core

Mean deviation

$$m = \frac{\sum (X - \bar{X})}{n}$$

Variance, mean square deviation

$$\sigma^2 = \frac{\sum (X\ \bar{X})^2}{n}$$

Standard deviation

$$\sigma = \sqrt{\left(\frac{\sum X^2}{n} - \bar{X}^2 \right)}$$

Coefficient of variation

$$\frac{2\sigma}{m} \times 100$$

SUPPLEMENT

S.1 INTRODUCTION

This supplement has been written to assist any future investigator organise a further programme of research to extend the findings of chapter seven. The author is particularly concerned to record her experience with respect to items (i) to (iv) on p268 in view of the fact that at the time this research was started very little was known about the HTT and how hoops of rock actually fail. Xu,S. et al described the test but the distribution of stress they described within the hoop was later found by the work of Chapter 4.2 to be incorrectly defined; further, Xu left no record of the mathematical distribution of that stress in print; John et al provided the correct distribution of that stress based on the results shown in Chapter 4.2 but still did not define how the magnitude of stress could be calculated. Park did not commence his work until the test programme described here has essentially been completed. The four items listed on p268 can be expanded as follows:

(i) Shape, particularly orthogonality of specimen end faces to specimen axis, is a major factor of practical significance during specimen preparation. The effect of parallelism, expressed as the angle that the upper or lower surface of the hoop specimen makes with the horizontal (some variations of which are shown in fig. S.1) has not been investigated. This information is required to establish the dependence of hoop stress at failure (or work at failure) as a function of specimen shape expressed here as the angle at which a hoop is cut orthogonally to the hoop's axis.

(ii) The configuration of the hoop allows it to be considered in either plane stress or plane strain with respect to the axis of the hoop. Hoop thickness should, in theory, not affect the distribution of stress within the sample; it was for this reason that the thickness of the hoop specimens was kept "constant" for the tests conducted in the course of this research (thickness varied between 42 to 52 mm, as shown in Appendix 7.1 p305 to p310). Although the distribution and magnitude of stress should not change with changing thickness, the work required

to create failure will change as the volume of the sample changes and this change of work with volume should be verified. It will therefore, be useful to examine several other thicknesses to establish how this parameter influences the results; any influence recognised will enable an optimum thickness to be established for the purpose of commercial testing.

(iii) The interval of each rate of loading needs to be smaller in order to establish the one at which the test becomes insensitive to its rate of execution. The rates used and reported in 7.2, p212, do not totally fulfil the object of the study, as the range of rates within the "ISRM" and "slow" rates is quite considerable giving results, as seen in fig. 7.4 and fig. 7.5, that are spread.

(iv) The ratio of diameters has been investigated in the four "classes" of hoops which have been used in the course of this research, the sizes of which are mentioned in table 6.3 on p190. A further investigation should point out the most appropriate ratio of diameters for the HTT. In some respects this is the same problem described for changing hoop thickness, because the volume of the hoop changes as its diameters change. Two important facts have been established about the hoop viz. that compression occurs as the outside radius increases and that this compression is the most likely cause for the differences seen with changing hoop size. This effect should be studied.

For all the above mentioned points it should be remembered that at present the performance of the HTT can only be seen in terms of Load and Displacement, and location and character of cracks.

S.2 GENERAL GUIDELINES FOR SAMPLE COLLECTION AND THE NUMBER OF SAMPLES TO BE TESTED:

When the samples used in this thesis were collected the sensitive behaviour of rock in extension was not sufficiently appreciated and neither the quality nor the numbers of specimens were really sufficient for the stated purpose of the research to be confidently concluded. Therefore, a sampling technique must be adopted

which considers

(a) the relation of the samples to the natural structural environment and

(b) homogeneity.

The first factor can be satisfied if the samples are collected in-situ and carefully marked in relation to the natural joints, ground level and orientation of the exposed quarry face from which they are collected (information required to determine the likely direction of local remnant, or residual, stresses). The second factor can be considered if the chosen blocks from which the samples will be prepared can be subjected not only to visual inspection but also to basic index tests such as measurement of P and S wave velocities.

The problem of sufficient quantity of material for the investigation of any one parameter must also be resolved. The number of samples used in the investigations for the influence of the rate of loading and other parameters was 5 to 6. This was shown to be enough to indicate trends but was not sufficient to inspire confidence in the results. Therefore the number of tests which must be used for further experimental investigation should be greater in number than 5 to 6 and the minimum number of 10 to 15 is suggested; the upper limit will be controlled by the homogeneity of the material and this in some materials is likely to impose severe restrictions on the amount of material that can be tested e.g. as when testing between particular bedding laminae.

S.3 TESTING PROGRAMMES FOR ESTABLISHING THE INFLUENCE OF VARIOUS PARAMETERS.

S.3.1 Testing programme for establishing the effect of parallelism.

The specimens to be used for the investigation of parallelism must be prepared in such a way that one group consists of the "flat" i.e parallel samples and the other groups are the non parallel samples. The guidelines to be followed for the sample preparation should be those applied for the preparation of cores used for the

determination of the uniaxial compressive strength of rock materials (Brown E.T. 1987). From the hoops used in this research, whose measurements are presented in Appx. 7.1 p305 to p310, it is seen that the maximum value of angle a° (which expresses the parallelism) is 1.26°. It is suggested that in addition to the group of "flat" samples three more groups of samples are prepared where angle a°= 2°, 4°, and 6° in variations as shown in fig. S.1. The location of the piston side of the platens must be marked on each sample and care must be taken to record if any particular side of the hoop fails first.

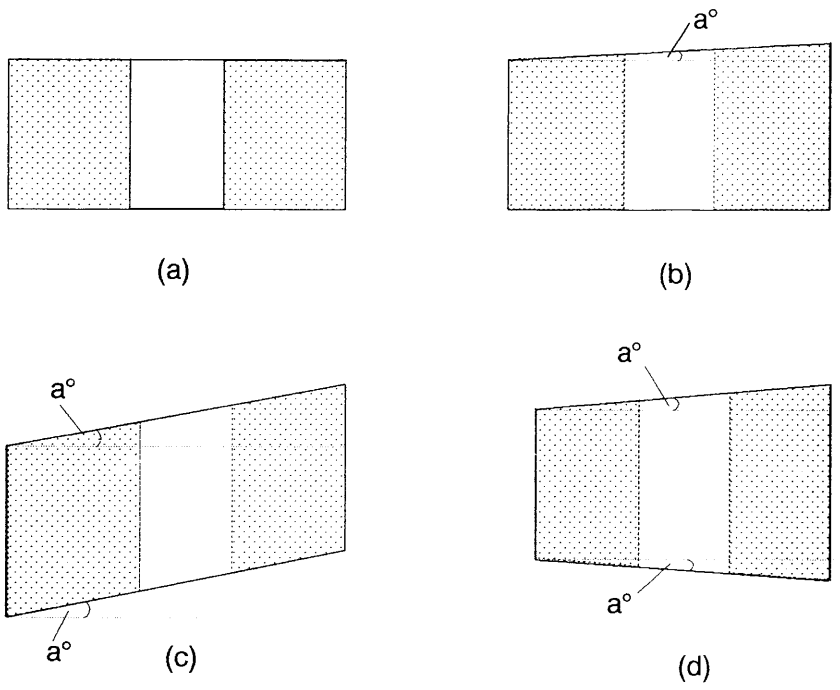


Fig. S.1 A schematic representation (exaggerated) illustrating the variations of parallelism of hoops used in the HTT.
Diagram (a) represents the "flat" samples and diagrams (b-d) represent the out of parallelism cases.

Seven sets of tests are required for any radius ratio R/r (where r is the radius of the platen, 50 mm and 30 mm, and R the outer radius) and any angle a° as shown in fig. S.2. The results may be plotted as Work or "maximum strength in extension" vs the angle of parallelism and its effect thus will be established.

S.3.2 Testing programme for the investigation of the influence of the hoop thickness.

The effect of the thickness of the hoop may be studied in conjunction with the FE modelling. Using the existing software the effect of thickness can be studied via the strain energy output for any deformation and load applied for hoops of 30, 50, and 70 mm thickness. The FE model will indicate the changes to strain energy output with changes in the hoop thickness; these same thicknesses may then be investigated experimentally. The values of Work or "maximum strength in tension" will then be plotted vs the thickness of the hoops (or volume of hoops) and a relationship may thus be established. The experimental plots required are shown in fig. S.3.

S.3.3 Testing programme for further investigation of the rate of loading.

The influence of the rate of loading has already been investigated and the procedure used was satisfactory. It is desirable to continue this investigation with better control over time to failure. A particular rate of loading will take in consideration the minimum response time of the GDS loading system and it is suggested that this range should be restricted to no more than 30 seconds. More rates of loading should be investigated, in addition to the three already examined, in order to obtain a curve from which the effects of other rates may be assessed by extrapolation: particular interest would focus on those rates encountered in the commercial processes of rock comminution. The experimental results may be plotted as shown in fig. S.4.

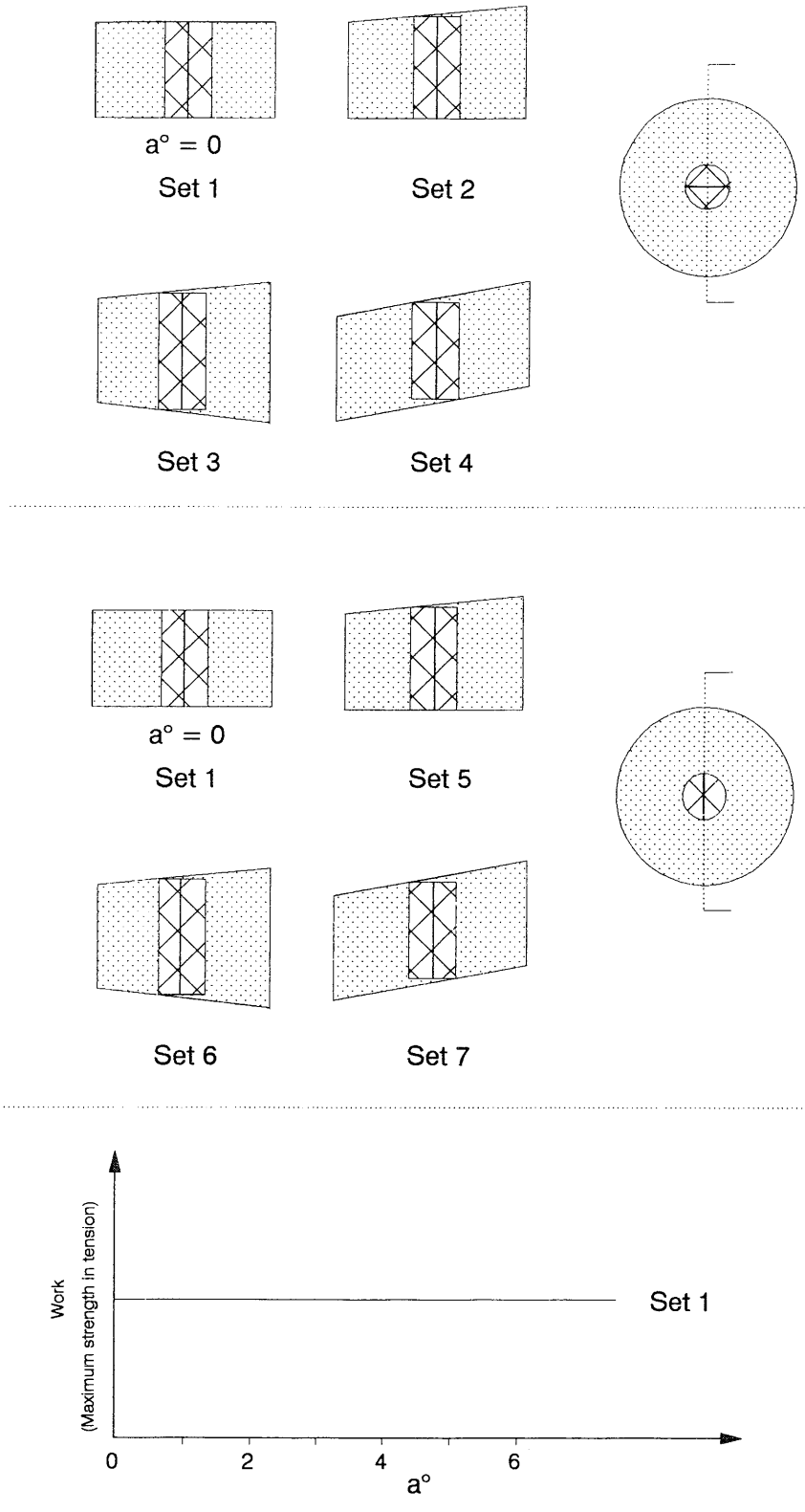


Fig. S.2 The seven sets of samples required to define influence of parallelism on the behaviour of HTT and an illustration of the graph for presenting results.

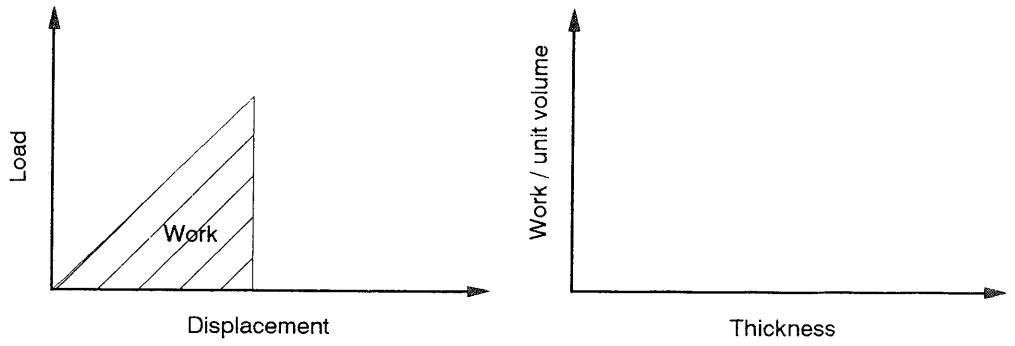


Fig. S.3 Suggested plots for data from tests investigating the influence of hoop thickness.

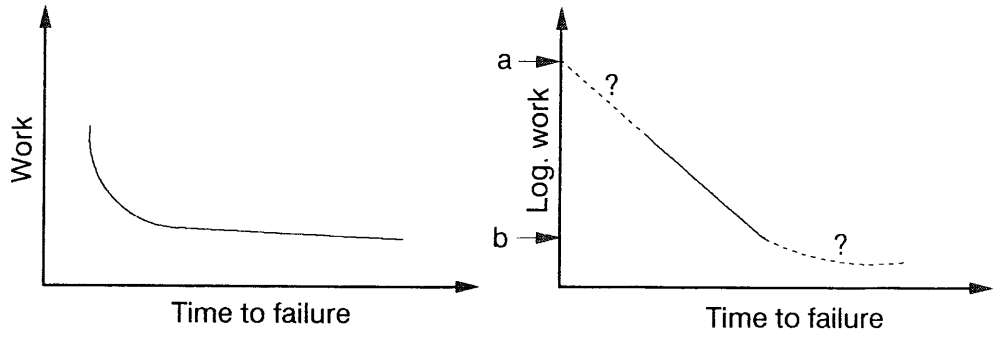


Fig. S.4 Suggested plots for data from tests investigating the influence of the rate of loading: 'a' and 'b' represent possible maximum and minimum values of intrinsic work per unit volume for failure.

S.3.4 Testing programme for the effect of different diameter ratios.

The effect of different diameters has been investigated and the results obtained in this thesis show that the amount of work (or "maximum strength in extension") required increases as the ratio of diameters increases: there appears to be a linear relationship (fig. 7.7 and fig. 7.8). This study must continue in conjunction with FE models and in broad terms is rather similar to (i) in as much as the behaviour of hoops of given ratios of inner and outer diameter, and E, ν values similar to those of real rock hoops to be tested, will be simulated and Load, Displacement for them predicted. These predicted values will then have to be verified experimentally and the obtained values of ultimate load and displacement compared with those predicted. What will then have to be established is the relationship between those parameters and the tensile strength obtained from the DTT i.e

Hoop strength for R/r = (x) x Tensile strength DTT, for similar volume

and whether (x) is simply a function of the dimensions that constitute the ratio of diameters. This is exactly the work about to be commenced by Park (PhD thesis in preparation).

It must be emphasised that in any of the above investigations, S.3.1 to S.3.4 only the specific parameter to be investigated should be allowed to vary in each test. Therefore, it is suggested that all samples are tested to begin with in oven dry condition with "smooth" platens.